"THE DEVELOPMENT OF AN ACOUSTIC TECHNIQUE FOR THE STUDY OF THE VISCOELASTIC PROPERTIES OF LIQUIDS AT MICROWAVE FREQUENCIES."

A Thesis submitted to the
Faculty of Engineering
of the
University of London
for the degree of
Doctor of Philosophy
(Electrical Engineering)
by

JOHN RICHTER

Electrical Engineering Department,
Imperial College of Science and Technology
University of London;

and

Electrical Engineering Department,
University of Glasgow.

July, 1966

ABSTRACT.

The development of an experimental electronic and acoustic system is described for viscoelastic investigations in the frequency range 300Mc/s to 2000Mc/s..

The viscoelastic properties of liquids are evaluated from measured values of the reflection coefficient when a plane shear wave is incident normally on a solid-liquid interface. Because of the high acoustic losses in isotropic materials at the frequencies of present interest it is necessary to use a low loss crystalline solid as the propagating medium. Theoretical investigations are carried out to assess the adequacy of the classical elasticity theory in describing microwave acoustic waves in anisotropic media. The dependence upon crystallographic orientation of all the important propagation and excitation properties for the three acoustic modes is fully determined in crystal quartz. A phenomenological theory, involving a viscosity tensor, is developed for the calculation of acoustic attenuation in an anisotropic viscoelastic medium. The anisotropic viscosity tensor of crystal quartz at room temperature is determined from precise attenuation measurements.

The experimental acoustic system employs a single crystal quartz rod. One end of the quartz is inside an electromagnetic cavity resonator and it acts as the electromechanical transducer operating by non-resonant surface excitation. A new theory of surface excitation is developed enabling the design and construction of a novel type of cavity resonator. The acoustic performance of the transducer system is determined by the piezoelectric field probe technique, developed for this purpose in the course of the present work.

The thesis also gives full description of the electronic system which has been developed. Owing to the high accuracy of the experimental system, it is possible to obtain excellent measurements of the real part of the mechanical impedance for liquids of any viscosity.

As an example of the application of this technique to the measurement of the viscoelastic properties on liquids, the temperature dependence of the limiting high frequency rigidity modulus of certain aromatic hydrocarbons is determined. To interpret these measurements a new theory is presented, relating the shear rigidity to free volume in a liquid.

ACKNOWLEDGEMENTS.

The author wishes to express his gratitude to Professor J. Lamb, who suggested the project and gave every encouragement and guidance during its execution. Sincere appreciation is expressed to Dr. A. J. Barlow for his continued interest in the research project. Thanks are also due to Dr. A. J. Matheson, Mr. J. H. Collins and other colleagues in the Electrical Engineering Department, University of Glasgow, for many helpful suggestions and discussions.

The author is indebted to Mr. R. Jefferyes and Mr. G. H. Robertson for their considerable help in programming, and to the University of Glasgow Computing Laboratory for their generous allocation of computing time.

The cooperation and assistance of the staff in the engineering workshops of the Electrical Engineering Departments of both Imperial College and Glasgow University are acknowledged.

The financial support of the National Engineering Laboratory, Ministry of Technology for a research program of which this work formed a part is thankfully acknowledged. Further support has been provided by Shell Research Ltd., the Worshipful Company of Clothmakers, and the Apparatus-on-Loan Scheme operated by Messrs Imperial Chemical Industries Ltd., for which thanks are expressed.

The author is grateful for personal assistance provided by a Hungarian Postgraduate Studentship of the London University Convocation Trust Fund (1959-1963), an award from the Department of Scientific and Industrial Research (1963), and the John and Frances Jones Supplementary Scholarship of the City and Guilds of London Institute (1959-1960).

CONTENTS.

ABSTRACT. 2
ACKNOWLEDGEMENT. 4
CONTENTS. 5
PRINCIPAL SYMBOLS. 9

PART I

FIELD OF STUDY.

CHAPTER 1. INTRODUCTION.

1.1 Historical 13
1.2 Present work 15
1.3 Presentation 17

CHAPTER 2. INTRODUCTORY THEORY FOR THE MACROSCOPIC DESCRIPTION OF A MATERIAL CONTINUUM.

2.1 The infinite anisotropic continuum 19
2.2 Dynamics 21
2.3 Balance of momenta 24
2.4 Energy balance 27
2.5 Linear constitutive relations 31
2.6 Linear viscoelastic response 33
2.7 Frequency-temperature superposition 39

PART II

THEORETICAL INVESTIGATIONS INTO SOME ASPECTS OF PROPAGATION AND EXCITATION OF ACOUSTIC WAVES AT MICROWAVE FREQUENCIES.

CHAPTER 3. SPECIAL FEATURES OF HIGH FREQUENCY ACOUSTIC WAVES.

3.1 Acoustic plane waves 42
3.2 Acoustic waves in anisotropic lossy media 43
3.3 Effect of couple stress 47
3.4 Piezoelectric interactions 56
3.5 Thermoelastic interactions 61

CHAPTER 4. PIEZOELECTRIC SURFACE EXCITATION.

4.1 Coupled waves 66

4.2 Simplified solution by wave superposition 70

4.3 The preferred directions of excitation 78

4.4 Practical conversion efficiency 86

CHAPTER 5. NUMERICAL RESULTS FOR THE ORIENTATION DEPENDENCE OF PROPAGATION AND EXCITATION PROPERTIES IN QUARTZ.

5.1 Organisation of the data 89

5.2 Presentation of results 92

PART III

THE EXPERIMENTAL SYSTEM.

CHAPTER 6. THE ELECTRONIC MEASURING SYSTEM.

6.1 General description 107

6.2 Pulse control unit 114

6.3 High voltage modulator 120

6.4 Planar triode oscillators 122

6.5 Circulator 127

6.6 TR devices 128

6.7 Mixer 135

6.8 IF amplifier 137

6.9 List of standard equipment 140

CHAPTER 7. THE TRANSDUCER SYSTEM 1: QUARTZ CRYSTALS.

7.1 Crystallographic orientation 142

7.2 Preparation of the crystal specimens 146

7.3 Parallelism and flatness 148

7.4 Surface finish 151

CHAPTER 8. THE TRANSDUCER SYSTEM 2: RESONANT CAVITIES.

8.1 Use of cavities 157

8.2 Physical arrangement of the single-tuned cavities 158

8.3 Physical arrangement of the tangential field cavity 161
8.4 Electrical properties 171
8.5 Field patterns in the cavities 178
8.6 Acoustic performance 190

CHAPTER 9. TEMPERATURE CONTROL.

9.1 General 198
9.2 High temperature thermostat 198
9.3 Low temperature thermostat 200

PART IV

VISCOELASTIC MEASUREMENT TECHNIQUE AND RESULTS.

CHAPTER 10. MEASUREMENT AND CALCULATION OF ANISOTROPIC ACOUSTIC ATTENUATION IN QUARTZ.

10.1 Measurements of attenuation 207
10.2 Attenuation by viscoelasticity 215
10.3 Conclusions 227

CHAPTER 11. THE MEASUREMENT OF MECHANICAL IMPEDANCE OF LIQUIDS. THEORY AND TECHNIQUE.

11.1 Mathematics of measurement 229
11.2 Measurement procedure 232
11.3 Accuracy considerations 235

CHAPTER 12. VISCOELASTIC RELAXATION AND THE LIMITING HIGH FREQUENCY MODULUS OF SOME LIQUIDS OF AROMATIC HYDROCARBONS.

12.1 Measurements of the temperature dependence of the rigidity modulus 241
12.2 Determination of the relaxation behaviour of sec-butyl benzene 253
12.3 Conclusions 256

PART V

APPENDICES.

A.	Symmetry and decomposition of Cartesian tensors	260
B.	Crystallographic symmetry operations of quartz	264
C.	Explicit forms of the tensors of strain, rotation and distortion	266
D.	Tables of admissible material coefficients for quartz when the antisymmetric stress is not neglected	268
E.	Expressions for tensor transformations in a medium possessing the crystalline symmetry of quartz	272
F.	Values of the material constants for quartz	278
G.	Propagation and reflection of acoustic plane waves in an anisotropic medium	282
H.	Details of computer calculations	289
I.	Analysis of operation of planar triode oscillators	292
J.	Density and viscosity data for the liquids investigated in Chapter 12	298

REFERENCES 299

PRINCIPAL SYMBOLS AND ABBREVIATIONS.

c_{ijkl}	elastic stiffness constant
C_{ij}	couple
C	effective elastic constant
D	effective dissipation constant
dB	decibel
D_n	electric flux density
E	effective (complex) elastic constant
e	effective piezoelectric coupling
E	energy
E_n	electric field strength
e_{ijk}	piezoelectric constant
e_i	excitation vector
FS	fast shear
f	frequency
f_i	force per unit area
F_i	force
f^M	force per unit area in mode M
G	rigidity modulus
G_{ijk}	couple stress
G	limiting high frequency rigidity modulus
H_m	magnetic field strength
J_j	flux
k	wave vector
L	longitudinal
M	mode (L, FS or SS)
$\hat{M}_i$	intrinsic angular momentum
n_j	unit vector normal to surface
R	resistance (electrical or mechanical)
$\hat{R}_i$	infinitesimal rotation
SS	slow shear

S_{kl}	strain
S	surface
s	entropy
T_{ij}	stress
$\hat{t}_i$	dual vector of antisymmetric stress
t	time
T	temperature
u_i	mechanical displacement
U	maximum displacement in an acoustic mode
U	specific internal energy
v	velocity of propagation
$v_i=\dot{u}_i$	displacement velocity
V	volume
X	(mechanical or electrical) reactance
x_i	space coordinate
$\hat{x}_{ij}$	local distortion
Z	(mechanical or electrical) impedance
α	attenuation per unit length
α'	attenuation per unit time
α_i	direction cosines of U
α	viscosity ratio
β	rigidity ratio
Γ_{ij}	Christoffel coefficient
Δ	Laplacian vector operator
ϵ_{ijk}	alternating tensor
ϵ_{ij}	dielectric constant
η	effective viscosity
η_{ijkl}	viscosity tensor
η_o	static viscosity of a liquid
Θ	internal preferred direction of excitation
θ	complex angle of reflection coefficient

ϑ	angle of rotated Y-cut
λ	wavelength
μ	magnetic permeability
ϱ	density
ϱ	reflection coefficient
Σ	entropy source density
τ	relaxation time
ϕ	energy deviation angle
ω	angular frequency
*	complex
$^+$	complex conjugate
$^-$	piezoelectrically stiffened
$^\wedge$	axial
^{S}	symmetric
^{A}	antisymmetric
^{D}	deviatoric
^{R}	recoverable
^{D}	dissipative

P A R T I .

FIELD OF STUDY .

CHAPTER 1.
INTRODUCTION.

1.1 HISTORICAL.

The classical theories of elasticity and viscosity classify deformable substances into the idealised categories of perfectly elastic solids or perfectly viscous fluids, according to the manner in which they respond to the application of stress. Solids are considered to respond by exhibiting strain which, according to Hooke's Law is directly proportional to stress. In fluids, as investigated by Newton, the response is viscous flow, where the applied stress is portional to the time rate of strain.

A few experimentally observed deviations from the behaviour of perfectly viscous liquids led Maxwell (1867) to introduce the concept of viscoelastic relaxation, characterised by the relaxation time τ. When a viscoelastic liquid is subject to a sudden application of stress, then for a time shorter than the viscoelastic relaxation time before viscous flow would accur, the liquid shows the characteristics of a solid. Voigt (1892) later defined the lossy solid which exhibits an increasing viscous effect as the time of observation becomes less than the viscoelastic relaxation time.

As sufficiently refined measurements were available it was realised that by assuming a spectrum of relaxation times, the exact viscous and elastic behaviour of all real liquids and solids could be adequately described. The relaxation spectrum is regarded here as a mathematical construction, resulting from the desire to give an easily manipulated mathematical expression for a complicated functional relationship between the stress and strain fields in a material body. No given component of the relaxation spectrum can

necessarily be identified with a single molecular process.

The rheological properties under consideration are assumed to be linear so that the superposition principle of stress and strain applies. In the case of small strains this assumption is realistic. Furthermore, by restricting the strain to be small, linear viscoelasticity avoids the use of more complex mathematics necessary to deal with finite strain.

Relaxation times vary from many years to picoseconds. As far as the theory of viscoelasticity is concerned, the difference between solid and liquid behaviour is attributed to a difference in the location of the relaxation on the time scale. For glasses and other solids the main part of the spectrum lies at times much larger than the time of ordinary laboratory experiments, as manifested for example by the flow of hard rock over geological times. For not very viscous liquids the main part of the relaxation occurs at times typically less than a nanosecond.

Experiments can be made readily in the laboratory to measure relaxation times from 1000 seconds to nanoseconds, over a logarithmic range of time of 12 decades. Using the principle of time-temperature superposition (e.g. Ferry, 1961), the relaxation behaviour of some liquid substances can be determined over 25 decades. This is a very wide range considering that the logarithmic time span from the beginning of the formation of the Earth to 1000 seconds is only about 14 decades.

For relaxation times shorter than a few fractions of a second, the most convenient method of determining the viscoelastic properties for small strains is that of subjecting the material to sinusoidal variations of shear stress and strain, for which case it is useful to define the relaxation frequency, f, as $f = 1/2\pi\tau$.

Electromechanical methods are used for investigations when relaxation frequencies are less than a few kilocycles per second (Mason, 1958; Lindon, 1965). The well-established measuring techniques in the range 10kc/s to 1Mc/s use resonant piezoelectric transducers, and the properties of the test liquids are evaluated from their altering the resonance parameters. In the 5 - 100Mc/s frequency range viscoelastic measurements are made by measuring the reflection coefficient when a plane shear wave is reflected at a solid-liquid interface. A survey of these various techniques is given by Barlow, Harrison, Richter, Seguin and Lamb (1961) and also by McSkimin (1964). H. Seguin (Lamb and Seguin, 1966) constructed an apparatus working at 3000Mc/s to investigate liquids of relatively high viscosity.

The development for commercial applications of polymers in which viscoelastic relaxation is of practical significance gave great impetus to theoretical and experimental work in the field of viscoelasticity (Ferry, 1961). Another practical application is in connection with lubrication (Barlow and Lamb, 1959).

Since any macroscopic deformation is accompanied by a complicated molecular readjustment, the macroscopically observed elastic and viscous phenomena arise out of the effects of various long-range and short-range molecular force fields. Viscoelastic investigations can then give an insight into the nature of these molecular forces leading to a better understanding of the fundamentals of the liquid state.

1.2 PRESENT WORK.

Liquids with simple molecules are desirable for the study of the effects of molecular structure upon relaxation behaviour. Such liquids, however, tend to have very short relaxation times,

and to study them a measuring system operating at correspondingly high frequencies is required. These high frequencies are also necessary to define the respective part of the relaxation spectrum of all viscoelastic substances. By extending the available frequency range it is possible to check the validity of the "reduction principle", based on time-temperature superposition (Barlow and Lamb, 1959) and widely used in analysing experimental results. Application of this reduction principle enables universal curves to be plotted by which the effect of an extension of the frequency range is simulated by a change of temperature.

The work described in this thesis is concerned with the development and use of an experimental system working at low microwave frequencies in the range 300Mc/s to 2000Mc/s, and capable of obtaining viscoelastic measurements of high precision on liquids of any viscosity. In the technique that has been developed one end of a cylindrical quartz crystal is placed inside an electromagnetic cavity resonator. On exciting the cavity with a pulsed oscillation a plane shear wave is generated in the quartz rod by piezoelectric surface excitation. The viscoelastic properties of the test liquids are calculated from the measured value of the reflection coefficient when the plane shear wave is reflected back towards the cavity by the quartz-liquid interface.

In contrast to fused quartz which is used exclusively in reflection coefficient techniques at lower frequencies and whose absorption of shear waves above about 300Mc/s becomes prohibitively high, (Jones et al. 1964) the present experimental system uses an anisotropic quartz crystal. A new theory of piezoelectric surface excitation is developed and in the light of the predictions of this theory a novel type of cavity resonator could be constructed. Due mainly to this new cavity-quartz transducer system, the experimental measurements are of high accuracy.

Theoretical investigations have been carried out to check whether microwave acoustic waves in an anisotropic medium possess any unusual properties that can affect the reflection coefficient measurements.

The new technique of excitation has been used with great success for precise measurements of acoustic attenuation in quartz. From these attenuation data it was possible to determine, for the first time, the anisotropic viscosity tensor of a crystal.

The variation with temperature of the limiting high frequency shear elasticity of liquids has been measured for certain aromatic hydrocarbons. The high frequency stress waves employed in the present technique enable one to obtain these measurements over a wide temperature range. $1/G_\infty$ has been found to vary linearly with temperature. This is in contrast to results of previous workers (Meister et al. 1960 ; Hirai, 1958) who obtained a different law for the temperature dependence from measurements at lower frequencies. The new measurements are interpreted by relating the shear rigidity to free volume in a liquid.

1.3 PRESENTATION.

This thesis is presented in five parts. Part I consists of general introduction and also introductory theory pertinent to the mathematical description of elastic and viscous phenomena in continuous material media. Part II gives the results of original theoretical investigations into the generation, propagation and attenuation of acoustic waves at microwave frequencies. In Part III the experimental system is described in detail. Part IV consists of the results of viscosity measurements on crystalline quartz and elastic rigidity measurements on some liquids of

relatively simple structure. Part V comprised of Appendices A – J gives additional information pertaining to the theory of high frequency acoustic waves, to the design of the experimental system and to viscoelastic measurements.

The results of theoretical calculations and experimental measurements are generally presented in the form of graphs, in order to give the information in a concise form.

CHAPTER 2.
INTRODUCTORY THEORY FOR THE MACROSCOPIC DESCRIPTION OF A MATERIAL CONTINUUM.

2.1 THE INFINITE ANISOTROPIC CONTINUUM.

In recent years the opinion has been expressed in various articles (Zubov and Firsova, 1956; Laval, 1957; Joel et al. 1958, 1960; Jaffe and Smith, 1961; Mindlin and Tiersten, 1962) that the "classical theory of elasticity" cannot account for some of the observed properties of elastic waves at very high frequencies. There is also some contraversy about the significance of the antisymmetric part of the stress tensor. In Section 3.3 of this thesis an attempt is made to decide the relevance of the "modern theories of elasticity" to microwave acoustics by testing some of their novel predictions. In this chapter the basic concepts of an elastic continuum are defined and the implicit assumptions reexamined, as they apply to the remainder of this thesis. The approach is considered unconventional. Parts of the material presented in this chapter are based on a set of duplicated notes for a postgraduate lecture series entitled "Modern Physical Acoustics" (Richter, 1962). The treatment will include the couple-stress, first proposed by the Cosserat Brothers (1909) and further developed by Toupin (1962, 1964) and Mindlin (1962) whose general lines of thought will be followed in this connection.

A solid or liquid medium is an aggregate of microscopic particles in dynamic equilibrium with each other. All the properties of such a medium ultimately depend upon the forces and movements relative to the constituent particles. In dealing with large scale motions, however, one can usually disregard the fine microscopic structure and take the medium as if it were an infinitely smooth continuum. The properties of the continuum are then

described by scalar, vector and higher rank tensor fields as functions of the time t and of the space coordinates in a reference frame x_i. (A short summary of those lesser known properties of tensors which play an important role in this and the following chapters is given in Appendix A.)

The macroscopic properties are averages of the microscopic values, the averages being evaluated over volumes of matter large enough to contain many particles, but negligibly small compared with all macroscopically significant dimensions. Although certain microscopic motions and forces are lost during the averaging process, they still contribute to macroscopically measured properties (e.g. internal energy, dielectric polarisation, etc.) That part of the internal energy that does not depend explicitly on macroscopic variables is defined as heat energy, and hence a link is established between continuum mechanics and thermodynamics.

The medium is assumed crystalline, isotropy being a special case. Its crystalline symmetry can be mathematically specified, differently from the usual practice of crystallographers, by giving the matrices of a group of linear operators, such that each operator is an identity operator due to the crystalline symmetry (Smith et al. 1963). This operator is useful in the practical calculation of the components of a tensor with a given crystallographic symmetry. The symmetry operators of the crystal class to which quartz belongs are listed in Appendix B.

All macroscopic movements in the continuous medium are described by the displacement field $u_i(x_i,t)$ where x_j is the position of the material particle at a reference time t_o. The infinitesimally small strain is defined as

$$S_{kl} = \frac{1}{2}\left(\frac{\partial u_k}{\partial x_l} + \frac{\partial u_l}{\partial x_k}\right) \qquad 2.1$$

The requirement of integrability imposed on the displacement gradients of Equation 2.1 gives the following compatibility condition (Prager, 1961, p.72)

$$\epsilon_{mik} \cdot \epsilon_{nkj} \cdot \frac{\partial}{\partial x_i} \frac{\partial}{\partial x_j} \frac{\partial u_k}{\partial x_l} = 0 \qquad 2.2$$

where ϵ_{ijk}, the alternating tensor, is defined in Appendix A. As in the rest of this work, the indices i to n can take the value of 1, 2 or 3 and summation over repeated indices is understood. Another form of the compatibility condition can be obtained by defining the axial vector of local rotation as

$$\hat{R}_i = \frac{1}{2} \epsilon_{ikl} \left(\frac{\partial u_k}{\partial x_l} - \frac{\partial u_l}{\partial x_k} \right) \qquad 2.3$$

(the time derivative of $\hat{R}_i$ is the angular velocity of local rotation, $\hat{\omega}_i$) and the tensor of local distortion as

$$\hat{x}_{ij} = \frac{\partial \hat{R}_i}{\partial x_j} \qquad 2.4$$

when

$$\epsilon_{imj} \frac{\partial}{\partial x_i} \hat{x}_{jl} = 0, \quad \hat{x}_{ii} = 0 \qquad 2.5$$

Therefore by Equation 2.5 the compatibility conditions require that the trace of the local distortion tensor be zero, when

$$\hat{x}_{ij} = \hat{x}^D_{ij} \qquad 2.6$$

Explicit forms of the tensors of strain, rotation and distortion are shown in Appendix C.

2.2 DYNAMICS.

Macroscopically there are two types of forces and couples acting on a small volume or mass element of the continuum:

a) Body forces and couples which are functions of position, and are proportional to the mass of the element. Microscopically, they are long-range interactions, arising as some distant action from within or outside the body.

b) Surface forces and couples. These are not assignable as functions of position, but are to be imagined as acting upon boundary surfaces in such a way as to be equivalent to the loading exerted by one portion of the material upon another. Microscopically they are caused by very short range interactions between adjacent microscopic elements.

The body forces and couples are described by vector fields. The surface forces and couples are described by mechanical stress tensor fields. In what follows it is assumed that no body forces or couples are present. Their inclusion in the treatment is of no practical value in connection with the present work.

Considering the elementary cube $dx_1 dx_2 dx_3$, the surface forces per unit area acting on the sides of the cube define the components of the ordinary stress tensor T_{ij}. The first index specifies the direction of the force and the second index shows the direction of the normal to the plane on which the force acts. The components of T_{ij} transform as those of a tensor of rank two.

When considering the equilibrium of a macroscopic body, not only forces, but also couples have to be taken into account. These couples cause the curved distortion of the unit cell and were first introduced into the theory of elasticity by the Cosserats (1909). Couple being the product of length and force is defined as

$$C_{ij} = \frac{1}{2}\left(x_i F_j - x_j F_i\right) = - C_{ji} \qquad 2.7$$

It is an antisymmetric tensor of rank two. In three dimensions such a tensor has 3 independent components, therefore it can be associated with a dual "axial" vector that has the same 3 components (Appendix A). It is necessary to distinguish between ordinary or polar, and axial vectors because their transformation properties are different when the coordinate transformation involves the inversion of one or all 3 of the axes, a situation often encountered when examining the symmetry of tensors in a crystalline medium.

Since couple is already a tensor of rank two, the couple stress G_{ijk} is a polar tensor of rank 3. The fact that the various couples on the sides of the cube are the components of a tensor can be proved by considering the equilibrium of a tetrahedron in an entirely analogous way as the tensorial character of the force stress is proved. The antisymmetry of the first two indices of G_{ijk} restricts the number of independent components from the general 27 to 9. Therefore the association of G_{ijk} with a (neither symmetric, nor antisymmetric) axial tensor of rank 2 with 9 components, $\hat{G}_{lk}$, is justified. Further details on the symmetry properties are found in Appendix A.

Considering a part of a material bounded by a stationary surface S, the forces and couples exerted on it by the contact loads are:

$$(\text{Total force})_i = \oint T_{ij}\, dn_j = \int \frac{\partial}{\partial x_j} (T_{ij})\, dV \qquad 2.8$$

$$(\text{Total couple})_{ij} = \oint (x_i T_{jl} + G_{ijl}) dn_l = \int \frac{\partial}{\partial x_l} (x_i T_{jl} + G_{ijl}) dV \qquad 2.9$$

The extreme right hand side of the above expressions have been obtained by the application of the Green-Gauss divergence theorems. The integrand of the volume integrals can be regarded

as effective body force F_i or couple G_{ij} per unit volume. If in Equation 2.8 the stress tensor is decomposed into symmetric and antisymmetric parts (c.f. Appendix A) and the antisymmetric part T^A_{ij} is described by its dual $\hat{t}_i$ according to the associating equation A.15, the effective force per unit volume is

$$F_i = \frac{\partial}{\partial x_j} T_{ij} = \frac{\partial}{\partial x_j} T^S_{ij} + \frac{1}{2} \mathrm{curl}_i \hat{t} \qquad 2.10$$

The tensors of rank three occurring in Equation 2.9 can be substituted by their axial duals. These duals decompose into two parts (Equation A.19), a spherical part $\frac{1}{3} \cdot \mathrm{tr} \hat{G} \cdot \delta_{ij}$ and a deviatoricpart $\hat{G}^D_{ij}$. The effective couple per unit volume is then

$$\hat{G}_i = -\hat{t}_i + \mathrm{grad}_i \frac{1}{3} \mathrm{tr} \hat{G} + \frac{\partial}{\partial x_l} \hat{G}^D_{il} + \epsilon_{ijk} x_j \left[\frac{\partial T^S_{kl}}{\partial x_l} + \frac{1}{2} \mathrm{curl}_k \hat{t} \right] \qquad 2.11$$

2.3 BALANCE OF MOMENTA.

The most successful unifying approach of electromagnetic and elastic field theories is to express quantities of physical interest in a balance equation, either of integral or differential form:

$$\frac{\partial}{\partial t} \int_V A \, dV = - \int_S \phi_A \, dS + \int_V \Sigma_A \, dV \, , \qquad 2.12$$

$$\frac{\partial A}{\partial t} = - \mathrm{div} \, \phi_A + \Sigma_A \qquad 2.13$$

with the following meaning. In a stationary volume V enclosed by surface S any change in the quantity $\int A dV$ is caused either by a flux of A, $-\int \phi_A \, dS$ or by a source of A, $\int \Sigma_A \, dV$. Since mass has no source, the conservation of mass can be expressed as

$$\frac{\partial \varrho}{\partial t} = - \mathrm{div} \, \varrho \, v_i = - \frac{\partial}{\partial x_i} (\varrho v_i) \qquad 2.14$$

where v_i is the particle velocity, $\frac{\partial u_i}{\partial t}$. With the help of Equation 2.14 and the differentiation rule for products, the material time derivative is defined as

$$\varrho \frac{dA'}{dt} = \varrho \frac{\partial A'}{\partial t} + \varrho \frac{\partial A'}{\partial x_j} \frac{\partial x_j}{\partial t} = \frac{\partial}{\partial t}(\varrho A') + \frac{\partial}{\partial x_j}(A' v_i) \qquad 2.15$$

where A' is referred to unit mass.

The change of linear momentum ϱv_i inside a stationary surface enclosing part of a material body is due either to convection of momentum by moving mass across the surface or to the accelerating action of forces. In differential form this balance equation is given by

$$\frac{\partial \varrho v_i}{\partial t} = - \frac{\partial}{\partial x_j} (\varrho v_i v_j) + F_i \qquad 2.16$$

With the definition of the material time derivative, Equation 2.16 yields the familiar form of Newton's law of motion:

$$\varrho \frac{dv_i}{dt} = F_i \qquad 2.17$$

The force is given by Equation 2.10, so the equation of motion in the continuum follows as

$$\varrho \frac{dv_i}{dt} = \frac{\partial}{\partial x_j} T_{ij} = \frac{\partial}{\partial x_j} T^S_{ij} + \frac{1}{2} \mathrm{curl}_i \hat{t} \qquad 2.18$$

The angular momentum density of the reference volume consists of intrinsic angular momentum per unit mass $\hat{M}_i$ and angular momentum density $\epsilon_{ijk} x_j v_k$ (= cross-product of $\underline{x}$ and $\underline{v}$) owing to the

rotation of the volume as a whole. Any change in the angular momentum of a material volume element is due to the action of couples, so the balance equation of angular momentum, obtained similarly to Equation 2.18 is given as

$$\rho \frac{d}{dt} (\hat{M}_i + \epsilon_{ijk} x_j v_k) = \frac{\partial}{\partial x_l} (\epsilon_{ijk} x_j T_{kl} + \hat{G}_{il}) \qquad 2.19$$

Taking the first moment of Equation 2.18 about an arbitrary origin gives

$$\rho \epsilon_{ijk} x_j \frac{dv_k}{dt} = \epsilon_{ijk} x_j \frac{\partial T_{kl}}{\partial x_l}$$

$$= \frac{\partial}{\partial x_l} (\epsilon_{ijk} x_j T_{kl}) - \epsilon_{ijk} \frac{\partial x_j}{\partial x_l} T_{kl} \qquad 2.20$$

Subtracting Equation 2.20 from Equation 2.19, and using the definition for the dual of the antisymmetric stress (Equation A.15) yields the balance of intrinsic angular momentum:

$$\rho \frac{d\hat{M}_i}{dt} = \frac{\partial \hat{G}_{il}}{\partial x_l} - \hat{t}_i \qquad 2.21$$

Let the continuum be divided into elementary rigid cubes of side 1. The intrinsic angular momentum per unit volume is the sum of the inertias of the constituent elementary cubes in a unit volume multiplied by a conveniently chosen mean angular velocity:

$$\rho \hat{M}_i = \left(\frac{1}{1^3}\right)\left(1^3 \rho \frac{1^2}{6}\right)\hat{\omega}_i = \rho \frac{1}{6} 1^2 \hat{\omega}_i \qquad 2.22$$

It can be seen that the intrinsic angular momentum is dependent

on a characteristic length l associated with the size of that part of the medium rotating together as a rigid body. Since l is about molecular size, it is much smaller than a characteristic length (wavelength) of a practical wave motion so the intrinsic angular momentum is negligible, compared with the angular momentum due to local rotation.

When $\hat{M}_i = 0$, Equation 2.21 gives

$$\hat{t}_i = \frac{\partial \hat{G}_{il}}{\partial x_l} \qquad 2.23$$

and the linear momentum equation can be rewritten as

$$\rho \frac{dv_i}{dt} = \frac{\partial}{\partial x_j} T^S_{ij} + \frac{1}{2} \epsilon_{ijk} \frac{\partial}{\partial x_j} \frac{\partial}{\partial x_l} \hat{G}^D_{kl} \qquad 2.24$$

The first term in Equation 2.24 has the generalised div operator acting on the symmetric stress tensor. The second term contains the curl operator acting on the gradients of the deviatoric couple stress. (The trace of G does not contribute to the force since the operator curl grad is identically zero). In the classical theory of elasticity this second term does not appear. The double differential operator might suggest that the effect of the couple stress can be more noticeable with waves of high frequencies.

2.4 ENERGY BALANCE.

Multiplying the balance equation of linear momentum (Equation 2.24) by v_i, the balance of kinetic energy is obtained:

$$v_i \rho \frac{dv_i}{dt} = \frac{d}{dt} \left(\tfrac{1}{2} \rho v^2\right)$$

$$= v_i \frac{\partial}{\partial x_j} T^S_{ij} + \frac{1}{2} v_i \epsilon_{ijk} \frac{\partial}{\partial x_j} \frac{\partial}{\partial x_l} \hat{G}^D_{kl} \qquad 2.25$$

The total energy is conserved: any change in the total energy is due to a flow of energy J^E across the boundaries (E = energy per unit mass):

$$\rho \frac{dE}{dt} = - \frac{\partial}{\partial x_j} J^E_j \qquad 2.26$$

The total energy per unit mass consists of kinetic energy, potential energy of long-range forces and internal energy. (This statement can serve as the definition of internal energy).

$$E = K + P + U \qquad 2.27$$

where all the energies are referred to unit mass. The efflux of energy J^E, (efflux, rather than influx, since the surface normal pointing outwards from the control surface is defined as positive) consists of work done on the boundaries of the system by external forces and couples, and also of heat flow:

$$J^E_j = - T_{ij} v_i - \hat{G}_{kl} \hat{\omega}_k + J^Q \qquad 2.28$$

(With the previous definitions of T_{ij}, v_i, $\hat{G}_{ij}$ and $\hat{\omega}_i$ positive work requires the negative sign).

The balance of internal energy is found, in the absence of long-range forces, as

$$\rho \frac{dU}{dt} = \rho \frac{dE}{dt} - \frac{d}{dt} (\tfrac{1}{2} \rho v^2) \qquad 2.29$$

therefore, by Equations 2.25, 2.26, 2.28 and 2.29

$$\rho \frac{dU}{dt} = T^S_{ij} \frac{\partial v_i}{\partial x_j} + \hat{G}^D_{ij} \frac{\partial \hat{\omega}_i}{\partial x_j} - \text{div } J^Q \qquad 2.30$$

or

$$\rho \frac{dU}{dt} = T^S_{ij} \frac{\partial}{\partial t} S_{ij} + \hat{G}^D_{ij} \frac{\partial}{\partial t} \hat{x}^D_{ij} - \text{div } J^Q \qquad 2.31$$

where S_{ij} is symmetric strain and $\hat{x}^{D}_{ij}$ is the deviatoric part of the local distortion tensor (Equation 2.5). In polarisable media the term $E_i \frac{\partial}{\partial t} D_i$ also occurs in Equation 2.31 with E_i and D_i as the electric field strength and flux density vectors, respectively.

The above expression for the internal energy does not contain antisymmetric stresses. In the usual derivation of the internal energy expression, when the couple-stresses are not taken into consideration, the stress and the displacement gradients contain both symmetric and antisymmetric parts. The antisymmetric part of the (rank 3) couple-stress does not occur in the internal energy expression because it is multiplied by the antisymmetric part of the (rank 3) local distortion tensor, which is zero as a consequence of the compatibility condition Equation 2.5.

The simultaneous presence of stresses and strains in a material medium is the cause of both recoverable and dissipated internal energy. The recoverable internal energy is available to do mechanical work, while the dissipated energy is converted into heat (Q) irreversibly.

It is proposed to regard the strain as consisting of two (additive) parts:

$$S_{ij} = {}^{R}S_{ij} + {}^{D}S_{ij} \qquad 2.32$$

these parts being defined by the requirement that the product of the stress and the recoverable strain gives the stored energy and the product of the stress and the dissipative strain gives the dissipated energy. The current literature of irreversible thermodynamics sometimes divides the stress (but not the strain) into the above two parts (deGroot and Mazur, 1962). Both representations are permissible. The now proposed division of the strain will give more convenient forms when the relaxational properties of liquids are examined.

The concept of entropy is introduced so that the rate of heat input $Q - \mathrm{div} J^Q$ could be written as a total differential:

$$Q - \mathrm{div} J^Q = T \rho \frac{ds}{dt} \qquad 2.33$$

where T is the temperature and s is the entropy per unit mass. Combining Equations 2.31, 2.32 and 2.33 gives the internal energy as

$$\rho \frac{dU}{dt} = T^S_{ij} \frac{\partial}{\partial t} {}_R S_{ij} + \hat{G}^D_{ij} \frac{\partial}{\partial t} {}_R \hat{x}^D_{ij} + \rho T \frac{ds}{dt} \qquad 2.34$$

or, in differential form

$$\rho \, dU = T^S_{ij} d_R S_{ij} + \hat{G}^D_{ij} d_R \hat{x}^D_{ij} + \rho T ds \qquad 2.35$$

The entropy is given as

$$\rho \frac{ds}{dt} = \frac{1}{T} T^S_{ij} \frac{\partial}{\partial t} D S_{ij} + \frac{1}{T} \hat{G}^D_{ij} \frac{\partial}{\partial t} D \hat{x}^D_{ij} - \frac{1}{T} \mathrm{div} J^Q_q \qquad 2.36$$

Equation 2.36 can be given in a slightly different form by application of the rule of the differentiation of a product

$$\rho \frac{ds}{dt} = \frac{1}{T} T^S_{ij} \frac{\partial}{\partial t} D S_{ij} + \frac{1}{T} \hat{G}^D_{ij} \frac{\partial}{\partial t} D \hat{x}^D_{ij} - \mathrm{div} \frac{J^Q_q}{T} - \frac{1}{T^2} J^Q_q \, \mathrm{grad}_q T \qquad 2.37$$

The balance equation of the entropy takes the following form (deGroot and Mazur, 1962):

$$\rho \frac{ds}{dt} = - \mathrm{div} J^S_q + \Sigma \qquad 2.38$$

where

J^S = entropy flow

Σ = entropy production (per unit mass and unit time).

Comparing Equations 2.37 and 2.38 it is found that

$$J_q^S = \frac{J_q^Q}{T} \qquad 2.39$$

$$\Sigma = \frac{1}{T} T_{ij}^S \frac{\partial}{\partial t} D^S{}_{ij} + \frac{1}{T} \hat{G}_{ij}^D \frac{\partial}{\partial t} D\hat{x}_{ij}^D - \frac{J_q^Q}{T^2} \operatorname{grad}_q T \qquad 2.40$$

The product of entropy production and temperature has the dimension of power, therefore it is convenient to define the dissipation function Δ as

$$\Delta = \Sigma T = T_{ij}^S \frac{\partial}{\partial t} D^S{}_{ij} + \hat{G}_{ij}^D \frac{\partial}{\partial t} D\hat{x}_{ij}^D - J_q^Q \frac{\operatorname{grad}_q T}{T} \qquad 2.41$$

According to Equations 2.40 or 2.41 irreversible entropy production occurs, or power is dissipated because of the presence of dissipative strain rates, dissipative distortion rates or because of heat flow across a temperature gradient. The second law of thermodynamics states that the entropy production (and hence the dissipation function) is always positive.

2.5 LINEAR CONSTITUTIVE RELATIONS.

Both the internal energy (Equation 2.35) and the dissipation function (Equation 2.41) are the sum of terms involving two variables. One of these variables can be regarded as the independent variable. Then the other variable is the response of the material medium, and the internal energy can be expressed with the help of the independent variables as

$$U = f(x, t, v_1, \ldots v_n, s) \qquad 2.42$$

where s is the entropy and $v_1 \ldots v_n$ are (reversible) mechanical, electromagnetic, chemical, etc. independent variables. Any small change in the thermodynamic state is given by the partial derivative

$$dU = \left(\frac{\partial U}{\partial s}\right) ds + \left(\frac{\partial U}{\partial v_1}\right) dv_1 + .. + \left(\frac{\partial U}{\partial v_n}\right) dv_n \qquad 2.43$$

Comparing Equations 2.35 and 2.43, the dependent variables are found as: (T temperature)

$$\frac{\partial U}{\partial v_n} = \tau_n , \qquad \frac{\partial U}{\partial s} = T \qquad 2.44$$

The material response function, (for the generalities c.f. Truesdell, 1960, pp. 700) inherent in Equation 2.42 is expressed by the sum of partial derivatives for small changes from equilibrium conditions as

$$\tau_n = \left(\frac{\partial \tau_n}{\partial v_m}\right)_o v_m \qquad 2.45$$

which can be regarded as the linear terms with constant coefficients of a Taylor series expansion of the general function, valid for small deviations τ_n and v_m from equilibrium. (The subscript o is indicating that the differential is to be evaluated at equilibrium.) The constant coefficients in Equation 2.45

$$\left(\frac{\partial \tau_m}{\partial v_m}\right)_o = \left(\frac{\partial^2 U}{\partial v_m \partial v_n}\right)_o \qquad 2.46$$

are parameters of the medium.

A functional relationship, characteristic to the material medium, also exists between the dependent and independent variables occuring in the dissipation function (Equation 2.41). It is usually sufficient to take this relationship as linear, and therefore establish a second set of linear constitutive equations whose constant coefficients are the dissipative parameters of the medium in question (deGroot and Mazur, 1962; Eringen, 1962).

The two sets of linear constitutive equations of a general medium involve all possible mechanical, thermal, electromagnetic and chemical variables. In most cases of practical interest it is permissible to consider special classes of materials in which only one or two of these variables are operating.

2.6 LINEAR VISCOELASTIC RESPONSE.

The variables that will be considered important for this medium are stress, strain, temperature and entropy. The strain is assumed to have both recoverable and dissipative parts, according to Equation 2.32. The recoverable strain is involved with the stress, the entropy and the temperature in a set of linear constitutive relations of the type of Equation 2.45, which, after rearrangement, has the form of

$$
\begin{aligned}
{}_{R}S_{ij} &= c^{-1}_{ijkl}\, T_{kl} + \beta_{ij}\, T \\
s &= -\beta_{ij} T_{ij} + \delta T
\end{aligned}
\qquad 2.47
$$

All the coefficient tensors are symmetric, since they have been drived from the internal energy by double partial differentiation, as indicated by Equation 2.46.

The dissipative strain rate plays a role in the dissipative constitutive relations:

$$
\begin{aligned}
{}_{D}S_{ij} &= \eta^{-1}_{ijkl}\, T_{kl} \\
J^{Q}_{q} &= \lambda_{qk}\, \mathrm{grad}_{k}\, T
\end{aligned}
\qquad 2.48
$$

In equation 2.48 the cross-coupling between the temperature gradient and the stress is deemed negligible in general. If it existed, the coefficient of coupling had the same symmetry as the

piezoelectric coefficient, and would therefore certainly be zero for isotropic media. The coefficient tensors are again symmetric as a consequence of the fact that each term in the dissipation function is positive, no matter in what coordinate system the variables are defined.

Differentiating the first equation of 2.47 with respect to time and adding to the first equation of 2.48 yields:

$$\frac{\partial}{\partial t} S_{ij} = (c^{-1}_{ijkl} \frac{\partial}{\partial t} + \eta^{-1}_{ijkl}) T_{kl} + \beta_{ij} \frac{\partial T}{\partial t}$$

$$s = -\beta_{ij} T_{ij} + \delta T \qquad 2.49$$

$$J_q = -\lambda_{qk} \operatorname{grad}_k T$$

These equations are found to describe the properties of relaxing viscoelastic substances. For the case of isotropy, Curie's Law (Curie, 1908; deGroot and Mazur, 1962) states that there is no coupling between quantities of differing tensorial character in the linear constitutive equations. After decomposing the symmetric stress and strain tensors into scalar and deviatoric parts (Equations A.10 and A.13) Equation 2.49 has the following specific form in case of isotropy:

$$\operatorname{tr} \dot{S}_{ij} = \kappa \frac{1}{3} \operatorname{tr} \dot{T}_{ij} + \frac{1}{\eta_v} \frac{1}{3} \operatorname{tr} T_{ij} + \bar{\alpha} \dot{T}$$

$$s = -\frac{1}{\varrho} \bar{\alpha} \operatorname{tr} T_{ij} + c \frac{T}{T_o} \qquad 2.50$$

$$J_q = -\lambda \operatorname{grad}_q T$$

$$\dot{S}^D_{ij} = \frac{1}{G} \dot{T}^D_{ij} - \frac{1}{\eta} T^D_{ij}$$

where

κ isothermal compressibility

η_v effective volume viscosity

G rigidity modulus (Twice the value of the tensor component)

η effective shear viscosity (Twice the value of the tensor component)

$\bar{\alpha}$ coefficient of volume expansion

c specific heat (at constant stress)

λ heat conductivity

The deviatoric parts of the stress and strain completely separate from scalar parts and from the thermal parameters. These deviatoric parts are more conveniently expressed as

$$T^D_{ij} + \frac{\eta}{G}\frac{\partial T^D_{ij}}{\partial t} = \eta \frac{\partial S^D_{ij}}{\partial t} \qquad 2.51$$

where $\eta/G = \tau$ defines the stress relaxation time. The propagation of shear waves only involves the deviatoric parts of the stress and strain tensors, and for simplicity Equation 2.51 will be written as

$$T + \tau \frac{\partial}{\partial t} T = \eta \frac{\partial}{\partial t} S \qquad 2.52$$

It has to be emphasised that all the above relationships represent a first-order approximation, and therefore are valid only for infinitesimally small amplitudes.

Considering sinusoidal time variation the following stress-strain relationship is given by Equation 2.52

$$T = \eta \frac{j\omega}{1 + j\omega\tau} S = G \frac{j\omega\tau}{1 + j\omega\tau} S \qquad 2.53$$

When for the frequency used in an experiment $\omega \ll \frac{1}{\tau}$,

$$T = \eta j\omega S \qquad 2.54$$

On the other hand, when $\omega \gg \frac{1}{\tau}$

$$T = G S \qquad 2.55$$

Equations 2.54 and 2.55 describe viscous and elastic behaviour, respectively. Materials exhibiting such viscoelastic behaviour were first examined by Maxwell (1867). He proposed the idea that if the shape of a volume of gas or liquid were instantaneously changed, this change would be opposed by elastic forces. However, in a length of time, characterised by τ the molecules will rearrange to relieve the stresses. The molecular flow consists of jumps of individual molecules from equilibrium position to equilibrium position, aided by thermal agitation. The time period between successive jumps depends on the probability of the molecule attaining sufficient thermal energy (activation energy) to overcome its potential barrier. Hence the relaxation time in a volume element small enough to contain only the immediate environment of the molecule in question is given by a probability function. A macroscopic volume element contains a large number of Maxwell-elements, and upon the application of the change of shape the resultant macroscopic stress is the sum of all microscopic stresses:

$$T = \sum T_n = \sum g_n \frac{j\omega\tau_n}{1 + j\omega\tau_n} \cdot S \qquad 2.56$$

When the number of the individual Maxwell-elements is very large the summation approaches an integral

$$T = \int_0^\infty g(\tau) \frac{j\omega\tau}{1 + j\omega\tau} d\tau \cdot S \qquad 2.57$$

where $g(\tau)\,d\tau$ is the contribution to the rigidity by those Maxwell-elements whose relaxation times lie between τ and $\tau + d\tau$.

At frequencies higher than the frequency corresponding to the shortest relaxation times $1+j\omega\tau \simeq j\omega\tau$, and hence

$$G_\infty = \int_0^\infty g(\tau)\,d\tau \qquad 2.58$$

The frequency-dependent complex rigidity can now be given as

$$G = G_\infty \int_0^\infty q(\tau)\,\frac{j\omega\tau}{1 + j\omega\tau}\,d\tau \qquad 2.59$$

where $q(\tau)$ is the normalised distribution of relaxation times:

$$\int_0^\infty q(\tau)\,d\tau = 1 \qquad 2.60$$

It is customary to express the frequency dependent real and imaginary parts of the complex rigidity modulus as

$$G = G' + jG'' = G' + j\omega\eta_{dyn} \qquad 2.61$$

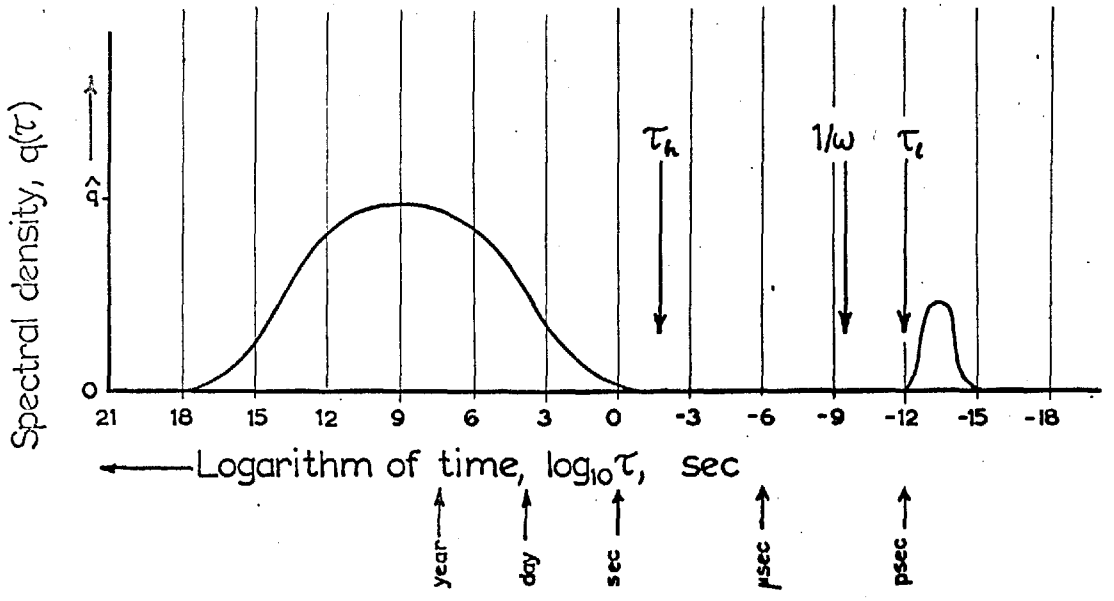
G' and η_{dyn} are dynamic rigidity and dynamic viscosity, respectively.

Liquids exhibit Newtonian viscosity at frequencies much lower than the one corresponding to the longest relaxation time, when

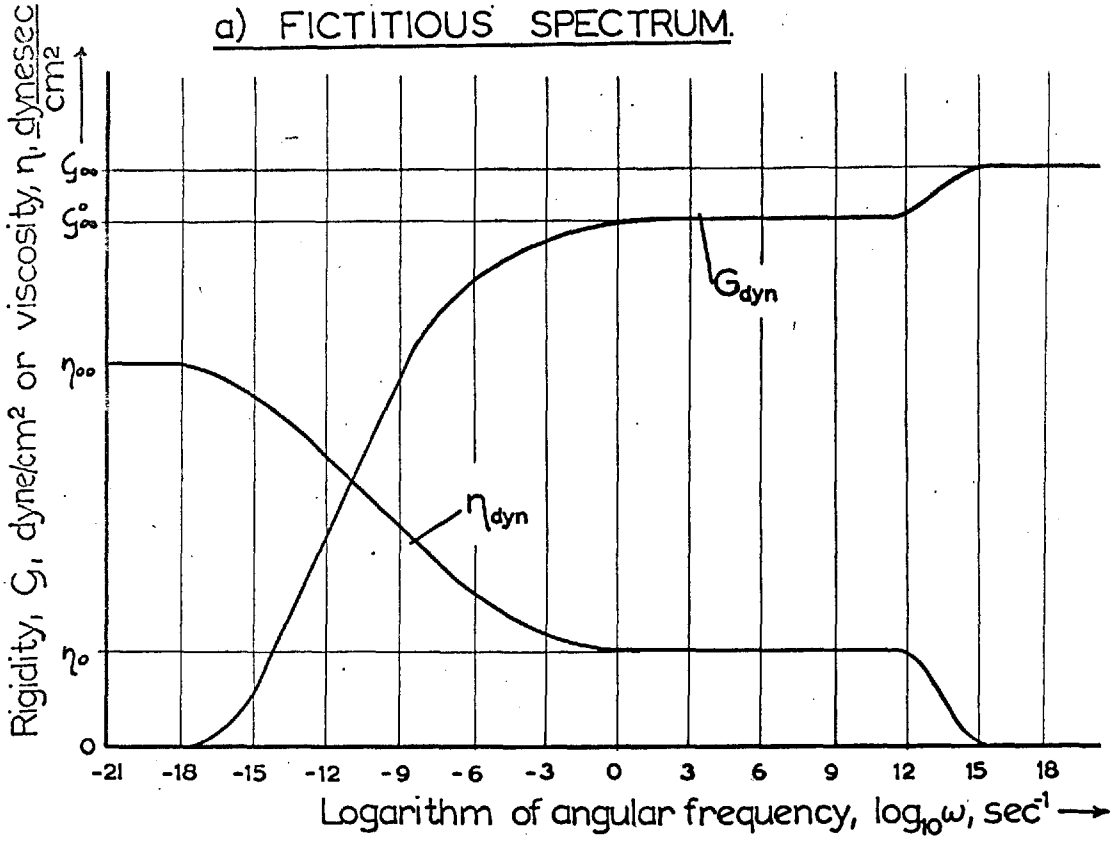
$$G = \int_0^\infty g(\tau)\,j\omega\tau\,d\tau = j\omega \int_0^\infty \eta(\tau)\,d\tau = j\omega\eta_0 \qquad 2.62$$

where η_0 is the steady-flow shear viscosity.

A lossy solid has a spectrum with relaxation times both longer and shorter than the characteristic time of the experiment. Such a fictitious spectrum (say, at room temperature) is shown in Fig. 2.1a, where in a frequency range $\frac{1}{\tau_h} < \omega < \frac{1}{\tau_l}$ around



a) FICTITIOUS SPECTRUM.



b) THE RESULTING DYNAMIC VISCOSITY AND RIGIDITY.

FIG. 2.1 RELAXATION BEHAVIOUR OF A SOLID.

the frequency of measurements the distribution density of the relaxation times is negligibly small. The complex rigidity of this material can be obtained approximately as

$$G = \int_0^{\tau_k} \frac{g(\tau)\, j\omega\tau}{1 + j\omega\tau}\, d\tau + \int_{\tau_\ell}^{\infty} \frac{g(\tau)\, j\omega\tau}{1 + j\omega\tau}\, d\tau \qquad 2.63$$

When $\omega\tau_k \gg 1$ and $\omega\tau_\ell \ll 1$, Equation 2.63 is simplified as

$$G = \int_0^{\tau_k} g(\tau)\, d\tau + j\omega \int_{\tau_\ell}^{\infty} g(\tau)\, \tau\, d\tau = G_o + j\omega\eta_o \qquad 2.64$$

In the frequency range that has been considered above both G_o and η_o are constants independent of the frequency. For frequencies covering the whole of the relaxation spectrum the dynamic rigidities and viscosities are shown in Fig. 2.1b.

2.7 FREQUENCY-TEMPERATURE SUPERPOSITION.

The material constants appearing in the constitutive relations, obtained for infinitesimally small deviations from equilibrium, are functions of the equilibrium conditions (c.f. Equation 2.45). In connection with this thesis, the most important macroscopic variable on which the material coefficients depend is the temperature. All liquids investigated seem to obey the principle of frequency-temperature superposition (Equation 2.67) (Ferry, 1961; Barlow, 1959), based on the following two postulates:

a) The temperature variation of the relaxation times is the same for all the relaxation components of the spectrum:

$$\frac{\tau_{(T)}}{\tau_{(T_r)}} = \alpha_{(T)} \qquad 2.65$$

b) The temperature dependence of the limiting high frequency modulus is the same for all the relaxation components of the spectrum:

$$\frac{G(T)}{G(T_R)} = \beta(T) \qquad 2.66$$

T_R refers to a selected reference temperature. Substitution of Equations 2.65 and 2.66 into Equation 2.59 gives

$$G_T = \beta\, G_{T_R} \cdot (\alpha\omega) \qquad 2.67$$

Hence varying the temperature has the same effect (through α) on the complex rigidty modulus as varying the frequency. In the limiting cases of very low frequencies:

$$\frac{\eta_T}{\eta_{T_R}} = \alpha\beta \qquad 2.68$$

and for very high frequencies

$$\frac{G_T^{\infty}}{G_{T_R}^{\infty}} = \beta \qquad 2.69$$

Therefore measurements of static viscosity as a function of temperature gives the value of $\alpha\beta$. Measurement of the limiting rigidity modulus at very high frequencies as a function of temperature gives the value of β.

By the application of the time-temperature superposition principle it is possible to cover the very large frequency (or time) range of 10^{24}:1, when both the frequency and the temperature is varied in a series of measurements.

PART II.

THEORETICAL INVESTIGATIONS INTO SOME ASPECTS OF PROPAGATION AND EXCITATION OF ACOUSTIC WAVES AT MICROWAVE FREQUENCIES.

CHAPTER 3.
SPECIAL FEATURES OF HIGH FREQUENCY ACOUSTIC WAVES.

3.1 ACOUSTIC PLANE WAVES.

The basic equation of motion is the balance of linear momentum, given in Equation 2.18. When the second order effect of variation in density with time is neglected for small amplitude disturbances, this balance equation can be given as

$$\rho \frac{\partial^2 u_i}{\partial t^2} = \frac{\partial T_{ij}}{\partial x_j} \qquad 3.1$$

With the help of the constitutive relations, connecting the stress to strain and other variables, the stress can be eliminated in Equation 3.1, giving a wave equation for the displacement vector u_i. The term ultrasonic waves will refer to longitudinal (compressional) vibrations, while the term acoustic waves will cover both longitudinal and transverse vibrations.

The constitutive relations (Equation 2.45) involve elastic, thermal and electromagnetic variables. Therefore the acoustic waves are coupled to electromagnetic and thermal waves through the piezoelectric constant and the thermal expansion coefficient. In order to avoid undue complications, the various coupling effects are examined separately. The actual coupling is found to be small in cases of practical interest. The piezoelectric coupling is non-dispersive and can be taken into account by a slight modification in the values of the elastic constants. Thermal coupling is dispersive, but it involves only the longitudinal mode. The presence of couple stresses could make the acoustic shear modes dispersive.

At microwave frequencies the wavelength of acoustic waves is of the order of microns. In practical applications the transverse

dimensions of an acoustic beam are at least a few millimetres, i.e. more than a thousand wavelengths. In these situations waveguide effects are negligible, and it is permissible to consider the acoustic waves as uniform plane waves. The propagation of these waves in a loss-free anisotropic medium was first investigated by Christoffel (1877) and further studies have been made by Musgrave (1954, 1956, 1959, 1961). Certain details connected with the propagation and reflection of these waves are considered in Appendix G.

3.2 ACOUSTIC WAVES IN ANISOTROPIC LOSSY MEDIA.

Christoffel's solution is generalised for a lossy medium (Lamb and Richter, 1966b) by assuming a complex elastic stiffness coefficient (c.f. Equation 2.64):

$$c^*_{ijkl} = c_{ijkl} + j\omega\eta_{ijkl} \qquad 3.2$$

The admissible coefficients of the c_{ijkl} and η_{ijkl} tensors are defined by the crystalline symmetry of the medium. The stress-strain relationship at a given frequency of sinusoidal small amplitude strain variations is given by

$$T_{ij} = T^S_{ij} = c^*_{ijkl}\, S_{kl} \qquad 3.3$$

when the only variables that are considered at the moment are the symmetrical stress and strain. Substituting Equation 3.3 for T_{ij} in Equation 3.1, and taking into account the symmetry of the c_{ijkl}, η_{ijkl}, T_{ij} and S_{ij} tensors, one obtains the following wave equation:

$$-\omega^2 \varrho u_i = (c_{ijkl} + j\omega\eta_{ijkl}) \frac{\partial^2 u_k}{\partial x_j \cdot \partial x_l} \qquad 3.4$$

A wave solution is assumed in the form of

$$u_i = u_i\, e^{j(\omega t - k^* r)} \qquad 3.5$$

where $k^* = k - j\alpha$ is the complex wave propagation constant and r is the

coordinate along the normal, n_i, to the wavefront. The displacement gradients are found as:

$$\frac{\partial u_k}{\partial x_j} = \frac{\partial u_k}{\partial r} \cdot \frac{\partial r}{\partial x_j} = - jk^* u_k \cos (n, x_j) \qquad 3.6$$

Substitution of Equation 3.6 into the wave equation 3.4 yields

$$\omega^2 \varrho u_i = \Gamma^*_{ik} \cdot (k^*)^2 u_k \qquad 3.7$$

where

$$\Gamma^*_{ik} = (c_{ijkl} + j\omega\eta_{ijkl}).\cos (n, x_j).\cos (n, x_l) \qquad 3.8$$

are the complex Christoffel coefficients.

A scalar wave equation for the modulus of the displacement U is obtained by multiplying both sides of Equation 3.7 by α_i^+, the complex conjugate of the direction cosines of the displacement $\alpha_i \left(= \frac{u_i}{U}\right)$:

$$\omega^2 \varrho U = E^* (k^*)^2 U \qquad 3.9$$

with

$$\alpha_i^+ \Gamma^*_{ij} = E^* . \alpha_j^+ \qquad 3.10$$

and

$$E^* = C + jD \qquad 3.11$$

A non-zero solution for α_i^+ from the set of homogeneous linear equations 3.10 exists if the determinant formed by the coefficients vanishes:

$$\begin{vmatrix} \Gamma^*_{11} - E^* & \Gamma^*_{12} & \Gamma^*_{13} \\ \Gamma^*_{12} & \Gamma^*_{32} - E^* & \Gamma^*_{32} \\ \Gamma^*_{13} & \Gamma^*_{23} & \Gamma^*_{33} - E^* \end{vmatrix} = 0 \qquad 3.12$$

Solving the determinant gives a cubic for E^*. Thus for any selected direction of propagation there are three values for E^* giving three effective elastic constants C with three corresponding dissipation

constants D. These determine the velocity of propagation $\left(\frac{\omega}{k}\right)$ and the attenuation (α) for the mode in question, since from Equation 3.9

$$(k - j\alpha)^2 = \frac{\omega^2 \rho}{C + jD} \qquad 3.13$$

and hence

$$k^2 - \alpha^2 = \frac{\omega^2 \rho C}{C^2 + D^2} \qquad 2\alpha k = \frac{\omega^2 \rho D}{C^2 + D^2} \qquad 3.14$$

The dissipation constant D can be rewritten as

$$D = \omega\eta \qquad 3.15$$

where η is the effective viscosity for the selected mode and direction.

The complex conjugates of the direction cosines of the particle displacement are given by the normalised cofactors of any line or column in the determinant of Equation 3.12 after substituting the appropriate value of E^* for the mode in question. Since the direction cosines are complex, the displacements, in general, are elliptically polarised. The axes of these ellipses are mutually orthogonal.

Two special cases merit further investigation:

a) In the case of small dissipation ($D^2 \ll C^2$) Equation 3.13 gives

$$k^2 = \omega^2 \frac{\rho}{C} \qquad 3.16$$

$$\alpha = \frac{\omega^2}{2\rho v^3}\eta \qquad 3.17$$

where v is the velocity of propagation:

$$v = \frac{\omega}{k} = \sqrt{\frac{C}{\rho}} \qquad 3.18$$

which is given by the same expression as the velocity in a non-dissipative medium. A vector parallel to the direction cosines α_k^M (now approximately real) is given for a particular mode M by the cofactors of any line or column in the determinant of Equation 3.12

containing only the real parts of the Christoffel coefficients. The three linearly polarised displacements are mutually perpendicular to each other. In general none of the displacements of the triad coincides with, or is perpendicular to, the direction of propagation. The mode with displacement nearest to the direction of propagation is the longitudinal mode (L mode), the other two are shear modes, distinguished by their phase velocities as fast shear mode (FS mode) and slow shear mode (SS mode).

Since, for small dissipation, Equation 3.10 is independently satisfied by the real and imaginary parts, multiplying the imaginary parts by α_k^M and summing gives the following expression for the effective viscosity:

$$\eta = \alpha_i^M \alpha_k^M \eta_{ijkl} \cos(n, x_j) \cdot \cos(n, x_l) \qquad 3.19$$

(There is no summing over the index M)

In the knowledge of the complete matrices of the stiffness and viscosity constants the velocity of propagation and the attenuation of a given mode can be calculated for a selected propagation direction. The anisotropic viscosity coefficients of a crystal have been determined for the first time in the present work (see Chapter 10) and have been described in a recent publication (Lamb and Richter, 1966b).

b) In the case of a liquid the symmetry of the complex elastic matrix is isotropic. Furthermore, at frequencies much below the lowest relaxation frequency, the real parts of rigidity components are zero, and, for shear waves, the following expressions are obtained from Equation 3.13 for the phase velocity and attenuation

$$v = \sqrt{\frac{2\omega\eta}{\rho}} \qquad 3.20$$

$$\alpha = \sqrt{\frac{\omega}{2}\rho\eta} \qquad 3.21$$

The penetration depth of shear waves defined as the distance over which the amplitude decays to 1/e of the original value is found from Equation 3.21 to be of the order of $\eta^{-\frac{1}{2}}$ microns at around 1000Mc/s for unrelaxed liquids.

3.3 EFFECT OF COUPLE STRESS.

A wave-type solution of Equation 3.1 in a medium where couple stresses are present was first obtained by Toupin (1962) and Mindlin and Tiersten (1962). Here a less general method will be adopted applied specially for quartz.

The above authors expressed the opinion that couple stress can have a noticeable effect on the propagation of shear waves in solids at high frequencies, especially near boundaries. The investigation described in this section has been carried out to establish whether classical elastic theory (which does not consider couple stresses) can be applied to microwave acoustics.

When the antisymmetric part of the stress is eliminated, Equation 3.1 has the form, reproduced here from Equation 2.24

$$\rho \frac{\partial^2 u_i}{\partial t^2} = \frac{\partial}{\partial x_j} T^S_{ij} + \tfrac{1}{2} \frac{\partial}{\partial x_j} \left(\epsilon_{ijk} \frac{\partial}{\partial x_l} \hat{G}_{kl} \right) \qquad 3.22$$

$$= \text{Div } T^S_{ij} + \text{Curl} \left(\frac{1}{2} \frac{\partial G_{kl}}{\partial x_l} \right) \qquad 3.23$$

Without loss of generality it can be assumed that plane wave propagation takes place in the x_1 direction. Therefore

$$\frac{\partial}{\partial x_2} = \frac{\partial}{\partial x_3} = 0 \qquad 3.24$$

The equation of motion, Equation 3.22, written explicitly for the three components of the displacement is then simplified as

$$\rho \frac{\partial^2 u_1}{\partial t^2} = \frac{\partial}{\partial x_1} \cdot T_{11}$$

$$\rho \frac{\partial^2 u_2}{\partial t^2} = \frac{\partial}{\partial x_1} \cdot T_{21} - \tfrac{1}{2} \frac{\partial^2}{\partial x_1^2} \hat{G}_{31} \qquad 3.25$$

$$\rho \frac{\partial^2 u_3}{\partial t^2} = \frac{\partial}{\partial x_1} \cdot T_{31} - \tfrac{1}{2} \frac{\partial^2}{\partial x_1^2} \hat{G}_{21}$$

The first equation of Equation 3.25 does not involve the couple stress; i.e. the pure longitudinal mode of the acoustic wave is not affected by couple stress. Only shear waves will be considered further.

To solve Equation 3.25b and c a constitutive relationship has to be found which expresses the couple stress G_{ij} in terms of displacement gradients. The required relationship is easily found since the balance equation of internal energy, Equation 2.31, contains terms that are the product of couple stress and the time rate of local distortion. The differential form of the internal energy equation is given below, where it is assumed that all processes are adiabatic and lossless, and when the contribution of dielectric energy is also added:

$$dU = T^S_{ij} \; dS_{ij} + \hat{G}^D_{ij} \; d\hat{x}^D_{ij} + E_m \, dD_m \qquad 3.26$$

According to the argument presented in connection with Equations 2.42 - 2.46, the following linearised relationship can exist between the independent variables T^S_{ij}, $\hat{G}^D_{ij}$, E_i and the dependent variables S_{ij}, $\hat{x}_{ij}$, D_i in the most general case:

$$T^S_{ij} = \frac{\partial T^S_{ij}}{\partial S_{kl}} S_{kl} + \frac{\partial T^S_{ij}}{\partial x_{kl}} \hat{x}_{kl} + \frac{\partial T^S_{ij}}{\partial D_m} D_m$$

$$\hat{G}^D_{ij} = \frac{\partial \hat{G}^D_{ij}}{\partial S_{kl}} S_{kl} + \frac{\partial \hat{G}^D_{ij}}{\partial x_{kl}} \hat{x}_{kl} + \frac{\partial \hat{G}^D_{ij}}{\partial D_m} D_m \qquad 3.27$$

$$E_n = \frac{\partial E_n}{\partial S_{kl}} S_{kl} + \frac{\partial E_n}{\partial x_{kl}} \hat{x}_{kl} + \frac{\partial E_n}{\partial D_m} D_m$$

with

$$T^S_{ij} = \frac{\partial U}{\partial S_{ij}}$$

$$\hat{G}^D_{ij} = \frac{\partial U}{\partial \hat{x}_{ij}} \qquad 3.28$$

$$E_n = \frac{\partial U}{\partial D_n}$$

By Equation 3.28 the following symmetry of the material constants is immediately established:

$$\frac{\partial T^S_{ij}}{\partial S_{kl}} = \frac{\partial^2 U}{\partial S_{ij} \partial S_{kl}} = \frac{\partial^2 U}{\partial S_{kl} \partial S_{ij}} = \frac{\partial T^S_{kl}}{\partial S_{ij}} = c_{ijkl} = c_{klij} \quad \text{(polar)}$$

$$\frac{\partial T^S_{ij}}{\partial \hat{x}_{kl}} = \frac{\partial^2 U}{\partial S_{ij} \partial \hat{x}_{kl}} = \frac{\partial^2 U}{\partial \hat{x}_{kl} \partial S_{ij}} = \frac{\partial \hat{G}^D_{kl}}{\partial S_{ij}} = b_{ijkl} \quad \text{(axial)}$$

$$\frac{\partial T^S_{ij}}{\partial D_n} = \frac{\partial^2 U}{\partial S_{ij} \partial D_n} = \frac{\partial^2 U}{\partial D_n \partial S_{ij}} = \frac{\partial E_n}{\partial S_{ij}} = d_{n-ij} \quad \text{(polar)}$$

$$\frac{\partial \hat{G}^D_{ij}}{\partial \hat{x}_{kl}} = \frac{\partial^2 U}{\partial \hat{x}_{ij} \partial \hat{x}_{kl}} = \frac{\partial^2 U}{\partial \hat{x}_{kl} \partial \hat{x}_{ij}} = \frac{\partial \hat{G}^D_{kl}}{\partial \hat{x}_{ij}} = a_{ijkl} = a_{klij} \quad \text{(polar)}$$

3.29

$$\frac{\partial G^D_{ij}}{\partial D_n} = \frac{\partial^2 U}{\partial x_{ij}\partial D_n} = \frac{\partial^2 U}{\partial D_n \partial \hat{x}_{ij}} = \frac{\partial E_n}{\partial \hat{x}_{ij}} = f_{n-ij} \qquad \text{(axial)}$$

$$\frac{\partial E_n}{\partial D_m} = \frac{\partial^2 U}{\partial D_n \partial D_m} = \frac{\partial^2 U}{\partial D_m \partial D_n} = \frac{\partial E_n}{\partial D_n} = \beta_{nm} = \beta_{mn} \qquad \text{(polar)}$$

With the above definition of material constants the Equations 3.27 have the form:

$$\begin{aligned} T_{ij} &= c_{ijkl}S_{kl} + b_{ijkl}\hat{x}_{kl} + d_{m-ij}D_m \\ \hat{G}_{ij} &= b_{klij}S_{kl} + a_{ijkl}\hat{x}_{kl} + f_{m-ij}D_m \qquad 3.30 \\ E_n &= d_{n-kl}S_{kl} + f_{n-kl}\hat{x}_{kl} + \beta_{nm}D_m \end{aligned}$$

In Equations 3.29 and 3.30 one can recognise 3 constants of the ordinary elastic theory:

c_{ijkl} --- elastic stiffness coefficients

d_{m-ij} --- piezoelectric strain coefficients

β_{nm} --- dielectric permittivity

The other 3 can be named as follows:

a_{ijkl} --- x-stiffness coefficients

b_{ijkl} --- acoustical activity coefficients

f_{m-ij} --- piezoelectric x-coefficients

The number of independent components of these coefficient tensors can be found as follows:

c_{ijkl}	components of 3x3x3x3 tensor:	81
	the symmetry $c_{ijkl} = c_{klij}$ gives 36 relations between them:	-36

further, $T_{ij} = T_{ji}$ therefore $c_{ijkl} = c_{jikl}$
giving 3x9 = 27 relationships, but 3 of
these have already been counted: -24
thus left: 21

a_{ijkl}

components of 3x3x3x3 tensor: 81
the symmetry $a_{ijkl} = a_{klij}$ gives 36 relations
between them: -36
$tr\hat{x} = tr\hat{G} = 0$ therefore
$a_{11kl}\hat{x}_{kl} + a_{22kl}\hat{x}_{kl} + a_{33kl}\hat{x}_{kl} = 0$ for all
9 combinations of kl, this furnishes 9
relationships: - 9
thus left: 36

β_{nm}

components of 3x3 tensor 9
the symmetry $\beta_{nm} = \beta_{mn}$ gives
3 relations between them: -3
thus left: 6

b_{ijkl}

components of 3x3x3x3 tensor 81
$T_{ij} = T_{ji}$: $b_{ijkl}\hat{x}_{kl} = b_{jikl}\hat{x}_{kl}$ giving
3x9 relationships between them: -27
$tr\hat{G}_{ij} = 0$ gives 9 further relationships of
which 3 have already been counted: - 6
thus left: 48

d_{m-ij}

components of 3x3x3 tensor 27
$d_{m-ij} = d_{m-ji}$ gives 3x3 relationships: - 9
thus left: 18

f_{m-ij}	components of 3x3x3 tensor:	27
	$f_{m-11} + f_{m-22} + f_{m-33} = 0$ gives 3 relationships:	-3
	thus left:	24

The above maximum number of independent components will be further reduced in a media possessing structural symmetry. The schemes of admissible coefficients for the crystallographic class of quartz are given in the tables of Appendix D. These tables, unpublished elsewhere, have been obtained by repeated applications of the 3rd and 4th rank tensor transformations, Equation A.1 or A.2, with $\frac{\partial x_i'}{\partial x_m}$ given in turn by the matrices of Appendix B. The material response, expressed by the given schemes of coefficients, is left unaltered by the density preserving changes of reference configurations given in Appendix B.

The stresses and couple stresses in Equation 3.25 can now be substituted by the differentials of the displacement with the help of the constitutive relations:

$$\rho \frac{\partial^2 u_2}{\partial t^2} = \frac{\partial}{\partial x_1}\left(c_{21k1}S_{k1} + b_{21k1}\hat{x}_{k1}\right) - \frac{1}{2}\frac{\partial^2}{\partial x_1^2}\left(b_{31k1}S_{k1} + a_{31k1}\hat{x}_{k1}\right)$$

3.31

$$\rho \frac{\partial^2 u_3}{\partial t^2} = \frac{\partial}{\partial x_1}\left(c_{31k1}S_{k1} + b_{31k1}\hat{x}_{k1}\right) + \frac{1}{2}\frac{\partial^2}{\partial x_1^2}\left(b_{21k1}S_{k1} + a_{21k1}\hat{x}_{k1}\right)$$

where (c.f. Appendix C)

$$S = \begin{pmatrix} \frac{\partial u_1}{\partial x_1}, & \frac{1}{2}\frac{\partial u_2}{\partial x_1}, & \frac{1}{2}\frac{\partial u_3}{\partial x_1}, \\ \frac{1}{2}\frac{\partial u_2}{\partial x_1}, & 0, & 0, \\ \frac{1}{2}\frac{\partial u_3}{\partial x_1}, & 0, & 0, \end{pmatrix} \qquad 3.32$$

and

$$\hat{x} = \begin{pmatrix} 0, & 0, & 0, \\ -\frac{1}{2}\frac{\partial^2 u_3}{\partial x_1^2}, & 0, & 0, \\ \frac{1}{2}\frac{\partial^2 u_2}{\partial x_1^2}, & 0, & 0, \end{pmatrix} \qquad 3.33$$

When the $x_1x_2x_3$ coordinates coincide with the crystallographic XYZ directions of quartz, Equation 3.31 describes shear wave propagation along the X axis. Then the symmetry of the coefficients given in Tables D.1 - D.5 of the Appendix affords further simplification, so that:

$$\begin{aligned} \frac{\partial^2 u_2}{\partial t^2} &= c_{66}\frac{\partial^2 u_2}{\partial x_1^2} + c_{14}\frac{\partial^2 u_3}{\partial x_1^2} - \frac{1}{2}(b_{66}+b_{77})\frac{\partial^3 u_3}{\partial x_1^3} + \frac{1}{4}a_{17}\frac{\partial^4 u_3}{\partial x_1^4} - \frac{1}{4}a_{77}\frac{\partial^4 u_2}{\partial x_1^4} \\ \frac{\partial^2 u_3}{\partial t^2} &= c_{14}\frac{\partial^2 u_2}{\partial x_1^2} + c_{44}\frac{\partial^2 u_3}{\partial x_1^2} + \frac{1}{2}(b_{66}+b_{77})\frac{\partial^3 u_2}{\partial x_1^3} - \frac{1}{4}a_{66}\frac{\partial^4 u_3}{\partial x_1^4} + \frac{1}{4}a_{17}\frac{\partial^4 u_2}{\partial x_1^4} \end{aligned} \qquad 3.34$$

A similar set of equations, with $c_{14} = 0$ results for propagation along the BC or AC directions.

When an exponential solution of the form

$$u = u\, e^{j(\omega t - kx_1)} \tag{3.35}$$

is assumed for Equation 3.34, the following dispersion equation is found:

$$(c_{66}k^2+\tfrac{1}{4}a_{77}k^4-\rho\omega^2)(c_{44}k^2+\tfrac{1}{4}a_{66}k^4-\rho\omega^2) - (c_{14}-\tfrac{1}{4}a_{17}k^4)^2 -$$

$$-\tfrac{1}{4}(b_{66}+b_{77})^2k^6 = 0 \tag{3.36}$$

The dispersion equation is quartic in k^2 for which an exact algebraic solution is obtainable (Turnbull, 1939). Of the 4 different positive roots two give the dispersion relations for the FS and SS shear modes, and the other two give two evanescent waves. A truncated power series solution yielded the following dispersion relation for shear waves:

$$\omega = \sqrt{\frac{c}{\rho}}\; k \left(1 + \frac{a_{66}+a_{77}+F(a,b,c)}{16c}\, k^2\right) \tag{3.37}$$

where c is the effective elastic constant of the mode in question

$$c = \frac{c_{44}+c_{66} \quad \sqrt{(c_{44}-c_{66})^2 + 4c_{14}^2}}{2} \tag{3.38}$$

and F, a combination of the a, b and c tensors, is always positive but is expected to be less than $a_{66}+a_{77}$. According to Equation 3.37 shear waves in elastic solids (even when isotropic, c.f. Toupin, 1962) should show a slight increase in phase velocity as the frequency is increased.

The velocity of the FS mode of a BC quartz specimen was

measured in the double-tuned cavity of Chapter 8 by the pulse interference method (McSkimin, 1964). Over a hundred interference minima were observed in each of two frequency bands centred around 500 and 1000Mc/s, and the corresponding frequencies were read off from a counter or wavemeter. No detectable difference was found in phase velocity at these frequencies.

As a further check to detect an effect due to couple-stress, the piezoelectric excitation via couple-stress was examined. Without detailing intermediate steps, when the full set of Equations 3.30 is substituted for the stresses in Equation 3.25, the following coupling is found between electric flux density and displacements gradients for propagation along the X axis:

$$\tfrac{1}{2}b_{66}\frac{\partial u_2}{\partial x} + \tfrac{1}{2}b_{41}\frac{\partial^2 u_3}{\partial x} + \tfrac{1}{4}a_{17}\frac{\partial^2 u_2}{\partial x^2} - \tfrac{1}{4}a_{66}\frac{\partial^2 u_3}{\partial x^2} = -f_{11}D_2 + f_{36}D_3$$

$$-\tfrac{1}{2}b_{17}\frac{\partial u_2}{\partial x} - \tfrac{1}{2}b_{77}\frac{\partial^2 u_3}{\partial x} - \tfrac{1}{4}a_{77}\frac{\partial^2 u_2}{\partial x^2} + \tfrac{1}{4}a_{17}\frac{\partial^2 u_3}{\partial x^2} = f_{17}D_2 \qquad 3.39$$

$$c_{66}\frac{\partial u_2}{\partial x} + c_{14}\frac{\partial u_3}{\partial x} + \tfrac{1}{2}b_{17}\frac{\partial^2 u_2}{\partial x^2} - \tfrac{1}{2}b_{66}\frac{\partial^2 u_3}{\partial x^2} = -d_{11}D_2$$

$$c_{14}\frac{\partial u_2}{\partial x} + c_{44}\frac{\partial u_3}{\partial x} + \tfrac{1}{2}b_{77}\frac{\partial^2 u_2}{\partial x^2} - \tfrac{1}{2}b_{41}\frac{\partial^2 u_3}{\partial x^2} = d_{14}D_2$$

In Equation 3.39 the piezoelectric coupling due to couple stress is expressed by the coefficient f. A suitable single crystal sapphire rod was obtained to check surface excitation through the piezoelectric f coefficient. While the elastic a, c and piezoelectric f matrices are found to have the same symmetry for sapphire as for quartz, the piezoelectric d coefficients are identically zero, rendering sapphire non-piezoelectric in the ordinary sense. Any

surface excitation in sapphire would be due to couple stress. But no excitation was found at 450Mc/s, with a minimum detectable signal 70dB lower than that needed to detect piezoelectric coupling in BC quartz.

Since neither dispersion nor excitation was found due to couple stress, the material coefficients (a, b, f) connected with couple stress must be negligibly small not to cause an effect even at microwave frequencies. The conclusion is drawn that as the consequence of the smallness of these coefficients, only the symmetric part of the stress plays a role in dynamic relations and therefore classical elastic theory applies up to the highest frequencies encountered in microwave acoustics.

3.4 PIEZOELECTRIC INTERACTIONS.

The interaction of electromagnetic and acoustic waves was first investigated by Kyame (1949) who obtained uniform plane wave solutions of Maxwell's electromagnetic field equations and Newton's equation of motion simultaneously. His results show that it is convenient to consider the interaction consisting of two parts:

a) "piezoelectric stiffening"

b) coupling between waves.

Piezoelectric stiffening will be considered here in the case of non-uniform plane waves.

The apparent increase in the elastic stiffness is due to the fact that the divergence of the electric flux density must be zero in a piezoelectric medium void of free electric charges:

$$\frac{\partial D_m}{\partial x_m} = 0 \qquad 3.40$$

But the flux density is proportional to both the applied electric field strength and the mechanical strain

$$D_m = e_{mij} S_{ij} + \epsilon_{mn} E_n \qquad 3.41$$

The stress is given as

$$T_{ij} = c_{ijkl} S_{kl} - e_{mij} E_n \qquad 3.42$$

The two sets of equations above are special forms of Equation 3.30 and the symbols have their usual meaning (e.g. Mason, 1958).

Consider (after Kyame, 1946) the propagation of a plane acoustic wave

$$a\, e^{j(\omega t - kx_2)}$$

along the x_2 coordinate axis, when

$$\frac{\partial D_m}{\partial x_m} = \frac{\partial D_2}{\partial x_2} = jkD_2 = 0 \qquad 3.43$$

The longitudinal component alone of the flux density causes the piezoelectric stiffening, because the partial differentials along the other two coordinate directions are zero for a uniform plane wave. The longitudinal component of the electric field strength, E_2, can be expressed (except for a spatially constant field) with the help of Equations 3.41 and 3.43 as

$$E_2 = -\frac{1}{\epsilon_{22}} (e_{2ij} S_{ij} + \epsilon_{2p} E_p) \qquad 3.44$$

where the index p (and the indices p, q and r in general) take the value of either 1 or 3 but not 2.

Substituting E_2 in Equation 3.41 and 3.42, the following "stiffened" equations result:

$$T_{ij} = \left(c_{ijkl} + \frac{e_{2kl} \cdot e_{2ij}}{\epsilon_{22}}\right) S_{kl} - \left(e_{pij} - \frac{e_{2ij} \cdot \epsilon_{2p}}{\epsilon_{22}}\right) E_p$$

$$D_q = \left(e_{pij} - \frac{e_{2ij}\, \epsilon_{2p}}{\epsilon_{22}}\right) S_{kl} + \left(\epsilon_{qp} + \frac{\epsilon_{q2}\, \epsilon_{2p}}{\epsilon_{22}}\right) E_p \qquad 3.45$$

One can write

$$T_{ij} = \bar{c}_{ijkl}\, S_{kl} - \bar{e}_{pkl}\, E_p$$

$$D_2 = \bar{e}_{qkl}\, S_{kl} + \bar{\epsilon}_{qp}\, E_p \qquad 3.46$$

where the upper bar represents the stiffened coefficients, defined by Equation 3.45. The modification of the material coefficients due to the restriction imposed on the longitudinal flux density by Equation 3.43 amounts to a correction of the order of 1% or less in quartz.

In situations of practical interest the amplitude of the wave over the wavefront is not constant. The distribution of amplitude (both mechanical displacement and electric field components) over a small enough portion of the wavefront can be described by

$$a = a_o(1 + \alpha_1 x_1 + \alpha_3 x_3) \qquad 3.47$$

where a_o is the amplitude in the centre of the plane portion, and α_1 and α_3 are real constants, since the wavefront is a plane of constant phase. The partial derivatives of the amplitude are listed below:

$$\frac{\partial u_i}{\partial x_1} = \alpha_1 u_i \qquad \frac{\partial u_i}{\partial x_2} = -jku_i \qquad \frac{\partial u_i}{\partial x_3} = \alpha_3 u_i$$

$$\frac{\partial E_i}{\partial x_1} = \alpha_1 E_i \qquad \frac{\partial E_i}{\partial x_2} = -jkE_i \qquad \frac{\partial E_i}{\partial x_3} = \alpha_3 E_i \qquad 3.48$$

Instead of Equation 3.44, the E_2 component of the electric field strength is expressed by the strain and the E_1 and E_3 electric field strength components as

$$E_2 = -\frac{e_{2ij} + j\frac{\alpha_r}{k} e_{rij}}{\epsilon_{22} + j\frac{\alpha_q}{k}\epsilon_{q2}} S_{ij} - \frac{\epsilon_{2p} - j\frac{\alpha_r}{k}\epsilon_{rp}}{\epsilon_{22} + j\frac{\alpha_q}{k}\epsilon_{q2}} E_p \qquad 3.49$$

Since α/k is ordinarily less than 10^{-4} and ϵ_{22} is never smaller than ϵ_o, the following approximation is permissible for E_2:

$$E_2 = \left[\frac{e_{2ij}}{\epsilon_{22}} + j\frac{1}{\epsilon_{22}}\left(\frac{\alpha_r}{k} e_{rij} - \frac{\alpha_q}{k}\frac{\epsilon_{q2}}{\epsilon_{22}} e_{2ij}\right)\right] S_{ij} +$$

$$+ \left[\frac{\epsilon_{2p}}{\epsilon_{22}} + j\frac{1}{\epsilon_{22}}\left(\frac{\alpha_r}{k}\epsilon_{rp} - \frac{\alpha_q}{k}\frac{\epsilon_{q2}\epsilon_{2p}}{\epsilon_{22}}\right)\right] E_p \qquad 3.50$$

The stress-strain relationship, Equation 3.41, has the following form after elimination of E_2:

$$T_{kl} = \left[c_{ijkl} + \frac{e_{2kl}e_{2ij}}{\epsilon_{22}} + j\frac{e_{2kl}}{\epsilon_{22}}\left(\frac{\alpha_r}{k} e_{rij} - \frac{\alpha_q}{k}\frac{\epsilon_{q2}}{\epsilon_{22}} e_{2ij}\right)\right] S_{ij} -$$

$$- \left[e_{pkl} - \frac{e_{2kl}\epsilon_{2p}}{\epsilon_{22}} - j\frac{e_{2kl}}{\epsilon_{22}}\left(\frac{\alpha_r}{k}\epsilon_{rp} - \frac{\alpha_q}{k}\frac{\epsilon_{q2}}{\epsilon_{22}}\frac{\epsilon_{2p}}{\epsilon_{22}}\right)\right] E_p \qquad 3.51$$

The imaginary parts, now appearing in the coefficients are connected to apparent attenuation owing to the spreading of the wave. For an ideal uniform plane wave α being zero, Equation 3.51 resorts to Equation 3.45a. For a plane wave with non-uniform amplitude the extra stiffening due to the non-constancy of the amplitude over the wavefront causes a further correction to the magnitude of the material constants. A relative change of 10^{-5} in the elastic constants would cause serious interference effects in practical applications. The second correction, however, being proportional to $(\alpha/k)^2$ is negligible compared to 10^{-5} in cases of practical interest.

The coupling between acoustic and electromagnetic waves is very simple in the case of infinite plane waves, and is summarised below for later use. The equation of motion for simple harmonic waves is obtained from Equations 3.1 and 3.45 as (Kyame, 1949)

$$\omega^2 \rho u_i = \bar{c}_{i2k2} k^2 u_k - j \bar{e}_{pi2} k E_p \qquad 3.52$$

From Maxwell's equations the following relationship is found between electric field and mechanical displacement, again for simple harmonic waves:

$$\mu \bar{\epsilon}_{qp} \omega^2 E_p - k^2 E_q = \mu \bar{e}_{qk2} \omega^2 jk u_k \qquad 3.53$$

A non-zero solution of the above 3+2 linear algebraic equations exists if the determinant of the coefficients vanishes, that is when

$$\begin{vmatrix} (-\rho\omega^2+\bar{c}_{1212}k^2) & \bar{c}_{1222}k^2 & \bar{c}_{1232}k^2 & -\bar{e}_{112}jk & -\bar{e}_{312}jk \\ \bar{c}_{2212}k^2 & (-\rho\omega^2+\bar{c}_{2222}k^2) & \bar{c}_{2232}k^2 & -\bar{e}_{122}jk & -\bar{e}_{322}jk \\ \bar{c}_{3212}k^2 & \bar{c}_{3222}k^2 & (-\rho\omega^2+\bar{c}_{3232}k^2) & -\bar{e}_{132}jk & -\bar{e}_{332}jk \\ \mu\bar{e}_{112}\omega^2jk & \mu\bar{e}_{122}\omega^2jk & \mu\bar{e}_{132}\omega^2jk & (-\mu\omega^2\bar{\epsilon}_{11}+k^2) & -\mu\omega^2\bar{\epsilon}_{13} \\ \mu\bar{e}_{312}\omega^2jk & \mu\bar{e}_{322}\omega^2jk & \mu\bar{e}_{322}\omega^2jk & -\omega^2\mu\bar{\epsilon}_{31} & (-\mu\omega^2\bar{\epsilon}_{33}+k^2) \end{vmatrix} = 0 \qquad 3.54$$

If the piezoelectric coefficients were allowed to vanish, the determinant would separate into two determinants: the third order determinant giving the 3 acoustic velocities, and the second order determinant giving the 2 velocities of the electromagnetic waves in the anisotropic medium. Fortunately the terms in the determinant involving the piezoelectric e_{ijk} coefficients are small, and neglecting them in the calculation of the 5 phase velocities causes a relative error only of the order of $(v_a/v_e)^2$ where v_a and v_e are the acoustic and electromagnetic phase velocities, respectively (Hutson and White, 1962).

3.5 THERMOELASTIC INTERACTIONS.

The constitutive equations for an isotropic medium, given in Equation 2.50, show the interaction between those elastic and thermal variables that are of scalar character. Hence compressional waves propagating through the medium are coupled to thermal waves. Shear waves do not involve the trace of the stress and the strain tensors (in isotropic media), therefore they are not accompanied by simple sinusoidal temperature variations

of the same frequency as the acoustic wave, and are not subject to thermoelastic interactions. The nature of the interactions is examined to find its effect on the attenuation of longitudinal acoustic waves in quartz.

For the sake of simplicity, only the ideal isotropic case will be considered with no structural relaxations ($\eta_v=0$). When Equation 2.50a is substituted in the equation of motion it is found that

$$\frac{\partial^2 \text{ tr } S_{ij}}{\partial t^2} = v_T^2 \frac{\partial^2}{\partial x_l \partial x_l} \text{ tr } S_{ij} - \frac{\bar{\alpha}}{\rho\kappa} \frac{\partial^2 T}{\partial x_l \partial x_l} \qquad 3.55$$

where v_T is the isothermal longitudinal velocity:

$$v_T = \frac{1}{\sqrt{\kappa_T \rho}} \qquad 3.56$$

On the other hand, substituting Equation 2.50c into the entropy balance equation 2.38 (without internal heat sources) gives

$$\rho T \frac{ds}{dt} = \lambda \frac{\partial^2 T}{\partial x_j \partial x_j} \qquad 3.57$$

which, together with Equation 2.50b yields the equation of temperature distribution:

$$c\rho \frac{\partial T}{\partial t} + \frac{\bar{\alpha} T_o}{\kappa} \frac{\partial}{\partial t} (\text{tr } S_{ij}) = \lambda \frac{\partial^2 T}{\partial x_j \partial x_j} \qquad 3.58$$

For a medium for which the temperature coefficient of expansion is zero, the two equations 3.55 and 3.58 separate into the ordinary wave equation of longitudinal waves and the equation of heat conduction, respectively. For the coupled waves a solution is assumed in the form

$$a = a_o e^{j(\omega t - k^* x)} \qquad 3.59$$

where the amplitude a contains both the mechanical displacement u, and the temperature T as components. When this is substituted in Equations 3.55 and 3.58, the two basic equations take the form given below:

$$T = ju\frac{\varrho K}{\alpha}\ \frac{-v_T^2(k^*)^2+\omega^2}{k^*} \qquad 3.60$$

$$u = T\frac{\kappa}{\alpha T_o}\ \frac{-j\varrho c\omega-\lambda(k^*)^2}{k^*\omega}$$

Following a method of solution given by Chadwick (1960), T/u is eliminated from the two equations, and normalised frequency together with normalised wave vector K are defined as

$$\Omega = \frac{\omega}{\omega_o} \qquad \text{with } \omega_o = \frac{\varrho c v_T^2}{\lambda} \qquad 3.61$$

$$K = k^*\frac{\lambda}{\varrho c v_T}$$

when the dispersion relation is obtained:

$$(\Omega^2 - K^2)(\Omega - jK^2) + \varepsilon\Omega K^2 = 0 \qquad 3.62$$

where the coupling coefficient ε is given by

$$\varepsilon = \frac{\alpha^2 T_o v_T^2}{c} \qquad 3.63$$

Since the dispersion relation is quartic it admits four solutions: a forward and a reverse elastic mode (with small, almost 90° out of phase temperature variation accompanying it in the adiabatic range) and a forward and reverse highly attenuated thermal wave. The exact variations of the phase velocity and

attenuation as functions of frequency are shown in Fig. 3.1 for the elastic type mode below:

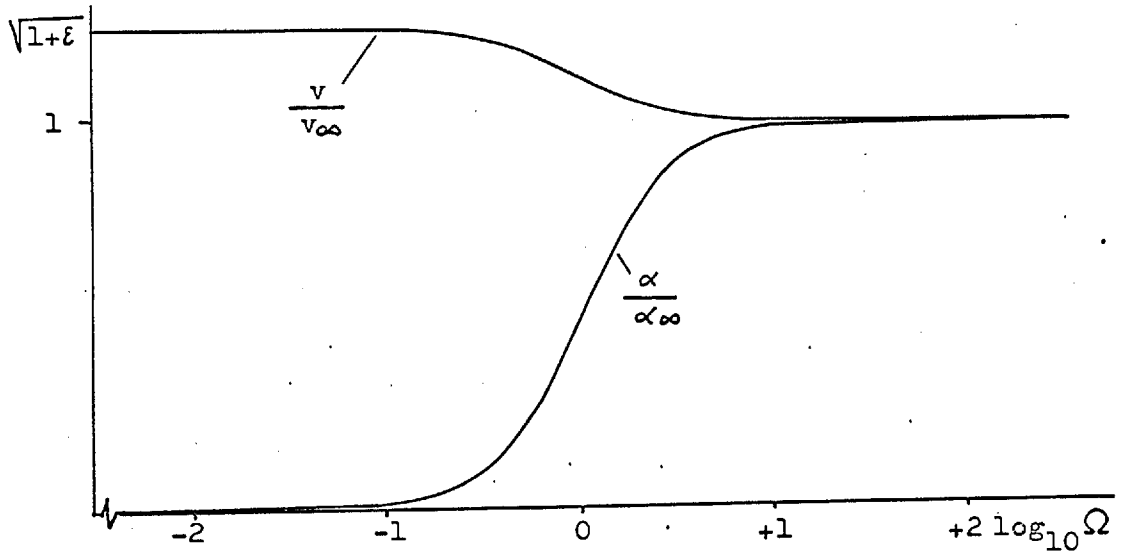


FIG. 3.1 THERMOELASTIC DISPERSION

The velocities and attenuations are given by the following infinite series expansion in ε (Chadwick and Sneddon, 1958) for the quasi-elastic mode:

$$v = v_T \left[1 + \frac{\varepsilon}{2(1+\Omega^2)} - \ldots \right]$$

$$\alpha = \frac{\omega_o}{v_1} \left[\frac{\varepsilon}{2} \frac{2}{(1+\Omega^2)} - \ldots \right] \qquad 3.64$$

and for the quasi-thermal mode

$$v = v_T \sqrt{2\Omega} \left[1 - \ldots \right]$$

$$\alpha = \frac{\omega_o}{v_1} \sqrt{\frac{\Omega}{2}} \left[1 - \ldots \right] \qquad 3.65$$

Equation 3.64 shows that the adiabatic-isothermal change for the longitudinal elastic mode can be described mathematically by a single relaxation up to first order approximation. The unusual feature of the thermoelectric relaxation is that the acoustic velocity becomes smaller as the frequency is increased. At very high frequencies the velocity is the one obtained from the isothermal elastic constant. At very low frequencies $v = v_T \sqrt{1+\varepsilon}$, which is exactly the adiabatic velocity. The fact, that (in contradiction to the widely held belief) the acoustic wave is adiabatic at low frequencies and isothermal at high frequencies was first pointed out by Herzfeld and Rice (1928) (c.f. also Herzfeld and Litovitz, 1959).

For crystal quartz at room temperature the following approximate numerical values characterise the thermoelastic interaction:

$$\omega_o = \frac{\rho c v_T^2}{\lambda} = 9.6 \times 10^{12} \text{c/s}$$

$$\varepsilon = \frac{\alpha^2 T_o v_T^2}{c} = 1.4 \times 10^{-4} \qquad 3.66$$

$$\alpha_\infty = \frac{\omega_o \varepsilon}{2 v_T} = 10^4 \text{dB/cm}$$

$$\alpha_{\text{at 1kMc/s}} = \alpha_\infty \left(\frac{\omega}{\omega_o}\right)^2 = 2.4 \times 10^{-2} \text{dB/cm}$$

The above figures show that thermoelastic dispersion takes place well above the practical microwave frequencies. (For metals, due to their higher conductivity and heat capacity, the situation might be different, c.f. Lücke, 1956). The resulting attenuation is approximately 200 times less than the attenuation due to structural relaxation (viscous effects). Therefore thermoelastic interaction will be regarded negligible at the frequencies of present interest. However, when the viscosity coefficients of crystal quartz are determined (Chapter 10), a very small part of the volume viscosity arises out of thermelastic effects and not structural relaxation.

CHAPTER 4.
PIEZOELECTRIC SURFACE EXCITATION.

4.1 COUPLED WAVES.

The interaction between the acoustic and electromagnetic field variables is expressed by the piezoelectric constitutive relations, (Equations 3.41 and 3.42) obtained through energetic considerations. With the usual definitions of scalar potential ϕ and vector potential A_i (e.g. Fano, Chu and Adler, 1960)

$$H = \text{curl } A$$

$$E = -\mu \frac{\partial A}{\partial t} - \text{grad}\phi; \qquad 4.1$$

$$\text{also div } A = -\epsilon \frac{\partial \phi}{\partial t}$$

Maxwell's equations result in the following set of inhomogeneous wave equations, when the electric flux density is substituted from the constitutive relations:

$$\Delta\phi - \epsilon\mu \frac{\partial^2 \phi}{\partial t^2} = \frac{1}{\epsilon}(-\varsigma^* - \text{div } e_{ikl} S_{kl})$$

$$\Delta A_i - \epsilon\mu \frac{\partial^2 A_i}{\partial t^2} = -J_i - j\omega e_{ikl} S_{kl} \qquad 4.2$$

where ς^* is the density of free charge, J_i is the electronic current density and $\Delta = \frac{\partial^2}{\partial x_j \partial x_j}$. (The dielectric constant ϵ and magnetic permeability μ were assumed isotropic for simplicity.)

The balance of linear momentum in a piezoelectric medium yields (c.f. Equation 2.18)

$$\frac{\partial^2 u_i}{\partial t^2} - \frac{\partial}{\partial x_j}\left(c_{ijkl}\ \frac{\partial u_n}{\partial x_l}\right) = -\frac{\partial}{\partial x_j}\left(e_{mij}\ E_m\right) \qquad 4.3$$

The wave equations 4.2 and 4.3 all have a source term on their right hand side. The acoustic equation 4.3 shows that a gradient in the product of piezoelectric constant times electric field strength (eE) is the source of acoustic displacement. The electromagnetic equation 4.2 indicates that the product of piezoelectric constant and strain acts as source for the electromagnetic waves through an effective piezoelectric charge density:

$$\bar{\varrho}^{*} = -\ \mathrm{div}\ e_{ikl}\ S_{kl} \qquad 4.4$$

and an effective piezoelectric current density:

$$\bar{J}_i = \frac{\partial}{\partial t}\ e_{ikl}\ S_{kl} \qquad 4.5$$

Taking the curl of both sides of Equation 4.2b gives a wave equation for the magnetic field (in the absence of free current):

$$\Delta H_i\ - \epsilon\mu \frac{\partial^2 H_i}{\partial t^2} = -\ j\omega\,\mathrm{curl}\ e_{ikl}\ S_{kl} \qquad 4.6$$

For a wave div eS, curl eS or div eE have values which are generally non zero, giving rise to a continuous interaction between the elastic and electromagnetic fields (e.g. plane wave solutions of Equation 3.53). At discontinuities the abrupt change in the field and material parameters make the differentials div or curl much larger than anywhere else in the continuum, so maximum conversion of acoustic type wave to electromagnetic type (or vice-versa) is expected at such discontinuities. Even if there were appreciable excitation over a long enough distance due to the inhomogeneity of the exciting field, the wavefront would be irregular causing little coherent detection. Therefore excitation only at a surface of discontinuity will be considered here.

Only the longitudinal component of the piezoelectric flux density (eS) contributes to piezoelectric charge in a plane wave. However, there is no such restriction on the piezoelectric current. Usual one-dimensional treatments of the subject do not mention piezoelectric currents and flux densities transverse to the direction of acoustic wave propagation, and thus neglect the possibility of acoustic excitation by transverse flux densities and fields.

The three-dimensional simultaneous wave equations 4.2, 4.3 and 4.6 are too complicated to give a practical exact solution in a general case. An exact solution, however, may sometimes be obtained by building up the electromagnetic and acoustic fields from elementary plane waves.

In connection with Equation 3.54 it has been shown (after Kyame, 1949) that 5 coupled plane wave solutions exist in a piezoelectric medium for a given direction of propagation. When two semi-infinite lossfree media are separated by the $x_2 = 0$ plane, with medium 2 on the left, and medium 1 on the right, then five different wave solutions exist in any direction of propagation for the combined electrodynamic and mechanical equations in each of the two media. Three out of the five phase velocities will be acoustic types, and two will be electromagnetic types. If a medium is not piezoelectric, these waves will be uncoupled acoustic and electromagnetic waves.

If there is a single wave incident on the interface, it gives rise in general to five reflected and five transmitted waves. The direction of propagation of the reflected and transmitted waves is determined from the condition that their component of the wave vector parallel to the surface must be equal to the same component of the wave vector of the incident wave. (c.f. Appendix G) The amplitudes of these waves (10 unknowns) can be determined dependent

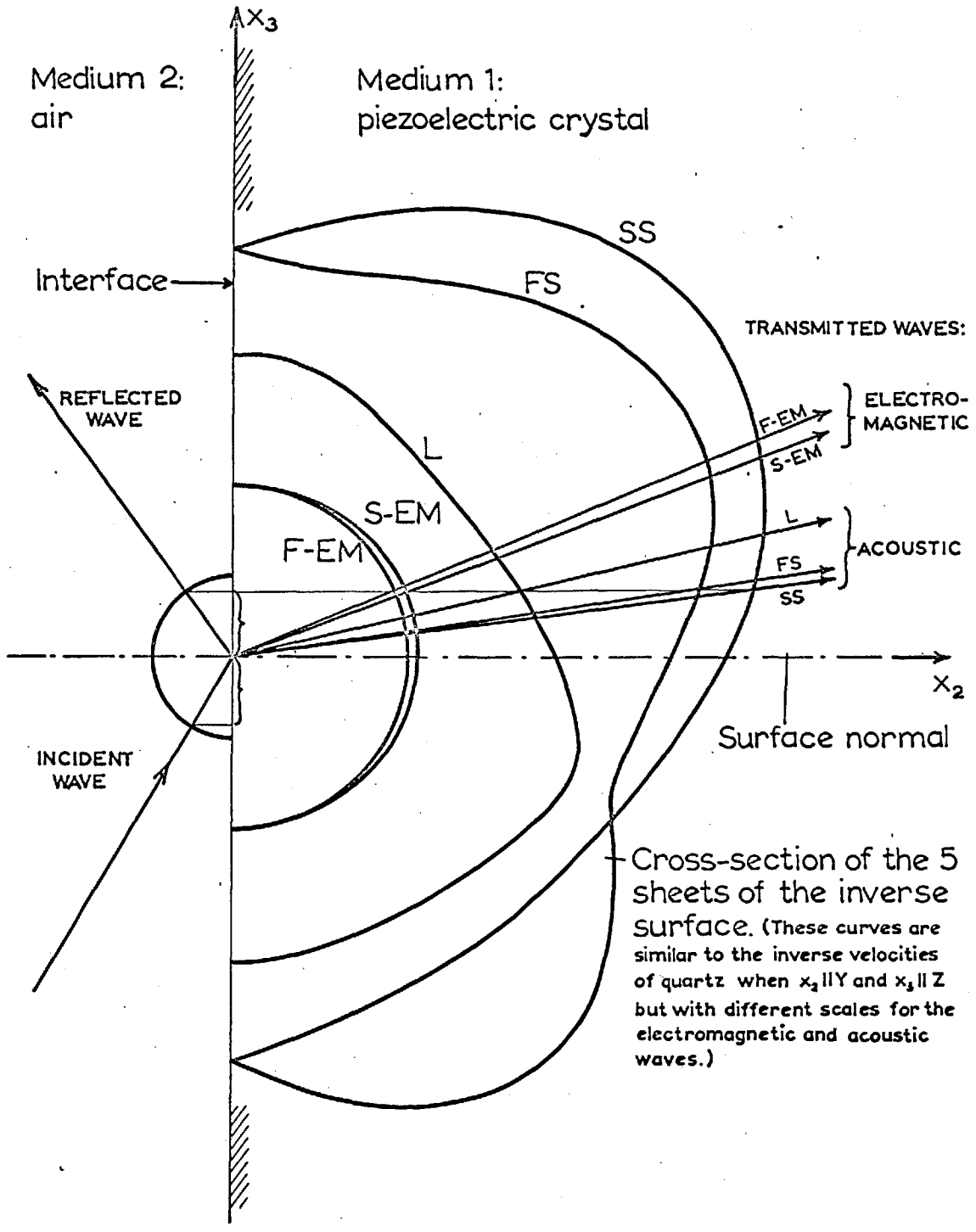


FIG. 4.1 GENERATION OF VARIOUS WAVES AT A CRYSTAL-AIR INTERFACE.

on the incident amplitude from the continuity conditions at the interface for the 3 components of stress, 3 components of displacement, 2 transverse components of E, 2 transverse components of H.

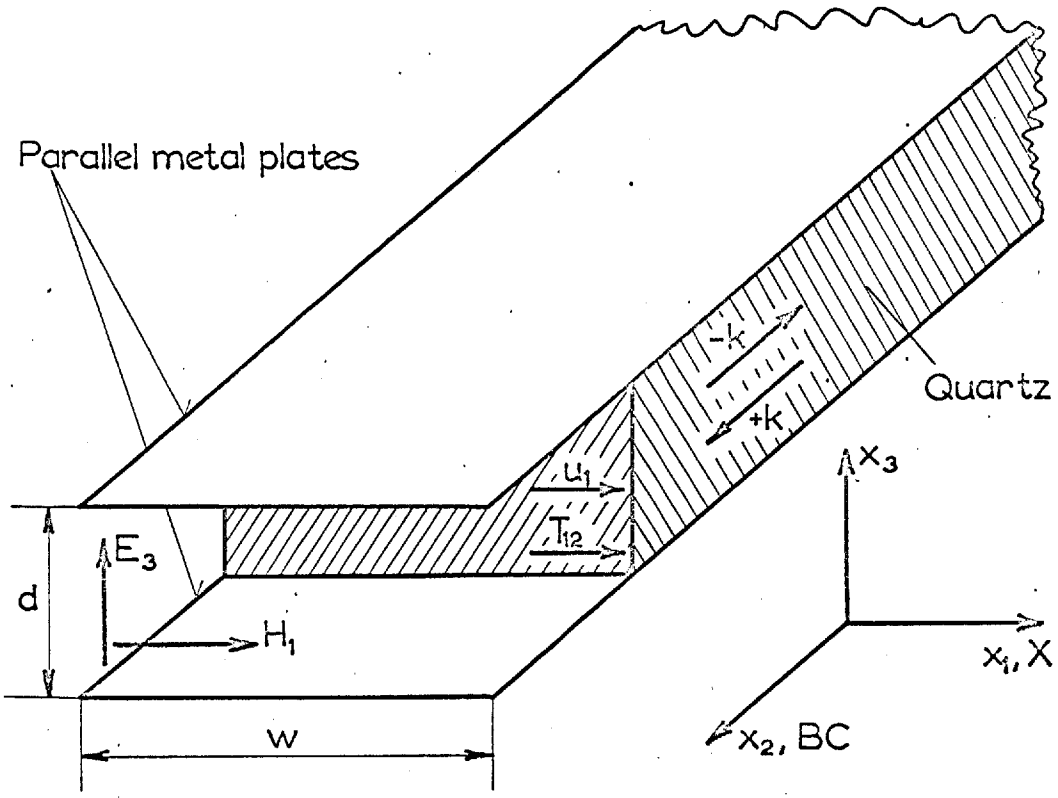
The situation at the interface of air and a fictitous piezoelectric medium is depicted in principle by Fig. 4.1. The various curves are intercepts of the inverse velocity surfaces with the plane of incidence. Since the inverse of the phase velocity is proportional to the wave vector, the direction of the various transmitted and reflected wave vectors are simply obtained by the construction indicated in the diagram. Because of their very different phase velocities, the generated acoustic waves will be practically normal to the interface for almost any direction of the incident electromagnetic wave.

4.2 SIMPLIFIED SOLUTION BY WAVE SUPERPOSITION.

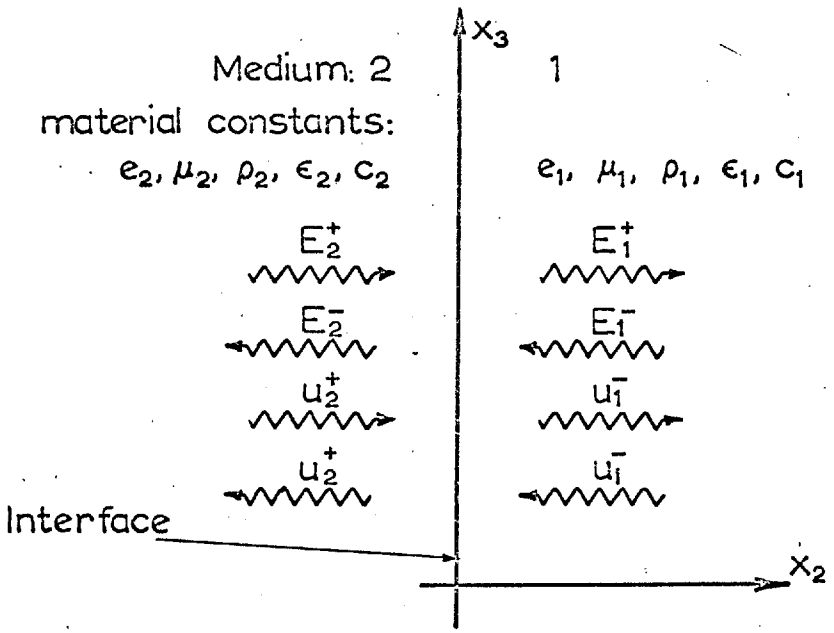
A combined solution of the electromagnetic and mechanical equations will be obtained for a situation with idealised geometry. The results found are usable for practical systems.

In the arrangement of Fig. 4.2a a block of quartz with its flat surface at $x_2 = 0$ is partly filling the air space between a pair of conducting metal plates. The crystallographic X and BC axes of the quartz are parallel to the x_1 and x_2 coordinate axes respectively. If the width w is large enough, the electromagnetic field configuration between the plates corresponds to simple plane waves.

In the piezoelectric medium the secular determinant (Equation 3.54) giving the 5 possible phase velocities has the following special form for the given crystalline orientation:



a) SIMPLIFIED ARRANGEMENT FOR SURFACE EXCITATION.



b) DEFINITION OF THE VARIOUS WAVES.

FIG. 4.2

$$\begin{vmatrix} -\rho\omega^2+\bar{c}_{66}k^2 & 0 & 0 & 0 & -\bar{e}_{312}jk \\ 0 & (-\rho\omega^2+c_{22}k^2) & c_{24}k^2 & -e_{122}jk & 0 \\ 0 & c_{24}k^2 & (-\rho\omega^2+c_{44}k^2) & -e_{132}jk & 0 \\ 0 & \mu e_{122}\omega^2 jk & \mu e_{132}\omega^2 jk & (-\omega^2\mu\epsilon_{11}-k^2) & 0 \\ \mu\bar{e}_{312}\omega^2 jk & 0 & 0 & 0 & -\omega^2\mu\bar{\epsilon}_{33}-k^2 \end{vmatrix} = 0 \qquad 4.7$$

This can be separated into the product of two determinants, one involving the coefficients of u_1 and E_3:

$$\begin{vmatrix} (-\rho\omega^2 + \bar{c}_{66}k^2) & -\bar{e}_{312}jk \\ \mu\bar{e}_{312}\omega^2 jk & (-\omega^2\mu\bar{\epsilon}_{33} + k^2) \end{vmatrix} = 0 \qquad 4.8$$

and another involving the coefficients of u_2, u_3 and E_1.

The determinant 4.8 gives the following equation for the velocities (with indices and bars omitted for the rest of this section):

$$(v^2 - v_a{}^2)(v^2 - v_e{}^2) - mv_e{}^2 v^2 = 0 \qquad 4.9$$

where $$v = \frac{\omega}{k}$$

$$v_a = \sqrt{\frac{c}{\rho}}$$

$$v_e = \frac{1}{\sqrt{\epsilon\mu}}$$

$$m = \frac{e^2\mu}{\rho} \qquad \text{(order of } 10^{-10}\text{)}$$

Solution of Equation 4.9 gives two velocities:

$$v = v_a\sqrt{1+m} \approx v_a$$
$$v = v_e\sqrt{1-m} \approx v_e \qquad 4.10$$

one having acoustic, the other electromagnetic orders of magnitude. Both of these waves have mechanical and electromagnetic components. The displacement lies in the x_1 direction and the electric field in the x_3 direction. These two waves correspond to the conventional pure shear acoustic mode in BC quartz and to the vertical polarisation of the electromagnetic wave. The ratio of the amplitude components $\frac{E}{u}$ is given by the ratio of cofactors of a selected line in the determinant 4.8:

$$\frac{E}{u} = \frac{\mu e\omega^2 jk}{k^2-\omega^2\mu\epsilon} = \frac{ck^2 - \rho\omega^2}{ejk} \qquad 4.11$$

From Equation 4.11 the ratio of all the field amplitudes can be obtained, giving for the acoustic mode

$$\left(\frac{E}{u}\right)_a = -jk_a\frac{e\mu c}{\rho}; \quad \left(\frac{f}{u}\right)_a = -jk_a c; \quad \left(\frac{H}{u}\right)_a = -j\omega e; \quad \left(\frac{E}{f}\right)_a = \frac{e\mu}{\rho} \qquad 4.12$$

and for the electromagnetic mode:

$$\left(\frac{u}{E}\right)_e = -j\frac{e\epsilon\mu}{k_e}; \quad \left(\frac{f}{E}\right)_e = -e; \quad \left(\frac{H}{E}\right)_e = \pm\sqrt{\frac{\epsilon}{\mu}}; \quad \left(\frac{j\omega u}{H}\right)_e = \frac{e\mu}{\rho} \qquad 4.13$$

In the above equations f is the force per unit area on the positive side of a plane perpendicular to the direction of propagation. The wave number k, and the sign in Equation 4.13c is positive for

the forward going wave, and negative for the reverse wave. The approximations made in neglecting $\left(\frac{v_a}{v_e}\right)^2$ compared to 1 are useful, but not necessary.

For the sake of generality the space in front of the quartz crystal is assumed to contain another piezoelectric dielectric in which the field variables lie entirely in the directions so far considered. The diagram of Fig. 4.2b defines the various travelling waves on the two sides of the interface.

The continuity of displacement, force, tangential electric and magnetic fields at the interface is expressed by the following four equations:

$$\begin{aligned} j\omega u_1 + m_1 H_1 &= j\omega u_2 + m_2 H_2 \\ f_1 - e_1 E_1 &= f_2 - e_2 E_2 \\ E_1 + m_1 f_1 &= E_2 + m_2 f_2 \\ H_1 - e_1 j\omega u_1 &= H_2 - e_2 j\omega u_2 \end{aligned} \qquad 4.14$$

In the above equations the mechanical variables associated with the electromagnetic type waves are expressed by the other electromagnetic variables from Equation 4.13, while the electromagnetic variables of the acoustic type waves are expressed by elastic variables from Equation 4.12, and the following notation is employed:

$$\begin{aligned} u_1 &= u_1^+ + u_1^- \\ u_2 &= u_2^+ + u_2^- \quad \text{etc.} \end{aligned} \qquad 4.15$$

also $$m_1 = \frac{e_1 \mu_1}{\rho_1}; \qquad m_2 = \frac{e_2 \mu_2}{\rho_2}$$

If the electromagnetic components of the acoustic wave and the mechanical components of the electromagnetic wave are disregarded, then there is an apparent discontinuity in all the elastic and electromagnetic variables at the interface:

$$
\begin{aligned}
j\omega u_1 - j\omega u_2 &= \Delta j\omega u = -m_1 H_1 + m_2 H_2 \\
f_1 - f_2 &= \Delta f = e_1 E_1 - e_2 E_2 \\
E_1 - E_2 &= \Delta E = -m_1 f_1 + m_2 f_2 \\
H_1 - H_2 &= \Delta H = e_1 j\omega u_1 - e_2 j\omega u_2
\end{aligned}
\qquad 4.16
$$

According to Equation 4.16a the magnetic field strength at the surface gives rise to an apparent surface slip, and the electric field strength gives rise to an effective surface force (Equation 4.16b). Similarly, the stresses cause a jump in the tangential component of the electric field strength (Equation 4.16c) and the displacement velocities cause a jump in the tangential component of the magnetic field strength (Equation 4.16d).

The right hand sides of Equation 4.16 can be formally regarded as defining surface slip, surface force, surface charge and surface current densities, respectively, caused by the piezoelectric effect. For practical purposes, however, it is more useful to regard the discontinuity equation (4.16) as defining the properties of an equivalent network, which transforms the set of four input quantities f_2, $j\omega u_2$, E_2 and H_2 to the output set f_1, $j\omega u_1$, E_1 and H_1. The transfer function of the network is obtained by simple rearrangement of Equation 4.16 as:

$$
\begin{aligned}
f_1 &= \alpha f_2 + 0 + \beta E_2 + 0 \\
j\omega u_1 &= 0 + j\omega u_2 + 0 + \delta H_2 \\
E_1 &= \delta f_2 + 0 + \gamma E_2 + 0 \\
H_1 &= 0 + \beta j\omega u_2 + 0 + \alpha H_2
\end{aligned}
\qquad 4.17
$$

with

$$
\alpha = \frac{1 + m_2 e_1}{1 + m_1 e_1} \approx 1
$$

$$
\beta = \frac{e_1 - e_2}{1 + m_1 e_1} \approx e_1 - e_2 \qquad 4.18
$$

$$
\gamma = \frac{1 + m_1 e_2}{1 + m_1 e_1} \approx 1
$$

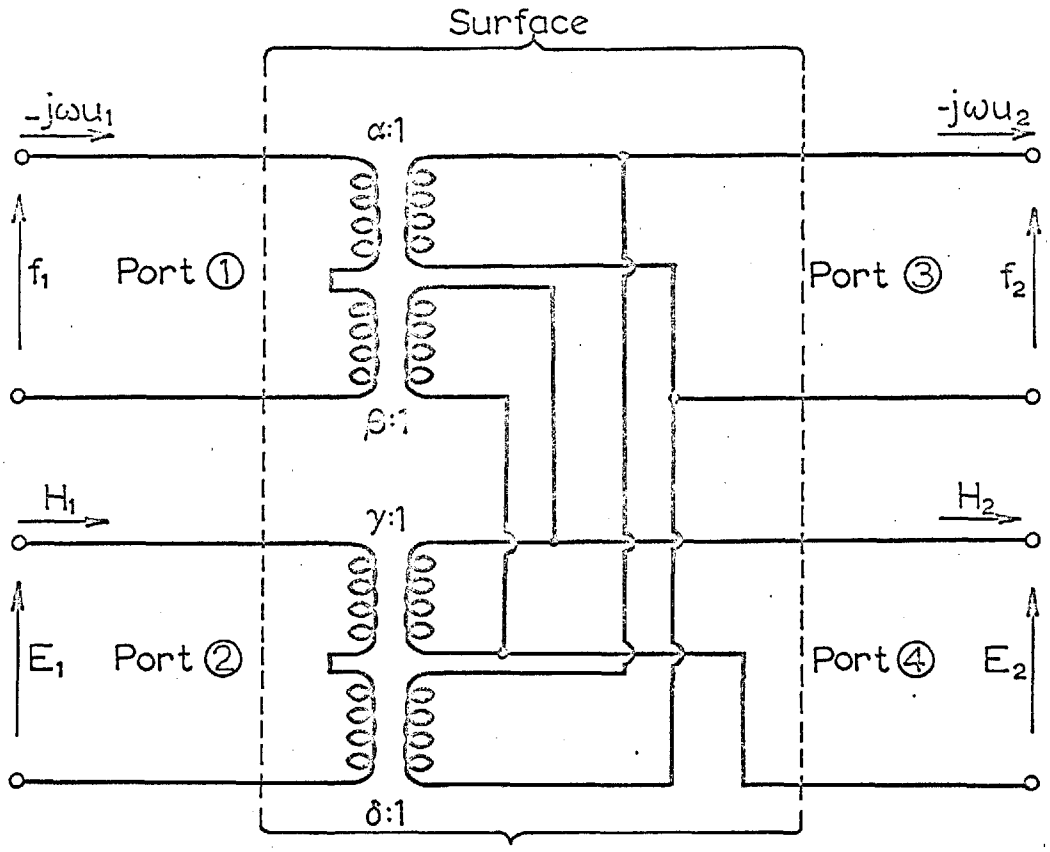
$$
\delta = \frac{m_2 - m_1}{1 + m_1 e_1} \approx m_2 - m_1
$$

The equivalent network indicated in Fig. 4.3a contains four ideal transformers. Equation 4.17 can be put in the form

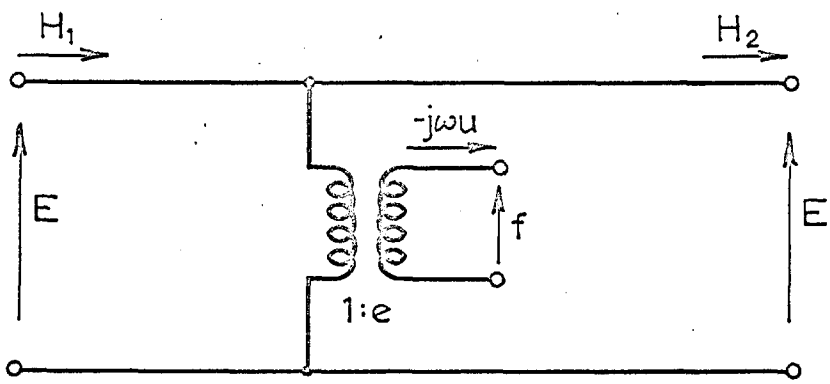
$$
\begin{aligned}
f_1 &= \alpha f_2 + \beta E_2 & \qquad j\omega u_2 &= \alpha j\omega u_1 - \delta H_1 \\
E_1 &= \delta f_2 + \gamma E_2 & \qquad H_2 &= -\beta j\, u_1 + \gamma H_1
\end{aligned}
\qquad 4.19
$$

It is easily seen, that the equivalent network gives the transformation described by Equation 4.19. In the special, practically important, case when medium 2 is air, the terminating impedance at port 3 is zero, and the equivalent circuit can be approximated to the form given in Fig. 4.3b.

When practical figures are substituted in Equations 4.17 and



a) EQUIVALENT CIRCUIT OF PIEZOELECTRIC DISCONTINUITY.



b) SIMPLIFIED FORM.

FIG. 4.3

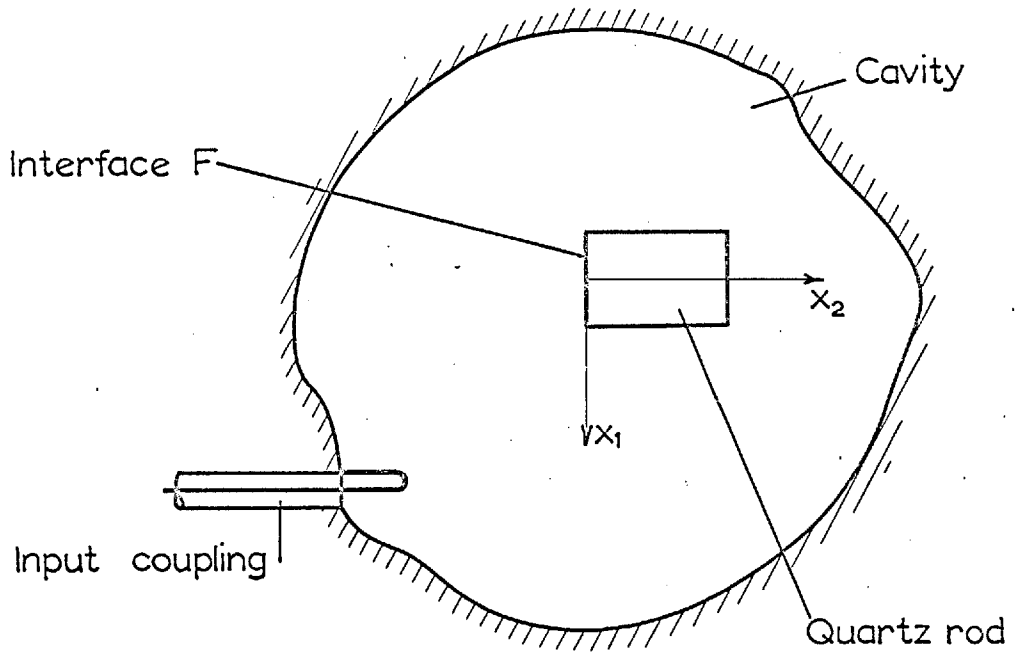
4.18 (for quartz $e = 10^{-1}$ As/m^2, $\frac{f}{j\omega u} = 10^7\Omega$, $\frac{E}{H} = 10^6\Omega$ in high Q cavity), the impedance of the acoustic system, as seen by the electromagnetic field is of the order of 10^3 times higher than the electromagnetic impedance. Correspondingly, the impedance seen by the acoustic waves is 10^3 times lower than the acoustic wave impedance. Because of this large mismatch it is safe to neglect the high acoustic impedance in shunt with the electromagnetic impedance. Also, the zero impedance seen by the acoustic waves at reflection is not significantly increased by the electromagnetic impedance. The above remarks are not valid when the acoustic system is resonant with a high Q as for example in the case of half wavelength resonant transducers.

4.3 THE PREFERRED DIRECTIONS OF EXCITATION.

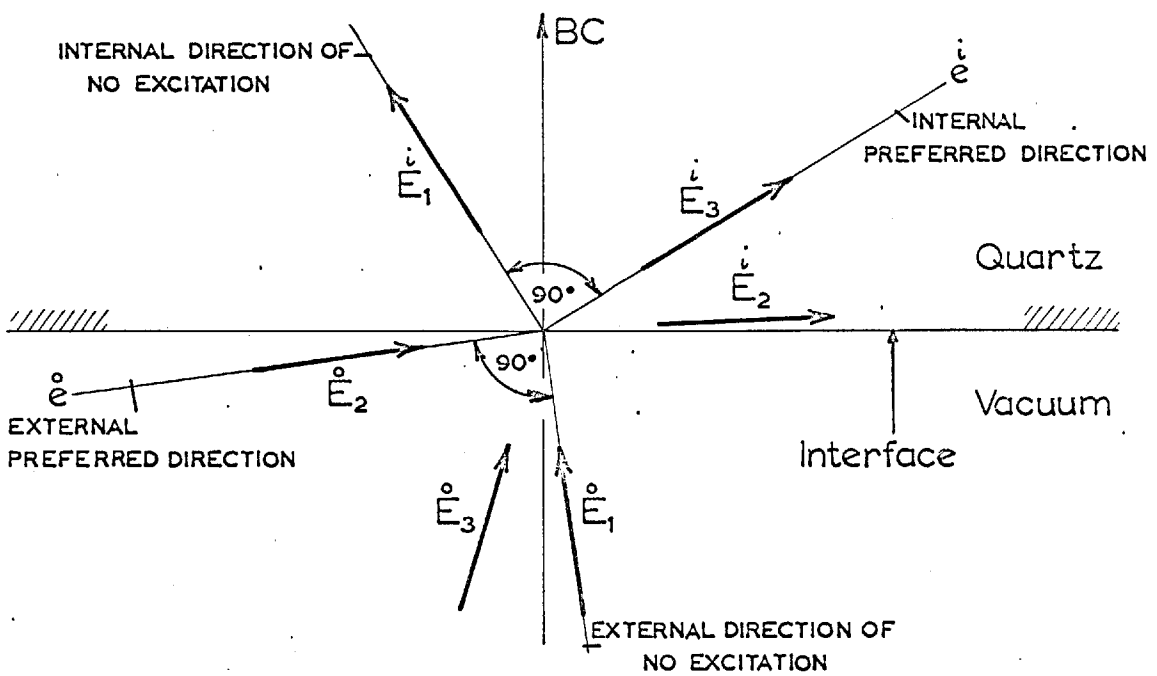
For the simple arrangement of Fig. 4.3b it has been found that the acoustic force per unit area, f, that has been excited by piezoelectric surface excitation is the product of the piezoelectric constant times the electric field. Now it is assumed that a similar equivalent circuit can be given in general for the excited force in each acoustic mode at the interface of a piezoelectric medium and air, and it will be proved that the amplitude of the force is given by

$$f^M = \left(e_i^M\right)_o \cdot E_i \qquad 4.20$$

according to which f^M, the force at the interface in mode M, is the scalar product of the excitation vector $\left(e_i^M\right)_o$ of the mode in question and the electric field strength vector at the air side of the interface. (Lamb and Richter, 1966c). The excitation vector $\left(e_i^M\right)_o$ is a suitably weighted combination of the components of the piezoelectric tensor e_{ijk}. Its direction is the "external preferred direction of excitation", since maximum excitation occurs when the electric field strength vector is orientated in this preferred direction, the magnitude of E remaining constant while its direction



a) SCHEMATIC ARRANGEMENT FOR SURFACE EXCITATION.



b) EXCITATION DIRECTIONS (FS) FOR BC QUARTZ.

FIG. 4.4

is varied. There is no excitation when the electric field vector lies in a plane normal to the preferred direction.

A general arrangement for surface excitation is shown in Fig. 4.4a. A piezoelectric crystal with a flat surface F is inserted in an electromagnetic cavity resonator. The origin of the Cartesian $x_1x_2x_3$ coordinate system is fixed at the centre of the flat surface with x_2 parallel to the surface normal. The transverse surface dimensions are assumed to be very much larger than the acoustic wavelength.

An external signal injected into the cavity by the coupling loop sets up a time varying distribution of electric and magnetic fields inside the cavity. At the dielectric discontinuity F the normal component of the electric flux density (D_2) and the tangential components of the electric field strength (E_1 and E_3) are continuous in the absence of electric and magnetic surface charges and currents. Therefore it is useful to regard the triad $(E_1\ D_2\ E_3) = \Gamma_m$ as the independent variables on the right hand side of the constitutive relations. Simple rearrangement of the Equations 3.41 and 3.42 gives the desired expression for the stress:

$$T_{ij} = (c_{ijkl} + \frac{e_{2ij}e_{2kl}}{\epsilon_{22}})S_{kl} - (e_{qij} - \frac{\epsilon_{2q}}{\epsilon_{22}} e_{2ij})E_q - \frac{e_{2ij}}{\epsilon_{22}} D_2 \qquad 4.21$$

or, more concisely

$$T_{ij} = \bar{c}_{ijkl}S_{kl} - \bar{e}_{mij}\Gamma_m \qquad 4.22$$

where the coefficients $\bar{c}_{ijkl}$ and $\bar{e}_{mij}$, are defined by Equation 4.21. The modified elastic stiffness constant $\bar{c}_{ijkl}$ is the same as the "piezoelectrically stiffened constant" previously considered (Equation 3.45).

Substitution of Equation 4.22 into the equation of linear momentum gives (with $e^{j\omega t}$ time variation and no change along the x_1 or x_3 coordinates):

$$\omega^2 \rho u_i + \frac{\partial}{\partial x_2}\left(\bar{c}_{i2k2}\frac{\partial u_k}{\partial x_2}\right) = \frac{\partial}{\partial x_2}\left(\bar{e}_{mi2}\Gamma_m\right) \qquad 4.23$$

The material coefficients $\bar{c}$ and $\bar{e}$ cannot be moved outside the differential operator $\frac{\partial}{\partial x_2}$ because they are not constant at or near the discontinuity. It is supposed that in a small region $-\varepsilon < x_2 < \varepsilon$ around the interface at $x_2 = 0$ the various elastic, dielectric and piezoelectric coefficients change from one value to the other and remain constant outside this region.

Integrating Equation 4.23 by dx_2 between the limits $+\varepsilon$ and $-\varepsilon$ gives

$$\omega^2 \int_{-\varepsilon}^{+\varepsilon} \rho u \, dx_2 + \left[\bar{c}_{i2k2}\frac{\partial u_k}{\partial x_2}\right]_{-\varepsilon}^{+\varepsilon} = \left[\bar{e}_{mi2}\Gamma_m\right]_{-\varepsilon}^{+\varepsilon} \qquad 4.24$$

If the width of the region tends towards zero, the limits in the first term of Equation 4.24 coincide, making the integral zero, since the integrand is finite. When the medium on the left is air, both the elastic and piezoelectric constants are zero at $-\varepsilon$. Hence

$$\left(\bar{c}_{i2k2}\frac{\partial u_k}{\partial x_2}\right)_{\text{at } +0} = \left(\bar{e}_{mi2}\Gamma_m\right)_{\text{at } +0} \qquad 4.25$$

(Equation 4.25 expresses the condition of stress-free surface).

In general three acoustic modes can be excited, and they all can contribute to $\frac{\partial u_k}{\partial x_2}$. In addition to the mechanical displacement in the acoustic waves, the resonant mode of the cavity field also has a very small mechanical displacement component associated with it. The relative error introduced by neglecting the latter contribution to $\frac{\partial u_k}{\partial x_2}$ in the case of uniform plane waves is found

from Equations 4.12 and 4.13 to be proportional to the ratio of acoustic to electromagnetic velocity, and hence it will be neglected in the general case, now considered. Expressing the displacement gradient on the left hand side of Equation 4.25 as that resulting from the three acoustic modes one has

$$\sum_{M=1}^{3} - jk^M \bar{c}_{i2k2} \alpha_k^M U^M = \bar{e}_{mi2} \Gamma_m \qquad 4.26$$

where k^M, α_k^M and U^M are the wave vector, direction cosines of displacement and amplitude of displacement, respectively, for mode M. There is no automatic summing over the index M. Taking into account that* (c.f. Equation 3.10)

$$\bar{c}_{i2k2} \alpha_k^M = C^M \alpha_i \qquad 4.27$$

where C^M, the eigenvalue(or effective elastic constant) of mode M, is a root of the determinental equation (δ = Kronecker delta)

$$\mathrm{Det} \left| \bar{c}_{i2k2} - \delta_{ik} C^M \right| = 0 \qquad 4.28$$

Equation 4.26 can be rewritten as

$$\sum_{M=1}^{3} - jk^M C^M \alpha_i^M U^M = \bar{e}_{mi2} \Gamma_m \qquad 4.29$$

Multiplying both sides by α_i^M gives*

$$- jk^M C^M U^M = \bar{e}_{mi2} \alpha_i^M \Gamma_m \qquad 4.30$$

as

$$\alpha_i^M \alpha_i^M = 1$$

$$\alpha_i^M \alpha_i^N = 0 \qquad 4.31$$

---

* The electromagnetic components of the coupled acoustic type waves are neglected together with mechanical displacement components associated with the electromagnetic modes.

owing to the orthogonality of the direction cosines* of the different modes. The left hand side of Equation 4.30 is the force* per unit area on a plane perpendicular to x_2 in mode M:

$$f^M = \bar{e}_{mi2}\, \alpha_i^M\, \Gamma_m \qquad 4.32$$

Resubstitution of $\bar{e}_{2i2}$ and Γ_m, and the continuity of Γ at the interface yields:

$$f^M = \bar{e}_{qi2}\, \alpha_i^M\, E_q + e_{2i2}\, \alpha_i^M\, \frac{D_2}{\epsilon_{22}} \qquad 4.33$$

$$= \bar{e}_{qi2}\, \alpha_i^M\, E_q^{\,o} + e_{2i2}\, \alpha_i^M\, \frac{\epsilon_o}{\epsilon_{22}}\, E_2^{\,o}$$

where $E_i^{\,o}$ represents electric field strength <u>outside</u> the dielectric. Therefore the force in the excited acoustic mode M is given by

$$f^M = \left(e_i^M\right)_o E_i^{\,o} \qquad 4.34$$

where the components of the "external excitation vector" are

$$\left(e_1^M\right)_o = \left(e_{1j2} - e_{2j2}\frac{\epsilon_{21}}{\epsilon_{22}}\right)\alpha_j^M$$

$$\left(e_2^M\right)_o = \left(e_{2j2}\frac{\epsilon_o}{\epsilon_{22}}\right)\alpha_j^M \qquad 4.35$$

$$\left(e_3^M\right)_o = \left(e_{3j2} - e_{2j2}\frac{\epsilon_{32}}{\epsilon_{22}}\right)\alpha_j^M$$

Equation 4.34 shows that the excited amplitude is the scalar product of the electric field strength (on the air side) and the external excitation vector $\left(e_i^M\right)_o$. The direction of $\left(e^M\right)_o$ will be designated as the external preferred direction of excitation for mode M.

---

* see footnote of previous page.

The excitation can be expressed in terms of the electric field on the dielectric side of the interface, too. If D_2 in Equation 4.33 is substituted from the constitutive relations, Equation 4.33 takes the following form:

$$f^M = e_{mi2}\alpha_i^M E_m^I + \sum_{N=1}^{3} \frac{(e_{2i2}\alpha_i^M)(e_{2k2}\alpha_k^N)}{\epsilon_{22} C^N} f^N \qquad 4.36$$

where e_{mi2} are the ordinary piezoelectric constants and E_m^I is the electric field strength inside the dielectric at the interface. Solving Equation 4.36 explicitly for f^M gives:

$$f^M = E_j^I \left(e_j^M\right)_I + \frac{\sum_{M=1}^{3} k_{2M}\left(e_i^M\right)_I}{1-k_{11}-k_{22}-k_{33}} \cdot E_1^I \qquad 4.37$$

where

$$\left(e_j^M\right)_I = e_{jk2}\alpha_k^M$$

and

$$k_{MN} = \frac{(e_{2i2}\alpha_i^M)(e_{2k2}\alpha_k^N)}{\epsilon_{22} C^N} \qquad 4.38$$

For quartz the values of the quantities described by k_{MN} are less than 10^{-2}, allowing to neglect the second term in Equation 4.3 without introducing an unacceptable error. With this approximation

$$f^M = \left(e_j^M\right)_I \cdot E_j^I \qquad 4.39$$

The direction of the vector $\left(e_j^M\right)_I$ defines, for materials with negligibly small piezoelectric coupling, an internal preferred direction of excitation. This direction, for the 3 modes along a selected direction of propagation can be found from the contour maps of Figs 5.9 - 5.11.

Both the internal and the external preferred directions of excitation are shown in Fig. 4.4b to the right scale for the FS

mode, when the normal of the vacuum-dielectric interface is parallel to the BC crystallographic direction. There are three pairs of corresponding external and internal electric field strength vectors shown in Fig. 4.4b.

a) For E_1 the external field strength vector makes an angle of 90° with the external excitation direction, and necessarily, the internal field strength vector, too, is normal to the internal excitation direction, therefore no excitation occurs.

b) E_2 is parallel to $\overset{o}{e}$ in vacuo, but is not parallel to $\overset{i}{e}$ in the dielectric. This situation corresponds to maximum excitation as the direction of E is varied, but the external field intensity is kept constant.

c) E_3 is parallel to $\overset{i}{e}$ in the dielectric, but is not parallel to $\overset{o}{e}$ in vacuo. This situation corresponds to maximum excitation as the direction of E is varied but the internal field intensity is kept constant.

When the preferred directions are either normal or parallel to the surface, the direction of E for maximum excitation is the same independently whether it is the internal or the external field intensity that is kept constant.

The intensity and direction of the electric field at the interface depend in a complicated way on the geometry of the cavity-piezoelectric crystal arrangement, and to find the arrangement for maximum excitation when the input power to the cavity is kept constant, is a difficult design problem. The preferred directions define directions which are furthest removed from those corresponding to no excitation.

4.4 PRACTICAL CONVERSION EFFICIENCY.

In cases of practical interest the dimensions of the piezoelectric medium are large enough allowing the acoustic type waves to be considered as simple plane waves, but too small to allow unrestricted travel of electromagnetic plane waves, and thus making the wave superposition method (Section 4.2) too complicated. To obtain a practical formula for the conversion efficiency it is assumed that the electromagnetic field is not affected by the presence of a piezoelectric medium in any other way than by its dielectric permittivity. (Such an assumption seems justified, since it was found in Section 4.2 that the impedance of the acoustic system is much higher than the electromagnetic impedance.) Then it is possible to solve Maxwell's equations with the given boundary conditions independently, neglecting piezoelectric effects. The electric fields so obtained can then be used to calculate the excitation of the acoustic waves. It is also accepted that excitation and reexcitation are reciprocal.

The electromagnetic field is contained in a cavity resonator of high enough Q to support only a single electromagnetic resonant mode at a given frequency. The behaviour of the resonator as seen by the coupling loop can be described by an equivalent circuit:



FIG. 4.5 EQUIVALENT CIRCUIT OF TRANSDUCER CAVITY.

V_o is defined along the path over which maximum voltage is developed. (Moreno, 1958). The electric field across the piezo-

electric surface is proportional to V_o

$$E = \frac{V_o}{\ell} \qquad 4.40$$

The direction of E and the value of ℓ can be calculated for a given resonator configuration.

The acoustic power is given by

$$P_A = A\, f \cdot j\omega u = A\, f^2 \frac{1}{Z_A} \qquad 4.41$$

where A is the area across which the acoustic power flows, and Z_A is the acoustic impedance

$$Z_A = \frac{f}{j\omega u} = \sqrt{\rho c} \qquad 4.42$$

Substitution of Equation 4.20 into Equation 4.41 gives

$$P_A = \frac{A e^2 E^2 \cos^2\psi}{Z_A} \qquad 4.43$$

where ψ is the angle between the electric field strength vector and the preferred direction.

The electromagnetic power (at resonance) is given by

$$P_E = \frac{V_o^2}{R_{sh}} \qquad 4.44$$

It has been assumed, that the acoustic energy is much smaller than the electromagnetic energy, therefore the efficiency can be given by

$$a = \frac{P_A}{P_A + P_E} \approx \frac{P_A}{P_E} \qquad 4.45$$

with $a \ll 1$. Hence

$$a = \frac{e^2}{Z_A} \cdot \frac{A}{\ell^2} \cdot \cos^2\psi \cdot R_{sh} \qquad 4.46$$

In the above expression for the efficiency

$$\frac{e^2}{Z_A} = \frac{e^2}{\sqrt{\rho c}} = k^2 v\epsilon = \gamma \qquad 4.47$$

(k is the usual piezoelectric coupling coefficient). γ is a property of the piezoelectric medium whose dimensions are that of electrical admittance. The rest of the product in Equation 4.46 will be designated by R^* .

$$R^* = \frac{A}{l^2} \cos^2\psi \, R_{sh} \qquad 4.48$$

R^* is an effective shunt resistance, whose value is dependent on the Q and the design of the resonator. With the definitions of γ and R^* the efficiency can be written in the simple form of

$$a = \gamma . R^* \qquad 4.49$$

It is significant that the above expressions for the conversion efficiency do not contain the frequency, showing that surface excitation is frequency independent. The expression of conversion efficiency hitherto available is due to Bömmel and Dransfeld (1960) showing an efficiency proportional to the acoustic wavelength. Such a frequency dependence would give rise to the anomaly of practically 100% surface excitation below a certain frequency. The formula obtained in this thesis is supported by experimental observations which do not indicate any significant change in the excitation efficiency from the lowest frequency of resonant transducers to almost optical frequencies.

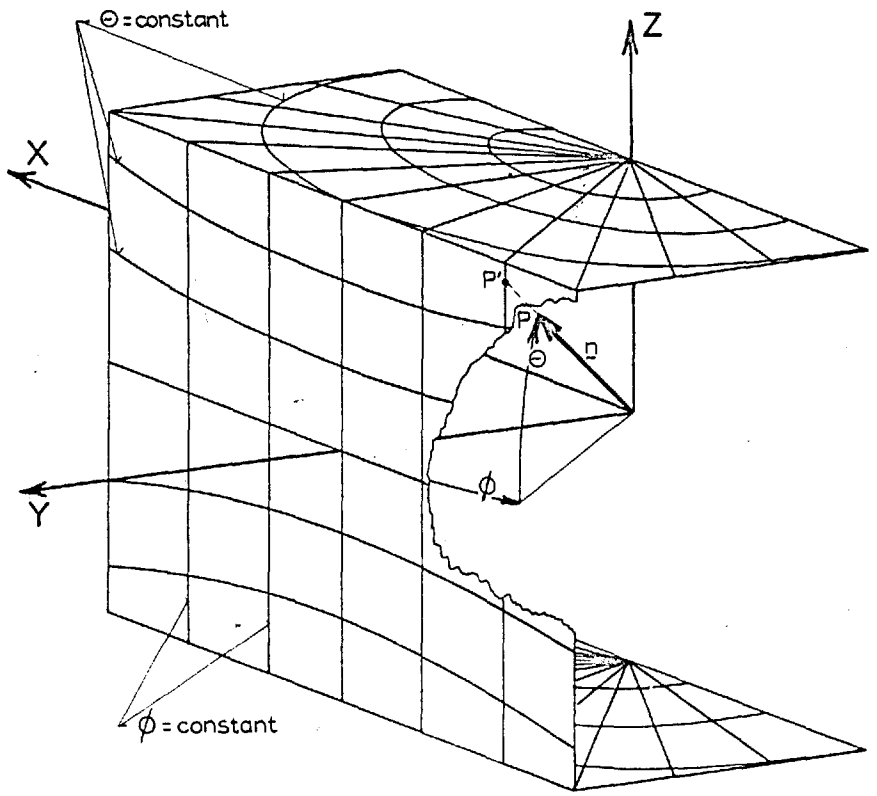
CHAPTER 5.
NUMERICAL RESULTS FOR THE ORIENTATION DEPENDENCE OF PROPAGATION AND EXCITATION PROPERTIES IN QUARTZ.

5.1 ORGANISATION OF THE DATA.

The phase velocity, polarisation, internal preferred direction and efficiency of excitation for all three modes of an acoustic plane wave in crystal quartz have been computed as functions of crystallographic orientation. The results of the computations are given in the form of contour maps in a suitably devised coordinate system. Such contour maps are available for the velocity and polarisation of acoustic waves in certain cubic and hexagonal media (Fein and Smith, 1952; Gold, 1950). The trigonal class, to which quartz belongs, has not been investigated in this manner before.

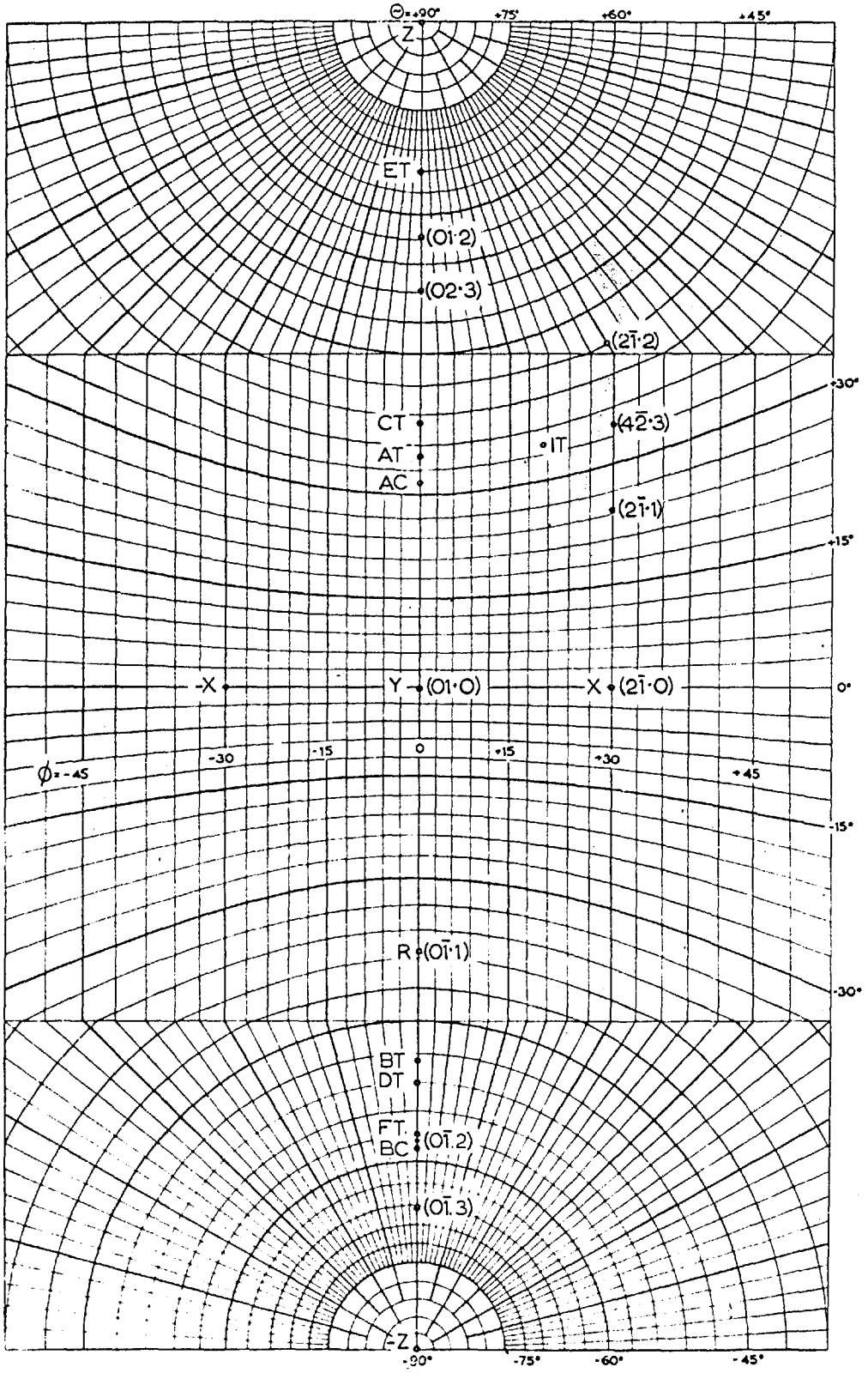
The construction of the coordinate grid system used in the calculations and in the presentation of the results is shown in Fig. 5.1. The point P is on the unit sphere, generated by the tip of the unit vector $\underline{n}$ lying in the direction of propagation (direction of phase velocity). P' is the projection of P from the centre of the sphere on to a vertical or a horizontal plane. The vertical plane is tangential to the unit sphere at the point corresponding to propagation along the Y crystallographic direction. The horizontal planes are tangential to the unit sphere at directions corresponding to the +z and -z crystallographic directions.

When the 3 projection planes are folded flat they give the coordinate grid of Fig. 5.2, where ϕ is the azimuth angle and θ is the elevation angle. The points corresponding to the most common cuts and orientations are labelled in this diagram by the letter notation of the cuts and the crystallographic 3-digit hexagonal Miller indices.



CONSTRUCTION OF THE COORDINATE GRID.

FIG. 5.1



IDENTIFICATION OF THE MOST COMMON CUTS AND ORIENTATIONS OF CRYSTALLINE QUARTZ.

FIG. 5.2

Due to the crystallographic symmetry, a suitably selected portion of the grid contains all crystallographically different orientations without repetition. The calculation of the acoustic and piezoelectric properties was performed over such a section at 3° intervals both ways in the range $0 \leqslant \phi \leqslant 30^\circ$, $-90^\circ \leqslant \theta \leqslant +90^\circ$. Additional denser grids were needed around the poles at 3° intervals in the range $0^\circ \leqslant \phi \leqslant 60^\circ$ and at 0.5° intervals in the range $78^\circ \leqslant \theta \leqslant 90^\circ$ and also for $0 \leqslant \phi \leqslant 25^\circ$, and $18^\circ \leqslant \theta \leqslant 33^\circ$ at 1° and 0.5° intervals, respectively.

The University of Glasgow DEUCE computer was used for the calculations. A short description of the method of calculation and programming is found in Appendix H.

Most of the information obtained from the calculations is presented in the form of contour maps. These maps have been obtained from about 50,000 individual data, which cannot be given in a tabulated form here. The contour maps show excellently the general pattern of variation of the calculated properties with crystallographic orientation, and the accuracy with which the values can be read off from the maps is acceptable for most practical purposes.

5.2 PRESENTATION OF RESULTS.

The contours of the phase velocity for the longitudinal (L), fast shear (FS) and slow shear (SS) modes in mm/μsec are given by Figs. 5.3, 5.4 and 5.5 respectively. In calculating the phase velocity, piezoelectric stiffening has been taken into account.

Figs. 5.6, 5.7 and 5.8 show the deviation (in degrees) of the mechanical displacement vector from the pure mode direction for the three modes (Displacement in pure mode — longitudinal: along

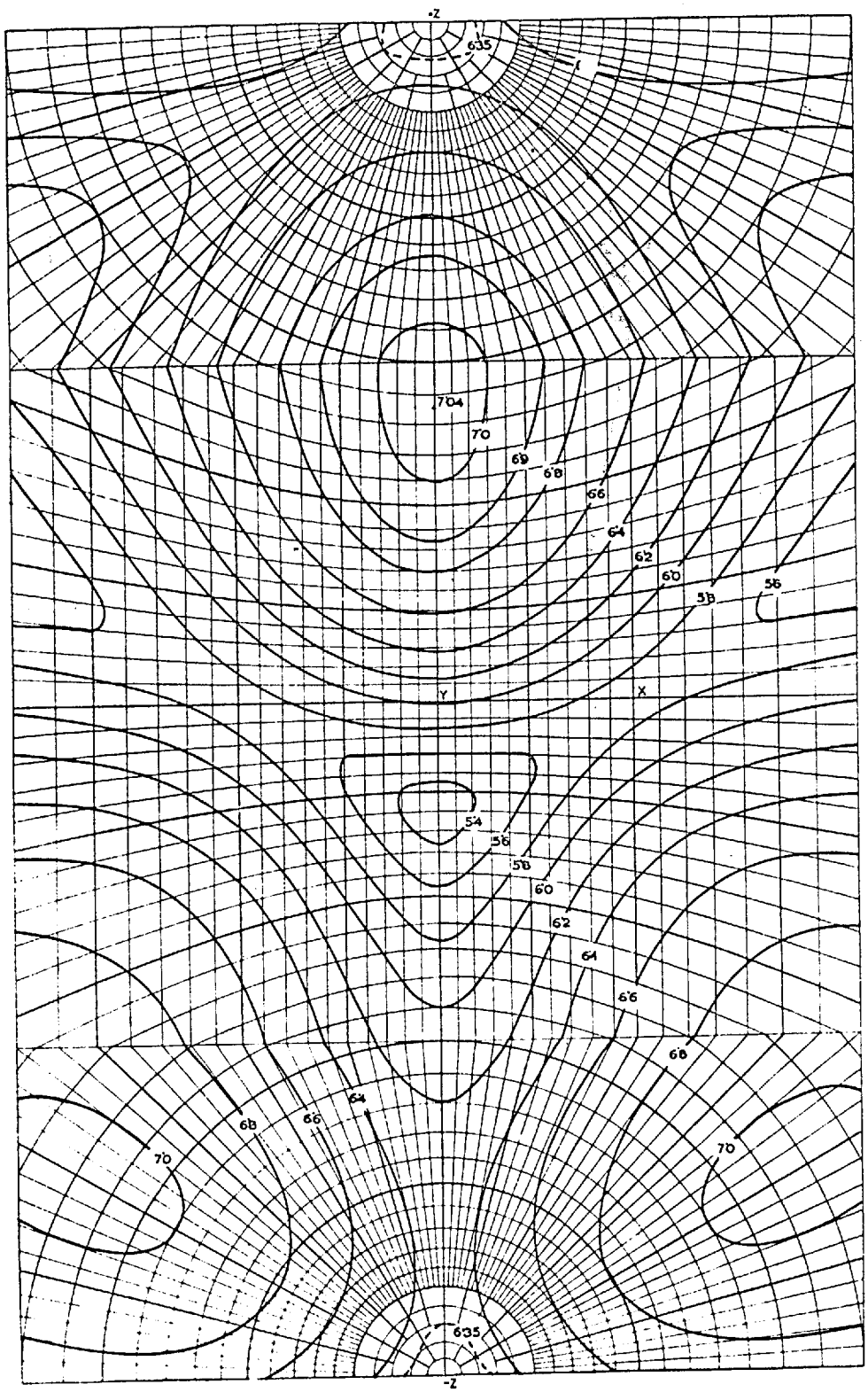
the direction of propagation, shear: transverse to the direction of propagation.

Figs. 5.9, 5.10 and 5.11 give the contours of the angle (in degrees) between the internal excitation vector (preferred direction of excitation inside the dielectric) and the plane of the flat excited surface for the three modes (90° = normal to the surface).

Figs. 5.12, 5.13 and 5.14 give contours of the relative conversion efficiency (proportional to γ of Equation 4.47) in decibels for the three modes. These contours show the relative efficiency for constant electric field intensity inside the dielectric when the direction of the internal electric field strength vector is parallel to the preferred direction.

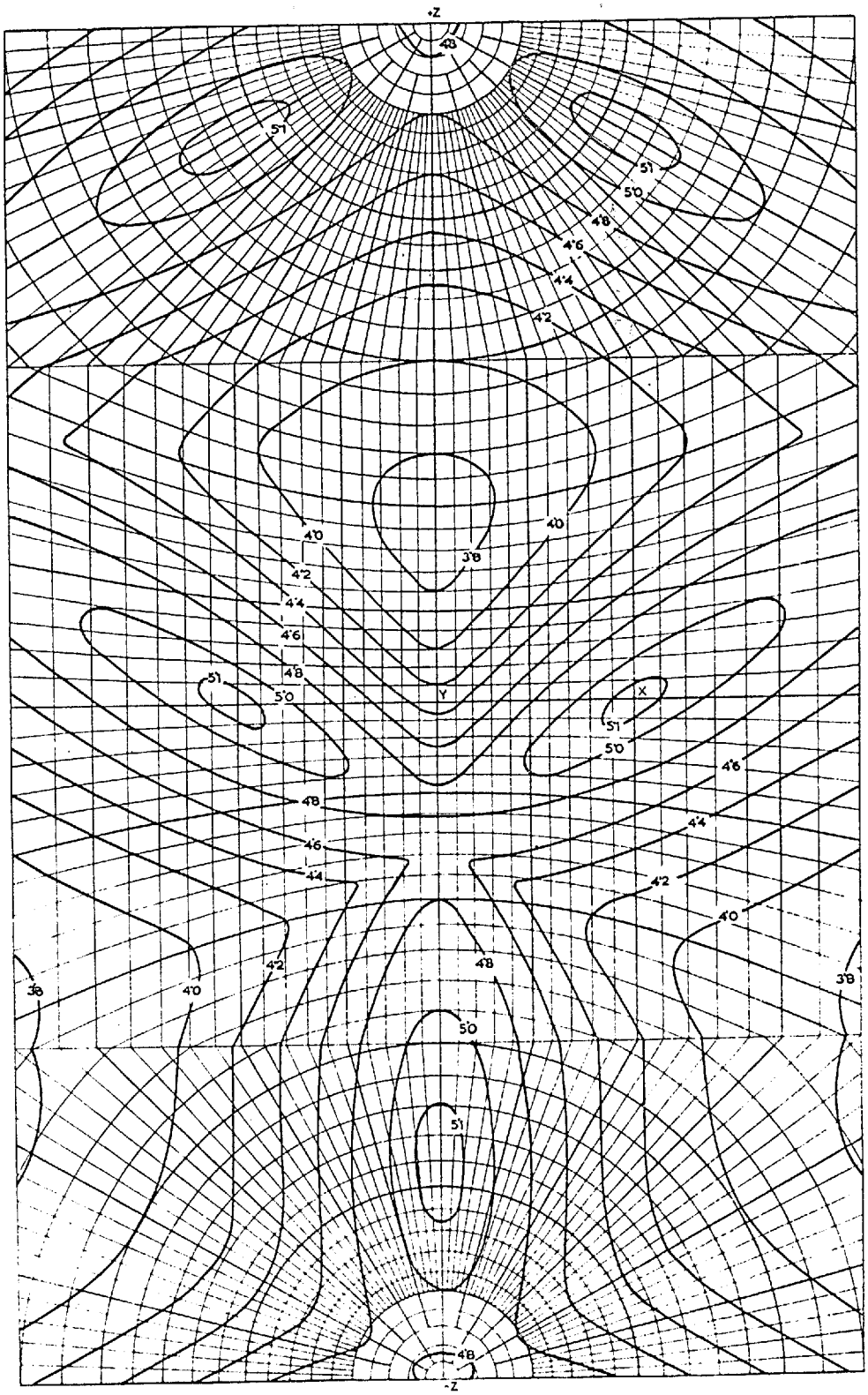
The numerical values of the elastic, piezoelectric and dielectric constants that have been used in the calculations are shown in the tables of Appendix E. These values were taken from the paper by Koga et al. (1958) with which later values, obtained by McSkimin (1962) are in sensible agreement.

Farnell (1961) gave graphs for the velocity and polarisation of acoustic waves in quartz for directions contained in the three coordinate planes, and the present data for these directions are in basic agreement with his.



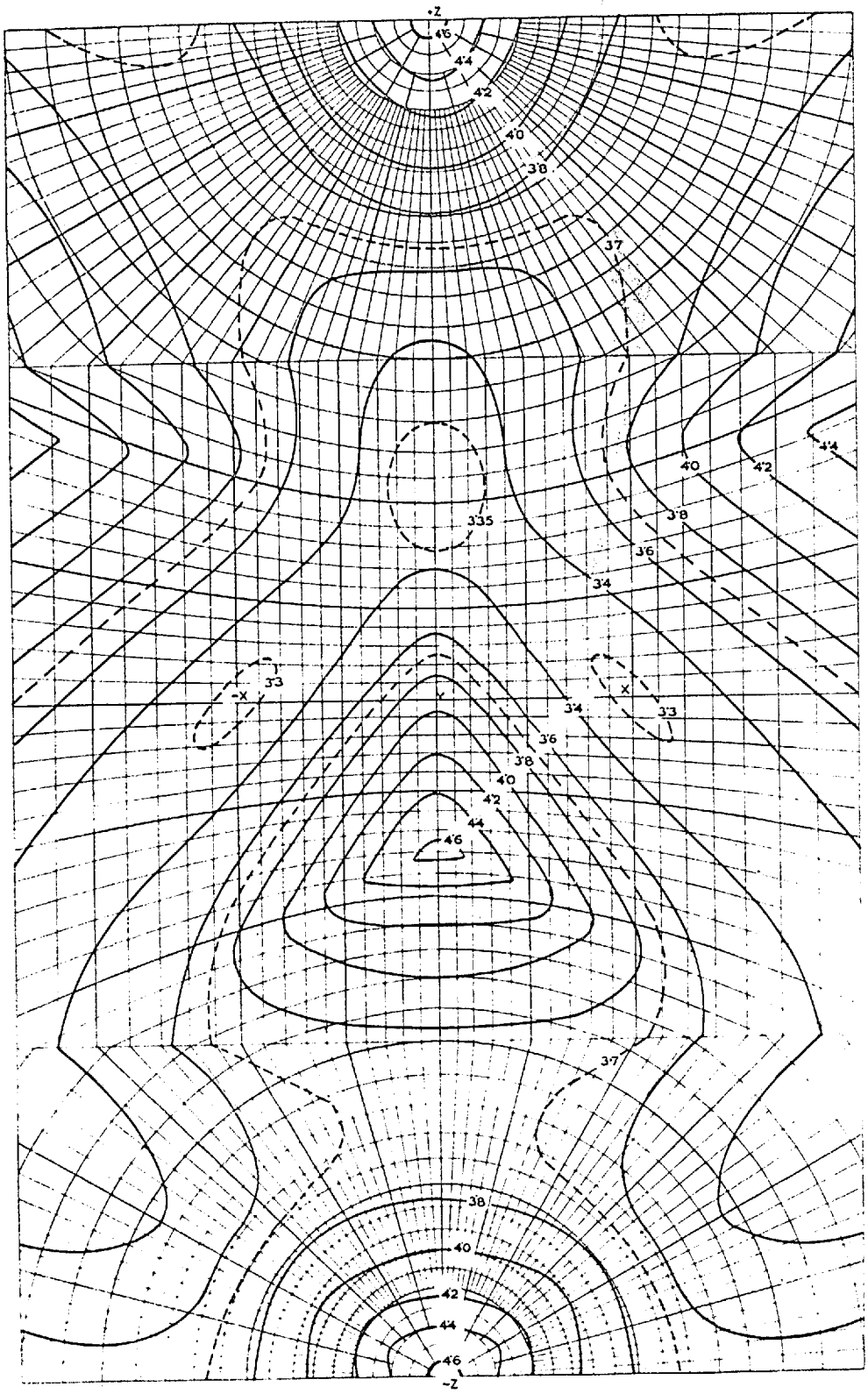
CONTOURS OF THE LONGITUDINAL VELOCITY. (IN mm/μs)

FIG. 5.3



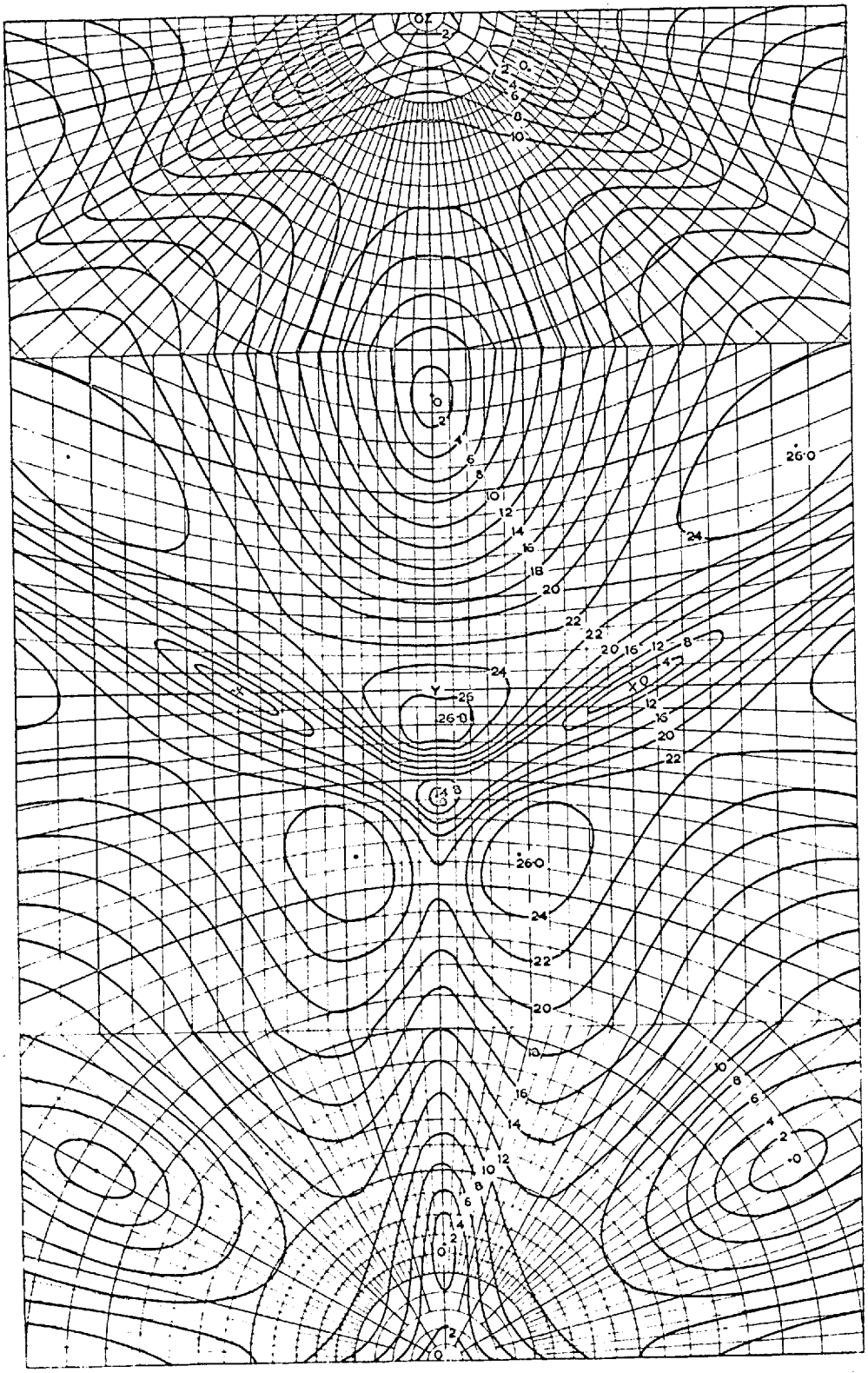
CONTOURS OF THE FAST SHEAR VELOCITY (IN mm/μs)

FIG. 5.4



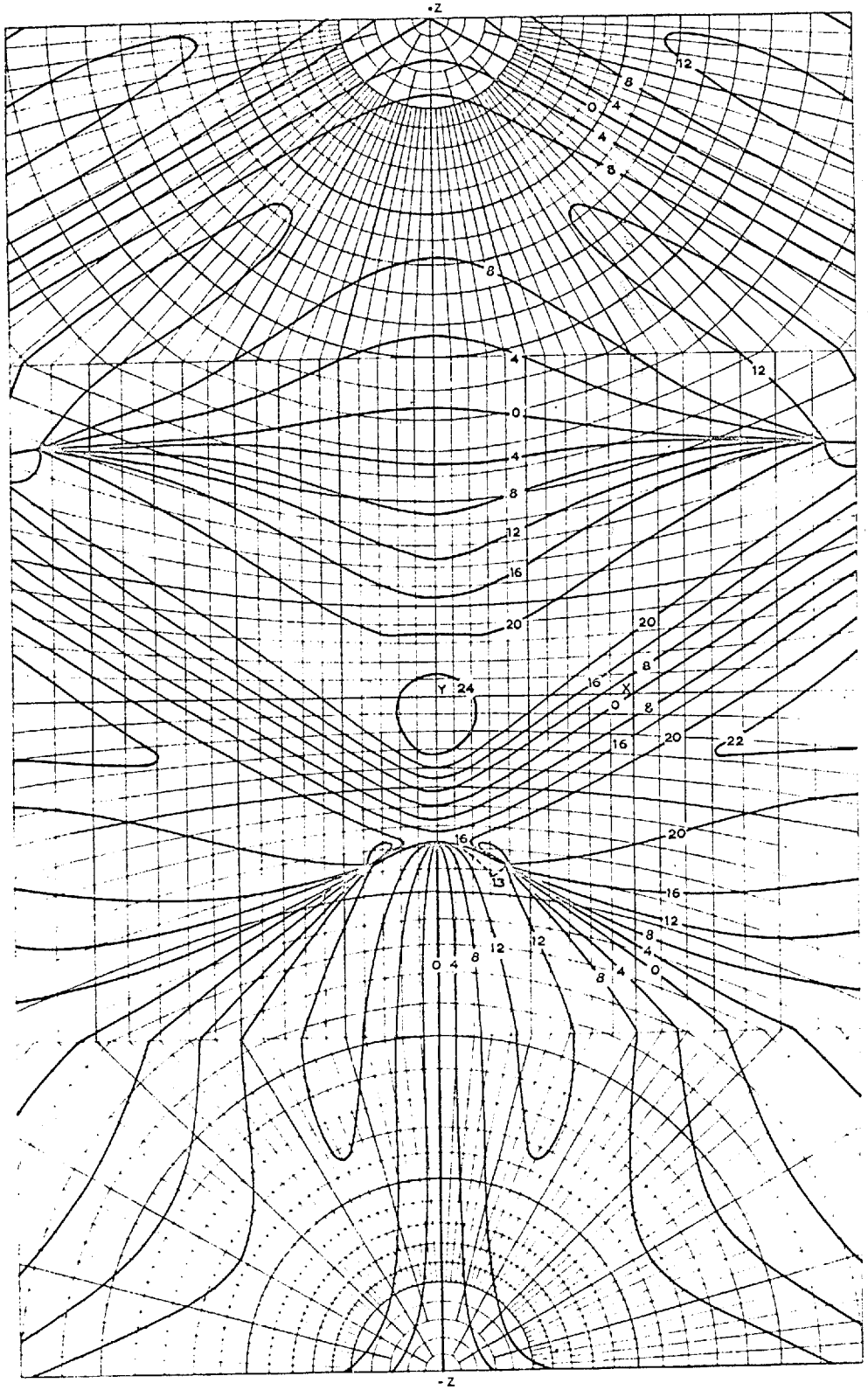
CONTOURS OF THE SLOW SHEAR VELOCITY. (IN mm/μs)

FIG. 5.5



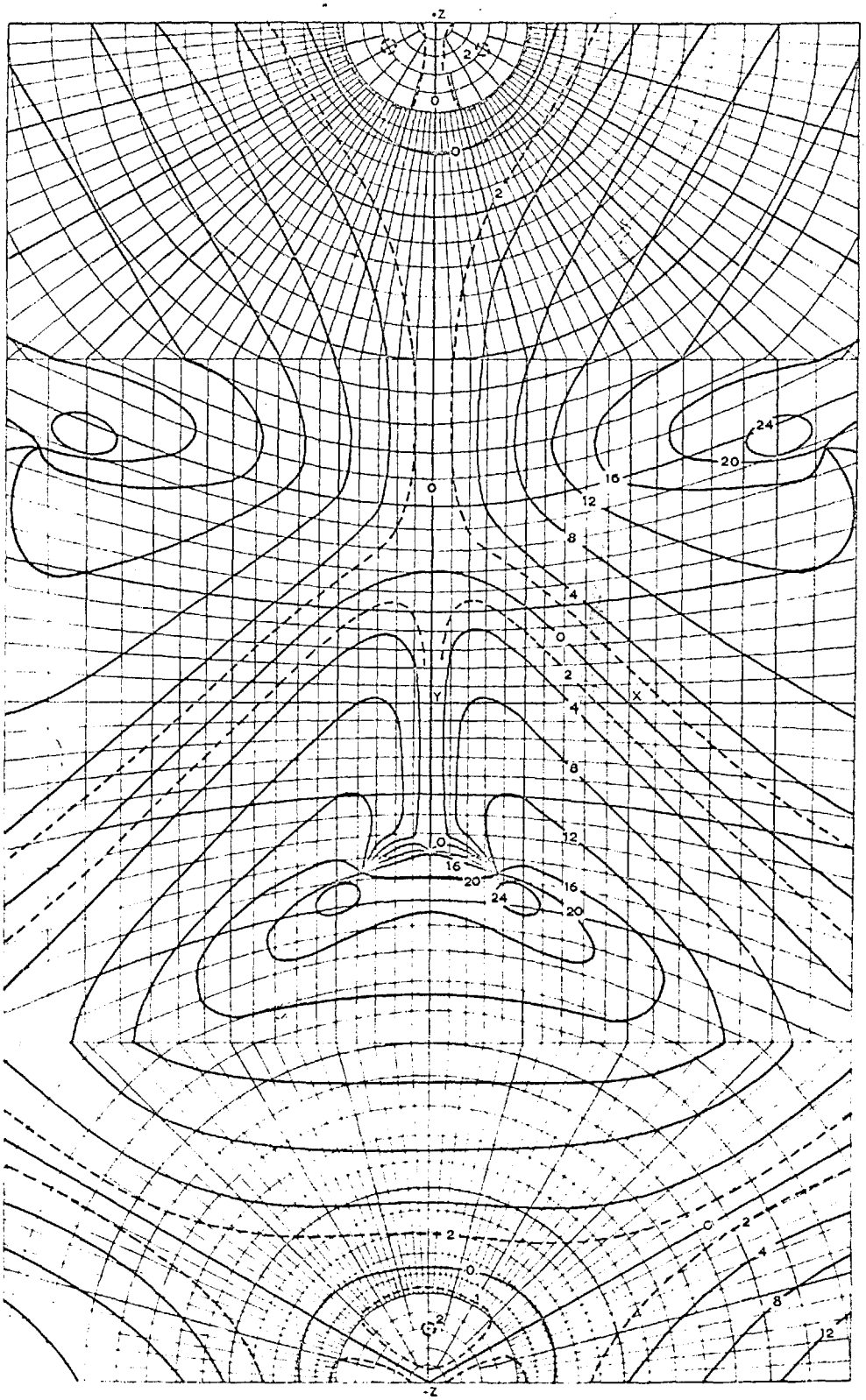
CONTOURS OF THE LONGITUDINAL MODE DISPLACEMENT ANGLE. (Degrees)

FIG. 5.6



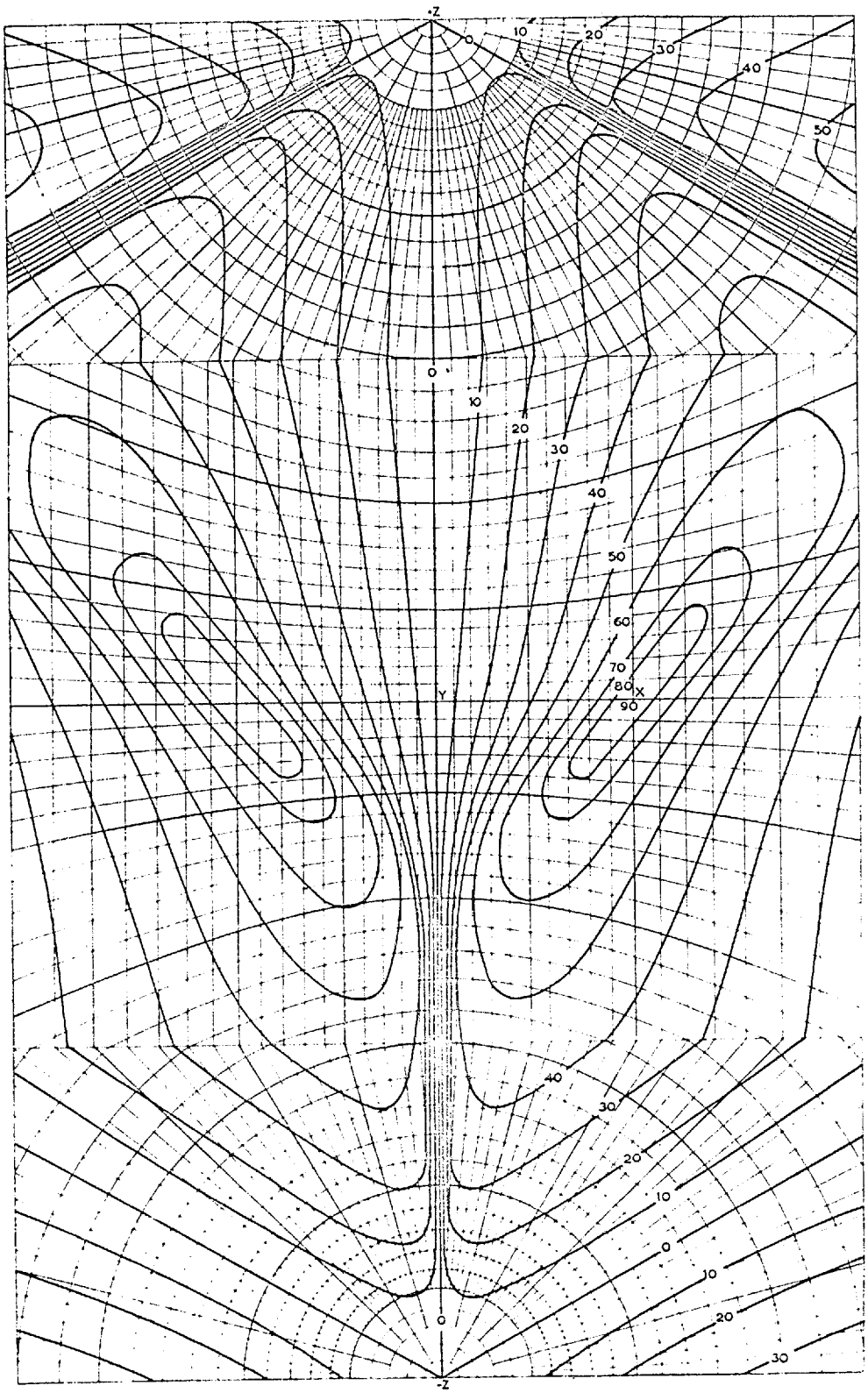
CONTOURS OF THE FAST SHEAR MODE DISPLACEMENT ANGLE. (Degrees)

FIG. 5.7



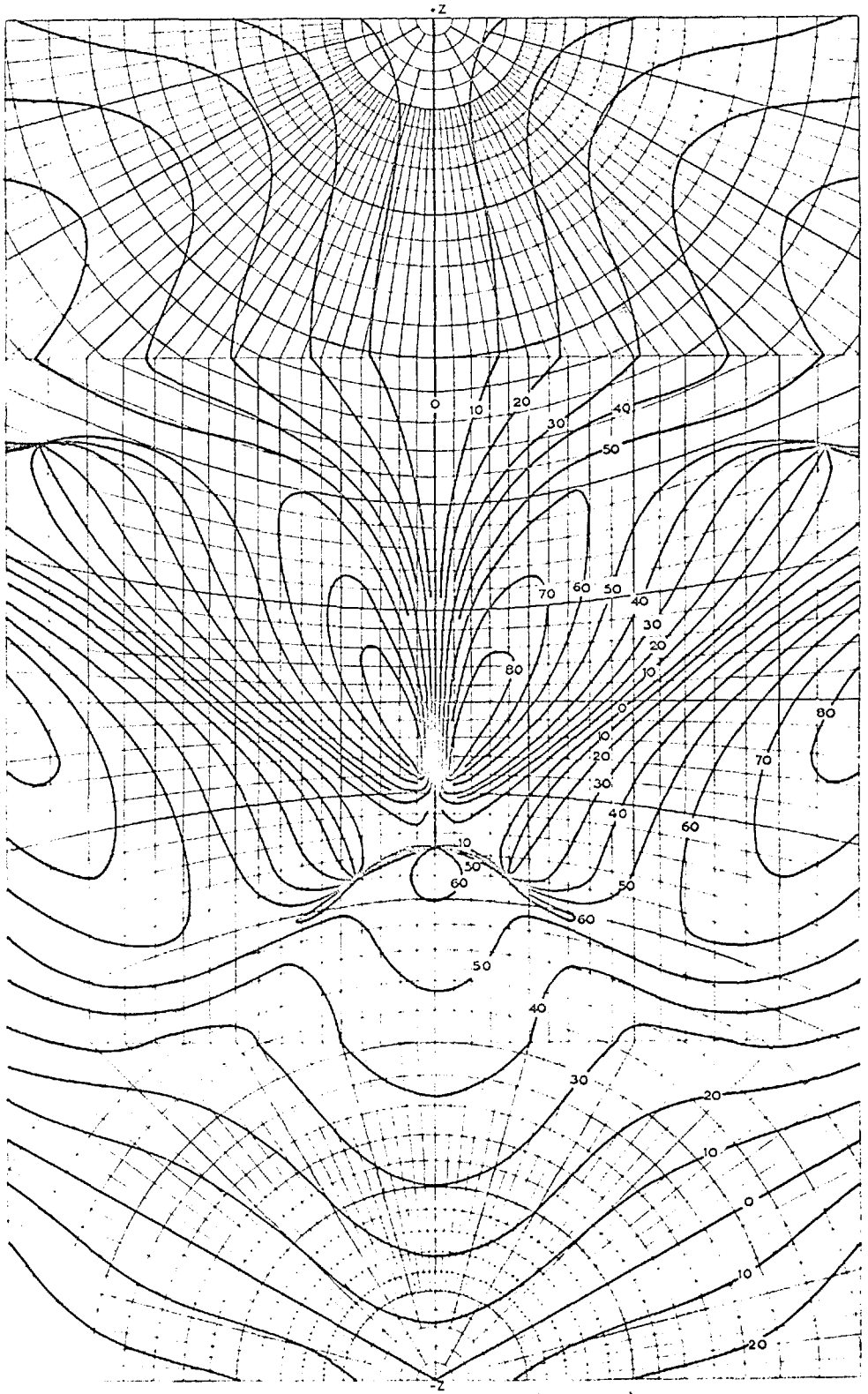
CONTOURS OF THE SLOW SHEAR MODE DISPLACEMENT ANGLE.(Degrees)

FIG. 5.8



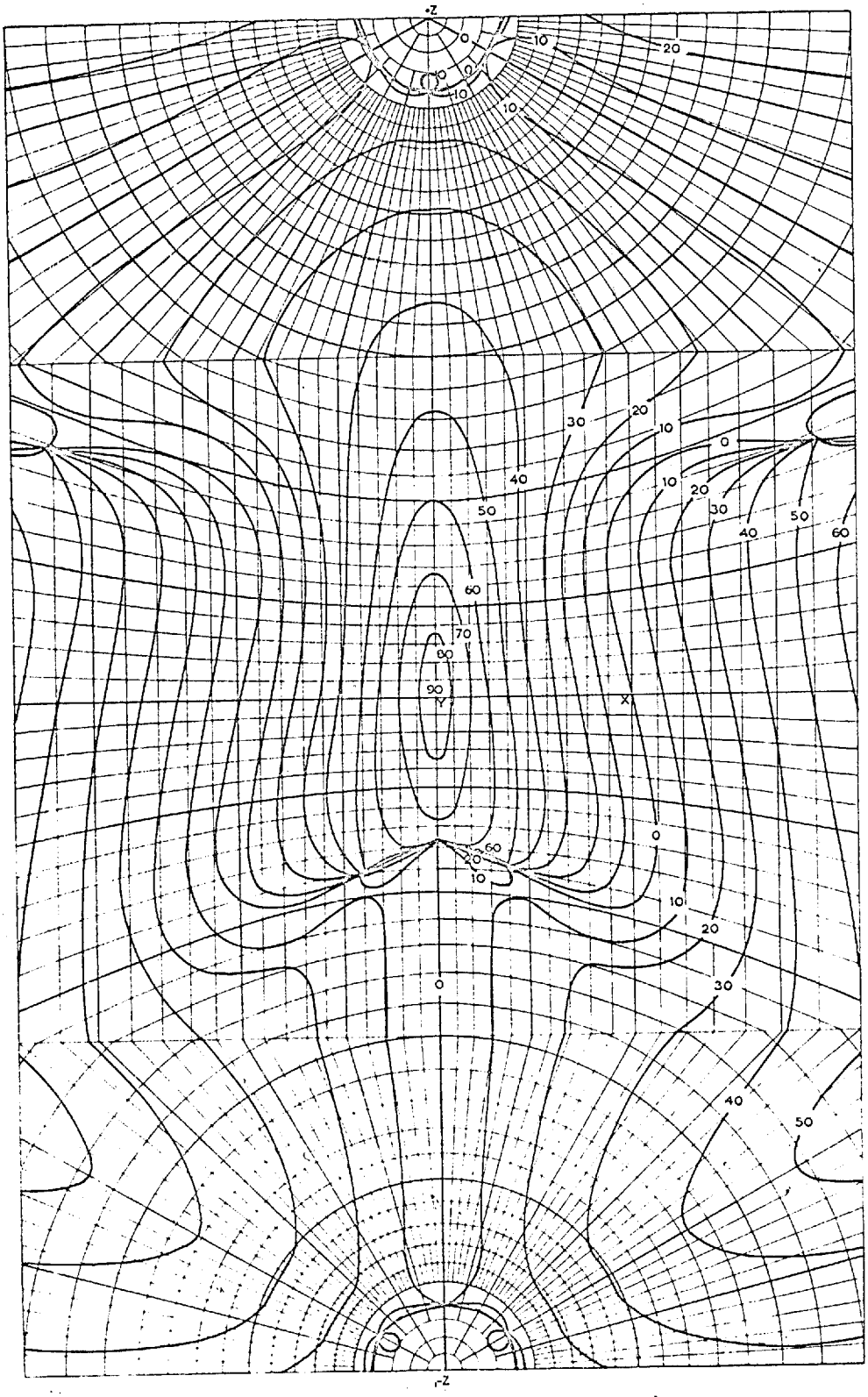
EXCITATION ANGLE. LONGITUDINAL MODE. (Degrees)

FIG. 5.9



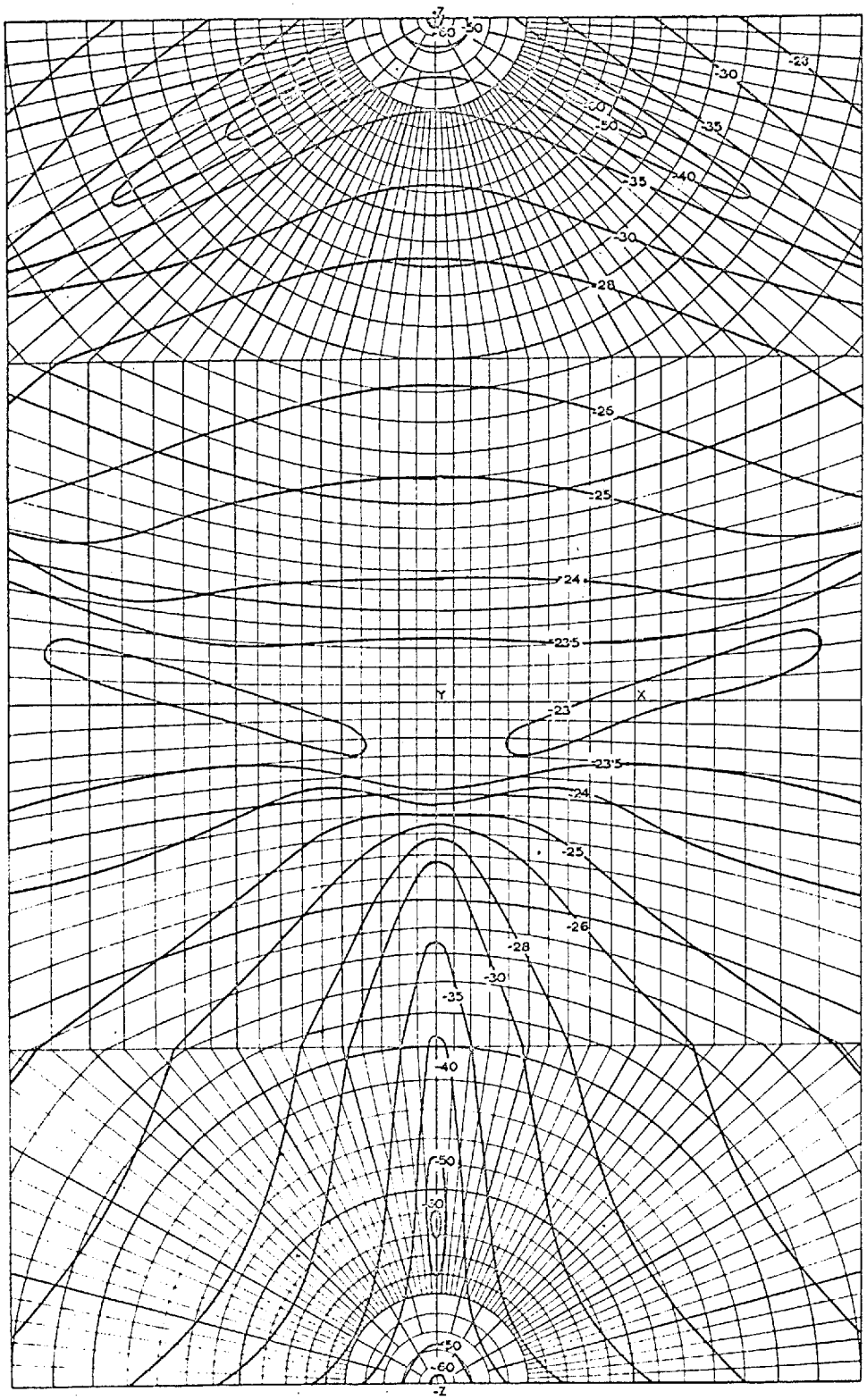
EXCITATION ANGLE. FAST SHEAR MODE. (Degrees)

FIG. 5.10



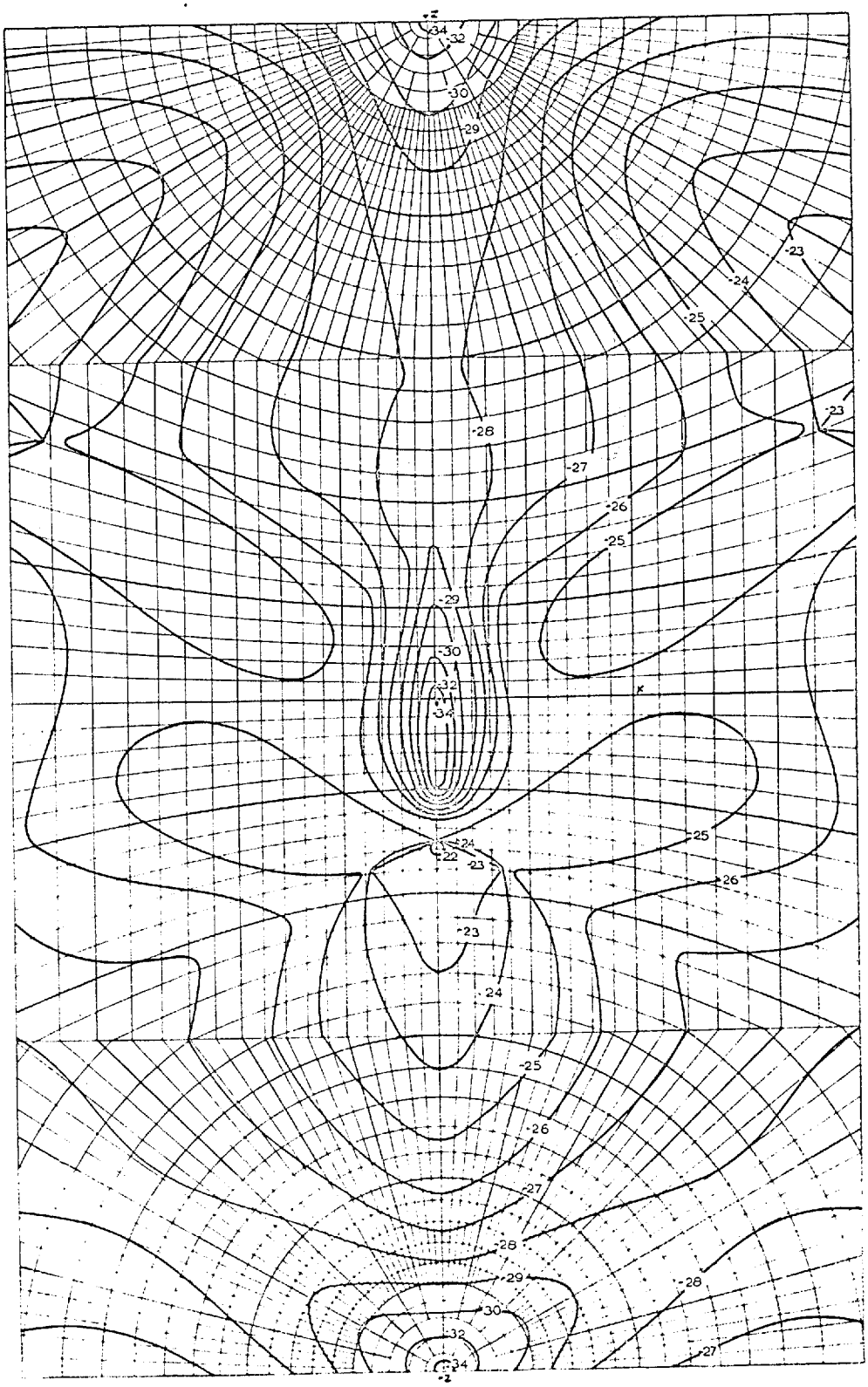
EXCITATION ANGLE. SLOW SHEAR MODE. (Degrees)

FIG. 5.11



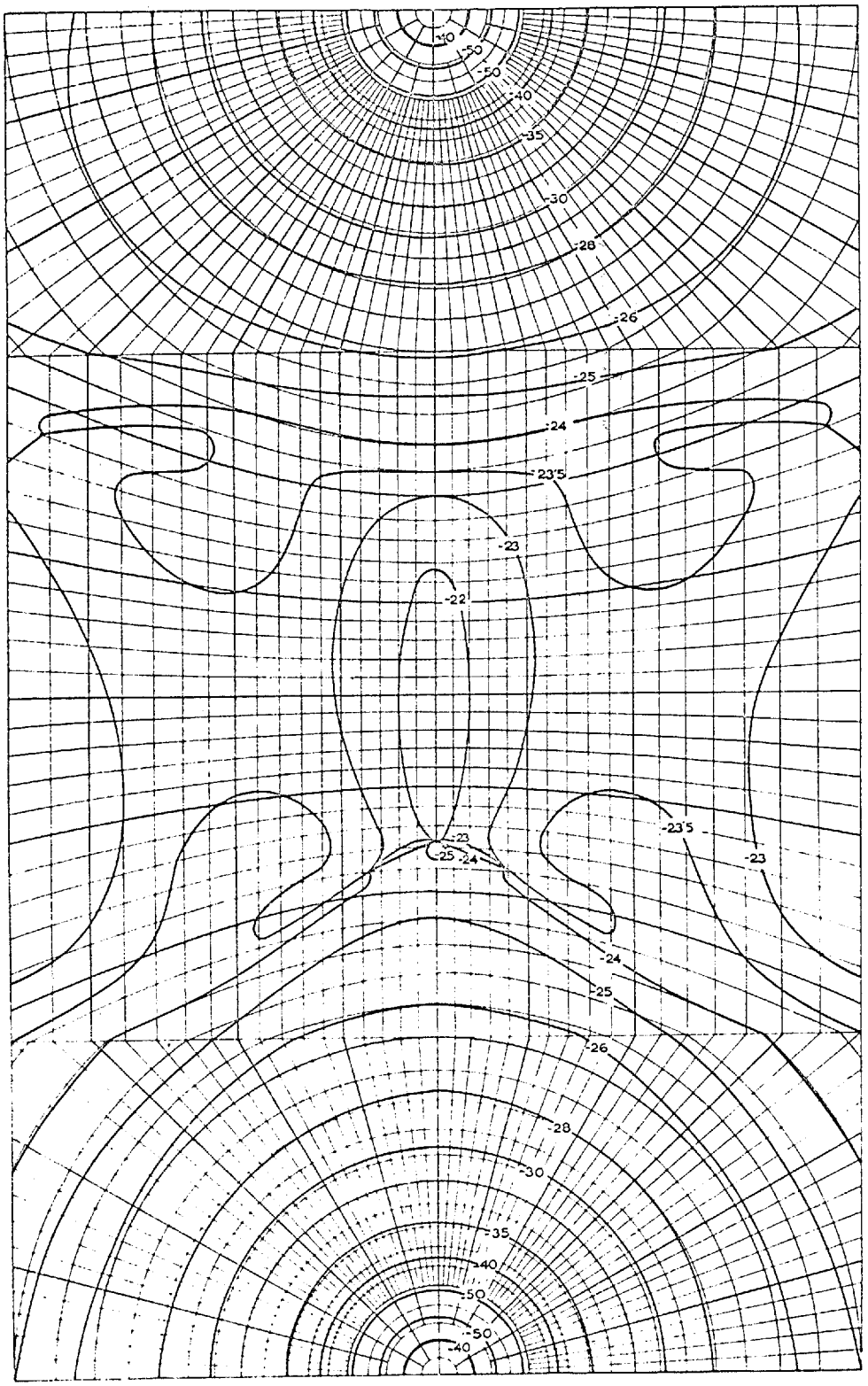
RELATIVE EFFICIENCY OF EXCITATION IN db'S. LONGITUDINAL MODE.

FIG. 5.12



RELATIVE EFFICIENCY OF EXCITATION IN db'S. FAST SHEAR MODE.

FIG. 5.13



RELATIVE EFFICIENCY OF EXCITATION IN db'S. SLOW SHEAR MODE.

FIG. 5.14

PART III.

THE EXPERIMENTAL SYSTEM.

CHAPTER 6.
THE ELECTRONIC MEASURING SYSTEM.

6.1 GENERAL DESCRIPTION.

A simplified general block diagram of the measuring system is shown in Fig. 6.1 below:

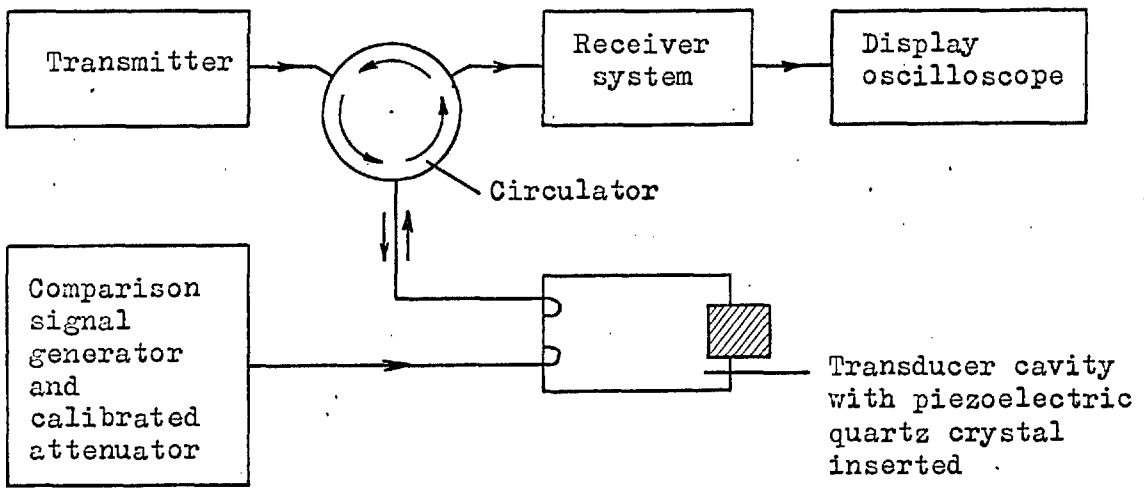


FIG. 6.1 BLOCK DIAGRAM OF MEASURING SYSTEM.

The transmitter supplies approximately 1kW of radio frequency power at a selected frequency in the range 350 - 1500Mc/s in the form of pulses of 0.6 - 2μsec duration. The r.f. power is fed to the transducer cavity via a circulator. The piezoelectric quartz crystal inserted in the cavity converts a portion of the electromagnetic energy into acoustic energy and it also reconverts some of the acoustic energy of the received echoes back into electromagnetic energy. The receiver system amplifies the echo pulses to a sufficient amplitude for display on an oscilloscope. A comparison signal of the same frequency as the main r.f. pulse is fed to the receiver system through a calibrated piston attenuator, and is displayed simultaneously with the echo train. The amplitude of a given

echo pulse is measured by adjusting the setting of the piston attenuator and noting the reading of the dial when the height of the echo and comparison pulses appear to be the same on the oscilloscope screen. All the timing and low level modulating pulses necessary for the operation of the system are obtained from a pulse control unit.

The transmitter unit consists of a microwave planar triode oscillator and a line-type modulator with its associated high voltage power supply. Microwave planar triode oscillators were chosen as the source of r.f. power because they easily satisfy the requirements that the pulse-modulation on-off ratio should be better than 160dB. Furthermore they offer advantages over klystrons, magnetrons and travelling wave tubes because of their relatively low supply voltage, very light weight, absence of focussing, cheapness and easy availability for the frequency band used. Frequency drifting due to electrode temperature effects was reduced by obtaining the filament heater supply from a constant voltage transformer. The slight frequency instability that remained is of no consequence in the present technique since no phase measurements are made.

The ferrite circulator isolates the transmitter from the receiver. When measurements were made at frequencies where no circulator was available, a straight-forward T-junction was used, resulting in a 6dB reduction in the amplitude of the received echoes.

The receiver system consists of a protective TR device. (TR = Transmit-Receive), a point contact diode mixer, a local oscillator, low-noise intermediate frequency preamplifier and main amplifier. To receive a large number of echoes the receiver system must have as good sensitivity as is practically possible, be fairly linear, and free from blocking and other time-constant effects. The

choice of a superheterodyne receiver was imperative as this is the one capable of the best noise performance. The low power disc seal triode local oscillators utilised high-Q resonant cavities as their tank circuits, so the noise power coupled out of them at a frequency 30Mc/s away from the local oscillator frequency was negligible and therefore a non-balanced mixer arrangement was chosen due to its simplicity and ease of frequency changing. A balanced mixer would have necessitated the duplication of most of the units of the receiver system for every selected frequency of operation but would have had the advantage of improved sensitivity by stopping the signal frequency getting into the local oscillator circuit.

A serious problem to be overcome in the design of the receiver system was the protection of the mixer diode from burn-out by the 2kW transmitter pulse. The use of a ferrite circulator to isolate the transmitter from the receiver reduces the transmitter power reaching the receiver by 10-30dB provided the circulator is properly adjusted and there is perfect match between circulator and load. Since it was desired to use the receiver at times when the transducer cavity either during adjustments or due to any other reason was not exactly on tune and therefore reflected most of the transmitter power back to the receiver, the mixer had to be able to withstand the application of the full transmitter power. First a thermionic mixer stage was built utilising a special EA52 disc-seal diode in a tunable cavity, but the noise figure achieved was found to be some 20dB worse than that of a receiver with a low-noise semiconductor diode. So a TR switch was constructed and placed between the mixer and the circulator affording the use of a low noise high quality mixer diode. A diode type 1N416F manufactured by Microwave Associates Inc. was found to be satisfactory. The TR switch is a passive nonlinear device limiting at 100mW. It gives an insertion loss of only 2dB for

signals below 100mW, but attenuates those signals above this level down to 100mW practically independently of original power. The TR device also acts as a frequency preselector, since only signals within the pass band of the TR cavity reach the receiver.

The effective bandwidth of the receiver is 2Mc/s with a Gaussian rather than a rectangular pass-band. The sensitivity of a pulse amplifier pass-band is 1.2 times the reciprocal pulse width (Lawson and Uhlenbeck, 1950) so 2Mc/s is optimum for the detection of a 0.7μsec pulse. The bandwidth is defined by the IF preamplifier. This relatively narrow bandwidth gives the displayed echo pulses a rounded top. Such a pulse shape proved to be ideal for pulse amplitude measurements when the echo pulse and a much wider comparison pulse are alternately displayed on the oscilloscope screen.

A pulse of variable width from the pulse control unit blanks the receiver until the transmitter fired. A safety switch breaks the triggering line to the thyratron of the modulator if the keep-alive power supply of the TR device is switched off.

A comparison signal was obtained from one of a number of UHF signal generators, as shown in the list of Section 6.9. All these signal generators contained a built-in calibrated piston attenuator. A separate piston attenuator motor driven, with push-button controls was also built from standard X-band waveguide, but was used for checking purposes only. As most of the measurements were carried out in the 450-1200Mc/s frequency range, the piston attenuator of the Hewlett-Packard 612A signal generator was modified to include a vernier dial giving a best readability and resettability of 0.04dB. No deviation from linearity was found on this piston attenuator even with the vernier dial, provided the top 15dB of the available output range was not used.

The most convenient way to inject the comparison signal is into the transducer cavity by a loosely coupled loop. Then the comparison pulse undergoes exactly the same processes of mixing, amplification, etc. as the echo pulses, and the comparison signal generator is sufficiently isolated from the transmitter. The echo and comparison signals amplified by the receiver system are displayed on an oscilloscope. A Tektronix type 585 is used because this was found to be unaffected by stray radiation from the high voltage pulse modulator.

The display is not demodulated: it fully contains the 30Mc/s IF carrier. Video noise due to crossmodulation in a video detector is thereby avoided and also it is less tiring on the eye during measurements. The various controls on the pulse control unit make it possible to chose between the following methods of comparison pulse display:

1) A narrow comparison pulse is injected in turn between the successive echo pulses and adjusted in height by the piston attenuator till it is of the same amplitude as the adjacent pulse.

2) The oscilloscope is triggered twice during the pulse repetition cycle. During the first half cycle the echo train is displayed and during the second half cycle the comparison pulse is shown resulting in an apparent superposition of the two signals without any beating effects. Adjusting the comparison signal amplitude until its height exactly coincided with the uppermost portion of the echo to be measured was very easy.

3) Simultaneous display of the comparison pulse both in the first and second half cycles. There was no detectable difference in the heights of the two comparison pulses except for the first 6μsecs after the transmitter firing when the TR and the receiver were not yet fully recovered.

The system needed a few hours operation to attain full

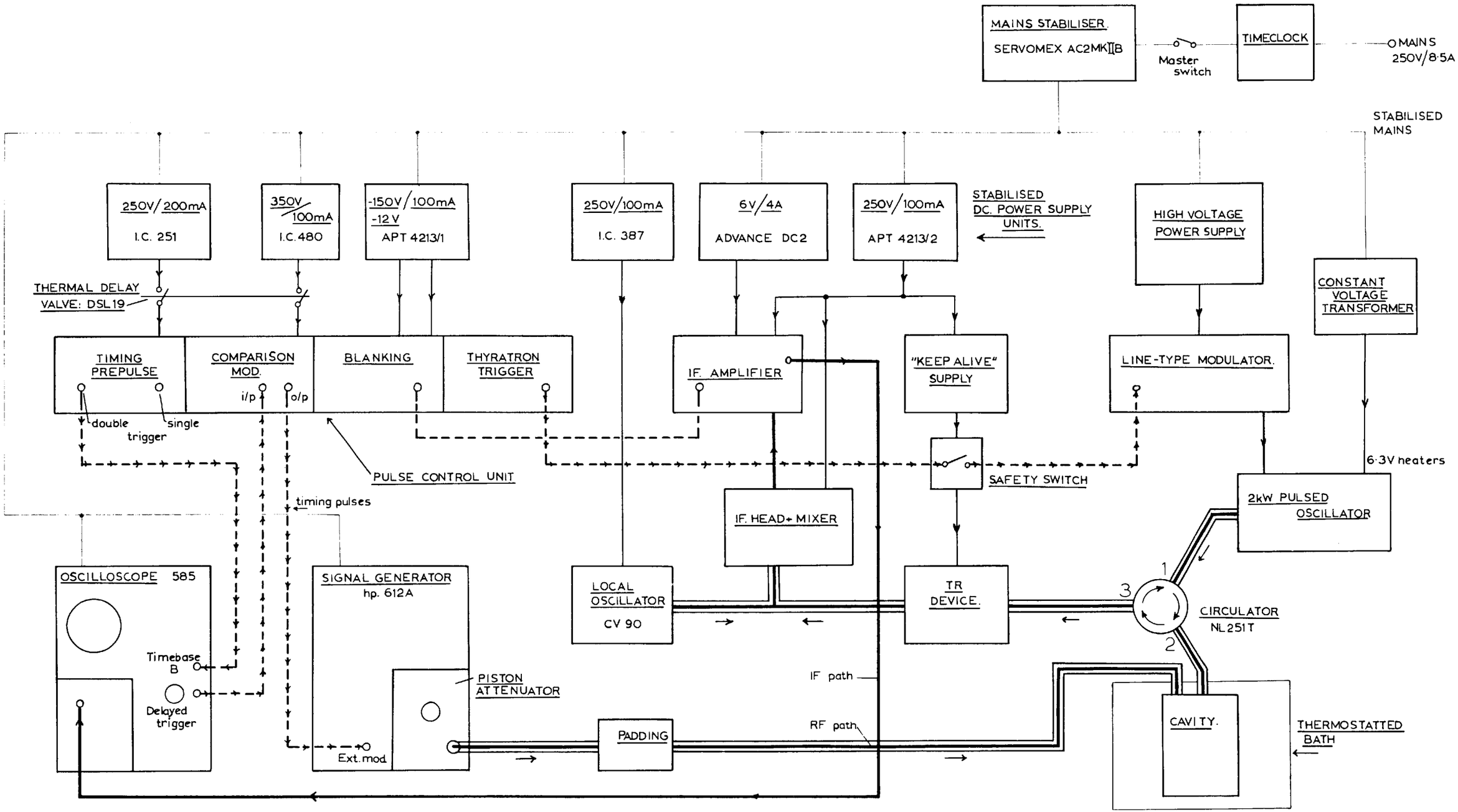


FIG. 6.2 BLOCK DIAGRAM & POWER SUPPLIES OF 1000Mc/s MEASURING SYSTEM.

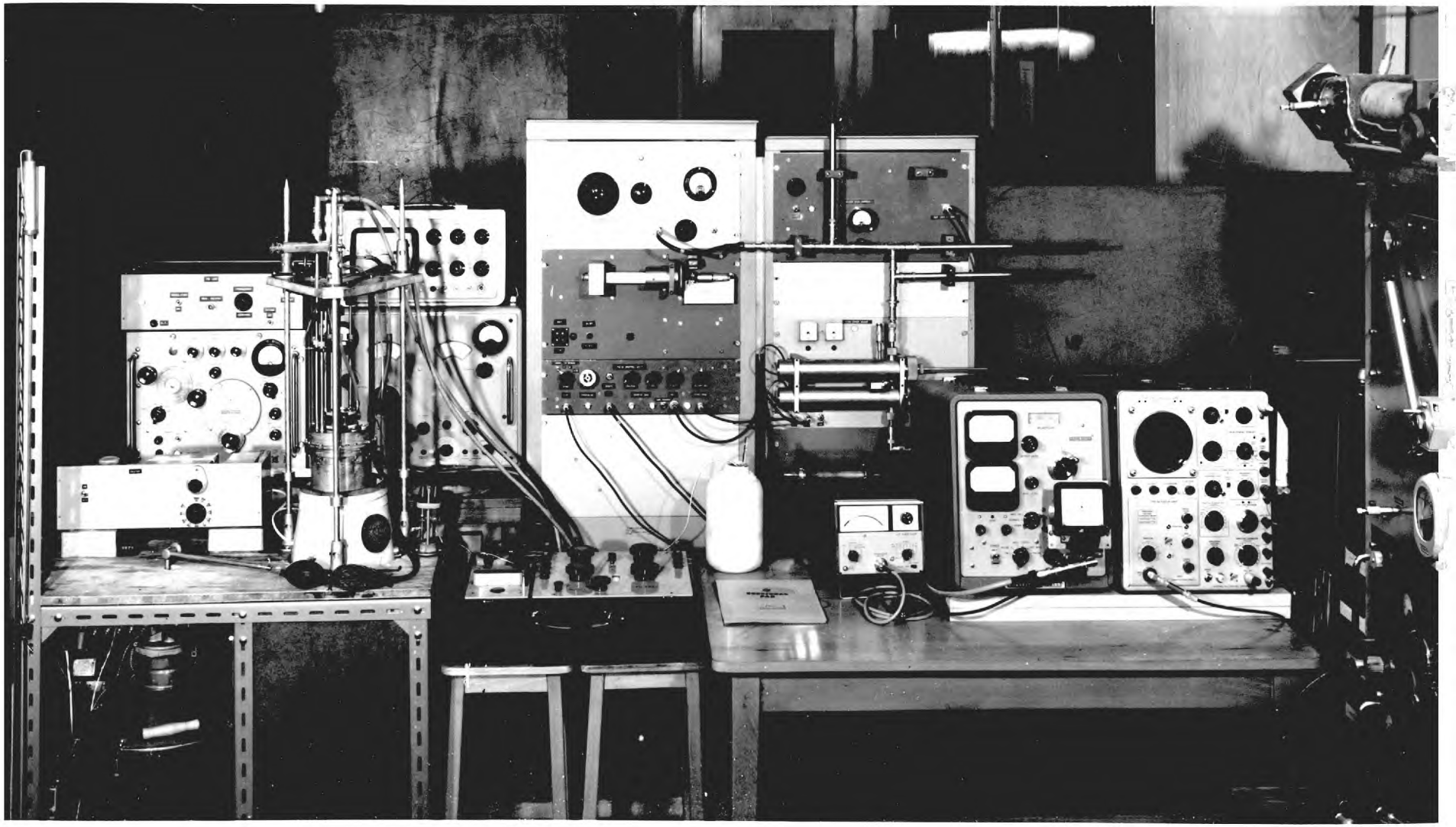


FIG. 6.3 GENERAL VIEW OF APPARATUS.

stability, therefore a timeclock was provided to switch it on 2 hours prior to the start of a measurement. The whole system is energised by a Servomex mains stabiliser giving a constant 240V output up to 9A loading. The various HT and filament voltages required for the operation of the electronic circuits were obtained from a number of stabilised power supplies.

A detailed block diagram is shown in Fig. 6.2 for operation at 1000Mc/s, while the photograph of Fig. 6.3 shows most of the electronic system with the exception of the transmitter rack. The photograph also shows one of the transducer cavities ready to be immersed into the low temperature thermostat.

The dotted lines of the block diagram represent the flow of timing pulses. The symbolised coaxial line shows the path of the r.f. signals. All actual r.f. connections are made by 0.420" O/D high quality coaxial cables, General Radio airspaced coaxial lines and GR or N-type coaxial connectors.

The constructional and operational details of those units that have been specifically designed and built in the course of the present work are described in the following subchapters. A list of standard equipment that has been made use of is given in Section 6.9.

6.2 PULSE CONTROL UNIT.

The pulse control unit was constructed to supply the necessary low-level triggering and modulating pulses for the measuring system. Its main sections as shown in the block diagram of Fig. 6.2 are described in detail below in conjunction with the circuit diagrams of Figs. 6.4-6.6. The power supplies are common to all sub-units. The HT supplies are applied through a 2 minutes thermal delay switch

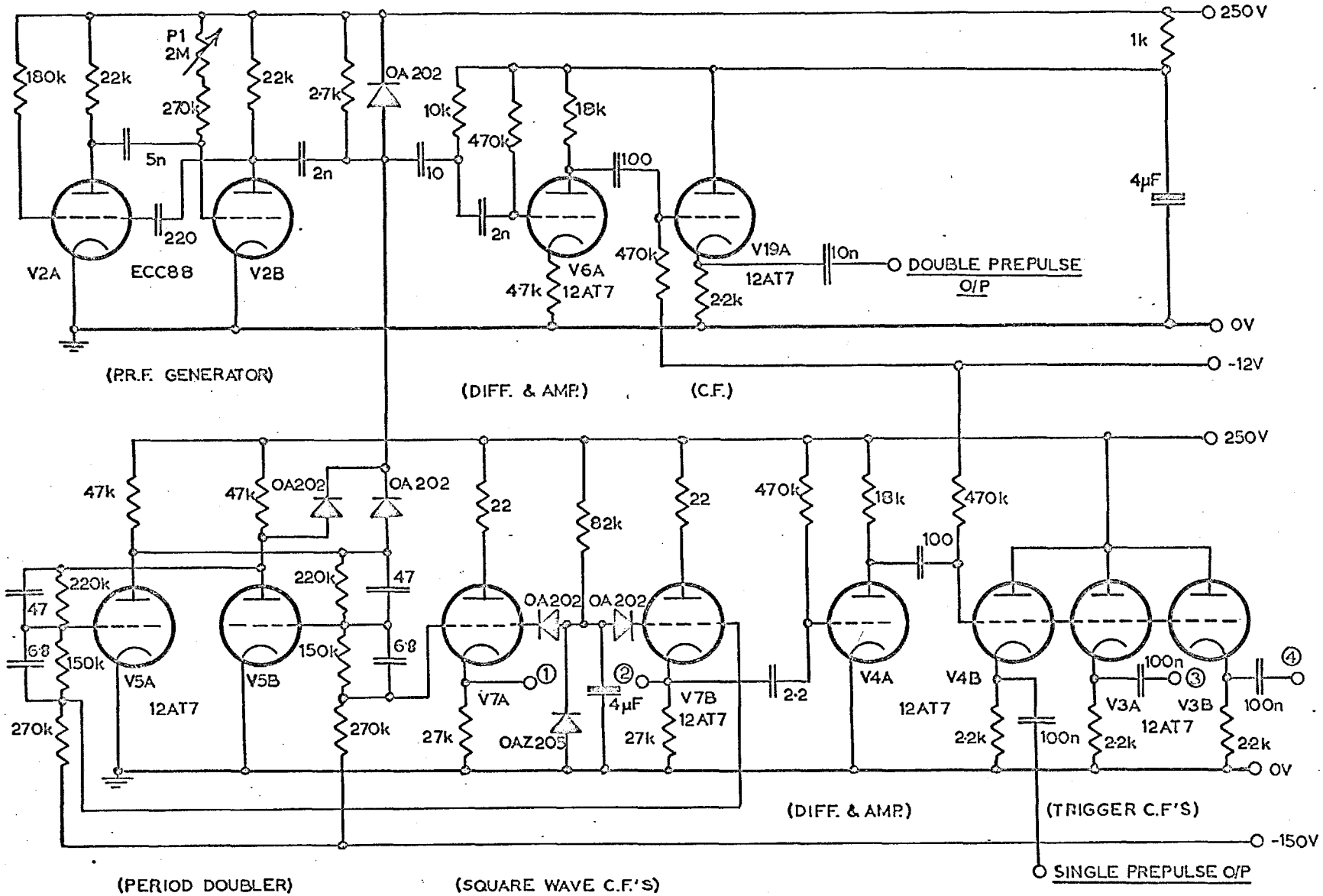


FIG. 6.4 TIMING UNIT

and are automatically disconnected in case the -150V supply is cut off. The pulse control unit consists of 3 main sections.

a) Timing section. A free-running multivibrator built around valve V2 defines the pulse repetition frequency of the whole measuring system. Valve V2B is off for 0.2msec. and on for 0.25 - 5msec. dependent on the setting of potentiometer P1. The negative-going edge of the resultant asymmetrical square wave is used both to obtain after differentiation and amplification a 30V positive spike called "double prepulse" connected to a socket on the front panel via the cathode follower V19A, and to trigger the bistable multivibrator V5B by two silicon diodes. The symmetrical square wave obtained from V5 at half the repetition rate of the double prepulse after shaping is available of either polarity at the cathode follower terminals 1 or 2 , and after differentiation, amplification and shaping produces the "single prepulse" of 30V amplitude at the cathodes of 3 separate cathode followers, at a repetition rate variable from 180 to 1100c/s. One of the single prepulse cathode followers is connected to a socket on the front panel, the other two drive the blanking and thyratron trigger units.

b) Comparison pulse section. A trigger obtained from the input socket on the front panel is shaped, amplified and gated by valves V1, V6B and V19B. Gating is achieved by connecting the cathode of V1B to the square waves of terminals 1 or 2 via a selector switch S1. Position 1 of the gate selector switch connects the cathode to HT thereby blocking the transmission of any trigger pulse through the gate. In positions 2 and 3 the cathode is connected to terminals 2 and 1 respectively resulting in the possibility of a trigger pulse either in the first or in the second half-cycle. In position 4 the gate is open at all times. The gated trigger pulse triggers the monostable multivibrator built

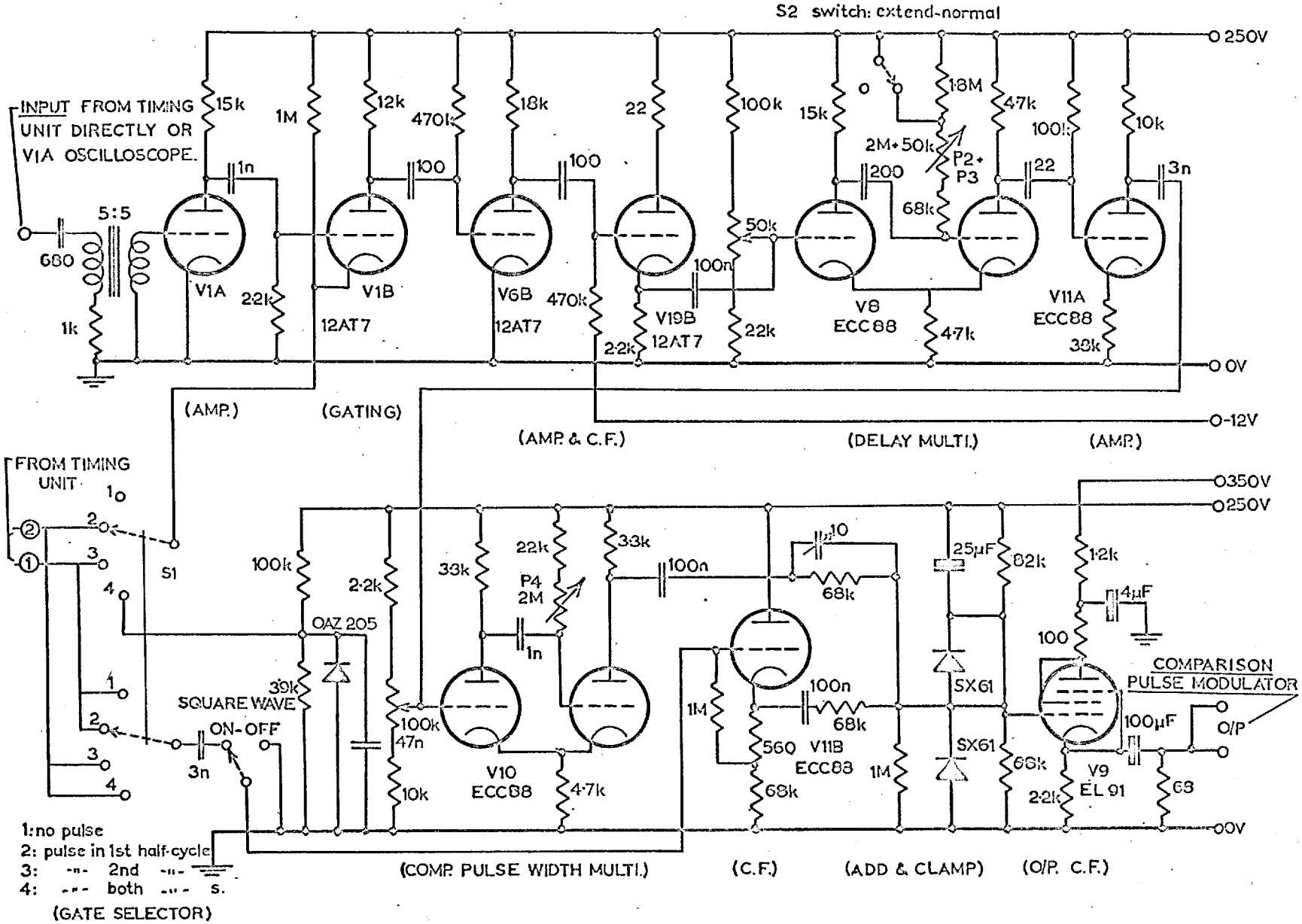


FIG. 6.5 COMPARISON PULSE UNIT.

around V8 to produce a delayed trigger whose delay is variable from 10 to 200 μsec in the normal position of switch S2, and from 180 to 400μsec in the extended position. The delayed trigger drives the comparison pulse monostable multivibrator (V10), the pulse width of which is adjustable by potentiometer P4 from 1 to 20μsec. A square wave fed via the on-off switch and a cathode follower is added in the right polarity to the comparison pulse to produce a square wave modulation in addition to the narrow pulse modulation. The combined pulse and square wave modulation, clamped to 10V amplitude, is available at two BNC sockets on the front panel from an effective 50Ω source impedance.

c) Blanking and thyratron trigger sections. The single prepulse from terminal 3 triggers a monostable multivibrator built around V12 to produce after some shaping and amplification a negative-going pulse of 60V amplitude. This pulse blanks the IF main amplifier while the high-power transmitter is on. The single prepulse from terminal 4 triggers a monostable multivibrator (V14) giving a positive trigger of 9μsec fixed delay to drive a blocking oscillator (V17 & V18). The output of the blocking oscillator is available from a socket on the front panel to produce a 150V spike of 0.3μsec duration across 75Ω.

The pulse control unit operates in conjunction with the oscilloscope time base . During routine measurements only the oscilloscope controls need adjustment. The operation is described assuming an alternate echo-comparison pulse display.

The timing section of the pulse control unit provides a prepulse ("double prepulse") at twice the operational pulse repetition rate to trigger timebase B of the Tektronix 585 oscilloscope. A "delayed trigger" is available from the oscilloscope, the delay being variable by a 10-turn potentiometer from 0 to 100%

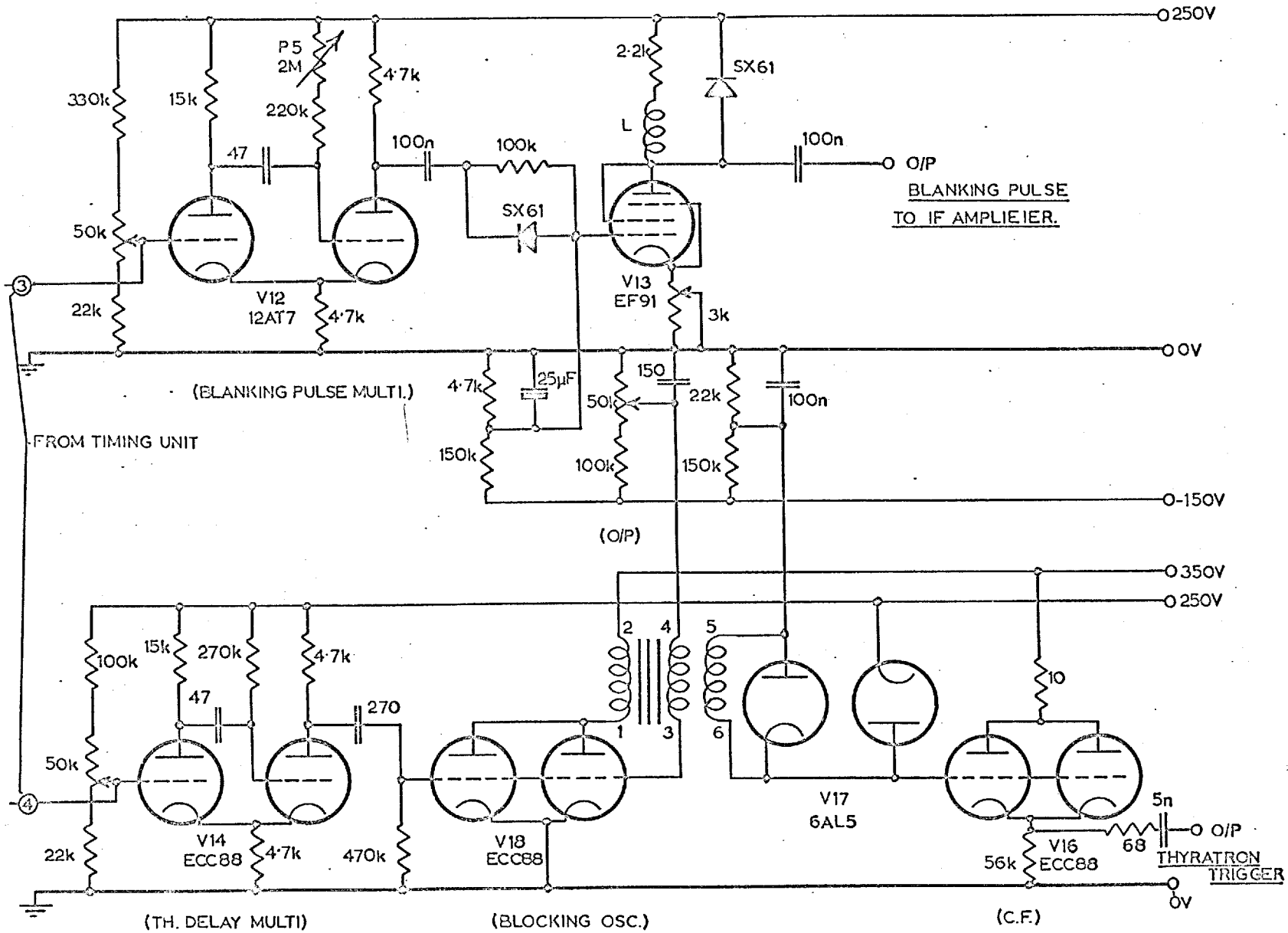


FIG. 6.6 BLANKING & THYRATRON TRIGGER UNITS.

of timebase B. This delayed trigger connected to the input socket of the comparison modulator section after some selected gating and delay triggers a modulator pulse to externally modulate the comparison signal generator. In position 2 of the gating switch (Fig. 6.5) only those alternate delayed double trigger pulses are allowed to turn on the comparison pulse modulator that come in the second half of the period between the single trigger pulses. Therefore the echoes and the comparison pulse will be displayed on the oscilloscope alternately.

In the "A intensified by B" position of the oscilloscope "horizontal display" switch a small portion of the trace is brightened up starting at a time defined by the "delayed trigger". The intensified portion of the trace can be made to include only one echo pulse and a superimposed comparison pulse. Putting the "horizontal display" selector to the "A delayed by B" position only the previously selected echo pulse and the comparison pulse appear on the screen, and then turning the 10-turn delay potentiometer has the effect of moving the echo train horizontally, while the comparison pulse behind them remains stationary.

6.3 HIGH VOLTAGE MODULATOR.

The modulator unit and its power supply was originally constructed by M. Redwood and E. Heasell and a detailed description of its operation is given by Redwood (1957). The power supply is capable to give an output continuously variable from 0 to 4000 volts at 50mA. The circuit diagram is reproduced in Fig. 6.7. Resonant charging is applied through the oil-insulated choke L and the thermionic hold-off diode HR8. The half-period of the resonant charging is 1msec, defining the maximum pulse repetition frequency as 1kc/s.

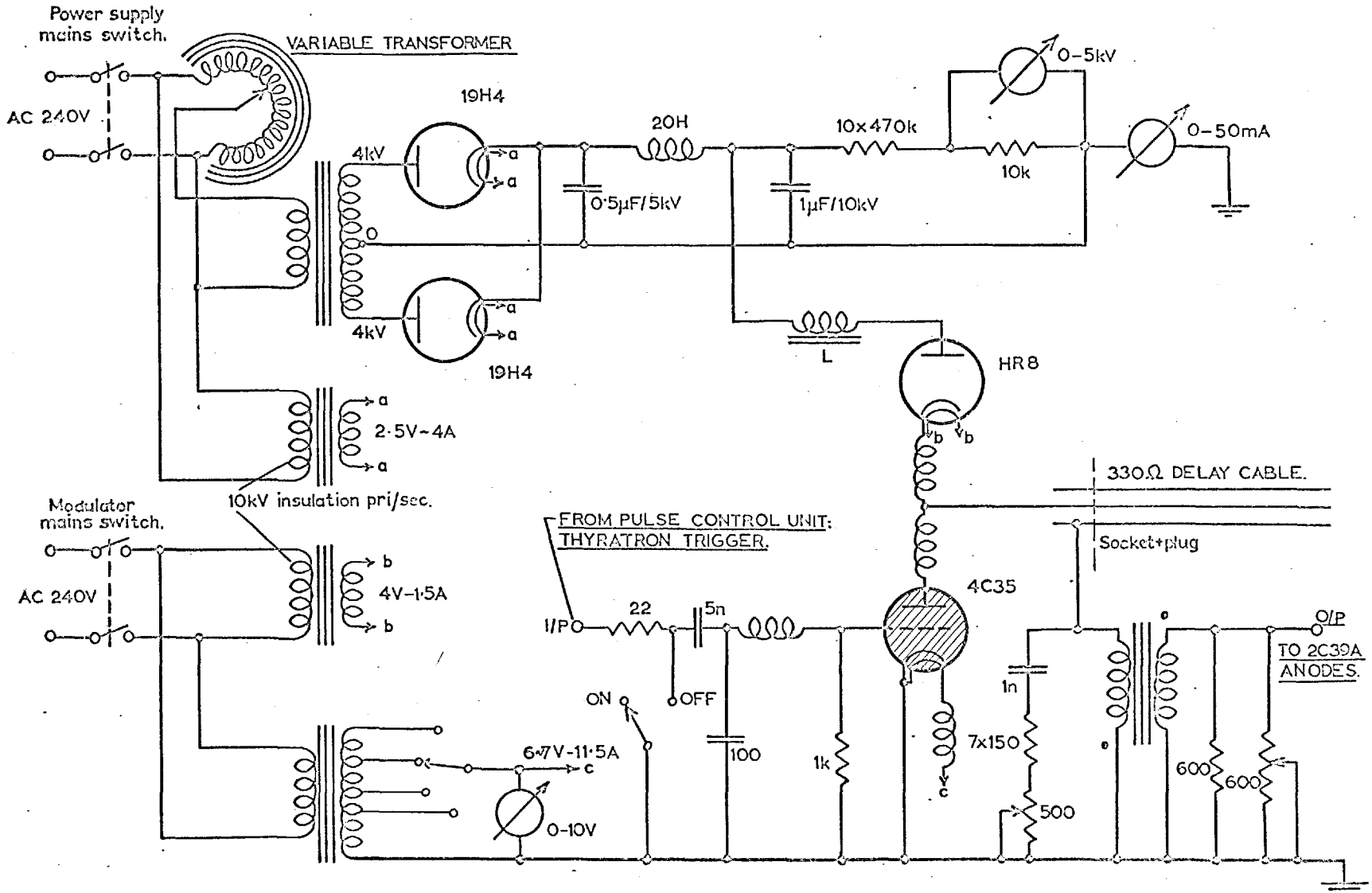
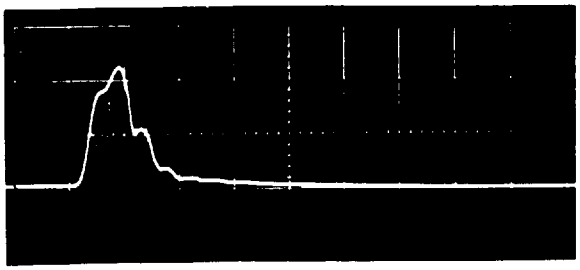


FIG. 6.7 HIGH VOLTAGE MODULATOR.

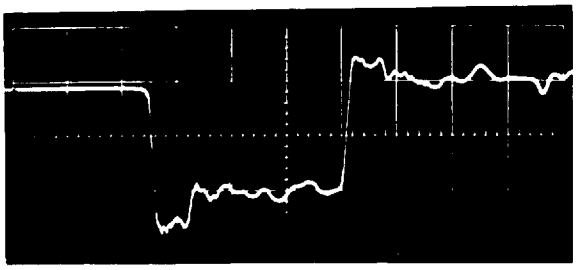
Since the modulator was called upon to deliver shorter pulses than those for which it had originally been designed, the thyratron type of the original modulator was substituted by a 4C35 and the associated circuit rearranged and modified to minimise the detrimental effect of stray capacitances on the pulse rise-time. Of the possible designs of a thyratron pulser the one adopted gave the best rectangular pulse shape. A telcon type Z3M delay cable of 330Ω characteristic impedance and 1.7μsec/100ft delay is discharged by the thyratron on application of a short 150V trigger pulse to the thyratron grid, and the polarity of the resultant output pulse is inverted by a high performance pulse transformer. Since the UHF planar triode oscillators represent a load of a few kΩ additional resistances were connected to both the primary and secondary sides of the transformer to match the total load to the 330Ω impedance of the cable. These added resistances also make the modulator relatively insensitive to variations of external load impedance. The required width of the modulating pulse was obtained by connecting a suitable length of cable to the thyratron anode, and the pulse amplitude was defined by the setting of the variable transformer. The flatness of the top of the pulse depended a great deal on the uniformity of the cable: it was found necessary to wind the cable accurately in one layer on a large insulating drum. Substantially rectangular pulses were obtained with 50nsec rise and fall-times as illustrated in Fig. 6.8.

6.4 PLANAR TRIODE OSCILLATORS.

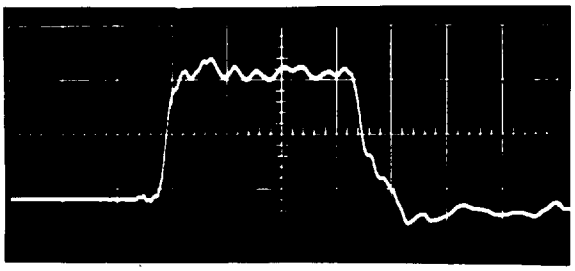
A number of high power oscillator units were designed and constructed using UHF planar triodes type 2C39A mounted in cavity resonators. The oscillators are basically grounded-grid amplifiers with positive feedback. The operation of such oscillators at low microwave frequencies is described in Appendix I together with the results of measurements on one of the cavities. The anode-grid circuit of the oscillator is a re-entrant cavity resonator consisting of a length of short-circuited coaxial transmission line shunted with the anode gap admittance. The real part of the anode gap admittance is low enough (c.f. Table A.1) so that the Q of the resonator is high. On the other hand the cathode gap conductance represents a fairly good match to the



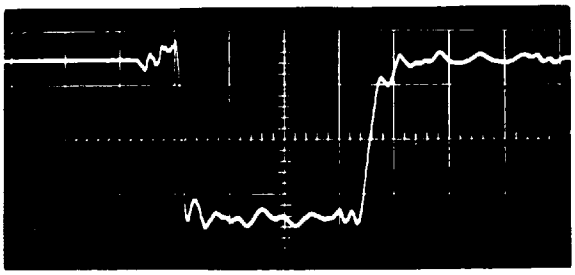
a) Trigger pulse on thyratron grid without the thyratron firing. Vertical scale 50V/cm. Timebase 0.2μsec/grid cm throughout.



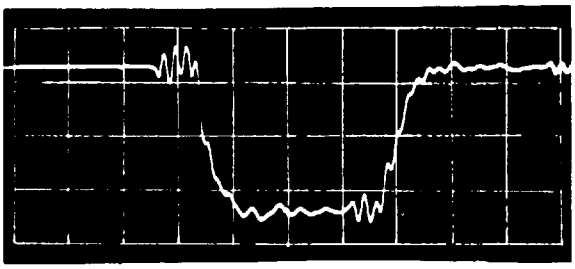
b) Waveform at the primary of the pulse transformer. Vertical scale 1000V/cm.



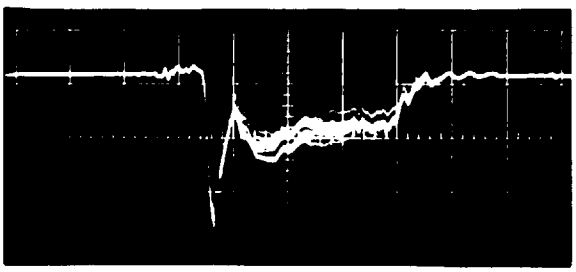
c) Waveform at the secondary. (The fast ripples on all the traces are due to the interference of the high power modulator with the operation of the oscilloscope.)



d) Rectified 500Mc/s rf. transmitter pulse.



e) As above, after passing through the pass-band of the double-tuned transducer cavity.



f) The TR device limiting the transmitter pulse. (Scale 200 times greater than in the previous two pictures.)

FIG. 6.8 MODULATOR WAVEFORMS AND RF. ENVELOPES.

characteristic admittance of coaxial lines of practicable dimensions making the cathode-grid circuit essentially non-resonant. The output power that can be coupled out of the anode-grid cavity is typically 2kW.

Constructional details are shown in Figs. 6.9 and 6.10. The cathode-grid circuit is coaxial with the grid-anode circuit and is placed inside it. All connections to the valve are made by phosphor-bronze spring fingers. The spring fingers contacting the anode ring of the valve are insulated from the rest of the oscillator which is at DC ground potential by a thin PTFE washer, and the connection from this anode ring to the EHT modulator is made via an r.f. choke. A typical modulator pulse is 3kV amplitude and 0.7μsec duration. The r.f. choke together with the capacitance of the gap containing the PTFE washer forms a low-pass filter with a cut-off frequency high enough to pass all the important harmonics of the modulating square wave but stopping the leakage of r.f. energy back to the modulator. The anode block of the valve with its cooling fins, the r.f. choke and the EHT connector are enclosed in a diecast box for screening and safety.

Three oscillator units have been constructed for a 50Mc/s band about the following frequencies: 500 or 1500Mc/s, 720Mc/s, 1000Mc/s. The position of the short-circuit block is fixed experimentally to give the required centre frequency, and fine tuning is obtained by screwing the 3 tuning slugs in or out of the cavity.

Power to the external circuit is coupled out of the anode-grid cavity by means of a rotatable coupler loop. Power has also to be fed back to the cathode-grid circuit to maintain oscillations. In the 720Mc/s and 1000Mc/s oscillators this is done by connecting a second loop placed in the anode-grid cavity straight

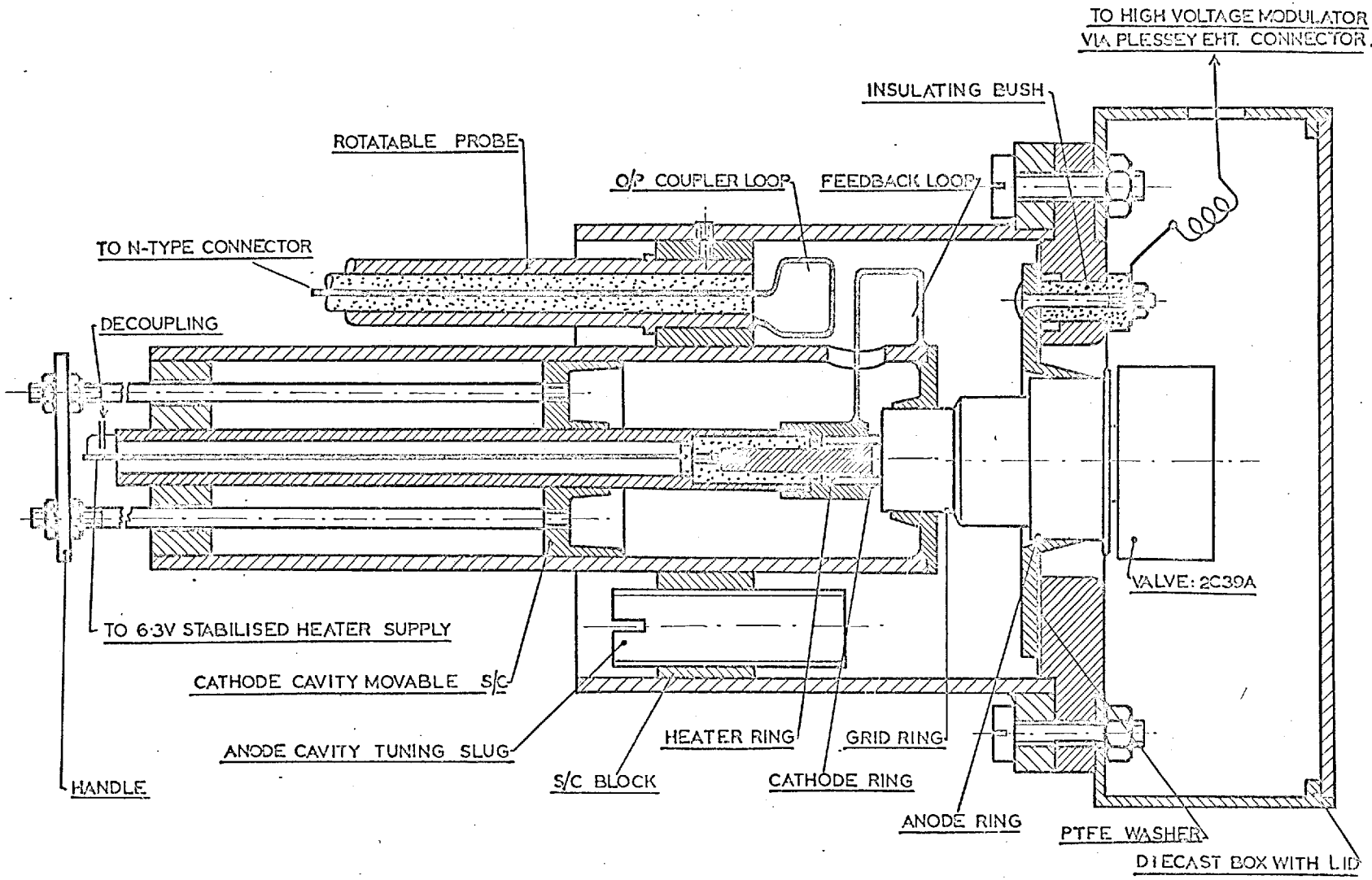


FIG. 6.9 1000Mc/s PULSED 2kW OSCILLATOR.

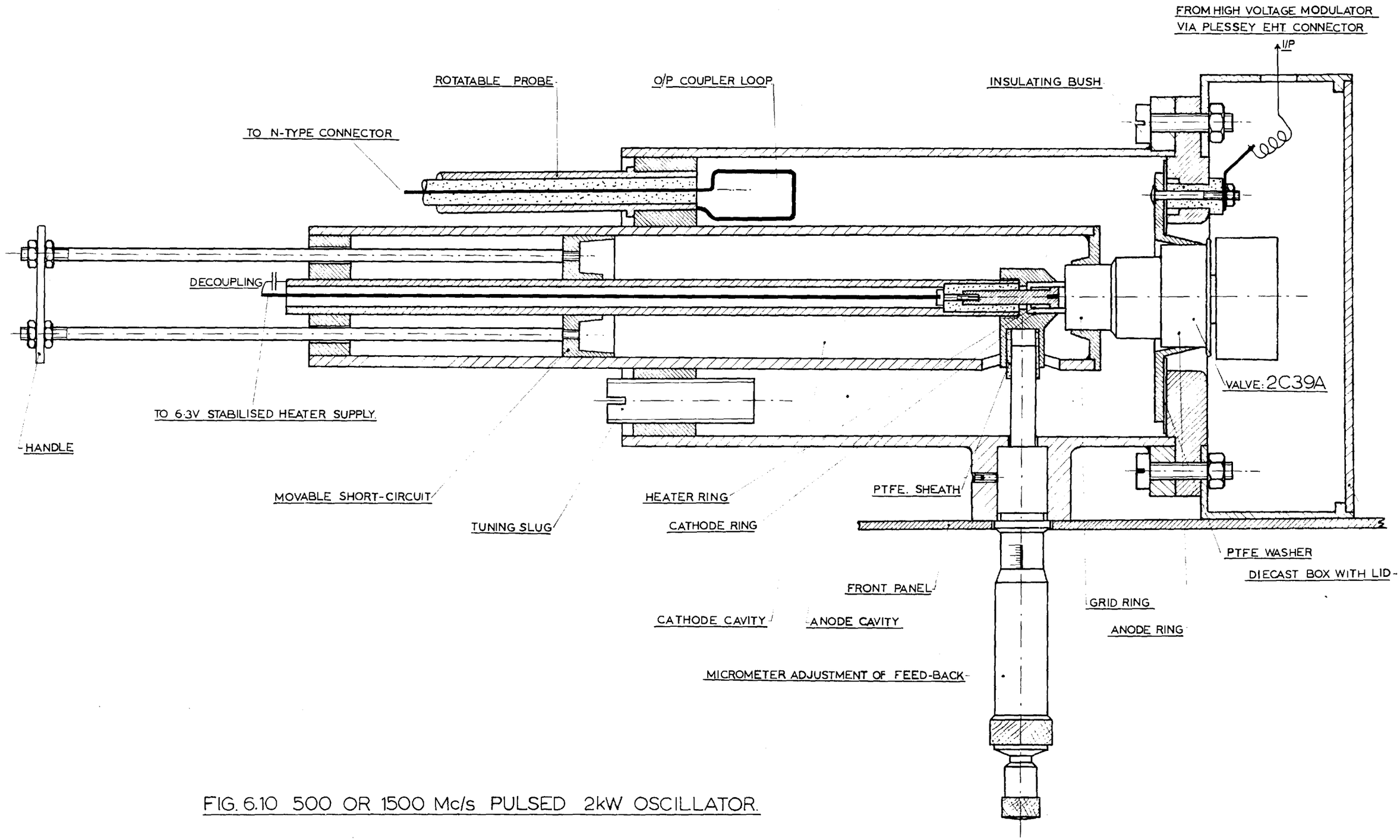


FIG. 6.10 500 OR 1500 Mc/s PULSED 2kW OSCILLATOR.

to the cathode. In the 500/1500Mc/s oscillator (Fig. 6.10) capacitive feedback is used, the degree of feedback being adjustable by a micrometer screw and the amount of feedback determining whether the oscillator be working at 500 or 1500Mc/s. The feedback capacitance is unusual in that it is formed between the micrometer barrel and a concentric cylinder fixed to the cathode contacting fingers, the intervening space being completely filled by a PTFE sheath to prevent sparking.

In all the oscillators a movable short-circuiting plunger is provided in the cathode-grid space. Thus the admittance seen by the feed-back loop is the sum of the admittance of the input gap of the valve and the susceptance of a length of short-circuited transmission line. Altering the position of the short-circuit alters this admittance and thereby varies the amount and phase of the feedback. Feedback is maximum when the length of the line is approximately quarter wavelength.

6.3V stabilised heater voltage is applied to the heater ring of the valve through the bore of the centre electrode of the cathode cavity and decoupled to it by a mica capacitor. The transmission line formed by the heater wire and the metal tube around it is a half wavelength long to stop r.f. leakage via the heater lead.

6.5 CIRCULATOR.

The Y-junction ferrite circulator incorporated in the measuring system is a Micromega NL215T as this was the only type available for a reasonably wide frequency band below 1kMc/s at the time of building the apparatus. It is of strip-line construction and operating in a narrow frequency band between the limits of 750 - 1000Mc/s depending on the strength of the biasing magnetic

field, which is provided by two axially magnetised hard-magnet discs on each side of the stripline structure containing the ferrite. The magnetic field can be increased or decreased by moving one of these permanent magnets nearer to, or away from the other magnet respectively, by a large central screw. Iron plates fixed to the outside of the circulator housing complete the magnetic path. It was found, that removing these plates so decreased the biasing field that the operating frequency range fell between 440 and 730Mc/s, with the performance of the circulator deteriorated, but still usuable. In the original working range typical isolation is 28dB with 0.2dB insertion loss. In the extended range isolation is 10dB with 1dB insertion loss.

When measurements had to be taken at frequencies outside the 440 - 1000Mc/s band simple non-circulating coaxial T junctions were used.

6.6 TR DEVICES.

The TR devices act as limiters to protect the receiver against burnout or aging. They are based on one or two TR cells mounted in the high electric field portions of cavity resonators. The r.f. gap of the TR cell contains an easily ionisable gas mixture and breaks down under the application of high r.f. fields across it, thus detuning the cavity stops the transmission of power from the input to the output terminals (Smullin and Montgomery, 1948).

At the beginning of the transmitter pulse there is an initial number of electrons present in the r.f. gap. As the transmitter voltage increases it accelerates these electrons until they attain sufficient energy to produce further ionisation through collisions. Then the electron density rapidly increases and begins to short-circuit the gap and reduce the power transmitted through the cavity.

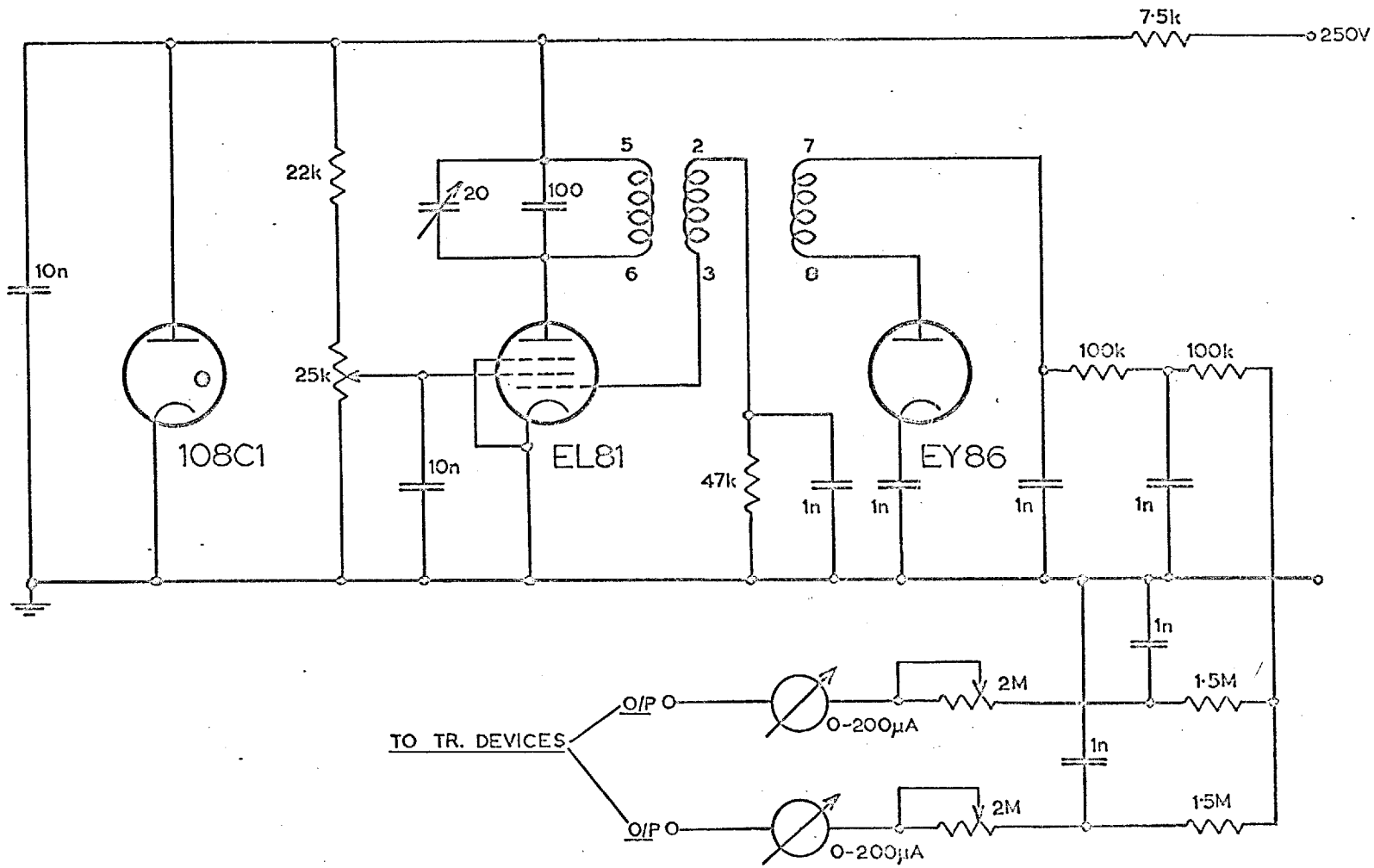


FIG. 6.11 "KEEP-ALIVE" POWER SUPPLY.

The rate of ionisation continues to increase as the power increases until an equilibrium is reached with the incident power. Typical transmitted waveform is shown in Fig. 6.8f. The waveform starts to rise with the unlimited pulse rise-time until the ionisation avalanche happens. Then the amplitude drops to a constant low level. With 1kW input power the spike energy was estimated to be 0.1erg/pulse.

The spike leakage energy varies inversely with the number of electrons initially present in the gap. To provide these electrons a continuous keep-alive discharge is maintained very near to the r.f. gap, but completely shielded from it, by a 1000V EHT power supply whose circuit diagram is shown in Fig. 6.11. The polarity of the field across the keep-alive gap is such that it tends to sweep the electrons into the r.f. gap through a small hole in the centre of the disc-seal electrode.

The keep-alive circuit is liable to relaxation oscillations. The rise of voltage on the keep-alive electrode is determined by the time constant RC formed by the charging resistor R of the order of Megohms and stray capacitances C. When this voltage reaches a sufficiently high value the gap breaks down and discharges the capacitor with the very small time constant $R_D C$ until the voltage drops to extinction level. The discharge then goes out and the voltage builds up as before. This sawtooth pattern is repeated periodically. It was impossible to completely suppress this relaxation oscillation, therefore it was made either to have such a high frequency ($\approx$ 1Mc/s) that even though the discharge is periodically extinguished, the density of electrons in the r.f. gap experiences only small fluctuations, by placing the current limiting resistor of 1.5MΩ right at the TR cell or, to have a frequency near the operational pulse repetition rate by increasing the shunt capacitance in which case the relaxation

oscillation synchronised with the transmitter pulse. Although the latter method resulted in somewhat higher spike leakage, it was found more satisfactory than the first, where every time when the keep-alive discharge struck a strong interference was picked up by the receiver resulting in an apparently increased noise.

The transmission of power by the TR unit (approximately 10mW for both TR devices built) after the spike is over is the result of a voltage drop across the r.f. discharge. It is the characteristic of ionising discharges that this drop is practically independent of the current in the discharge, but is dependent on the gas filling and its pressure.

After the power has fallen to zero the r.f. gap deionises during the recovery period by diffusion, collision with positive ions, and mainly by the capture of electrons by H_2O gas included for this reason in the gas filling mixture due to its high electron capture cross-section. The measured recovery time constant is 3μsec.

Two TR units were constructed, one to cover each of the 300-600Mc/s and the 600-2000Mc/s frequency ranges.

The 600-2000Mc/s TR device (Fig. 6.12) consists of a coaxial re-entrant cavity whose re-entrant gap contains a Ferranti type QF10 TR cell. The cavity is tunable by turning the tuning shaft which drives a short-circuiting plunger by a steel pin through a slot along the inner conductor of the cavity. Good contact between the plunger and the metal walls is assured by helical contacting springs closely wound from thin gauge phosphor-bronze wire placed in grooves cut in the cylindrical surfaces of the plunger. The position of the plunger is indicated by a digital counter placed next to the tuning knob. (600Mc/s = 0054; 1000Mc/s = 0590)

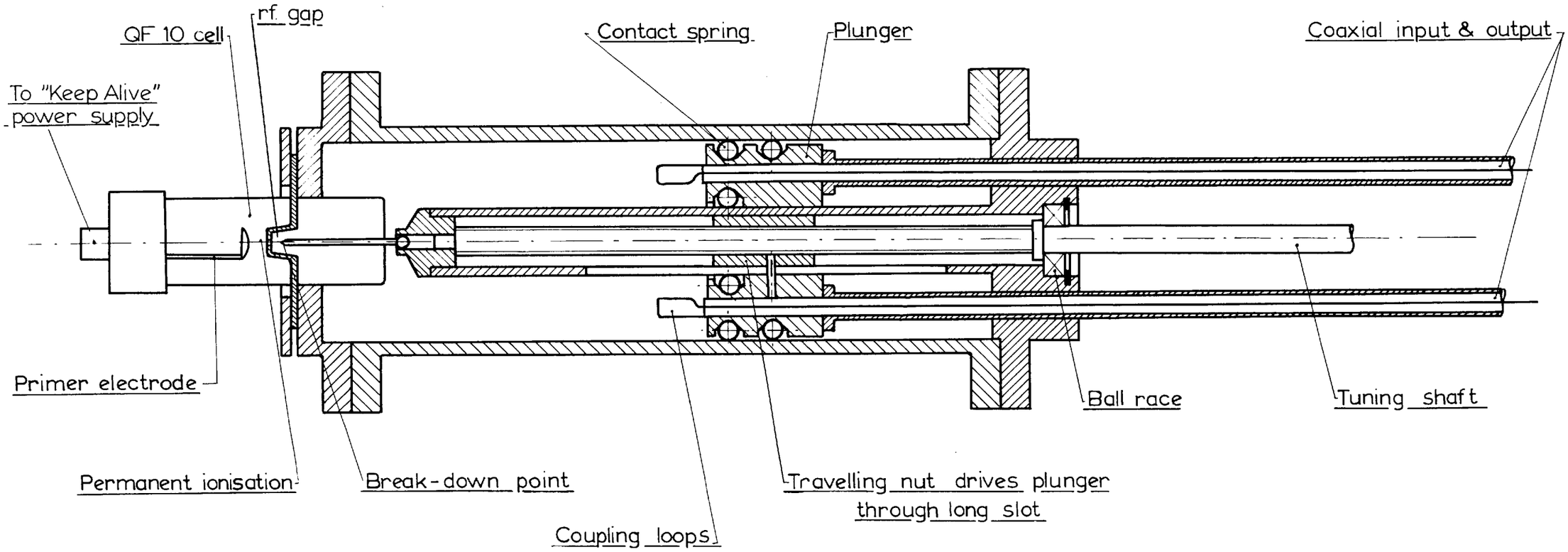


FIG. 6.12 600-2000 Mc/s TR DEVICE.

Coupling to and from the cavity is made by fixed coupling loops. The Q of the cavity is 250 at 1000Mc/s giving the approximate width of its passband as 4Mc/s.

The 300-600Mc/s TR device (Fig. 6.13) consists of two coaxial re-entrant cavities coupled together stronger than critical to increase the bandwidth. The construction of the cavities is rather unusual since the high-current end with the rotating coupling loops is fixed and the re-entrant gap is movable. One Ferranti type QF10 cell is fixed into each moving gap assembly. Electrical contact between the gap assembly and the outer cylinder of the cavity, and also between the centre conductor and the end wall is obtained by helical spring contacts as before. Although the spring is in a place of high electric fields there are no sparking problems since under high power conditions the TR cell gap breaks down first before sparking could occur at the springs or at sharp corners near them.

Tuning is achieved by moving the gap assembly axially with the help of the cavity centre electrode. Coarse frequency setting is by loosening the locking screw and shifting axially the coarse tuning knob. Fine tuning can be obtained by tightening the locking screw, thereby clamping the centre electrode to the spring-loaded sliding plug and then rotating the fine tuning screw.

Input and output couplers are rotatable loops. Mutual coupling between the two cavities is also accomplished by two large loops connected together by a short coaxial line (see Fig. 6.13) and rotatable by worm-gear drive. The angular position of the plane containing the two loops is identified by the reading of the vernier dial. The low-power frequency response from input to output terminals was checked by a Philips type GM2877 sweep generator as a function of dial setting, and is shown in the

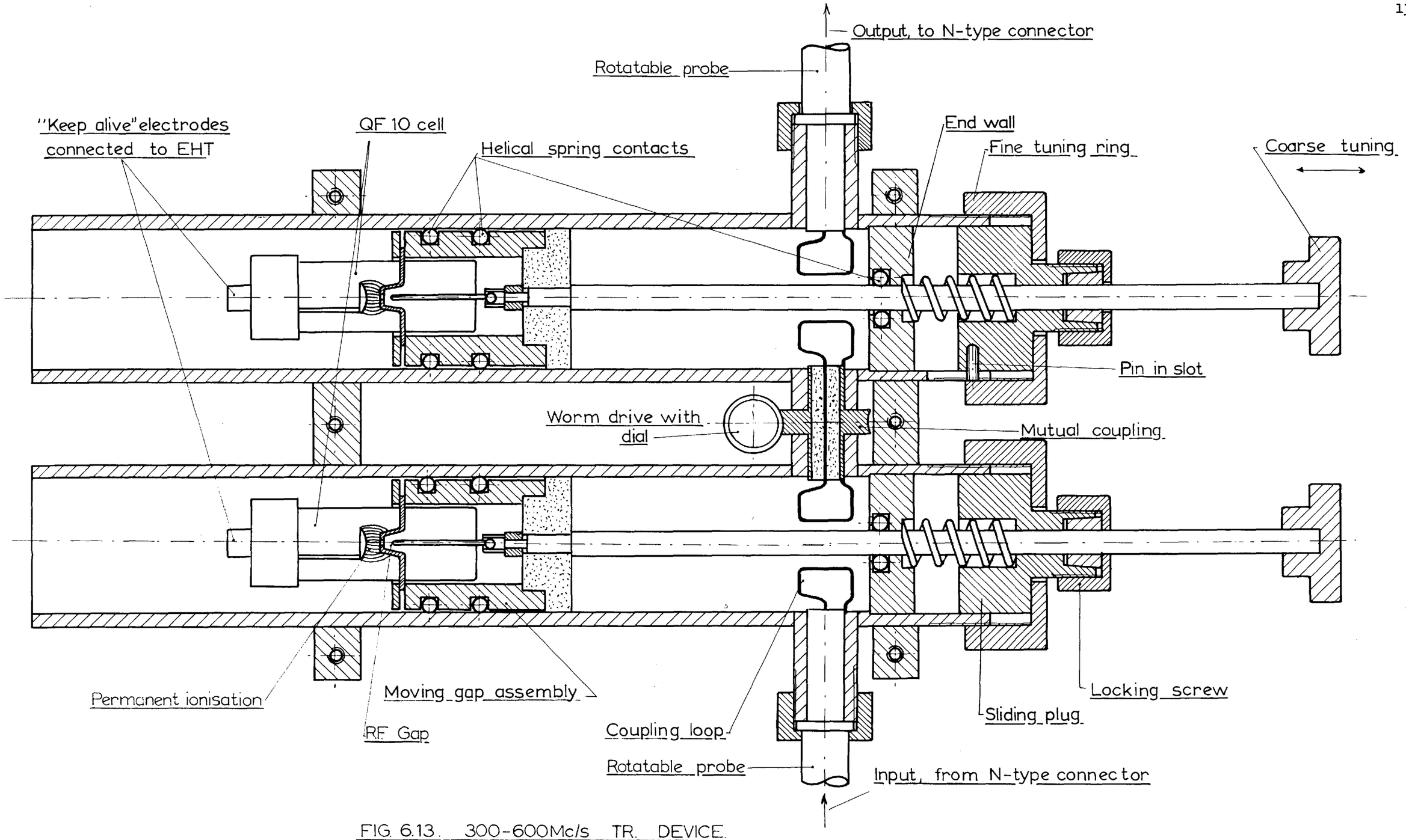


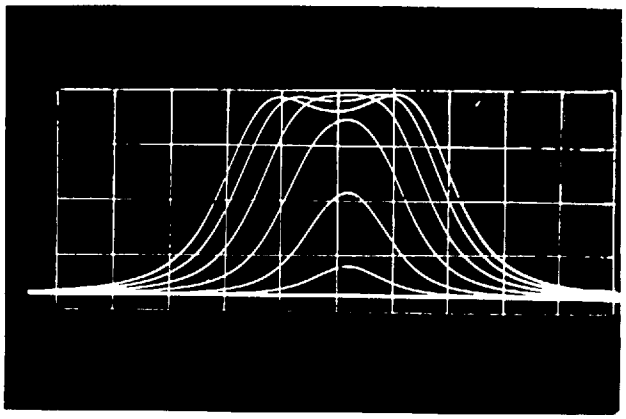
FIG. 6.13. 300-600Mc/s TR. DEVICE.

photograph of Fig. 6.14a, where centre frequency is 330Mc/s and sweep rate is 0.5Mc/s/cm. The curves corresponding to settings 0.00 and 1.00 coincide with the base line. Strongest coupling shown is 7.00 when the loops are nearly in the same position as shown in the drawing of Fig. 6.13. At higher frequencies the mutual coupling is stronger and at 600Mc/s the response curve at maximum coupling divides into two separate humps. 600Mc/s is the upper limit of operation of this unit because then in the $\lambda/4$ mode the dielectric ring of the moving gap assembly is right at the coupling loops, and although operation at higher frequencies in the $3\lambda/4$ mode would be possible in principle the performance of the device would not be satisfactory due to the self-resonance of the large loops.

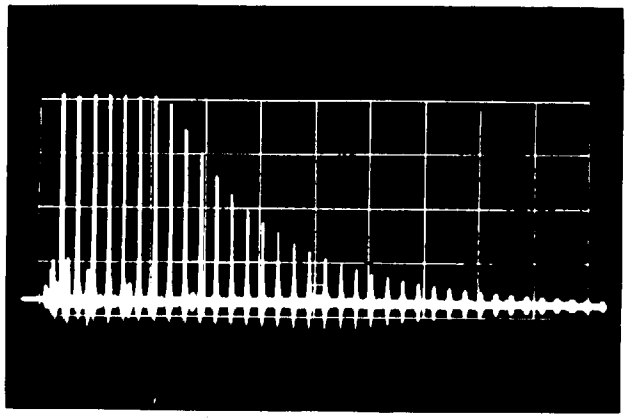
6.7 MIXER.

The heterodyne single-ended mixer was adopted from a GR 874MR rectifier mixer. It consists of a short section of coaxial line with a 250Ω series resistor and a Microwave Associates type 1N416F silicon mixer diode (see Fig. 6.15). The output of the local oscillator is applied to the diode through the resistor, while the signal is applied directly. The 250Ω resistor assures that the impedance presented to the signal frequency will always be reasonably high and independent of local oscillator matching.

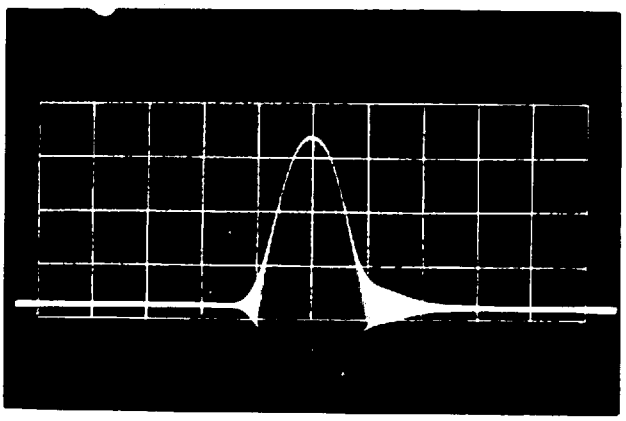
The mixer did not represent 50Ω for the signal. (The VSWR varied between 4 and 7.) To obtain a better match two or three stub tuners were placed in front of the mixer. These stubs were so adjusted that while they improved the match from the TR cavity to the mixer at the signal frequency, they also transformed the very low impedance of the TR cavity coupling loop at local oscillator frequency to a high shunt impedance at the diode.



a) Low level frequency response of double cavity TR device. Sweep rate 0.5Mc/scm, centre frequency at 330Mc/s. The various traces are due to the coupling control set at 0.00, 1.00 (indistinguishable from base line), 2.00, 3.00, 4.00, 5.00, 6.00 and 7.00.



b) The echo train as seen after passing through the receiver. BC No 1 rod in tangential field cavity at room temperature. 20μsec/cm horizontal scale.



c) One of the echo pulses from the train above. The 30Mc/s IF carrier is just perceptable. 0.5μsec/cm horizontal scale.

FIG. 6.14 FREQUENCY RESPONSE OF TR DEVICE AND VARIOUS RF. ECHOES.

The r.f. signal is heterodyned down to the intermediate frequency of 30Mc/s. Various commercial oscillators and signal generators (c.f. Section 6.9) served as local oscillators. Best noise performance was obtained when the local oscillator power and matching stubs were so adjusted that the rectified current as monitored by a milliammeter was 0.5mA. The impedance of the crystal dc return is 100Ω. The IF signal is fed through a low-pass filter with cut-off frequency of 40Mc/s to the IF head amplifier.

6.8 IF AMPLIFIER.

The head amplifier is a cascode circuit (Fig. 6.15) built inside a small diecast box right at the IF connector of the mixer. When operated at 0.5mA rectified crystal current the mixer presents an effective 400Ω impedance to the grounded cathode first stage of the amplifier. This 400Ω is near the optimum grid input impedance for low noise performance. A neutralising coil is provided to tune out the grid-anode capacity obtaining a slight improvement in noise figure. Due to the high gain of the first stage the noise figure of the whole amplifier depends predominantly on the noise introduced by the first stage.

The second stage is a grounded grid stage forming the anode load of the first valve. The low input impedance of the grounded grid circuit results in good stability and good power match between the stages.

The complete head amplifier gave the following performances figures:

Centre frequency	30Mc/s
Bandwidth	2Mc/s
Noise figure	1.5dB
Gain	30dB

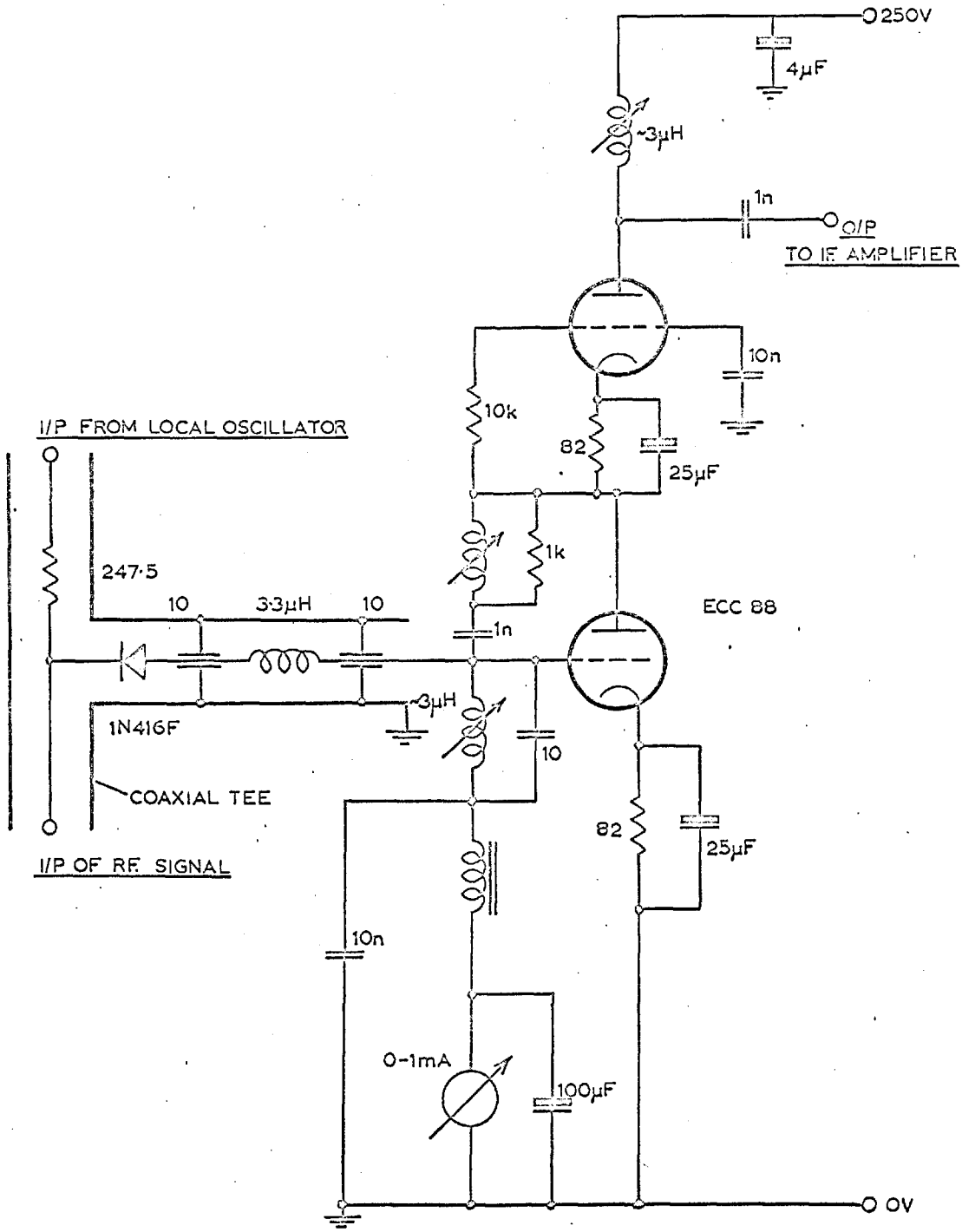


FIG. 6.15 MIXER & IF HEAD AMPLIFIER.

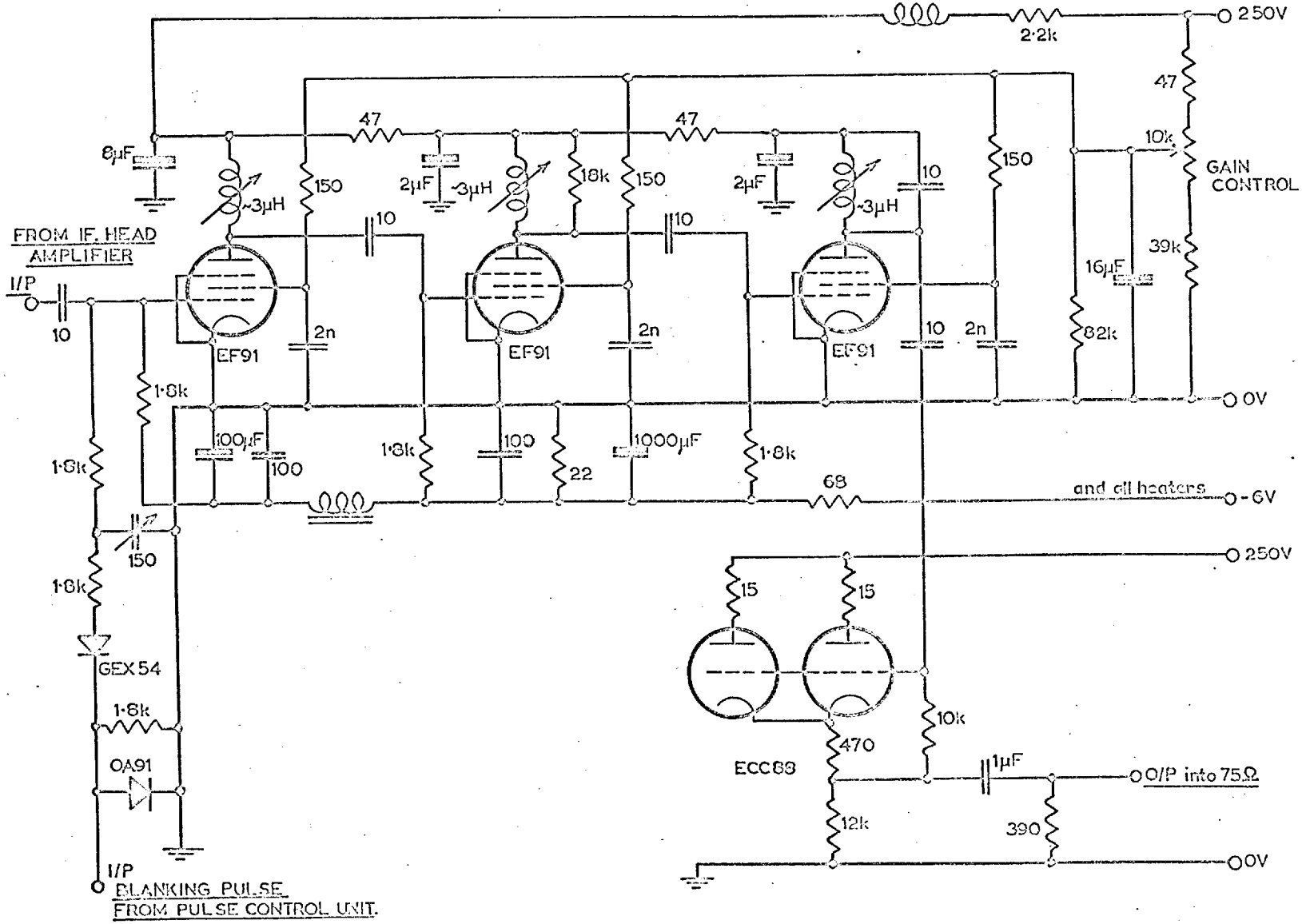


FIG. 6.16 I.F. AMPLIFIER.

The main amplifier (Fig. 6.16) consists of 3 stagger-tuned stages and a cathode follower to provide a non-demodulated output into 75Ω. The 5Mc/s bandwidth of the main amplifier makes the alignment of the head amplifier relatively simple. The input grid of the first valve is driven beyond cut-off by a 50V negative blanking pulse from the pulse control unit whilst the main transmitter oscillator fires. Semiconductor diodes clamp the blanking pulse and isolate the blanking circuit from the IF amplifier. A variable gain control without noticeable detuning effects is provided by altering the screen-grid voltage of the pentodes. All filament heating is obtained from a 6V/4A dc power supply. Great care was taken during the construction of the amplifier to minimise blocking effects and also to have a good square-wave response even at very low pulse repetition frequencies.

The overall sensitivity of the receiver system was -103dBm for a 1:1 signal-to-noise ratio resulting in a noise figure of 8dB at 500Mc/s. Overall voltage gain was 75dB, substantially linear for r.f. input voltages less than 0.1mW.

Typical amplified pulses are shown in Figs. 6.14b and 6.14c.

6.9 LIST OF STANDARD EQUIPMENT.

Signal generators:

Hewlett-Packard 612A (450-1200Mc/s)
Hewlett-Packard 614A (800-2100Mc/s)
Advance Instruments L1/20 (300-1000Mc/s)
Marconi TF 801 (10-470Mc/s)
Philips GM 2877 sweep generator

Oscillators:

General Radio Unit Oscillator GR 1208-C (65-500Mc/s)

General Radio Unit Oscillator GR 1209BL (180-600Mc/s)

Oscilloscopes:

Tektronix 585

Hewlett-Packard 185B 1000Mc/s sampling oscilloscope

Power meters:

Hewlett-Packard 430C Thermistor power meter

Hewlett-Packard 431B "

Hewlett-Packard 477B Thermistor mount

Hewlett-Packard 478A "

Power supplies:

Servomex AC2MkIIB mains stabiliser

APT 4213/1

APT 4213/2

Advance DC2

Advance Volstat CV150A constant voltage transformer

Miscellaneous:

GR 874 LBA slotted line

GR 1602 B UHF admittance bridge

Sanders VSWR amplifiers MkIII

AEI Selective amplifier Mk3D

Sanders Diode mounts CON/S16

Hewlett-Packard frequency meter 536A

GR coaxial elements

Coaxial line oscillator (180-500Mc/s) constructed according to drawings supplied by STC

CHAPTER 7.
TRANSDUCER SYSTEM 1: THE QUARTZ CRYSTALS.

7.1 CRYSTALLOGRAPHIC ORIENTATION

The transducer system of the present work consists of a quartz rod and an electromagnetic cavity resonator. One of the flat surfaces of the rod acts as a piezoelectric surface transducer, while the cavity, into which the quartz rod is inserted provides an electric field of high intensity and of suitable direction and spatial distribution at the piezoelectric surface.

Below about 100Mc/s fused quartz is used extensively for viscoelastic measurements. At higher frequencies however, the intrinsic attenuation of fused quartz becomes too high for accurate viscoelastic measurements even at room temperature; below liquid nitrogen temperatures there is a very wide absorption peak where the attenuation increases to several hundred dB/cm at 1kMc/s, (Jones et al. 1964). At the outset of this work it was realised that a medium with much less attenuation has to be used. Silicon single crystals were tried (in the 111 orientation degenerate for shear waves) which gave an improvement of about 3 times over fused silica, but the very serious problem of attaching resonant shear transducers to the silicon still remained. So crystal quartz was selected as the propagating medium - its attenuation was known to be less than that of fused quartz, and being piezoelectric, surface excitation could be used. The abolition of resonant transducer and bond contributed greatly to the high accuracy and repeatability of the present system.

Although direct surface excitation of microwave acoustic waves was first observed by Baranskii (1957), the theory of surface excitation has only been developed for the first time in connection with the present work (Chapter 4).

Bömmel and Dransfeld (1960) and Jacobsen (1959, 1960) succeeded in generating and detecting both longitudinal and shear waves along certain crystallographic directions in quartz. In all these experiments the electric field was normal to the excited surface as in a conventional attached transducer. Tangential fields were used by Bechman (1960) to excite an AT-cut thickness shear resonator around 1Mc/s. The fact that any of the three acoustic modes can be surface excited practically independently of crystallographic orientation by lining up the electric field with the preferred direction of excitation (Equation 4.20) has not been realised before.

The quartz crystals take the form of short circular cylinders closed by carefully polished flat parallel surfaces. A portion of their surface acts as the source of acoustic energy. The diameter of the acoustic beam is usually much smaller than the diameter of the rod. The length of the rod defines the maximum pulse length for good separation between successive echoes. The rod axis is oriented along a selected direction in the crystallographic coordinate system.

For the investigation of the viscoelastic properties of liquids under cyclic shear stress, the first requirement from the selected crystallographic direction is that it should be able to propagate a pure shear wave. From Figs. 5.6 and 5.7 it is evident that seven groups of such directions exist, generating seven closed curves on the surface of the unit sphere. All the rotated-Y directions (directions in the YZ crystallographic plane) and the X crystallographic direction are among the group capable of supporting a pure shear mode.

It is useful if the velocity surface of the acoustic mode in question has a maximum or a minimum in the selected crystallographic direction. Then a small misorientation obviously does not cause

appreciable change in the value of acoustic velocity and impedance. More important, however, is the fact that in these directions the energy propagates parallel to the phase velocity vector, i.e. the rod axis. (The beam direction is normal to the tangent plane of the inverse surface (Appendix G) which is now also at a stationary value.) When the beam angle deviates from the direction of phase propagation there is no cumulative error at reflection. The beam returns on itself when reflected from a plane surface which is parallel to the surface of excitation: the power flow is given by

$$P_i = - T_{ij} j\omega u_j = -\omega k c_{ijk2} u_k u_j \qquad 7.1$$

and all three components change sign when the sign of k is changed. At large beam deviation angles the acoustic beam is reflected between portions of the end surfaces which are not directly opposite to each other and might be considerably out of parallelism. When the axial length of the rod is relatively large, the acoustic beam can be reflected by the side surfaces and be completely lost for further coherent detection. The construction to find the angle of reflection in this curious case of parallel incidence is shown in Appendix G (Fig. G.2).

There are five possible orientations where the shear velocity is either maximum or minimum, three of which are pure shear orientations. These are the X, AC and BC directions.

Those orientations that possess a degenerate shear mode (e.g. Z-cut quartz or the 111 direction in a cubic crystal) are considered particularly useful when a separate resonant shear transducer has to be attached to the anisotropic crystal rod, since then there is no need to line up the movement of the transducer with the polarisation of the required mode in the crystal. In the above mentioned two examples, however, the velocity surfaces cross each

other forming a double cone. For silicon the external semicone angle $\beta = 12^{\circ}$, so the energy deviates from the axis also by 12° in a direction normal to the direction of mechanical displacement (Musgrave, 1956). A slight misorientation δ of the rod axis from the true crystallographic 111 direction produces a difference in the velocities of the (now non-degenerate) shear modes, with

$$\frac{\Delta v}{v} = \tan\beta \cdot \tan\delta \qquad 7.2$$

It is not possible in practice to keep the misorientation angle δ small enough and the two modes always arrive back for detection with appreciable phase difference, causing serious interference effects. On removing and replacing the transducer it is likely that the phase difference is changed and that the acoustic beam is reflected from a different portion of the reflecting surface, than originally. This might explain the lack of reproducibility of the decay patterns when a 111 oriented silicon rod was used for acoustic attenuation and some checking purposes in visco-elastic measurements. For this 1.5cm long silicon specimen the difference in the two shear velocities was so great that after the 11th echo the decay pattern separated into two sets of pulses. The measured velocity difference between the two modes indicated a misorientation angle of 2.5°.

Another requirement from the crystallographic orientation is to allow the excitation of the selected shear mode with maximum efficiency with the other two modes only very slightly excited. Figs. 5.12 to 5.14 show that the Z orientation does not excite the longitudinal mode at all. There is another minimum in the longitudinal excitation near to the BC orientation.

The preferred directions of excitation, unlike the directions of mechanical displacement, are not mutually perpendicular, and

even if the electric field lies entirely in the preferred direction of the wanted mode, there is no guarantee that it will not excite the unwanted modes. For both the BC and AC orientations the preferred direction of excitation of the pure shear mode makes an angle of 90° with the preferred direction of the other two modes, thus allowing to suppress the unwanted modes by careful cavity design. For the X orientation the preferred directions of excitation of the two shear modes coincide.

It is most important that the crystallographic direction selected for viscoelastic measurements had a low attenuation for the pure shear mode. After developing a successful exciting cavity, the attenuation of the excitable modes of the available quartz specimens have been measured. The results of these measurements are given in Chapter 10. The pure shear mode (=FS) of the BC and the FS mode of the X orientations have the lowest possible attenuation for an acoustic wave in quartz.

On account of the foregoing arguments the pure shear (FS) mode of the BC will be used, as the most suitable, for viscoelastic measurements. Its preferred direction of excitation for the wanted shear mode lies in the YZ plane making an angle of approximately 60° with the internal surface normal. The acoustic displacement is in the X crystallographic direction. The only disadvantage of the BC pure shear mode is its high acoustic impedance ($1.4 M\Omega$).

7.2 PREPARATION OF THE CRYSTAL SPECIMENS.

The quartz specimens that have been used for viscoelastic or acoustic attenuation measurements are listed in Table 7.1. They are all X-cuts or rotated Y-cuts. The sides are usually marked with two fine lines to define the position of the YZ or XZ planes, whichever is appropriate.

With the exception of specimens no. 3 and 4, all the rods were cut from the natural occuring rock crystal. No difference in acoustic behaviour was found between the natural and the synthetic crystals. The latter, however, were etched more easily, and the surface could become pitted under accidental electrode sparking. No detrimental effect of sparking was found on the natural crystals.

The following are the basic requirements from the prepared rods:

To be homogeneous single crystal without apparent defects.

Axis of rod to be in the specified direction within the allowed manufacturing error.

To have optically polished end surfaces, flat and parallel within at least 10 seconds of arc.

The crystallographic axes of the raw material were identified by some of the characteristic faces of the unpolished crystal and the cylinders cut in the required orientations by the supplier. The X, Y and Z crystals have their rod axis parallel to the appropriate crystallographic axes within 30'. The specification of the rotated Y-cut BC, AC, etc. directions requires a prior knowledge of the elastic constants of quartz. The BC specimens obtained by this laboratory in 1959 and before had their angles at $-59^{\circ}00'$. BC crystals ordered after 1960 had their angles specified at $58^{\circ}15'$. (With the present knowledge of the elastic constants the angle is put at $58^{\circ}29'$.) The Hackbridge Works of the Marconi Co. Ltd. could keep a manufacturing tolerance of 12' on this angle, although the misorientation out of the YZ plane was not guaranteed better than 30'. They worked to half of these tolerances in cutting, but additional errors arose in lapping and polishing.

Once the crystals were in rod or disc form their orientation could be checked by X-rays only. With the X-ray equipment available only rough checks were possible to be made on the orientations. These checks showed that the orientations were nearer to the symmetry planes than guaranteed. The rotation angles of the used rotated Y-cuts being not contained in crystallographic dense planes could only be checked within $\pm 1^{\circ}$ for relative position between some more symmetric direction; (e.g. (01.2) and (01.3) for the BC cut - see Fig. 5.2).

The electromagnetic coupling of a few of the crystals was found abnormally low. Therefore specimen no. 3 (the worst in this respect) was lightly etched in HF solution to remove the top surface layers which might have got damaged and randomly recrystallised during sawing or any other mechanical working. After careful repolishing the electromechanical coupling was up to standard. It was thought that other bad crystals which did not have this treatment also improved somewhat during use.

7.3 PARALLELISM AND FLATNESS.

If it is required that the whole of the excited plane wavefront should arrive back to the exciting surface during each echo in uniform phase, then the distance travelled by any point on the wavefront should be very nearly the same even after several echoes, therefore the parallelism of the end faces must be very good.

Considering an idealised uniform piston source of diameter 2r the total signal received over this same area is given as

$$A = \int_{-r}^{+r} \int_{-\sqrt{r^2-x^2}}^{\sqrt{r^2-x^2}} e^{-jk2n\delta x} \, dy \, dx \qquad 7.3$$

where n is the number of double pathlengths travelled by the

wavefront in the z direction in a homogeneous medium, δ is the non-parallelism of the endfaces in radians and k is the acoustic wavevector (Carr and Strandberg, 1962). Integration by dy and change of variables yields

$$A = -2r^2 \int_{\pi}^{0} e^{-jk2n\delta r\cos\theta} \sin\theta .\ \sin\theta .d\theta \qquad 7.4$$

Then integration by parts gives Sommerfelds integral:

$$A = \frac{2r^2}{jk2n\delta\, r} \int_{\pi}^{0} e^{-jk2n\delta r\cos\theta}\ \cos\theta .d\theta = r^2 \frac{2J_1(k2r\delta n)}{k2r\delta n} \qquad 7.5$$

If the argument of the first order Bessel function is written as

$$k2r\delta n = \alpha n \qquad 7.6$$

where α is the non-parallelism in acoustic wavelengths over the piston area and n is the echo number (as previously), then the change in amplitude due to non-parallelism is given by

$$\frac{2\ J_1(\alpha n)}{\alpha n} \qquad 7.7$$

This function is plotted in Fig. 7.1. It can be seen that if the attenuation introduced by non-parallelism is to be less than 1dB over a train of 40 pulses, the non-parallelism over the piston area has to be better than 1/40 acoustic wavelength.

The parallelism of the rods was checked by a Twyman-Green interferometer. Typical interferograms are shown in the photographs of Figs. 7.2 as obtained for specimen no. 2. For the upper photograph the instrument was initially adjusted to give a uniform brightness all over the field. Introduction of the quartz rod with non-parallelism Δ caused a phase difference of

$$\phi = 2\left(\frac{\Delta}{\lambda_q} - \frac{\Delta}{\lambda_{air}}\right)2\pi \qquad 7.8$$

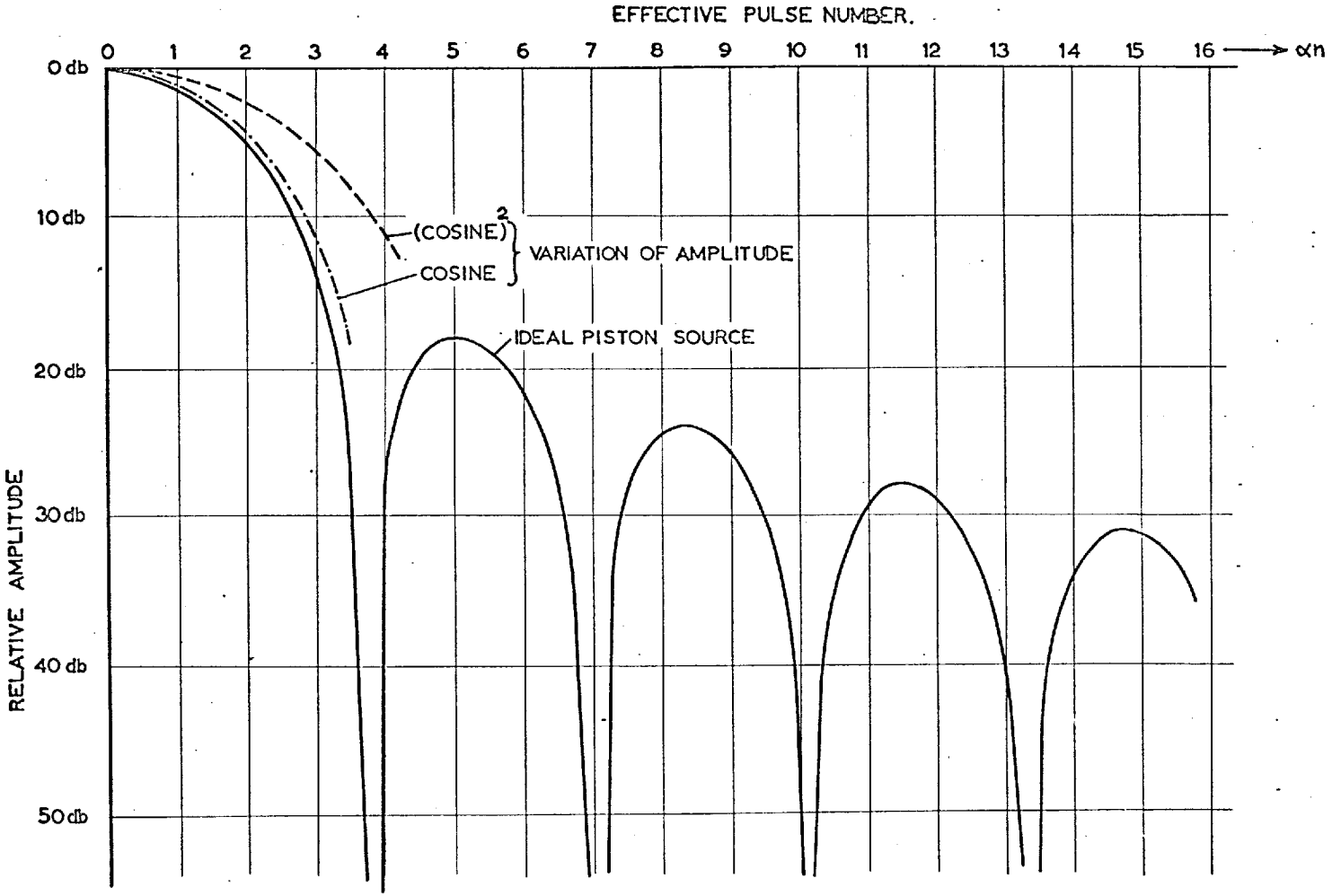


FIG. 7.1 REDUCTION IN SIGNAL AMPLITUDE DUE TO NON-PARALLELISM.

giving rise to the interference pattern. (λ_{air} and λ_q are the wavelengths of green mercury light in air and in quartz respectively). The number (N) of interference fringes observed under the above conditions is related to the non-parallelism as

$$\Delta = N.\lambda_{air}\frac{1}{2(\nu-1)} = N.\lambda_{air}\ 0.9 \qquad 7.9$$

where ν is the refractive index of quartz. The whole of the area bounded by the circular dark fringe has a parallelism better than 1/2 fringe, equivalent to 1/40 acoustic wavelength at 500Mc/s.

The lower interferogram of Fig. 7.2 can be interpreted as cross-sections of the surface cut parallel to the rod axis if the background lines are dense enough. Examination of pictures of this kind reveals that the surfaces of the specimen are not absolutely flat, but are very slightly convex. This proved to be an advantage rather than an embarassment, because it enabled the selection of small (say 3 x 3mm) portions of the two opposing surfaces which for all purposes were flat and parallel to their counterpart. (E.g. in the middle of white central area non-parallelism is 0, while the average angle over the whole sphere is 5" of arc.

7.4 SURFACE FINISH.

Scratches and polishing marks scatter the beam incident on a reflecting surface and thus cause a change in the phase and a reduction in the amplitude of the reflected wave as compared with an ideally smooth reflector. The change in phase gives the apparent effect of slightly reducing the length of the specimen, as indeed Koga (1958) found in connection with the determination of the elastic constants of quartz that the effective thicknesses of his plates with a milky white lustre finish were 1.1μ less than the measured thicknesses. While it is important to know the exact

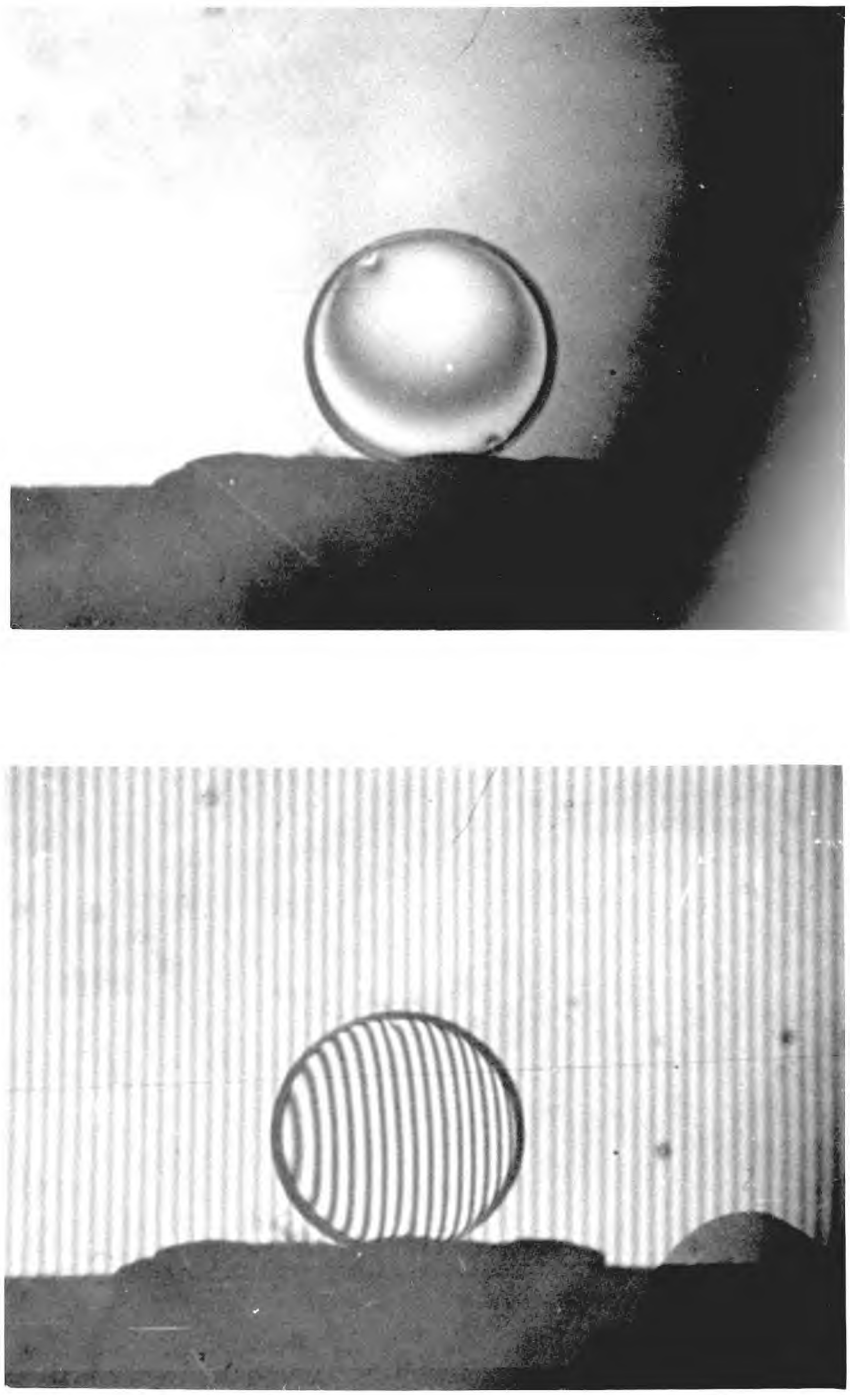


FIG. 7.2 TYPICAL INTERFEROGRAMS.

position of the reflecting surfaces in precision velocity and phase measurements, it is of no consequence in the present technique.

To calculate the loss in coherent reflected signal due to end-surface scattering it is necessary to know the shape of the surface. In order to simplify the calculation it will be assumed at the moment that the surface has randomly distributed parallel square grooves along the direction of the shear displacement polarisation. (It will be found that the result of the calculation is not very sensitive to the actual form of the surface cross-section.) The depth of the grooves is b and their average number is r per unit length. (Fig. 7.3) They are dependent mostly upon the particle size of the final grade polishing powder used in the preparation of the surface. The chosen direction of the grooves assures that no conversion occurs between acoustic modes at reflection. Then following the method of Raleigh (1945) the Fourier spectrum is obtained for the above random binary function, and the scattering loss by each Fourier component is calculated. Because of the complete randomness of the surface the total scattering loss is obtained by summing the component losses.

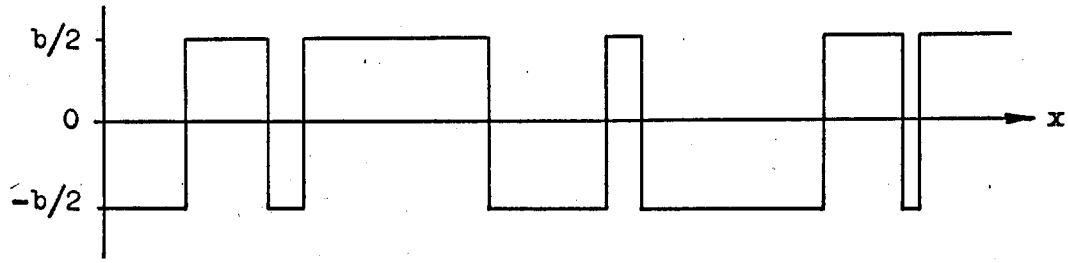


FIG. 7.3 SURFACE CROSS SECTION

The shape shown in Fig. 7.3 is identical to the "random binary telegraph signal" whose Fourier power spectrum is given by textbooks on information theory (e.g. Schwartz, 1959 p448.) as

$$a_n^2 = \frac{b^2/8r}{1 + (k_n/4r)^2} \qquad 7.10$$

with $$k_n = \frac{2\pi n}{L}$$

where L is the length of the surface in the direction normal to the grooves. Since there is no unique relationship between waveform and spectrum of random signals, a large number of different types of signals have the same spectrum. For example the power spectrum of the random telegraph signal is identical with the spectrum of white noise passed through an RC network with time constant RC = 1/4r, so the previous assumption of surface cross-section, however arbitrary, is likely to produce realistic results.

Let the incident plane wave of unity amplitude described by

$$u_i = e^{j(\omega t - kz)}$$

be scattered by a sinusoidal corrugation of the form (Raleigh 1945 II p 89):

$$f(x) = a_n \cos k_n x$$

In isotropic medium, for simplicity, the reflected wave will have the form (with the omission of the time-varying factor)

$$u_r = A_o e^{jkz} + A_1 e^{j\mu_1 z} \cos k_n x + A_2 e^{j\mu_2 z} \cos 2k_n x + \ldots \qquad 7.11$$

with $$\mu_1^2 = k^2 - k_n^2$$

$$\mu_2^2 = k^2 - 4k_n^2 \quad \text{etc.} \qquad 7.12$$

For any real value of $\mu = \mu_p$ the corresponding term in the expression of Equation 7.11 is

$$A_p e^{j\mu_p z}\cos pk_n x = \tfrac{1}{2}A_p\left\{e^{j(\mu_p z - pk_n x)} + e^{j(\mu_p z - pk_n x)}\right\} \qquad 7.13$$

representing plane waves reflected at inclined angles of $\sin^{-1}\frac{pk_n}{k}$ giving rise to the pth order lateral diffraction.

If $k > k_n$, μ is imaginary, and at distances far away from the reflecting surface all higher order diffracted waves are died out. In other words when the wavelength of the sinusoidal surface roughness is less than that of the incident plane wave, normal reflection occurs and in summing the series (Equation 7.11) only those terms with $k_n < k$ have to be considered. Then k_n^2 can be neglected when compared with k^2 giving

$$\mu \approx k$$

thus
$$u_r = e^{jkz}(A_o + A_1\cos k_n x + A_2\cos 2k_n x + \ldots) \qquad 7.14$$

The condition of stress-free surface requires that

$$\frac{\partial u_i}{\partial z} + \frac{\partial u_r}{\partial z} = 0 \qquad 7.15$$

at the surface (i.e. when $z = a_n\cos k_n x$), therefore

$$-jke^{-jkz} + jke^{jkz}(A_o + A_1\cos k_n x + \ldots) = 0$$

or
$$e^{-2jka_n\cos k_n x} = A_o + A_1\cos k_n x + A_2\cos 2k_n x + \ldots \qquad 7.16$$

Comparing Equation 7.16 term by term with the Bessel expansion

$$e^{-j\alpha\cos\beta x} = J_o(\alpha) - \sum_{p=1}^{\infty} 2(j)^p J_p(\alpha)\cos p\beta x \qquad 7.17$$

shows that

$$A_o = J_o(2ka_n) \qquad 7.18$$

and therefore the intensity of the normally reflected wave from the given Fourier component of the surface corrugation is

$$J_o^2(2ka_n) \qquad 7.19$$

and the amount of energy lost by scattering from this surface component is

$$S_n = 1 - J_o^2(2ka_n) \qquad 7.20$$

Based on 0.1μ diameter final size polishing powder, the depth of the grooves is taken as 0.1μ and their average number as 10^5 per cm. Then it is found that the second term in the denominator of Equation 7.10 is negligible compared to 1 and is independent of n:

$$a_n^2 = \frac{b^2}{8r} \qquad 7.21$$

Furthermore at 1000Mc/s $k \approx 2.10^4 cm^{-1}$, so $2ka_n \ll 1$ and the approximation

$$J_o(\alpha) = 1 - \left(\frac{\alpha}{2}\right)^2 \qquad 7.22$$

is justified. Therefore

$$S_n = k^2 a_n^2 \qquad 7.23$$

and the total scattering loss is given by

$$S = \sum_{n=0}^{n_{max}} k^2 a_n^2 = n_{max} k^2 \frac{b^2}{8r} = k^3 \frac{Lb^2}{16\pi r} \qquad 7.24$$

For a length of 5mm substitution of the previously chosen data gives a total scattering loss of 0.001dB/reflection at 1000Mc/s, which is completely negligible. However, the loss increases with the cube of frequency. At higher frequencies much more stringent requirements have to be imposed on the quality of the surface finish. The previously (maybe pessimistically) assumed surface roughness causes 1dB/reflection loss at 10kMc/s. It is estimated that under typical conditions this 1dB scattering loss can give rise to 10% error in viscoelastic measurements.

CHAPTER 8.
THE TRANSDUCER SYSTEM 2: RESONANT CAVITIES.

8.1 USE OF CAVITIES.

From the theory of piezoelectric excitation it can seen (Section 42) that the excitation is proportional to the electric field across the piezoelectric-air discontinuity. The resonant cavity provides this electric field of high intensity at the flat surface of the quartz rod in the desired direction and spatial amplitude distribution. The required direction of the electric field should be near the preferred direction of the mode, and is dependent on the crystallographic orientation of the quartz rod in use; it can be of any direction from tangential to normal to the surface. The amplitude distribution should approximate that of a piston source with the amplitude smoothly falling off towards the edges.

The cavity resonator also acts as an impedance transformer: it transforms the voltage on the 50Ω input transmission line to a much higher value across the equivalent shunt resistance of the cavity, thereby improving the power match between the electromagnetic and acoustic systems.

It is not absolutely necessary to use cavity resonators for the above purposes. The open circuit voltage at the end of a transmission line can be made to have an increased value by means of multiple reflections, introduced by suitably placed shunt stub tuners. Proper cavities, however, are easier to tune and to match to the source.

Cavities constructed for viscoelastic work must allow measurements to be taken while immersed in thermostats.

All the cavities constructed during the present study are working in a hybrid TEM coaxial mode. They consist of a length of coaxial line terminated in the reentrant gap capacitance, and can be classified into two groups: single-tuned normal-field and double-tuned tangential-field cavities. The gap region of the normal-field cavity produces an electric field mainly perpendicular to the exciting surface of the piezoelectric crystal, while the electric field in the gap of the double-tuned cavity can be either parallel or normal to the crystal surface, depending on tuning conditions.

8.2 PHYSICAL ARRANGEMENT OF THE SINGLE-TUNED CAVITIES.

During preliminary investigations a number of these cavities were constructed following the original designs of Bömmel and Dransfeld (1960), and without any thermostatting facility. They were used to study the basic effects of surface excitation and to obtain some indication of the attenuation of the various quartz specimens. One of these developmental cavities is shown in Fig. 8.1.

Fig. 8.2 shows one half of a twin cavity arrangement fixed-tuned at 720Mc/s. The whole structure could be immersed into a thermostat bath. The truncated cone end of the crystal holder kept the quartz rod in a well-defined position with the help of a strong compression spring. A drop of the sample liquid was placed on a thin glass microscope slide to be raised into contact with the lower end of the quartz rod by the liquid applying mechanism actuated by rotating the cam-shaft. Capillary action ensured that the total quartz surface was covered by the liquid. Removing the screwed cover allowed the whole crystal holder to drop out for cleaning and recharging.

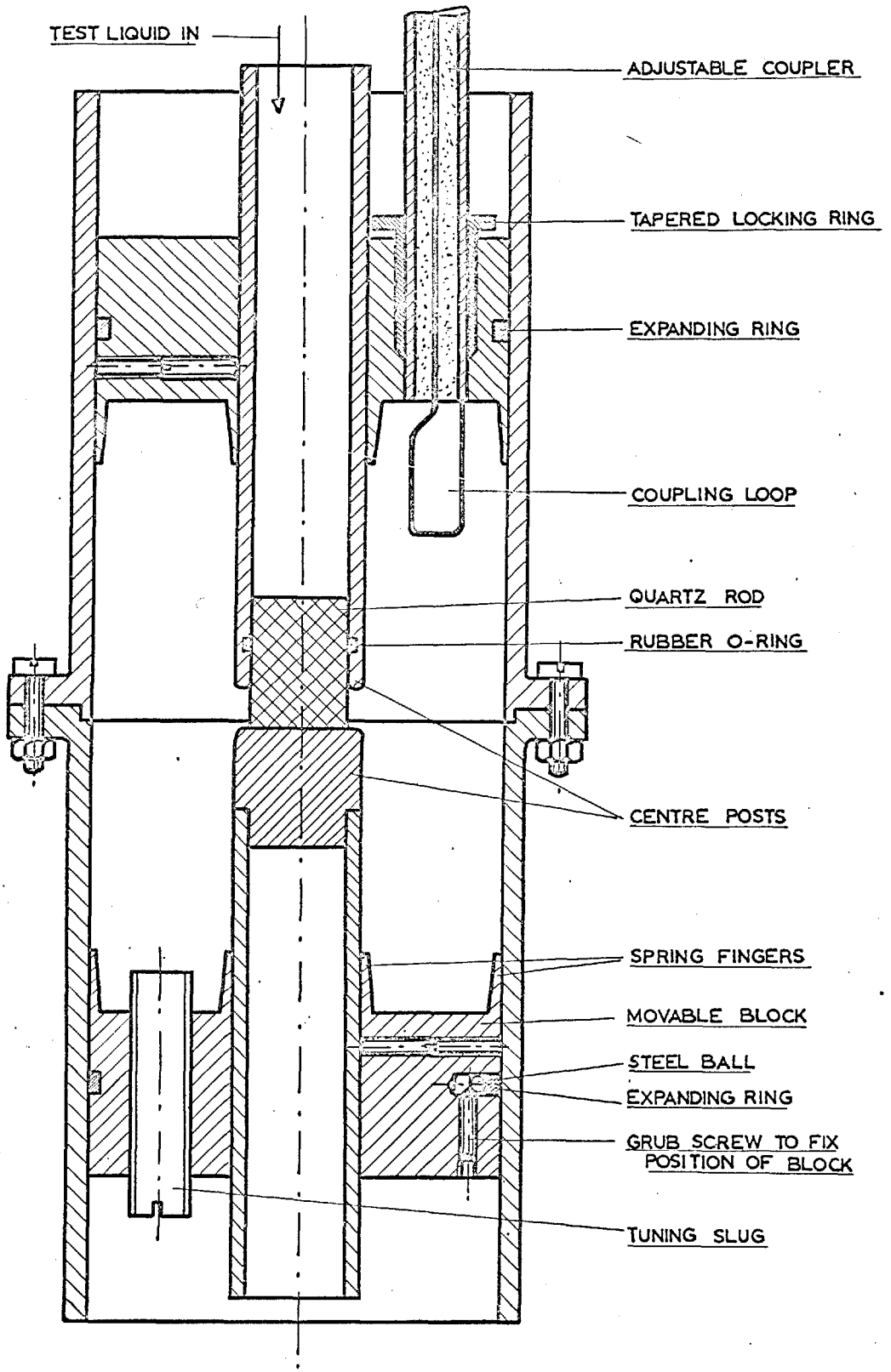


FIG. 8.1 DEVELOPMENTAL NORMAL-FIELD CAVITY.

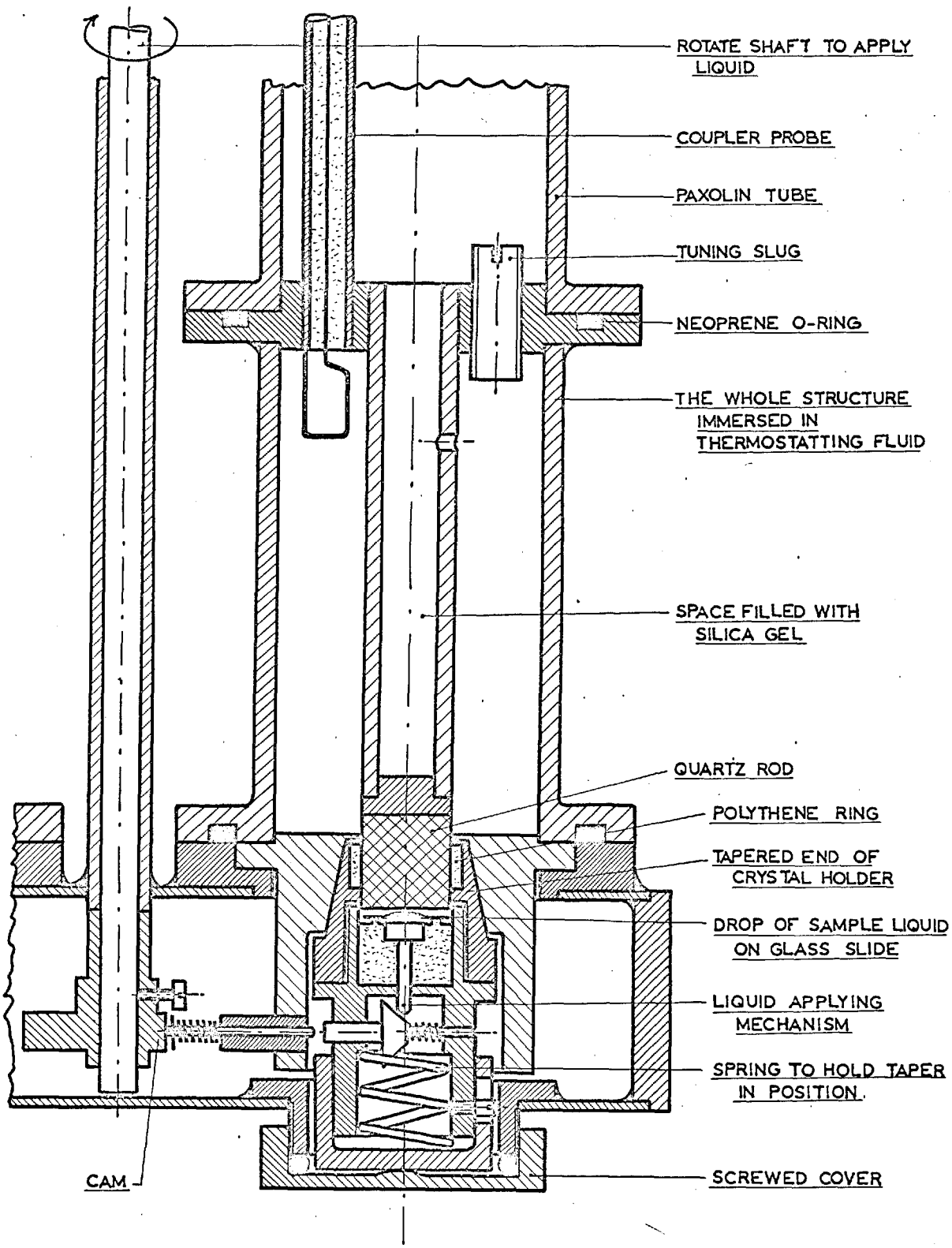


FIG. 8.2 NORMAL-FIELD CAVITY

The failure of this cavity to give reproducible and sensible measurements prompted the construction of the cavity shown in Fig. 8.3. The free surface of the quartz rod in this design is easily available from the outside for investigations into the acoustic field pattern. Most of the metal parts of the cavity were surrounded by circulated thermostatting fluid contained by a cylindrical jacket. The structure was mounted on a trolley.

This cavity is tunable from 500 to 1500Mc/s by rotating the threaded shaft via 90° bevel gears from the front of the instrument. The nut riding on the thread drives the plunger through an axial slot, thus effecting the tuning. The pole-piece at the end of the centre conductor is changeable; on the diagram a stycast disc of dielectric constant 12 is shown to concentrate the field to the middle of the quartz surface. The sample liquid injected by a syringe is driven through a coiled stainless steel tube for intimate thermal contact with the thermostatting fluid and dropped on the free top surface of the quartz rod by a hypodermic needle.

With suitable pole-pieces good longitudinal measurements could be made using an X-cut rod and some shear measurements using a Y-cut rod. The measurements of the distribution of acoustic field intensities over the quartz surface area were first made in this cavity as described in Section 8.5. The study of these field plots led to the construction of the novel type tangential-field cavities.

8.3 PHYSICAL ARRANGEMENT OF THE TANGENTIAL-FIELD CAVITY.

A simple tangential crystal holder was constructed first (Fig. 8.4) tuned by GR stub tuners to study the effects of tangential excitation qualitatively, since tangential electric fields had not been used before for microwave piezoelectric

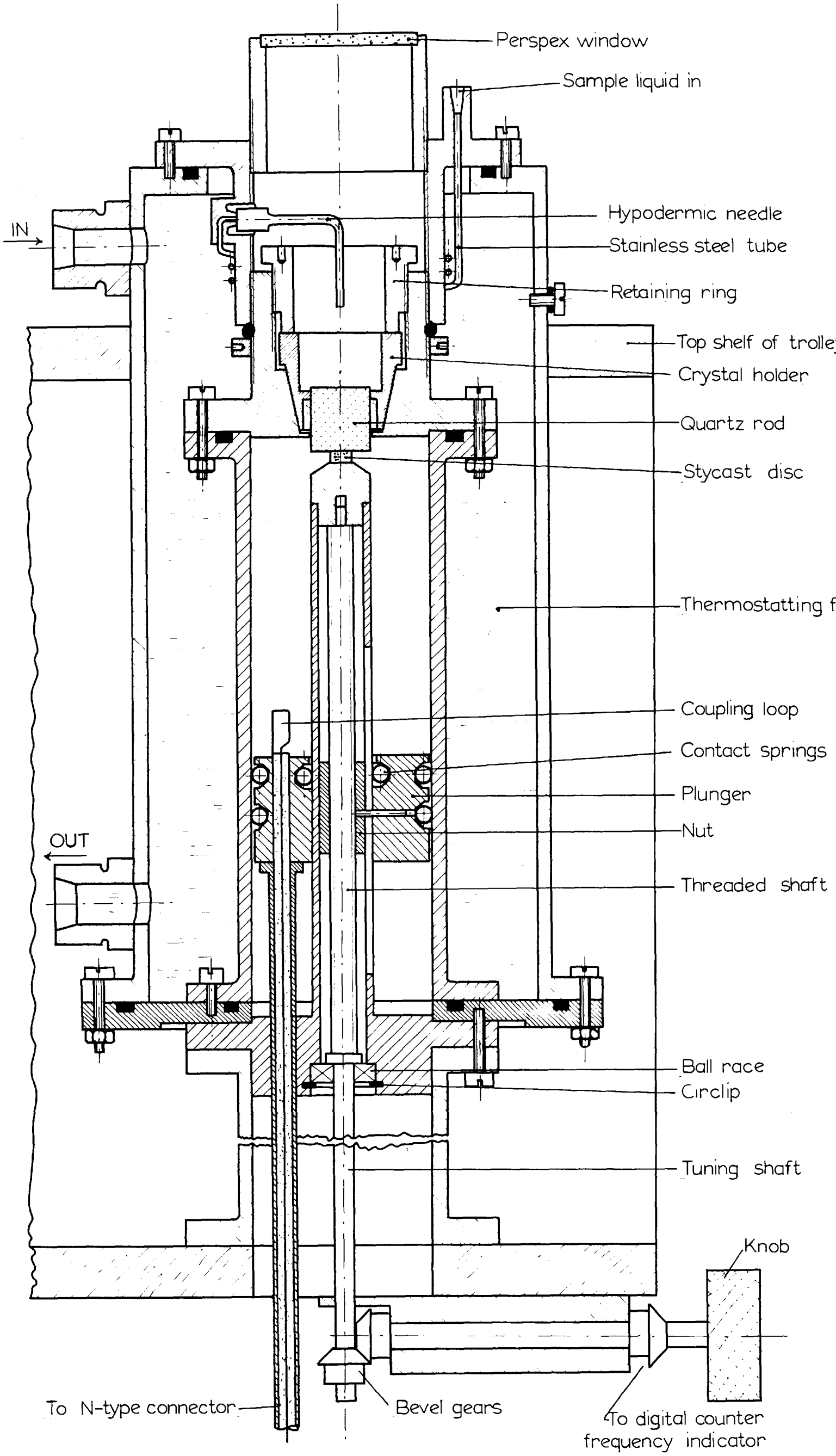


FIG. 8.3 NORMAL-FIELD CAVITY WITH THERMOSTATTING JACKET.

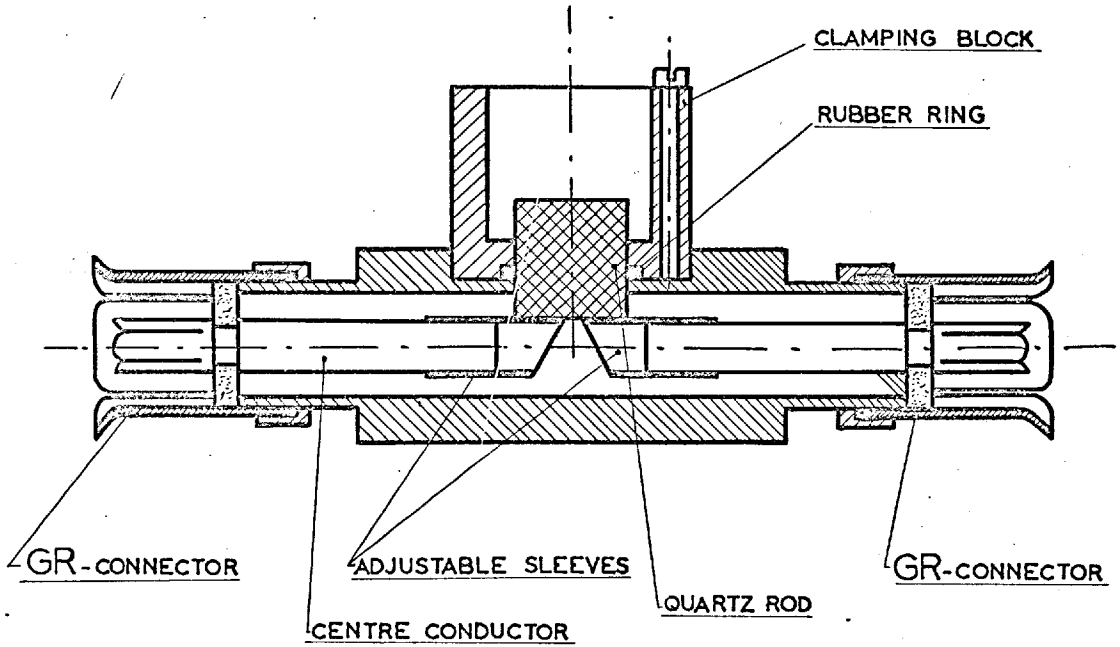


FIG. 8.4 SIMPLE TANGENTIAL-FIELD CRYSTAL HOLDER.

excitation. Making use of the experience obtained by this simple unit a cavity system was constructed that proved to be very successful for microwave acoustic and viscoelastic work.

The schematic diagram of the final version tangential-field cavity is shown in Fig. 8.5 while the workshop assembly drawing is shown in Fig. 8.6 at a scale slightly larger than 1:2. This cavity consists of two quarter-wavelength shortcircuited lines folded for space economy and coupled together by the gap region. The quartz rod is placed over the centre conductors in the gap region.

The frequency range when operated in the lowest frequency mode is 300 to 1600Mc/s. Each line is separately tunable by moving the shortcircuiting plunger fixed to a slide through an axial slot cut in the cavity wall. Good contact between the moving parts is obtained by phosphorbronz helical contacting springs. A spring loaded antibacklash nut is fixed to the slide enabling it to be moved up or down by rotating the large screw coupled to the external tuning shaft via a flexible coupler. The positions of the two tuning plungers are indicated by digital counters operated via gear links and are visible through the two silica windows of the top cover. The above described details can be seen (in addition to the engineering drawing) in the photographs of Figs. 8.7 and 8.8.

Electromagnetic energy is fed in or out of the cavity by two loops rotatable for optimum coupling. The loop rotating mechanism is also fixed to the slide (see Fig. 8.7 for example). It consists of an N-type female connector, a 90° elbow, rotatable joint and a short length of coaxial line fixed to the loop. 2kW power handling capacity and constant 50Ω characteristic impedance is maintained throughout. The loop is inserted into the

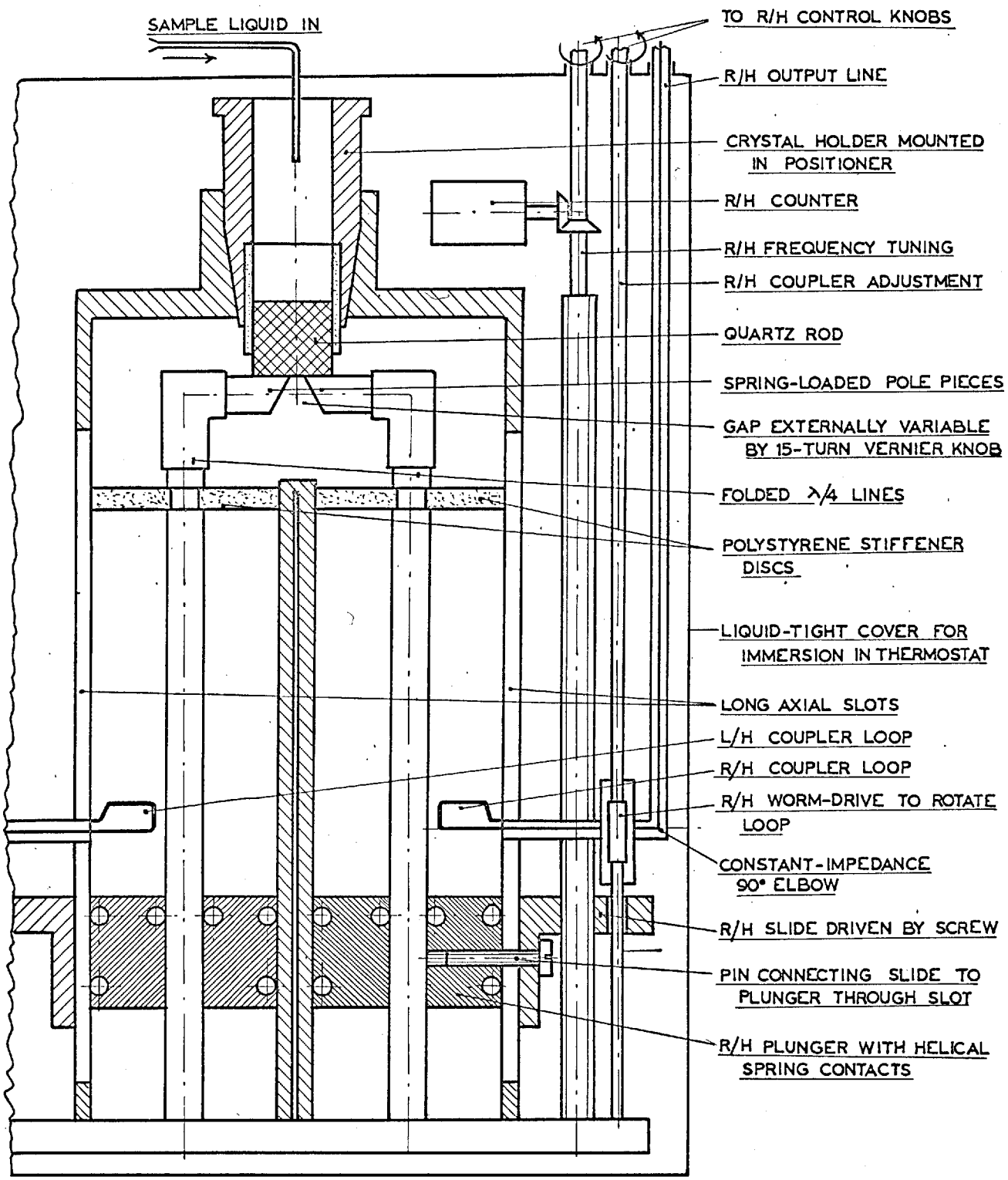
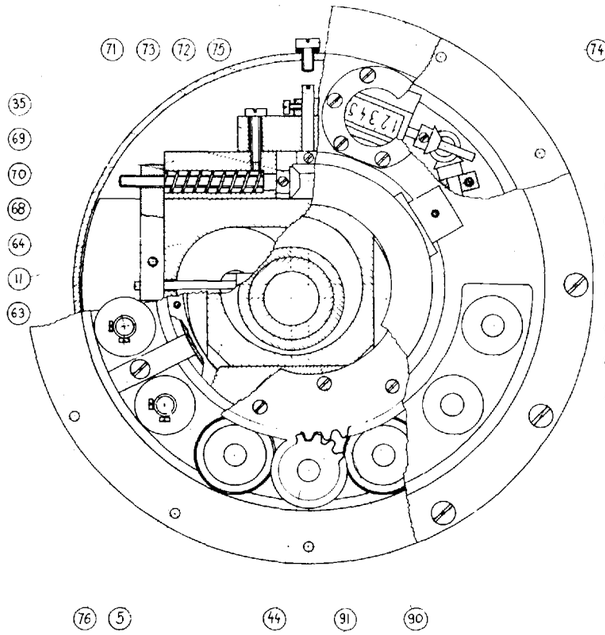
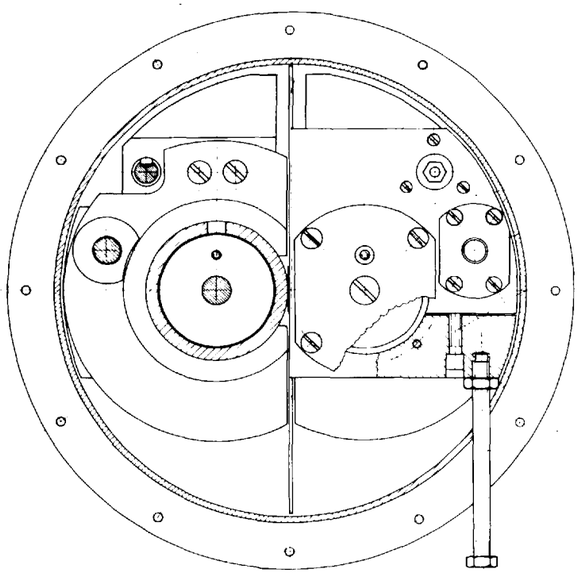
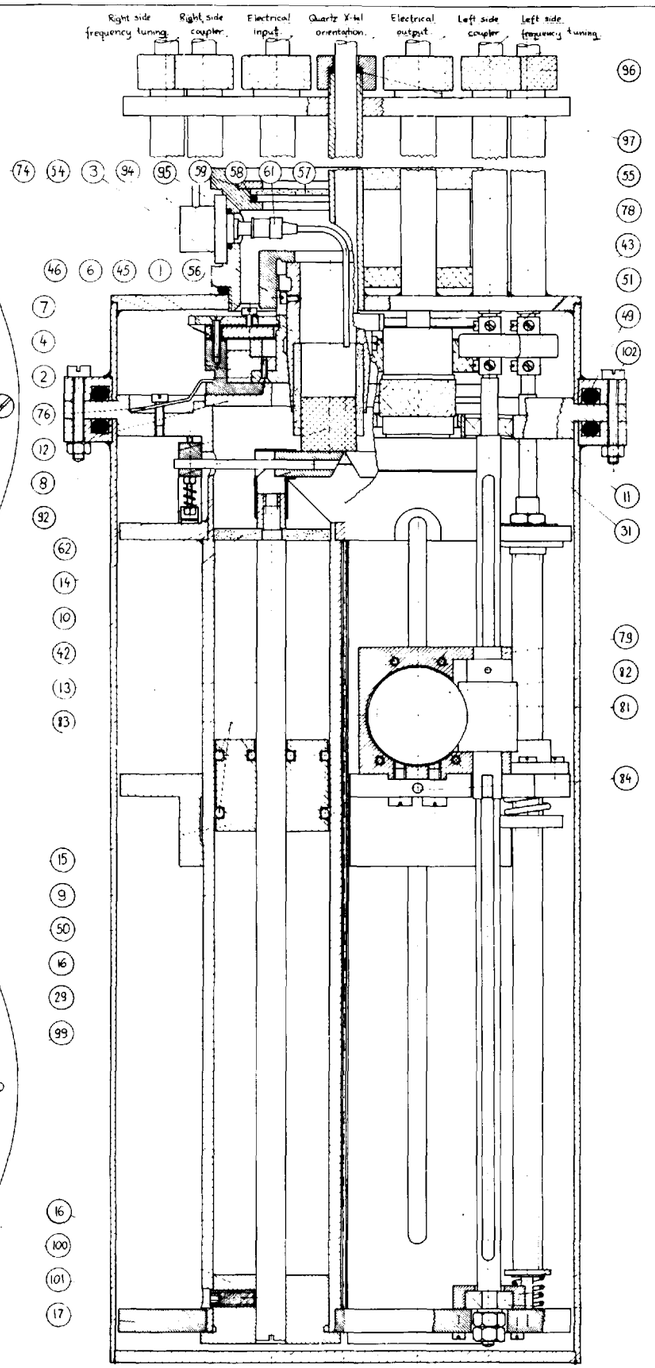
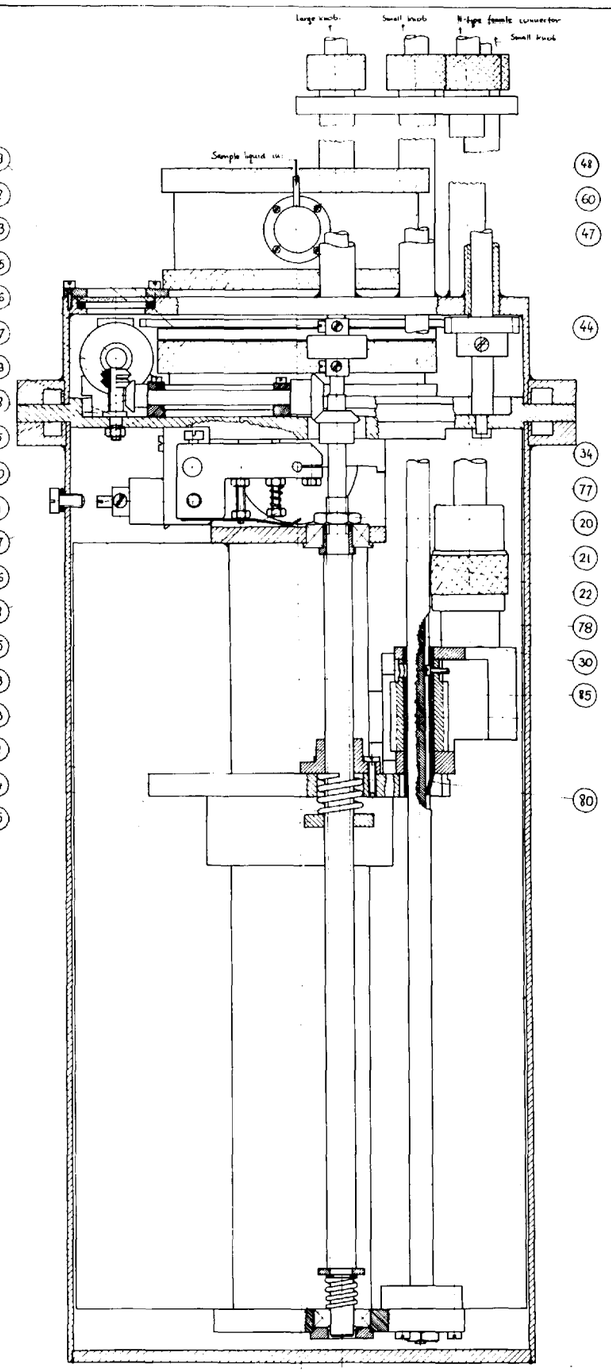


FIG. 8.5 SCHEMATIC DIAGRAM OF TANGENTIAL FIELD 340–1600Mc/s CAVITY.









			69	Spring	2
			68	Gap adjustment screw	2
			67	Steel rod	2
			66	Tension adjustment screw	2
			65	Height adjustment screw	2
			64	Plate	2
			63	Fused silica rod	2
			62	Pole-piece	2
			61	Hypodermic needle	2
			60	Coupler output shaft (see 95)	2
			59	Window ring	1
			58	O-ring (under window)	1
			57	Glass window	1
			56	O-ring a	1
			55	Screw-on top	1
			54	Counter window ring	2
			53	O-ring (over counter)	2
			52	Glass disc	2
			51	Top cover	1
			50	Bottom cover	1
			49	O-ring (in flanges)	2
			48	Tuning o/p. shaft	2
			47	Rotating o/p. shaft	1
			46	Spacer cylinder	6
			45	Large gear	1
			44	Small gear	1
			43	Flexible coupler	4
			42	Dielectric ring	2
			41	Steel rod	2
			40	Bearing block	4
			39	Pin (for double bevel)	2
			38	Counter base	2
			37	Counter	2
			36	Double bevel	2
			35	Small bevels	7
			34	Large bevels	4
102	Screws in flange	4BA	12	33	Hub	2
101	Worm screw	2BA	2	32	Ball race BAI 4x13x5mm	2
100	Temporary leg		2	31	Ball race Hoffmann 3/16"x9/16"	2
99	Sockethead screw	4BA	2	30	Coupler shafte	2
98	Tensioning flat spring		2	29	Cover plate	2
97	O-ring		7	28	Ball race 1/16"x 5/16"x 3/16"	2
96	Knurled nut		7	27	Circlip	2
95	O-ring		3	26	Washer	2
94	Liquid input cone		3	25	Anti-backlash nut	2
93	Spring (under detun. rod)		2	24	Spring	2
92	Quartz crystal		1	23	Nut	2
91	Screening plate		1	22	Sleeve	2
90	Position locating screws	6BA	3	21	Stepped ball race	2
89	Springy washer		1	20	Hex nut 1/4" slot	2
88	X-tal orientation knob		1	19	Drive shaft	2
87	Frequency tuning knob		2	18 A/B	Slide (top each)	2
86	Coupling adjustment knob		2	17	Bottom bracket	1
85	Coupler assembly		2	16	Plug	2
84	Driving pin		2	15	Plunger	2
83	Contacting spring		6	14 1/2	Endpiece with elbow (1/2)	2
82	Coupler gear		2	13	Centre electrode	2
81	Worm		2	12 1/2	Cavity cover plate	1
80	Sleeve with key		2	11	Cavity top	1
79 A/B	Coupler block (top each)		2	10	Top bracket	1
78	N-type female connector		2	9	Cavity tube	2
77	Input tube & N-type male		2	8	Polythene tube	12
76	Flat spring		4	7	Rotating base	1
75	O-ring		1	6	Top slide	1
74	Screw	6BA	1	5	Cross slide	1
73	Retaining ring		1	4	Bottom slide	1
72	Spindle with slot		1	3	Clamping screw	1
71	Bridge piece		1	2	Taper	1
70	Block		2	1 1/16	Crystal holder	4
No.	Description:		Qty	No.	Description	Qty

Grooved tapped dowel screwings, 3.2.64 TP

TANGENTIAL FIELD RESONANT CAVITY.
(for the generation of ultrasonic waves.)
TUNING RANGE: 340 - 1600 Mc/s.

G.U. ELECTRICAL ENG. DEPT. 10/1/1964.

FIG. 8.6

cavity through the axial slot. Good electrical contact between its grounded side and the internal cavity wall is realised by spring fingers. The loop with its short coaxial structure is rotated by a worm-gear drive operated by a slotted paxolin rod, a flexible coupler and the external coupling adjustment shaft. A length of rigid coaxial line freely sliding in one of the vertical tubes of the top cover connects the loop assembly to the external N-type connector. Care was taken during design not to allow the part of the cavity behind the plunger or the coupling and driving rods to become resonant structures at the operating frequency or its multiples.

The horizontal parts of the centre conductors of the cavity are termed pole-pieces on the schematic diagram. They make contact with the vertical centre conductors by L-shaped springs (see Fig. 8.8) and are held in position by 0.1in diameter fused silica rods clamped into the side-plates (item 64 of the assembly drawing). Each of the side-plates has a steel pin (67) attached to it that can turn or slide in a block (70) thereby allowing the pole-pieces vertical or axial movements. In the vertical direction the pole-pieces are spring loaded (98) not to introduce stresses into the quartz rod that touches them. The axial position, and thereby the gap width, is set symmetrically by the knob with the attached counter dial through bevel gears and spring loaded screws. The vertical and axial movements are independent: the gap width can be altered with the pole-pieces depressed.

The quartz rod is held in a polythene sleeve, which is clamped tight by the crystal holder (1). The tapered crystal holder is seen on the left of Fig. 8.7 with a black rubber seal to increase the liquid tightness of the polythene sleeve-quartz rod combination. The crystal positioner is seen in the centre of the top part of Fig. 8.8. It allows translational movement of the

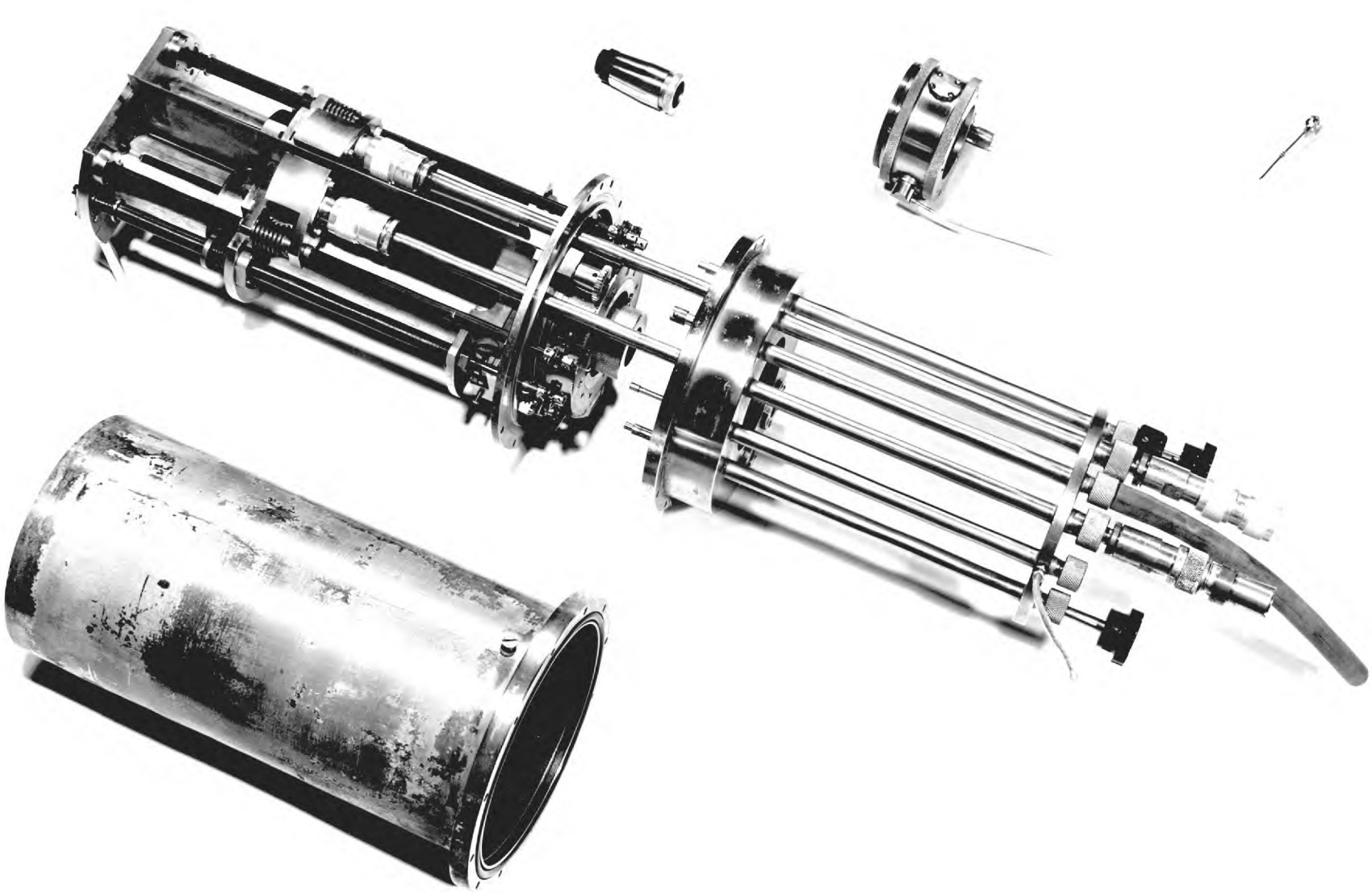


FIG. 8.7 VIEW OF DOUBLE-TUNED CAVITY.

crystal holder in the horizontal plane (but not rotation) to position a selected portion of the surface over the gap area. The required position is fixed by tightening the two diagonally placed screws. Now the crystallographic orientation of the quartz rod can be lined up with the field of the cavity by rotating the whole quartz holder about the centre of the previously selected area. This is effected by turning the small gear externally by the crystal orientation shaft, with the angular position visible next to the right hand side tuning indicator through one of the windows.

The small hole bored in the crystal holder and visible in Fig 8.8 allows a thermocouple probe to be plugged in. This way the thermocouple junction could be in close vicinity to the sample liquid.

The three flanges belonging in turn to the bottom lid, the cavity, and the top cover are screwed together with neoprene O-rings in between. (Removing the small screw visible on the side of the lid (Fig. 8.7 or item 74 in Fig. 8.6) allows adjustment of the gap width with a screwdriver when the lid is in position.) Replacing the screw-on top (shown on the left of Fig. 8.7) makes the unit liquid-tight.

The sample liquid is injected on to the quartz top surface during measurements by a stainless steel hypodermic tube fixed to the screw-on top. A large silica window allows visual inspection of the state of cleanliness of the quartz surface just prior to the liquid injection. It also allows to check that the test liquid is covering the quartz surface completely and that it does not contain air bubbles.

The external tuning shafts are made air-tight by tightening

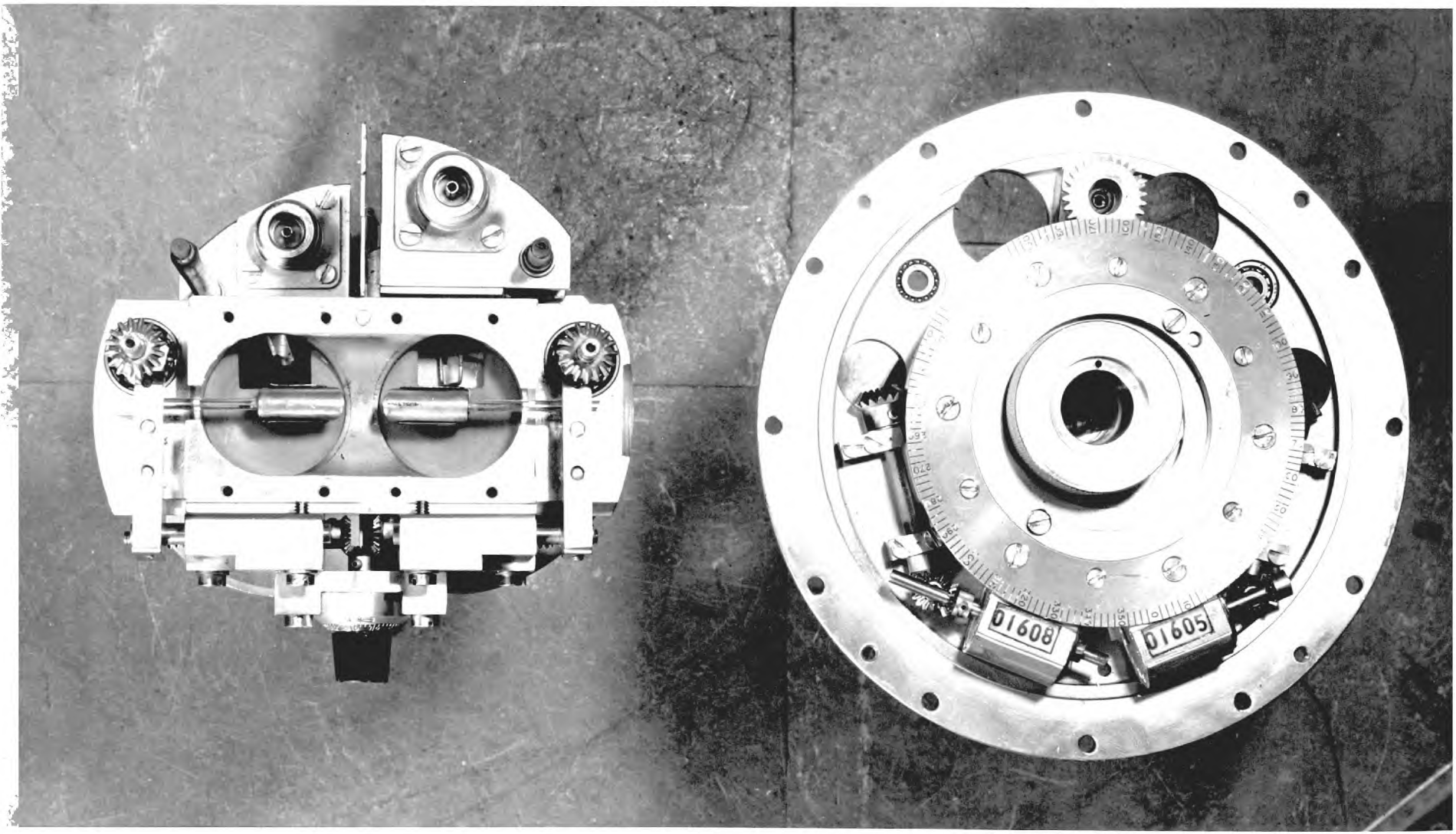


FIG. 8.8 INTERNAL DETAILS OF DOUBLE-TUNED CAVITY.

the knurled nuts (96). The crystal orientation shaft has a central bore through which dried and carbondioxide-free air can be pumped right down to the bottom of the cavity to flush out the system before cooling to subzero temperatures.

8.4 ELECTRICAL PROPERTIES.

The single reentrant cavity is widely used in microwave engineering, and will not be treated in detail here. Its resonant frequency can be calculated from

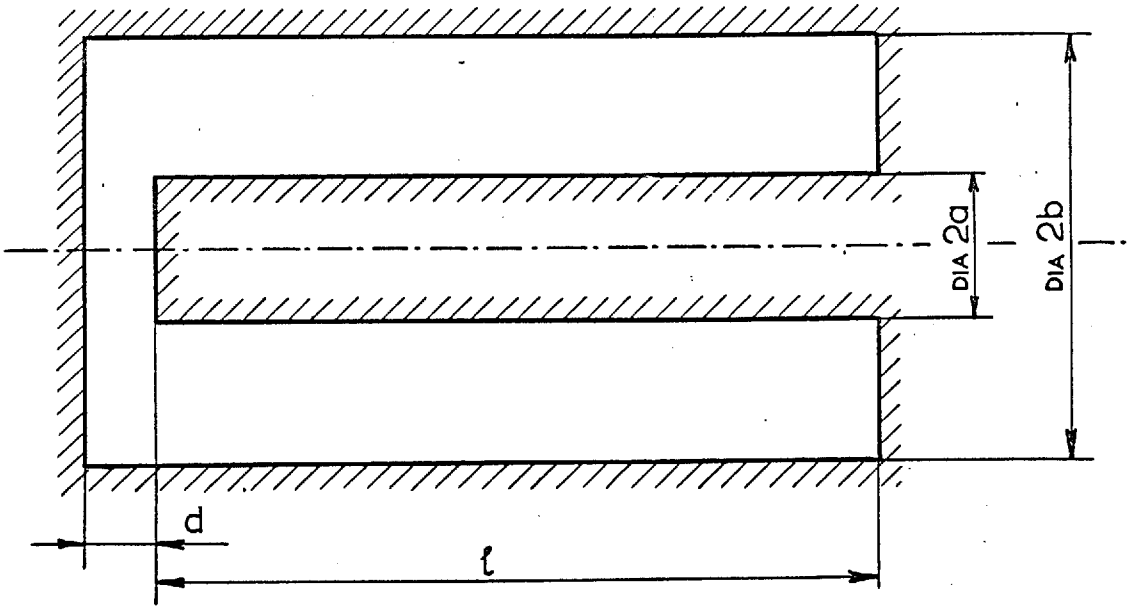
$$\omega^2 = \frac{1}{LC} \cdot \qquad 8.1$$

C is the effective gap capacitance and L is the equivalent inductance of the line section:

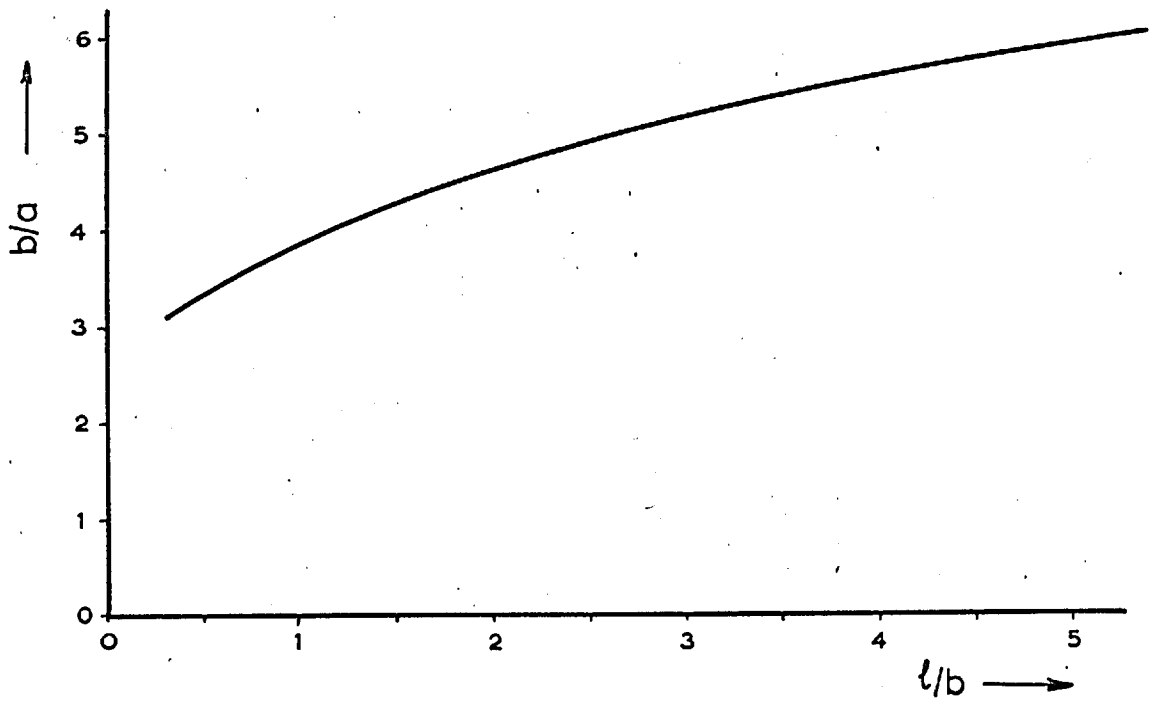
$$L = \frac{1}{\omega} Z_o \tan\frac{2\pi}{\lambda} \qquad 8.2$$

where Z_o is the characteristic impedance of the lines, λ is the electromagnetic free space wavelength, and ℓ is the length of the centre electrode (approximately $\lambda/4$). There are a number of methods to determine the effective gap capacitance taking into account the effect of fringing fields, (Fujisawa, 1958). To a first approximation the effective gap capacitance equals the capacitance of the reentrant gap. Since the dimensions of the gap region are much smaller than the wavelength of operation, it is possible to regard the fields in this region as electrostatic fields with sinusoidal time variation. While no effort has been made to calculate for idealised geometries these fields or the effective gap capacitance, the piezoelectric field-probe technique has been developed to determine empirically the electric fields at the quartz surface in the actual working cavities.

The shunt impedance of a cavity of the type shown in Fig. 8.9a, when there are no dielectric losses, is given approximately by



a) DIMENSIONS OF REENTRANT CAVITY.



b) OPTIMISED DIAMETRAL RATIO FOR BEST EFFICIENCY.

FIG. 8.9

(Moreno, 1958)

$$R_{sh}\frac{\delta}{\lambda} = 60\pi\left(\frac{2\ell}{\lambda}\right)^2 \frac{\ln^2(b/a)}{2\ln(b/a) + \ell\left(\frac{1}{a}+\frac{1}{b}\right)} \qquad 8.3$$

where δ is the skin depth of the metal, λ is the electromagnetic wavelength, and a, b, ℓ are cavity dimensions. The practical electromechanical conversion efficiency is proportional to (Equation 4.48)

$$\frac{A}{d^2} R_{sh} \qquad 8.4$$

When the piezoelectric crystal completely fills the gap, the area of the beam cross-section is the flat area of the centre electrode $a^2\pi$, so the efficiency is proportional to

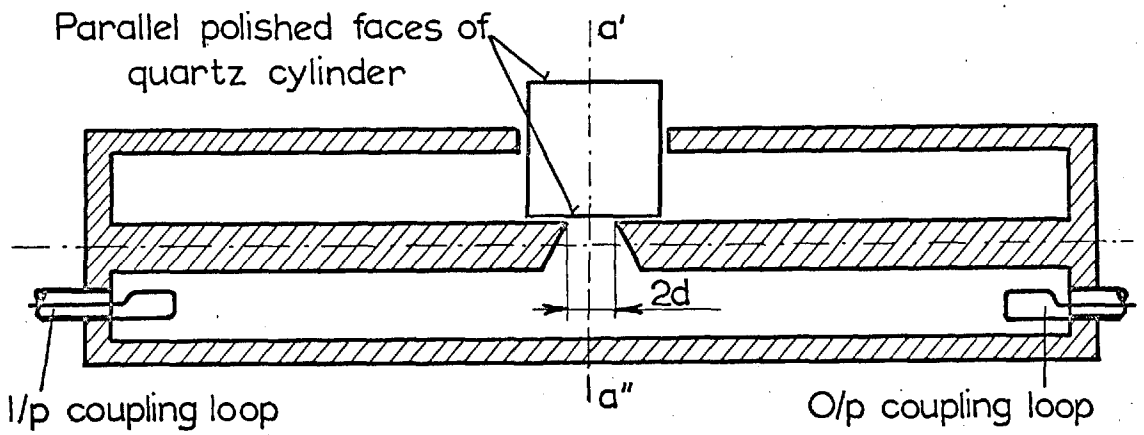
$$\frac{\ln^2 (b/a)}{\left(\frac{b}{a}\right)^2\left[2\ln\frac{b}{a} + \frac{\ell}{b}\left(1+\frac{b}{a}\right)\right]} \qquad 8.5$$

The optimum b/a ratio for maximum efficiency is 1.5 for a cavity length $\ell = 2b$. In the practical cavities the gap width d is much smaller than the length of the quartz rod, therefore an opening is cut in the cavity wall opposite the flat end of the centre electrode. The excited area is now proportional to the circumference of the centre electrode (c.f. Fig. 8.21), so the efficiency is proportional to

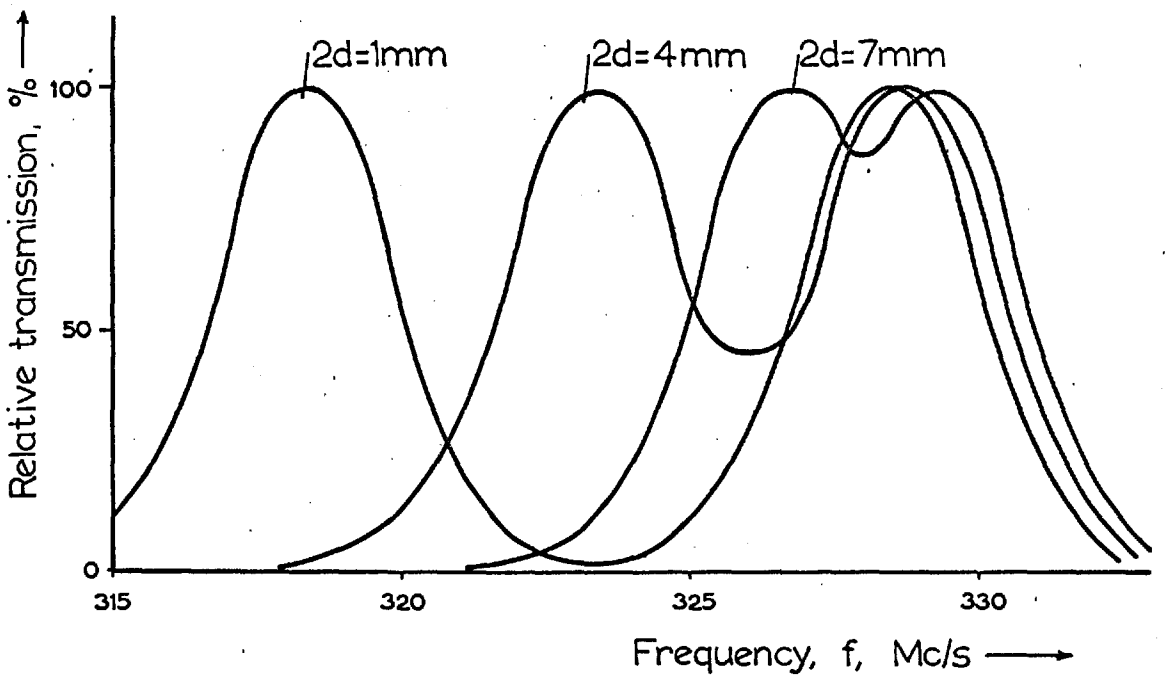
$$\frac{\ln^2 (b/a)}{\frac{b}{a}\left[2\ln\frac{b}{a} + \frac{\ell}{b}\left(1+\frac{b}{a}\right)\right]} \qquad 8.6$$

The optimised b/a ratio for this case is given in Fig. 8.9b as function of the ℓ/b ratio. For all the cavities that have been constructed the diametral ratio has been chosen between 4 and 5.

The electrical properties of the double reentrant cavity are not well known. Its schematic arrangement is shown in Fig. 8.10a (Lamb and Richter, 1966a). It is not generally recognised that



a) SCHEMATIC LAYOUT OF THE DOUBLE-TUNED CAVITY.



b) RESPONSE (WITH QUARTZ ROD REMOVED).

FIG. 8.10

such a cavity has two fundamental resonant frequencies.* Since the plane a'—a" is a plane of geometrical symmetry, it is customary to substitute it by an imaginary metal plate, thus dividing the double re-entrant cavity into two identical single cavities with gap d each. The introduction of the metal plate imposes the restriction that the electric field must be axial at the plane a'-a", while the original symmetry condition is also satisfied by an electric field distribution where the electric field remains radial in the gap region. The latter mode does not exist in a single re-entrant cavity.

The resonant structure can be regarded as two coaxial lines each approximately quarter-wavelength long connected together through the gap capacitance. The short-circuited transmission line on the right in series with the gap capacitance is the terminating impedance for the transmission line on the left. The input impedance Z_i at the plane of the input loop is given by standard lossless transmission line theory as

$$\frac{Z_i}{Z_o} = \frac{Z_L/Z_o + j \tan\beta\ell}{1 + j \frac{Z_L}{Z_o} \tan\beta\ell} \qquad 8.7$$

where Z_o is the characteristic impedance of the line sections, Z_L is the terminating impedance, $\beta = 2\pi/\lambda$, and ℓ is the equivalent length of the centre electrode of the line sections. Because of fringing fields not taken into consideration ℓ only approximately equals the physical length. Substituting the above defined terminating impedance gives

---

* At the time of writing a letter was received from Prof. Chang, Stanford University, in response to the paper Lamb and Richter, (1966a) to point out that he has been using for some time a double-tuned cavity in maser experiments at 3000Mc/s (Chang et al. 1959).

$$\frac{Z_i}{Z_o} = j \frac{1 - \frac{1}{Z_o \omega C \tan\beta\ell}}{\frac{1}{Z_o \omega C} + \frac{1}{\tan 2\beta\ell}} \qquad 8.8$$

where C/2 is the capacitance between the centre electrodes. Resonance occurs when $Z_i = 0$, that is when

a) $Z_o \tan\beta\ell = \frac{1}{\omega C}$ - resonance condition of a single re-entrant cavity with gap d and capacitance C between centre electrode and metallic plane at a'-a" (Equation 8.2). This resonant mode (out-of-phase mode) gives an electric field distribution with odd symmetry about the plane a'-a". The electric field in the gap region is substantially parallel to the cavity axis, i.e. tangential to the quartz surface.

b) $1/\tan 2\beta\ell = \infty$ i.e. $2\ell = \lambda/2$ - resonance condition of a half wavelength resonator formed by closing a transmission line with two short-circuits. This resonant mode (in-phase mode) gives an even symmetry for the electric field about the mid-plane. The electric field in the gap region is substantially radial.

Measurements of resonant frequency versus gap opening 2d are shown in Fig. 8.11 for a given setting of the tuning plungers in the cavity of Figs. 8.5 - 8.8. It can be seen, that for practical gap widths ($2d < 4$mm) the resonant frequency in the in-phase mode is almost independent of the gap width, and separation of the two modes is always more than 20Mc/s. The transmission of signal from the input to the output loop is shown by the tracing of an oscilloscope photograph in Fig. 8.10b when the frequency is swept between 315 and 335Mc/s. The various traces correspond to the following gaps between the centre conductors: 2mm (largest

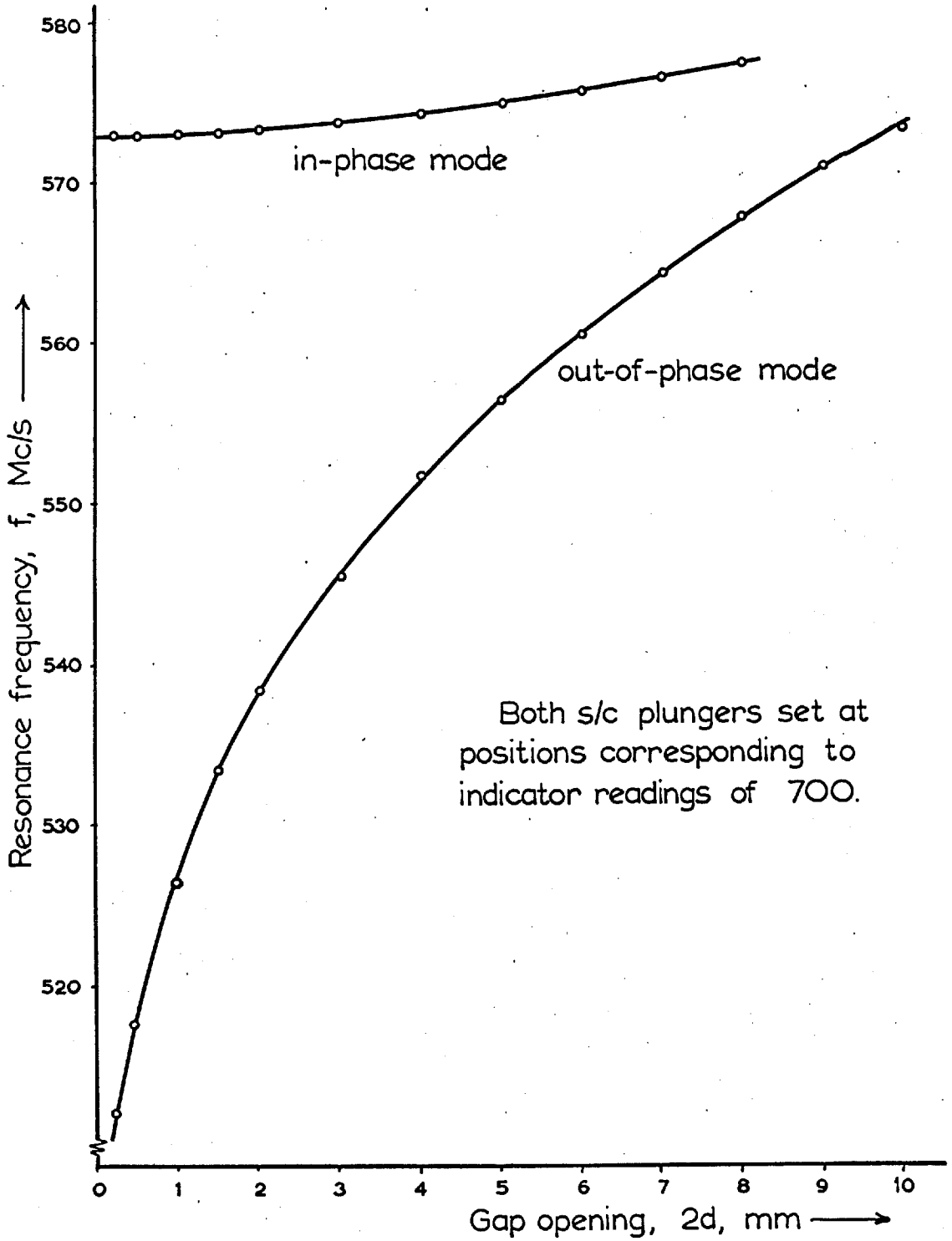


FIG. 8.11 RESONANCE CONDITIONS OF THE DOUBLE-TUNED CAVITY AT CONSTANT TOTAL LENGTH.

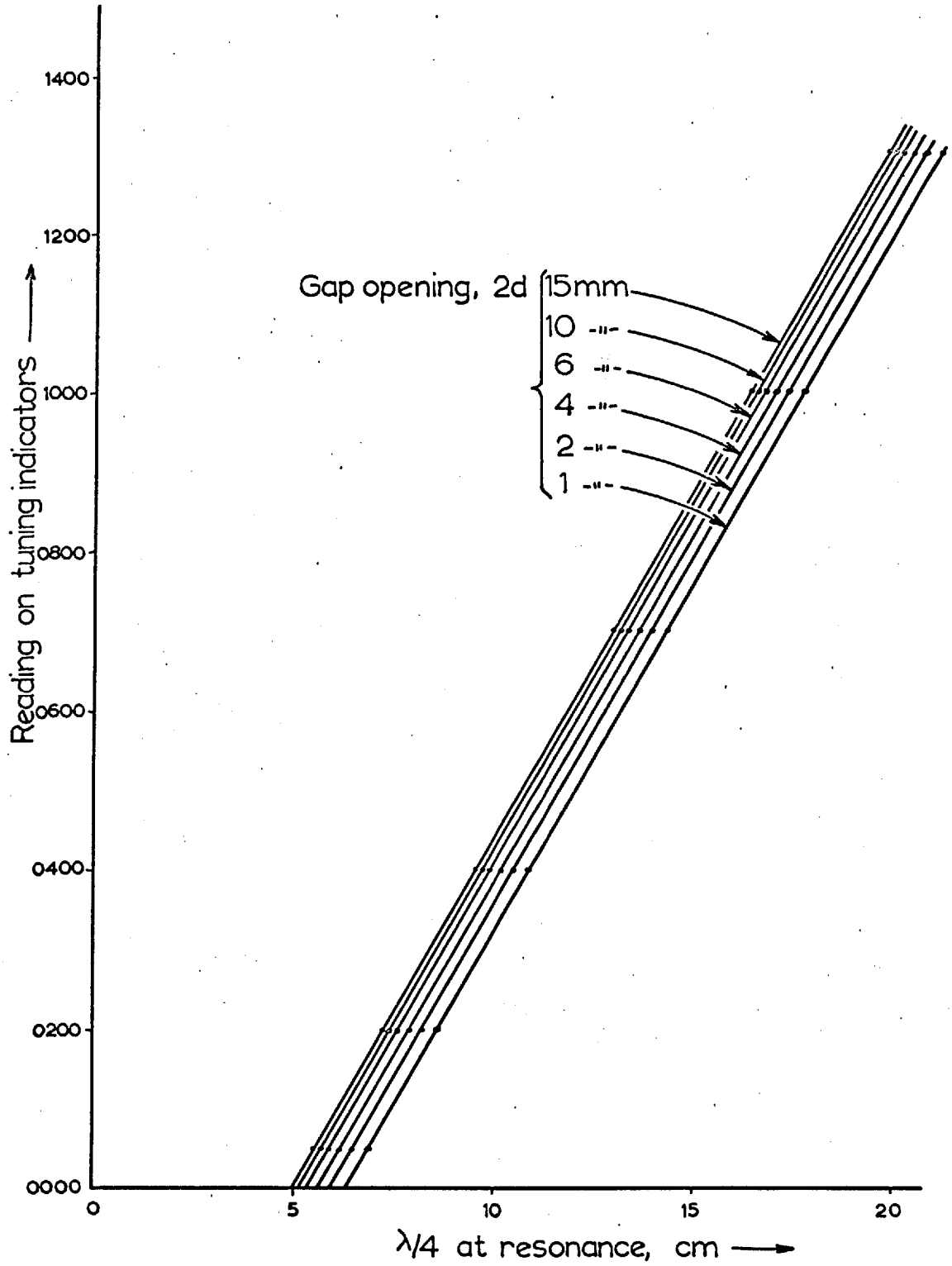


FIG. 8.12 TUNING CONDITIONS OF THE ANTISYMMETRIC MODE.

separation of peaks), 4mm, 6mm, 8mm, and 10mm.

The length of the centre electrodes is defined by the position of the short-circuiting plungers, and the plunger position is indicated by the digital counters. The dependance of the resonant frequency (or rather resonant quarter-wavelength) upon the counter reading is shown in Fig. 8.12 for the out-of-phase mode at various gap settings. (The two plungers were simultaneously adjusted, so that the length of the two half-cavities was always equal.) The resonance of the in-phase mode at almost closed gaps corresponds to the line of 2d = 10mm in the diagram.

The double-tuned cavity can have the following approximate equivalent circuit:

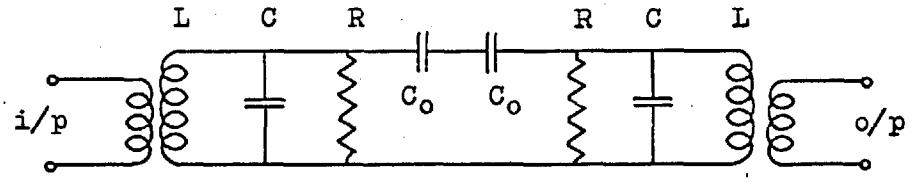


FIG. 8.13 EQUIVALENT CIRCUIT OF DOUBLE-TUNED CAVITY.

When the loading of R is negligible, the above circuit has two resonances:

$$\omega_1^2 = \frac{1}{LC} \qquad \omega_2^2 = \frac{1}{LC\left(1 + \frac{C_o}{C}\right)} \qquad 8.9$$

giving a behaviour consistent with the experimental observations. In contrast to resonant circuits coupled by mutual inductances the frequencies at which the peaks occur in the transmission of capacitance-coupled circuits are not very sensitive to circuit losses.

Another equivalent circuit is shown in Fig. 8.14 overleaf (Schelkunoff, 1944)

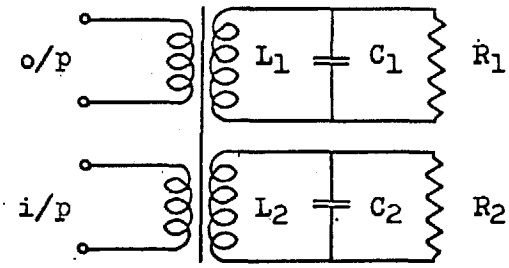


FIG. 8.14 RESONANT MODE REPRESENTATION.

Here the resonant circuit comprising L_1 C_1 and R_1 is defined by the resonant frequency and Q of the in-phase mode, while L_2 C_2 and R_2 are defined by the resonant frequency and Q of the out-of-phase mode, with the usual convention for the definition of the shunt impedance (Moreno, 1958).

The expression for the shunt impedance as defined in Fig. 8.13 is given by Equation 8.3. For both the in-phase and out-of-phase modes the area of the excited surface is proportional to the diameter of the centre electrode, so the optimised diametral ratios are the same as for the single re-entrant cavity, and are given by Fig. 8.9b.

8.5 FIELD PATTERNS IN THE CAVITIES.

Since the amplitude of the excited acoustic wave is proportional to the component of the electric field lying in the preferred direction of excitation of the acoustic mode in question (Equation 4.20), it is important to know both the magnitude and the direction of the electric field vector over the piezoelectric quartz surface. The piezoelectric field-probe technique has been developed to determine this electric field distribution experimentally, without disturbing the fields (Lamb and Richter, 1966c). The gap region of the various cavities was small enough to neglect over

it any phase changes in the electric or magnetic field components.

The schematic arrangement of the probe is shown in Fig. 8.15. A small diameter coaxial probe consisting of a tuned $\lambda/4$ coaxial line with its centre conductor extended by 2mm out of the outer conductor is held over the quartz rod, almost touching its free surface. Tuning is achieved by adjustment of a standard GR stub tuner. Any signal picked up by the probe is coupled to the receiver through a loop built into a GR parallel tee unit. The probe unit is held by a micro-manipulator allowing movement in two perpendicular directions in the horizontal plane. The position of the probe can be read off from vernier scales.

When the acoustic wave travelling from the excited bottom surface is first reflected by the free top surface, an electric field is set up due to the piezoelectric discontinuity. The intensity of the electric field in the air very near to the surface is proportional to the acoustic amplitude, and its direction is in the external preferred direction of the acoustic mode (Equation 4.20). During one single trip diffraction effects do not change noticeably the amplitude distribution of the acoustic waves, so the intensity of the electric field picked up by the probe at the first reflection is not only proportional to the acoustic intensity at that top plane, but also to the component of the electric field intensity taken in the preferred direction at the bottom surface, which excited the acoustic wave. Thus it is possible to map the electric field intensities at the piezoelectric interface inside the cavity without actually inserting any measuring device.

Because of its axial symmetry the coaxial probe is sensitive to electric field components normal to the crystal surface. If the electric field is not uniform over the quartz surface the coaxial

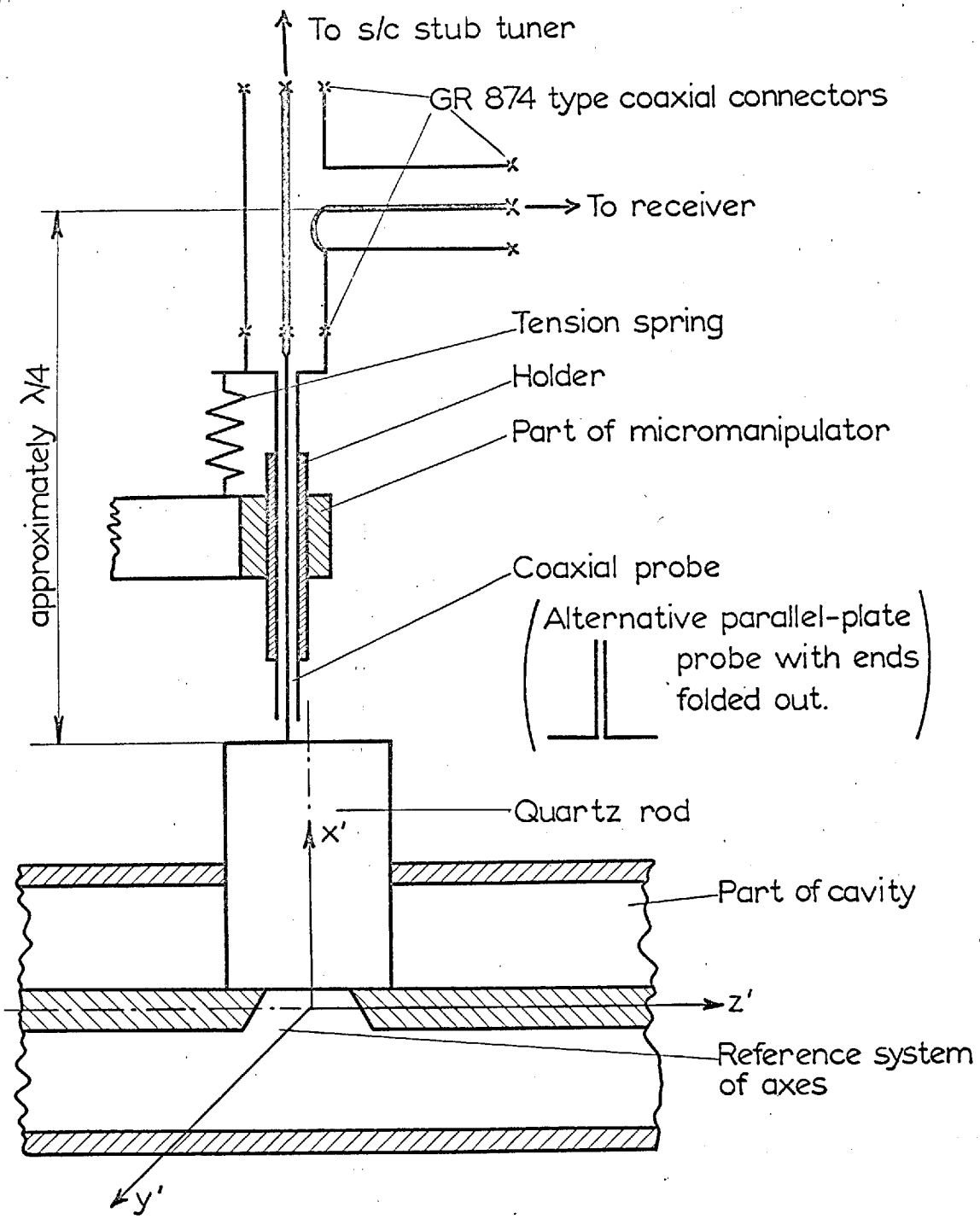


FIG. 8.15 SCHEMATIC ARRANGEMENT FOR PIEZOELECTRIC FIELD PROBING.

probe is also sensitive to the local gradient of the tangential component of the electric field. (The gradient is taken along the tangential component of the preferred direction.)

The parallel-plate probe on the other hand is sensitive to the tangential electric field component taken in the direction normal to the parallel plates, and also to the local gradient of the normal component of the electric field taken again in the direction normal to the parallel plates.

Most of the field mapping measurements were taken with a 5cm long X-cut quartz rod and the coaxial probe. The longitudinal acoustic mode for this orientation (X parallel to x') produces an electric field which is normal to the quartz surface under the probe. So by measuring the amplitude of the picked up signal due to the longitudinal mode over the entire quartz surface the map is obtained of the x' component of the exciting field. (The various acoustic modes are easily distinguished by their different delays.) The shear modes give rise to an electric field at the top surface parallel to the Y crystallographic orientation. Therefore if the Y crystallographic axis and the normal to the plates of the parallel-plate probe are lined up with the y' reference axis, the signal obtained from the probe is proportional to the y' component of the electric field inside the cavity at the quartz surface. Rotation of the quartz rod and the probe by 90° gives the x' component.

The above method to map the transverse fields did not give an acceptable resolution due to the large area covered by the parallel-line probe. There was also some difficulty experienced near the edges. So the smaller coaxial probe was used, which is sensitive to the differential of the acoustic amplitude in this case. Graphical integration of signal amplitude along the preferred direction then gives the acoustic amplitude. Fig. 8.16

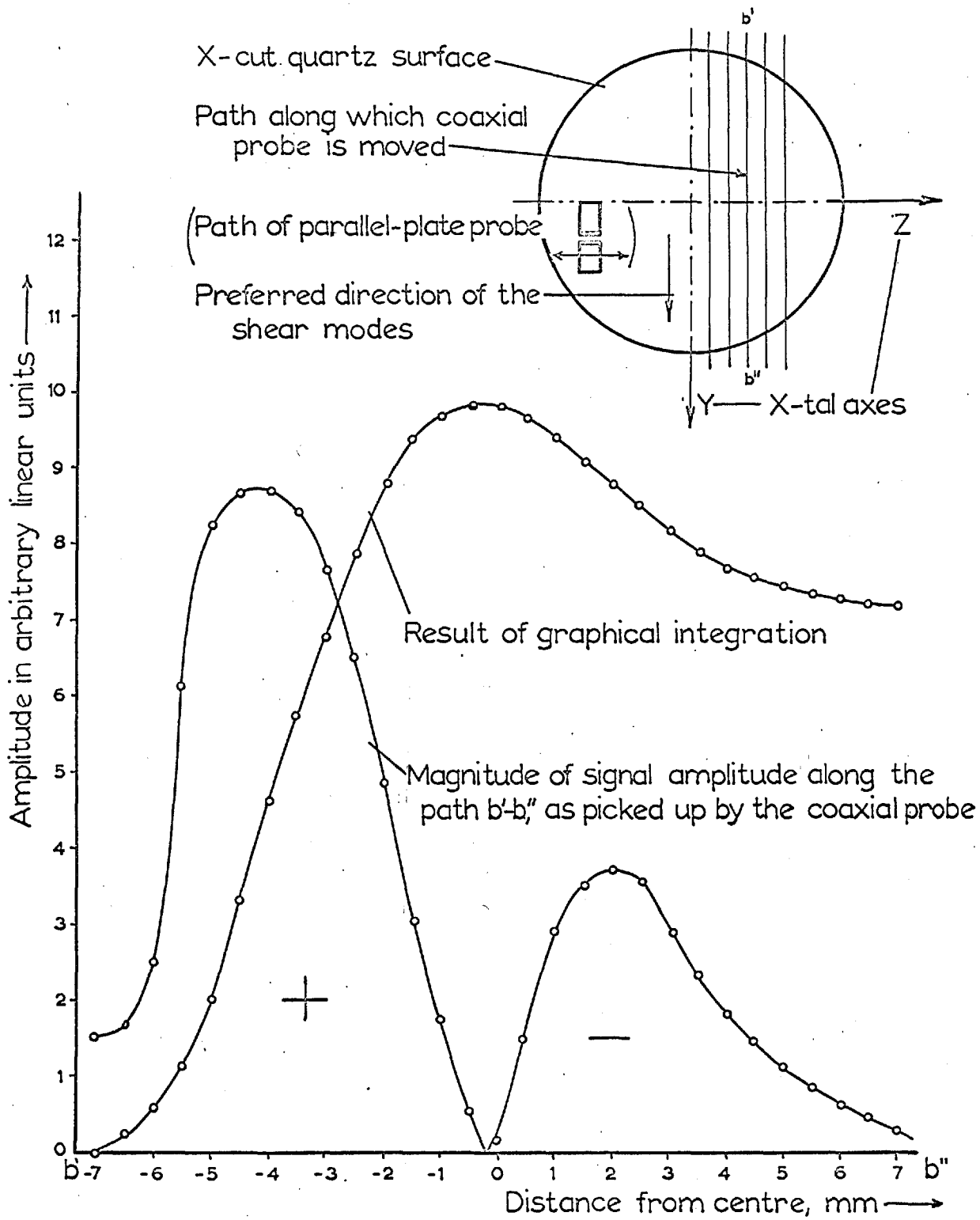


FIG. 8.16 TYPICAL TANGENTIAL FIELD PLOTTING.

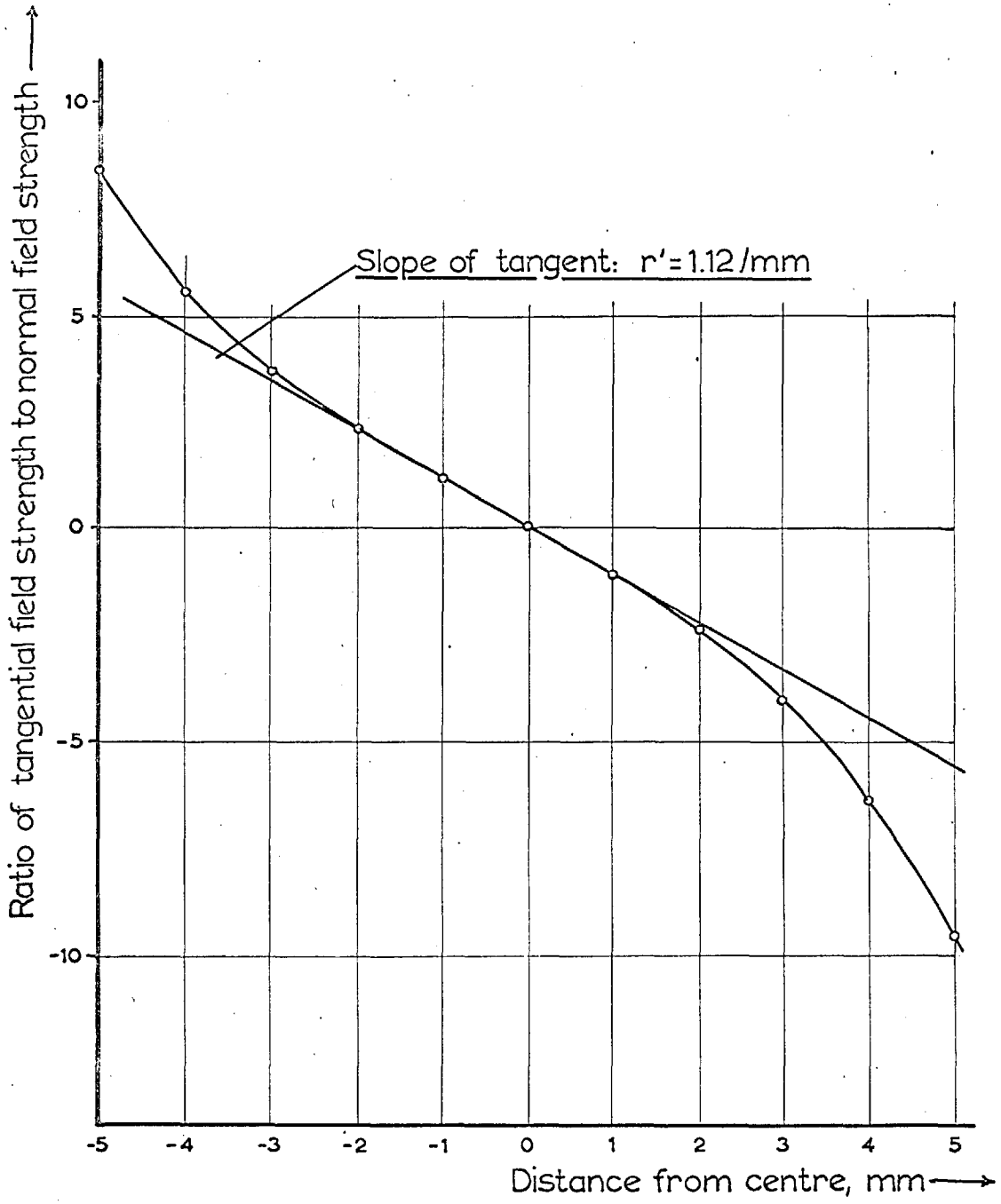


FIG. 8.17 THE RATIO $E_{y'}/E_{x'}$ FOR THE IN-PHASE MODE WITH CLOSED GAP.

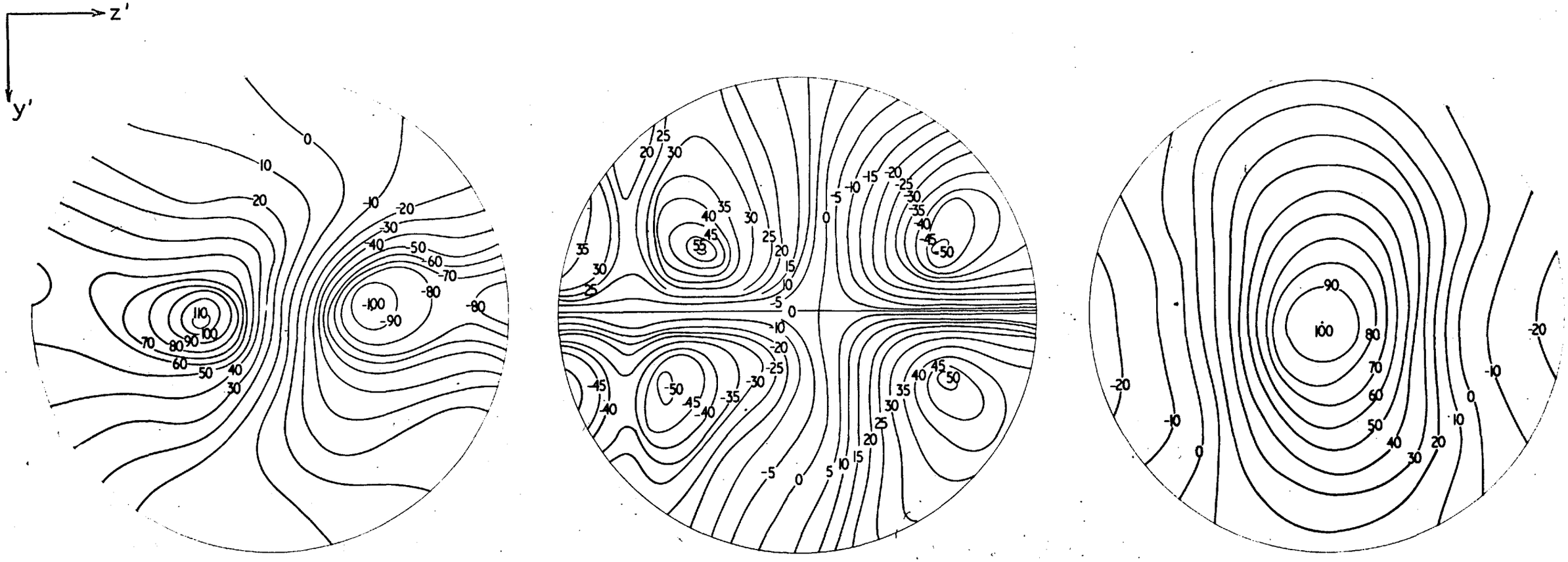
shows the signal obtained by the coaxial probe over the path b'-b", together with the result of the graphical integration.

The comparison method of amplitude measurement (Section 6.1) does not allow one to decide whether there is a change of sign in the amplitude differential as it passes at or near zero. The phases of the signals on the two sides of a minimum were always checked to remove this sign ambiguity. To find the constant of integration the parallel-plate probe was moved along the indicated direction over a path that gave a slow field variation. To find the scale factor between the plots obtained by the parallel-plate probe and by graphical integration, a plot was obtained with the parallel-line probe moved along the Y direction. To find the scale factor between the normal and the transverse field plots the following procedure was used. A plot along a selected line of the normal and transverse y' fields was obtained, as described above, in the double-tuned cavity with the gap closed. The ratio $r' = E_y/E_x$ was plotted against distance y from the centre line, as shown in Fig. 8.17. The centre electrode touched the dielectric surface of the quartz below the centre line. Since the electric field is normal to the metal electrode of circular cross-section, the field direction in air near the centre line at the quartz bottom surface is therefore fixed. The continuity of the tangential component of the electric field and the normal component of the flux density gives then

$$r = \frac{E_y}{E_x} = \epsilon_r \frac{y}{a} \qquad 8.10$$

where ϵ_r is the relative dielectric constant of quartz and a is the diameter of the centre electrode. Comparing the known value of

$$\frac{dr}{dy} = \frac{\epsilon_r}{a} \qquad 8.11$$



a) FIELD DIRECTION: x' (NORMAL)

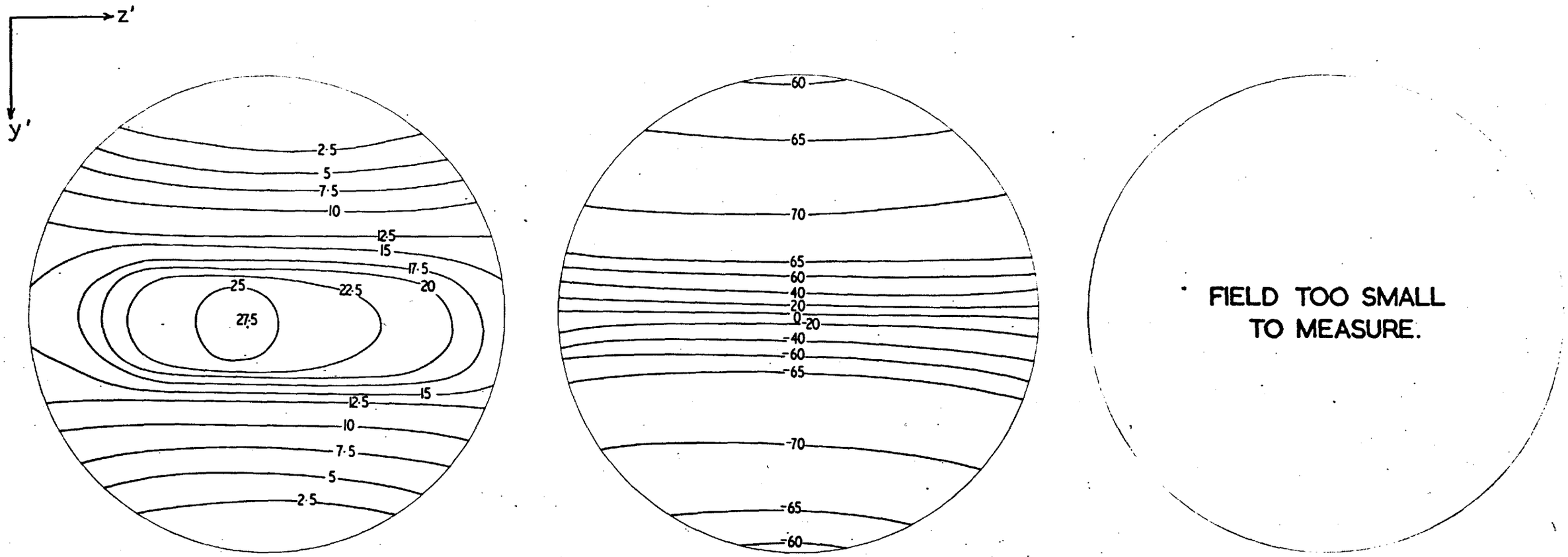
b) FIELD DIRECTION: y' (TANGENTIAL)

c) FIELD DIRECTION: z' (TANGENTIAL)

MEASURED AMPLITUDE DISTRIBUTION OF THE THREE COMPONENTS OF THE EXCITING ELECTRIC FIELD VECTOR OVER THE QUARTZ SURFACE.

I. DOUBLE-TUNED CAVITY, ANTISYMMETRIC MODE.

FIG. 8.18



a) FIELD DIRECTION: x' (NORMAL)

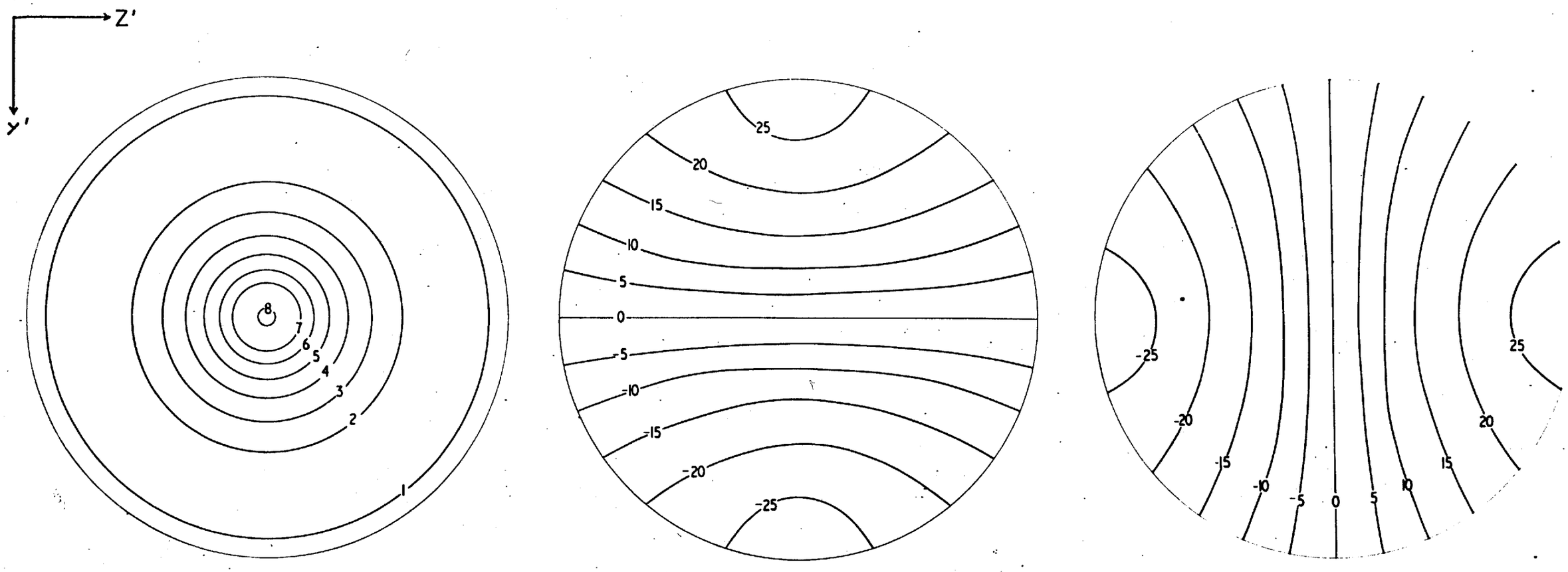
b) FIELD DIRECTION: y' (TANGENTIAL)

c) FIELD DIRECTION: z' (TANGENTIAL)

MEASURED AMPLITUDE DISTRIBUTION OF THE THREE COMPONENTS OF THE EXCITING ELECTRIC FIELD VECTOR OVER THE QUARTZ SURFACE.

II. DOUBLE-TUNED CAVITY, SYMMETRIC MODE.

FIG. 8.19



a) FIELD DIRECTION: x' (NORMAL)

b) FIELD DIRECTION: y' (TANGENTIAL)

c) FIELD DIRECTION: z' (TANGENTIAL)

MEASURED AMPLITUDE DISTRIBUTION OF THE THREE COMPONENTS OF THE EXCITING ELECTRIC FIELD VECTOR OVER THE QUARTZ SURFACE.

III. AXIALLY SYMMETRIC CAVITY.

FIG. 8.20

near the centre line with the slope $\frac{dr'}{dy}$ of the r' graph gives the desired scale factor between the normal and transverse fields.

The field maps of the two possible tuning modes of the double-tuned cavity are shown in Fig. 8.18 and Fig. 8.19. Similar maps for the axial cavity of Fig. 8.9 with a rounded small centre post are shown in Fig. 8.20. The circles represent the 15mm diameter quartz surface. The field samples were measured at 0.5mm intervals in both directions over each circle.

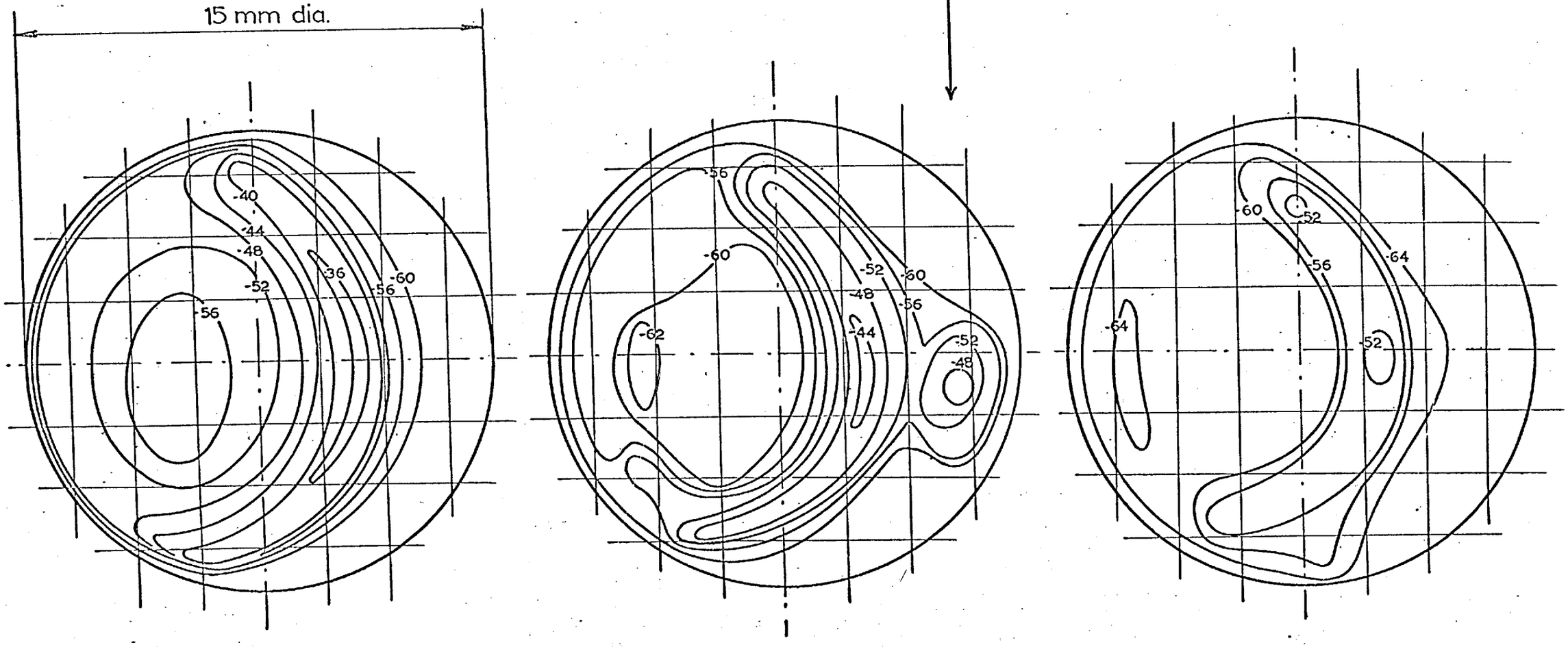
8.6 ACOUSTIC PERFORMANCE.

The best conversion efficiency was of the order of -30dB one way, achieved in the double-tuned cavity with a BC-cut quartz rod. The conversion efficiency only slightly depended on frequency, as predicted by Equation 4.46.

It was found that for a good exponential decay pattern of the received echoes the distribution of amplitude across the acoustic beam should approximate to a Gaussian or a $(\text{cosine})^2$ shape.

Fig. 8.21 shows the signal received by the coaxial probe (in dB's) at the outside surface of an AT-cut quartz rod , due to the SS mode of the acoustic wave excited in an axial cavity with flat centre post, similar to the one shown in Fig. 8.2. For this mode and orientation the direction of energy propagation makes an angle of about 5° with the rod axis. The mapping of the first received pulse clearly shows that the excitation was confined to a very narrow annulus near the circumference of the quartz rod. The pattern is shifted to the left because of the oblique energy propagation, and almost half of the power is lost by scattering from the cylindrical surface. The amplitude distribution is changed considerably by diffraction when the wave travelled 15

CRYSTALLOGRAPHIC DIRECTIONS:
AT - normal to surface
X - lying in the surface.



1st received pulse (5 cm path)

2nd pulse (15 cm)

3rd pulse (25 cm)

FIG. 8.21 SIGNAL (IN dB'S) PICKED UP BY THE COAXIAL PROBE OVER THE SURFACE OF AN AT QUARTZ ROD PROPAGATING THE SS MODE. EXCITATION IN AXIAL-FIELD CAVITY WITH FLAT CENTRE POST. f = 400Mc/s.

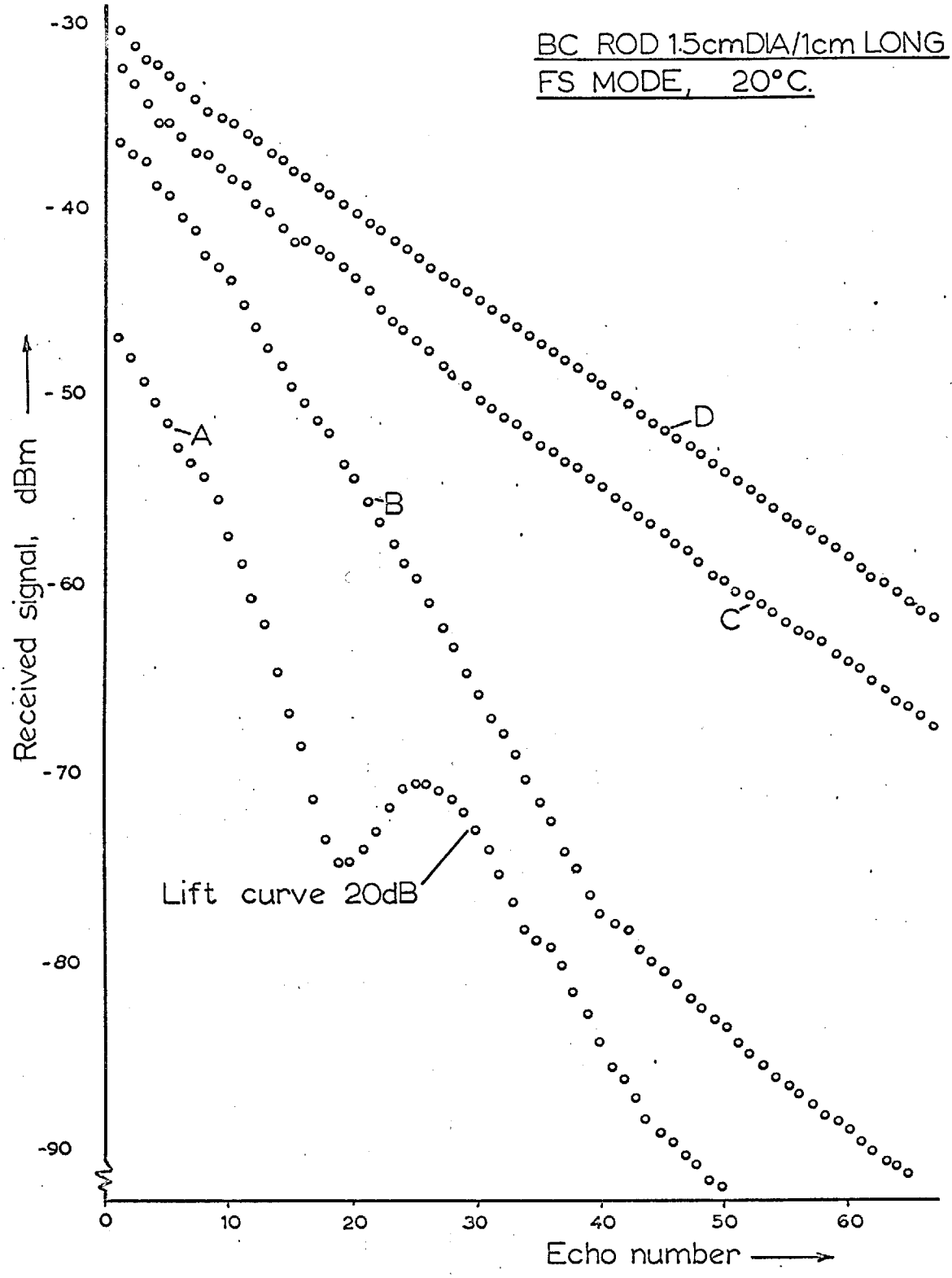
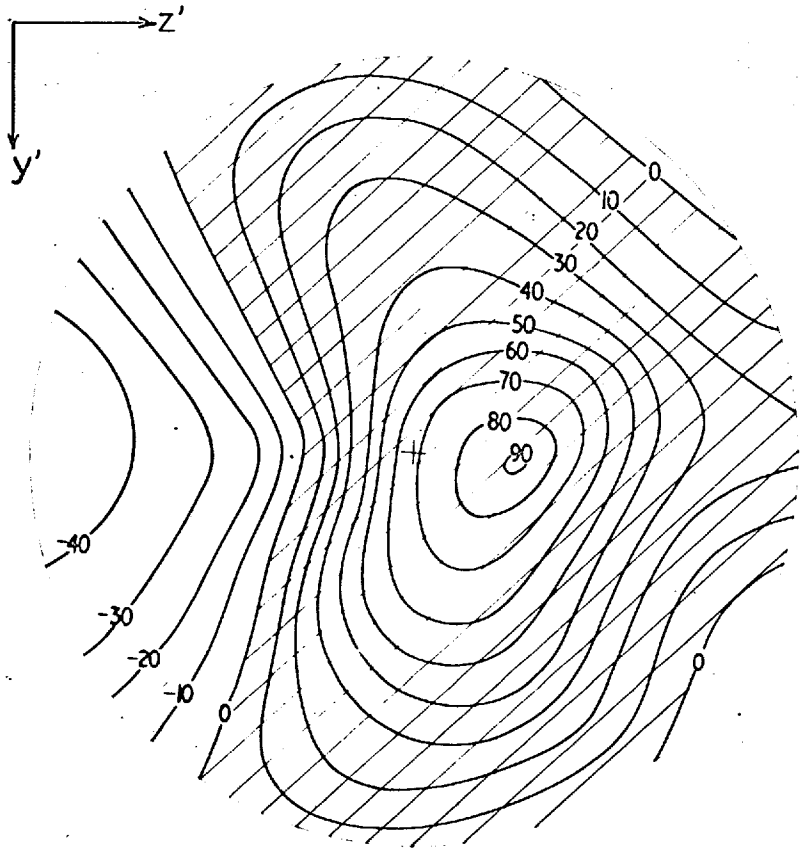


FIG. 8.22 ECHO PATTERNS OBTAINED BY THE SAME QUARTZ SPECIMEN IN VARIOUS EXCITING CAVITIES AT 375Mc/s.

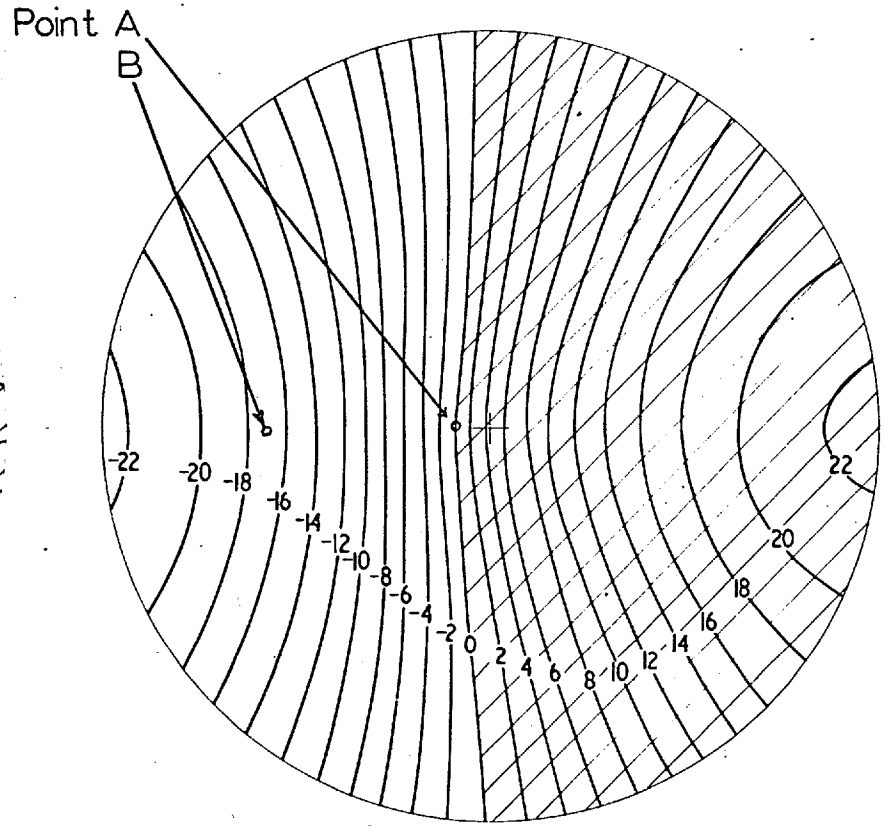
and 25cm.

Echo patterns obtained for the FS mode in a BC-cut rod 1cm in length at 375Mc/s and 20°C are shown in Fig. 8.22 (Lamb and Richter, 1966a). The echo train A was obtained using the cavity of Fig. 8.3 with the quartz rod placed with one end against the flat end of the centre electrode, as the AT crystal of the previous paragraph. The electric field in this arrangement is everywhere normal to the quartz surface. The excitation is concentrated near the circumference of the rod, as verified by Fig. 8.21. The non-exponential decay is due to diffraction effects always present with a wavefront of complicated amplitude distribution, and also to the unavoidable non-parallelism near the edge of the end faces, where reflection principally occurs. Some results could be obtained with this excitation arrangement when the direction of energy propagation deviates from the rod axis, moving the hollow acoustic beam away from the side walls.

The echo train B was obtained with the centre electrode of the previous cavity shaped into a long truncated cone with a diameter at the quartz surface equal to one fifth that of the quartz rod and rounded edges. This caused the acoustic beam to propagate more in the centre of the rod, but it was found that the normal electric field strength was much smaller than the tangential field strength. Moreover, the tangential field is in opposite directions at opposite ends of a diameter in the surface. The amplitude distribution of the exciting electric field with this electrode arrangement is shown in Fig. 8.20. For the FS mode along the BC orientation the preferred direction makes an angle of 30° with the crystal surface inside the quartz. The resultant amplitude distribution from both normal and tangential excitation is shown in Fig. 8.23b. There are two almost equal areas of the crystal surface, where the vibrations excited differ in phase by 180°.



PLOT a)



PLOT b)

AMPLITUDE OF ACOUSTIC WAVES OVER THE CROSS-SECTION OF A BC-CUT QUARTZ ROD (FS MODE)

a) EXCITED BY THE ANTISYMMETRIC MODE OF THE DOUBLE-TUNED CAVITY.

b) EXCITED IN AXIALLY SYMMETRIC CAVITY WITH SMALL RADIUS CENTRE POST.

(Contribution of shaded area to re-excited signal: a) 94.4%, b) 57.3%.)

FIG. 8.23

As the two areas interact through diffraction, there is an apparent attenuation in the received signal. The change in pulse height against echo number over a point of zero excitation near the centre of the surface at point A is shown in Fig. 8.24, as picked up by the coaxial probe. The signal picked up at point B is also shown for comparison. At about the 12th echo the amplitude seems to be settled. For further echoes the net received signal in the cavity is the difference of two much larger quantities, hence the smallest upsetting of the equilibrium of the rod (thermal differences, stressing) causes large changes in the echo pattern.

Echo train C was obtained when the same quartz rod was placed centrally over the gap region of the double-tuned cavity, with the X crystallographic axis arranged normal to the cavity axis. The amplitude distribution in this case is nearly ideal as is shown in Fig. 8.23a. The deviation from a true exponential decay rate (straight line on dB plot) is attributed to slight non-parallelism of the centre region of the two end faces of the quartz rod. However, the crystal holder allowed any selected portion of the quartz surface to be placed over the gap region. Since the polished end faces are always slightly convex (seen for example in Fig. 7.2), it is possible in this way to so position the quartz rod laterally in the cavity with respect to the gap, that the highest intensity centre part of the acoustic beam is reflected between a pair of surfaces which are parallel despite the overall non-parallelism of the whole surface. The crystal holder of the double-tuned cavity allows the above positioning without rotating the crystallographic axes (c.f. Section 8.3). For the rod in question optical-interferometer measurements showed that the ends were not parallel to better than 5".

Echo train D represents the best exponential decay pattern that was observed in this particular rod by suitably adjusting the

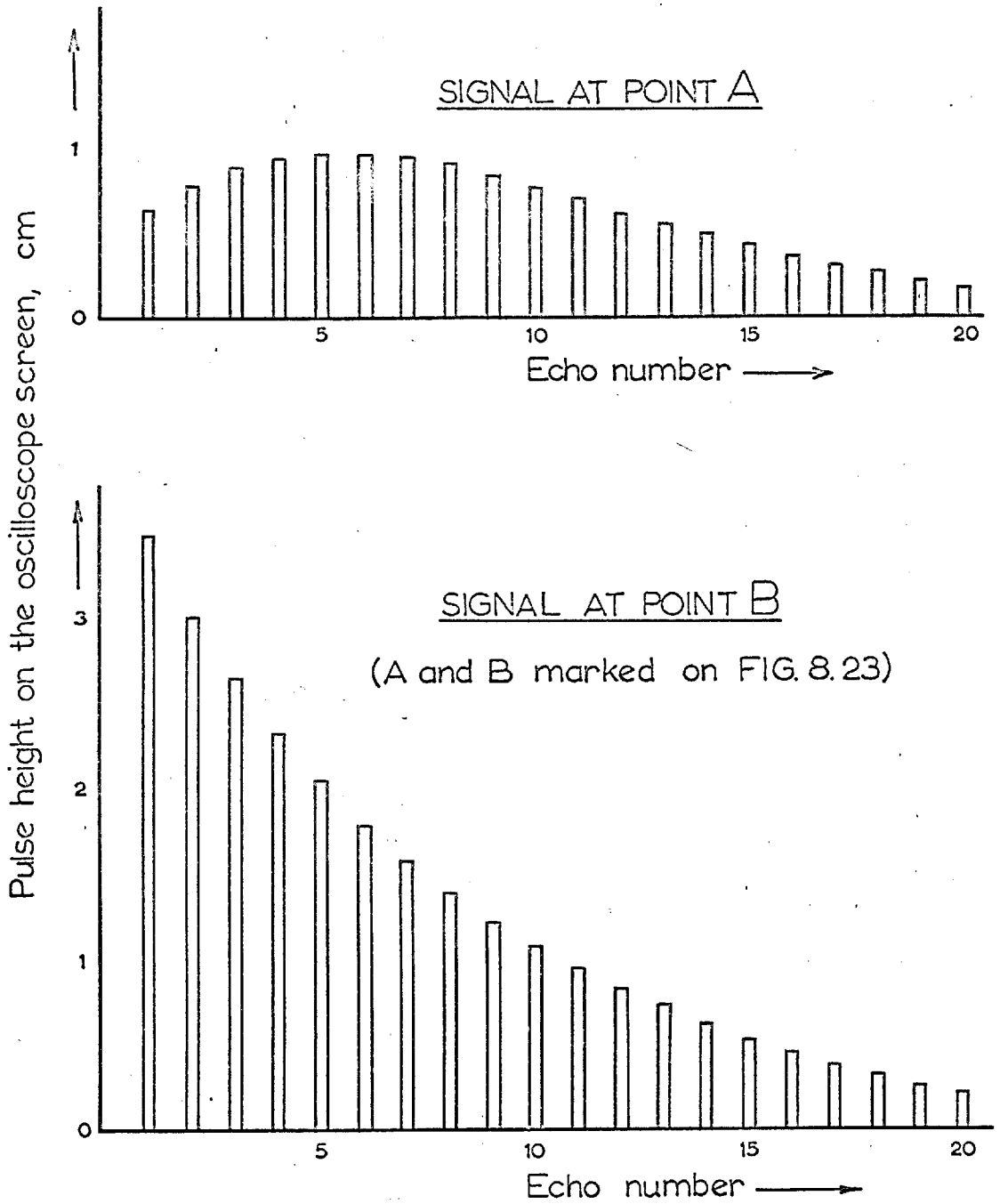


FIG. 8.24 THE ECHO SIGNALS AS PICKED UP BY THE COAXIAL PROBE AT TWO DIFFERENT POINTS OF THE QUARTZ SURFACE. (COPY FROM PHOTOGRAPHS.)

lateral position of the end surface of the rod with respect to the gap. For repeatable and reliable attenuation and viscoelastic measurements an echo train as good as this has to be used.

The double-tuned cavity is always capable of producing an acoustic field intensity distribution approaching a $(\text{cosine})^2$ shape. When the internal preferred direction of the mode to be excited is in the range $0 - 60^{\circ}$ from the plane of the surface, the out-of-phase mode gives the best result, with amplitude distribution similar to 8.18c. When the preferred direction is nearer to the surface normal, the in-phase mode gives the best excitation with an amplitude distribution similar to 8.19a.

Although the axial cavity is suitable to excite a mode with preferred direction normal to the surface, there is the additional advantage when the double-tuned cavity is used for normal excitation that the unwanted modes can often be eliminated by lining up their preferred directions with the z' direction of the cavity. This is not possible with the Bömmel-Dransfeld type of axial cavity excitation, where, for example, the unwanted shear-wave excitation is of the same order of amplitude as the longitudinal mode for an X-cut quartz rod.

CHAPTER 9.
TEMPERATURE CONTROL.

9.1 GENERAL.

The liquid measurements are critically dependent on temperature. For this reason all measurements were made with the transducer cavities in thermostatted baths. Great care was taken to determine the exact temperature of the sample liquids in order to realise the necessary accuracy of the measurements.

Certified thermometers were used in the 10-50°C range. Lower temperatures were measured by a number of carefully prepared Copper-Constantan thermocouples and a National Bureau of Standards calibration table, checked against fixed reference temperatures.

Two thermostat baths were constructed. One was to work above room temperature up to 50°C and the other at subzero temperatures down to -155°C. In addition to these two thermostats a LEC model LTV26 refrigerator unit was also available whose alcohol-filled tank is temperature controlled between 10 and -60°C.

9.2 HIGH TEMPERATURE THERMOSTAT.

The schematic diagram of this thermostat bath is shown in Fig. 9.1. The temperature of the hot water in the heat exchanger was set only a few degrees above the required bath temperature, and the jet of warm water entering the bath was directed straight at the mercury bulb of the contact thermometer. The flow control valve and speed of the pump and motor unit were set such that the on-off ratio was nearly 1:1.

With the above precautions the maximum temperature variation

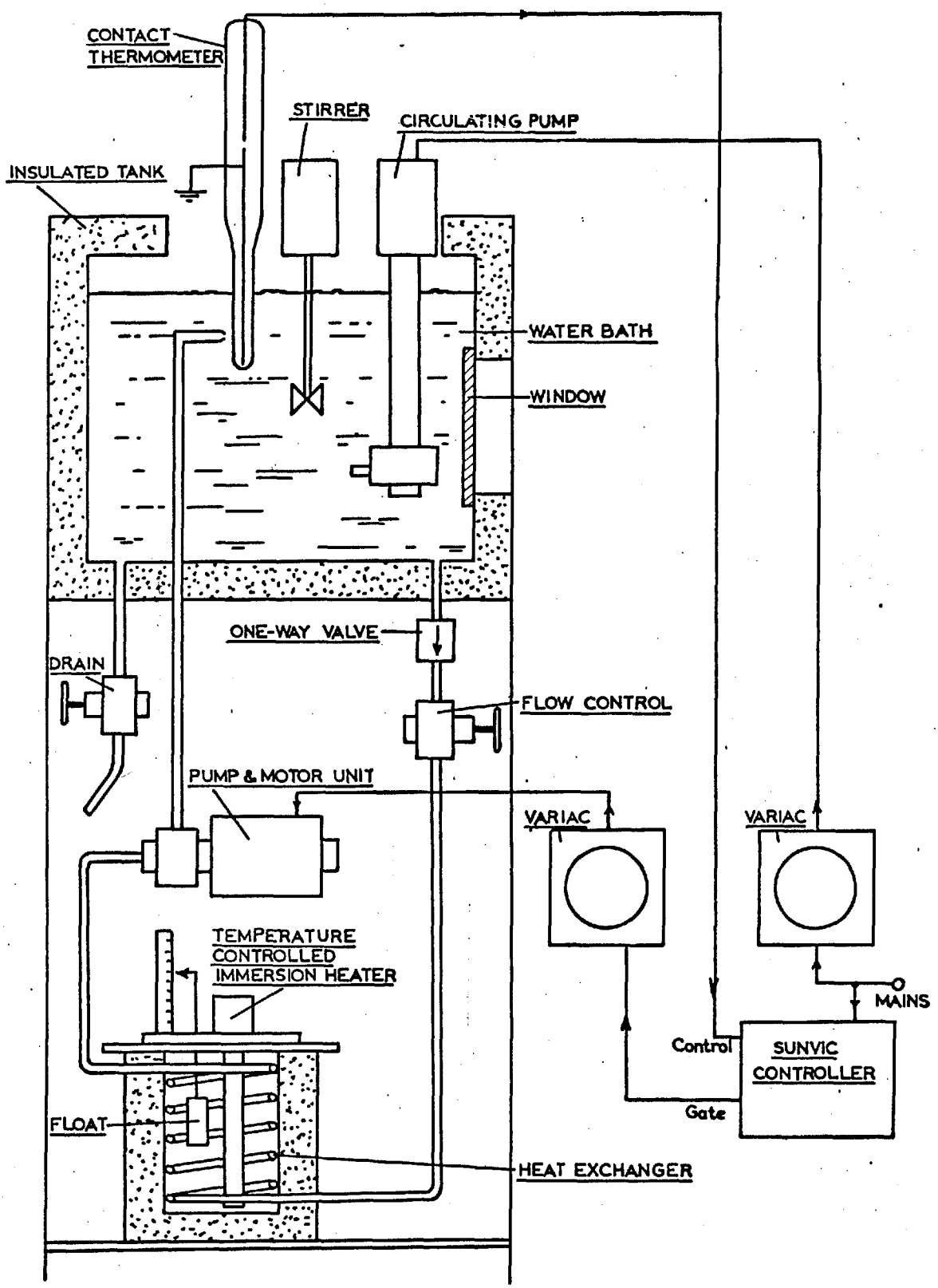


FIG. 9.1 HIGH TEMPERATURE THERMOSTATTING UNIT

of the thermostat due to the on-off cycling was 10°mC. as measured on a Beckman thermometer. Long term stability is better than 0.05^{o}C.

9.3 LOW TEMPERATURE THERMOSTAT.

This thermostat consists of a 9" diameter Dewar vessel containing iso-pentane. Iso-pentane was chosen as the thermostatting fluid because it has the lowest freezing point (-160.5^{o}C) of all substances that are liquids at room temperature. It boils at 27°C. The schematic diagram is shown in Fig. 9.2, while a photograph of it can be seen on the left of Fig. 6.3.

Two tubes wound in the shape of helical coils are placed inside the thermostatting Dewar, and liquid nitrogen is pumped through them to the bottom of the vessel. The tube having the smaller bore is used down to -100°C bath temperature, while the larger bore tube is used below this. The tubes are adequately long for the liquid nitrogen to evaporate inside them. The cold nitrogen gas ejected at the bottom end of the tube violently bubbles through the bath producing an efficient stirring action.

Liquid nitrogen is obtained from a Leybold 10 ℓt storage Dewar through a syphon. The syphon is made of double-walled tubing, the space between the walls being evacuated for the sake of thermal insulation. An airtight lid is held down by springs over the opening of the Dewar. Due to evaporation of the liquid nitrogen pressure is developed inside the storage Dewar driving liquid nitrogen through the syphon. To increase evaporation a heater coil is immersed in the liquid. The pressure is monitored by a 6 feet high water manometer and can be released by opening the electromagnet operated valve.

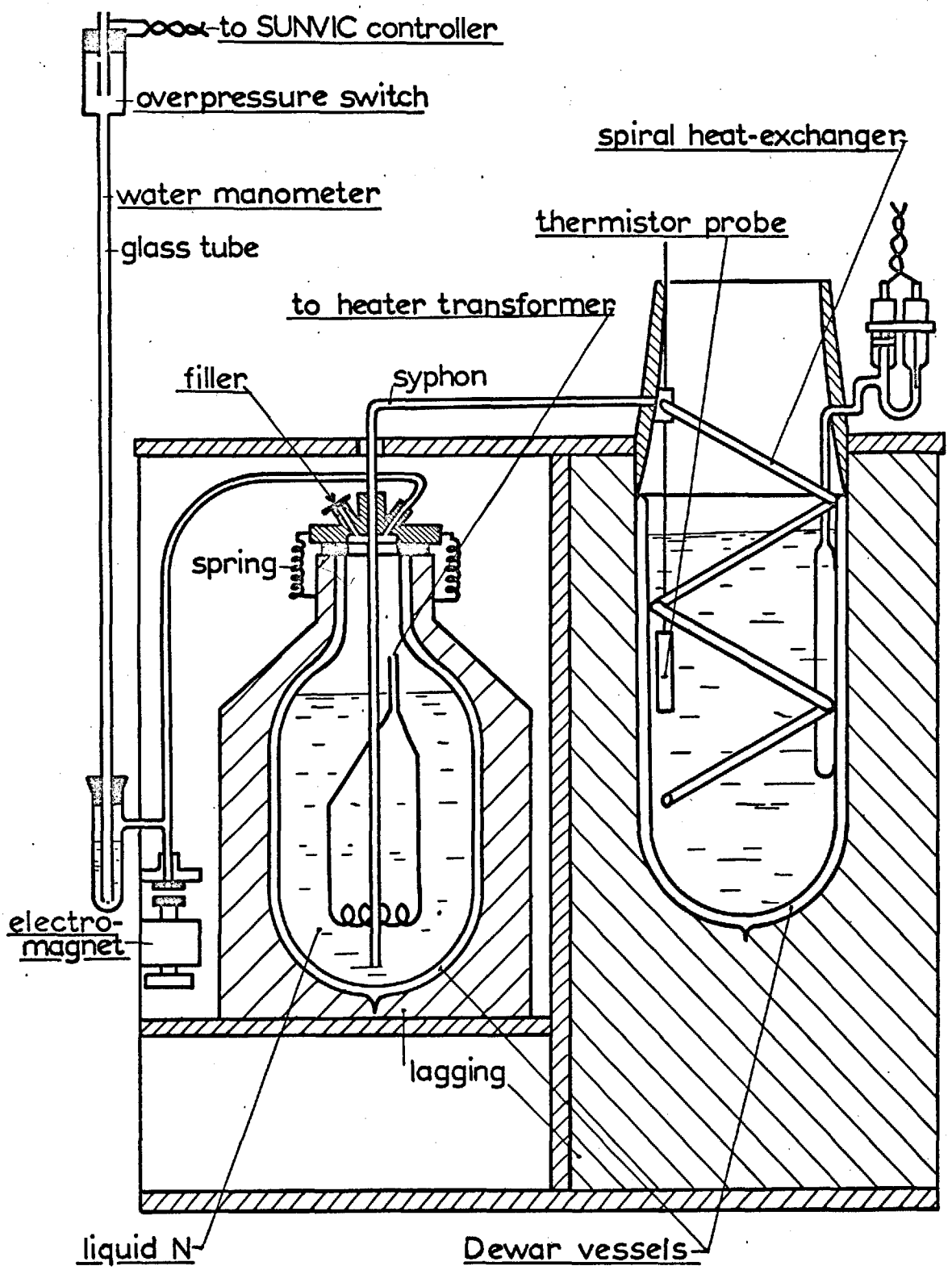


FIG. 9.2 LOW TEMPERATURE THERMOSTAT BATH.

The block diagram of the temperature control is given in Fig. 9.3. The temperature of the thermostatting liquid is sensed by a thermistor probe containing 6 glass-bead thermistors (STC F22) all parallel connected to reduce their total resistance. The probe forms part of the thermistor bridge set to balance at the required temperature. The bridge (Fig. 9.4) is based upon a circuit by Tempest (1963). All bridge and amplifier elements are contained in a temperature-controlled oven.

When the resistance of the probe thermistors decreases due to an increase in their temperature the bridge output turns on the gate of a Sunvic controller and thereby actuates the electromagnet to close the valve and pressurise the storage Dewar. The resulting flow of cold nitrogen reduces the bath temperature and by changing the unbalance of the bridge to the opposite sense causes the valve to release the driving pressure. Then the bath temperature starts to rise again and the cycle is completed. The number of times the valve is actuated is counted by a Post Office type digital counter for checking purposes.

At the same time when the valve is closed the heater is turned on inside the storage vessel, the heat output being variable up to 30W by a Variac. (The ambient heating is equivalent to about 10W). Since the stirring in the thermostat is effected only by bubbling it is important to set the off times as short as possible. By adjusting the Variac 10sec/10sec on/off times can be achieved.

Below $-120^{\circ}C$ the resistance of the thermistors becomes too high to be able to set the bridge to balance. Then a mercury-in-glass controller filled with iso-pentane can be used to operate the bridge.

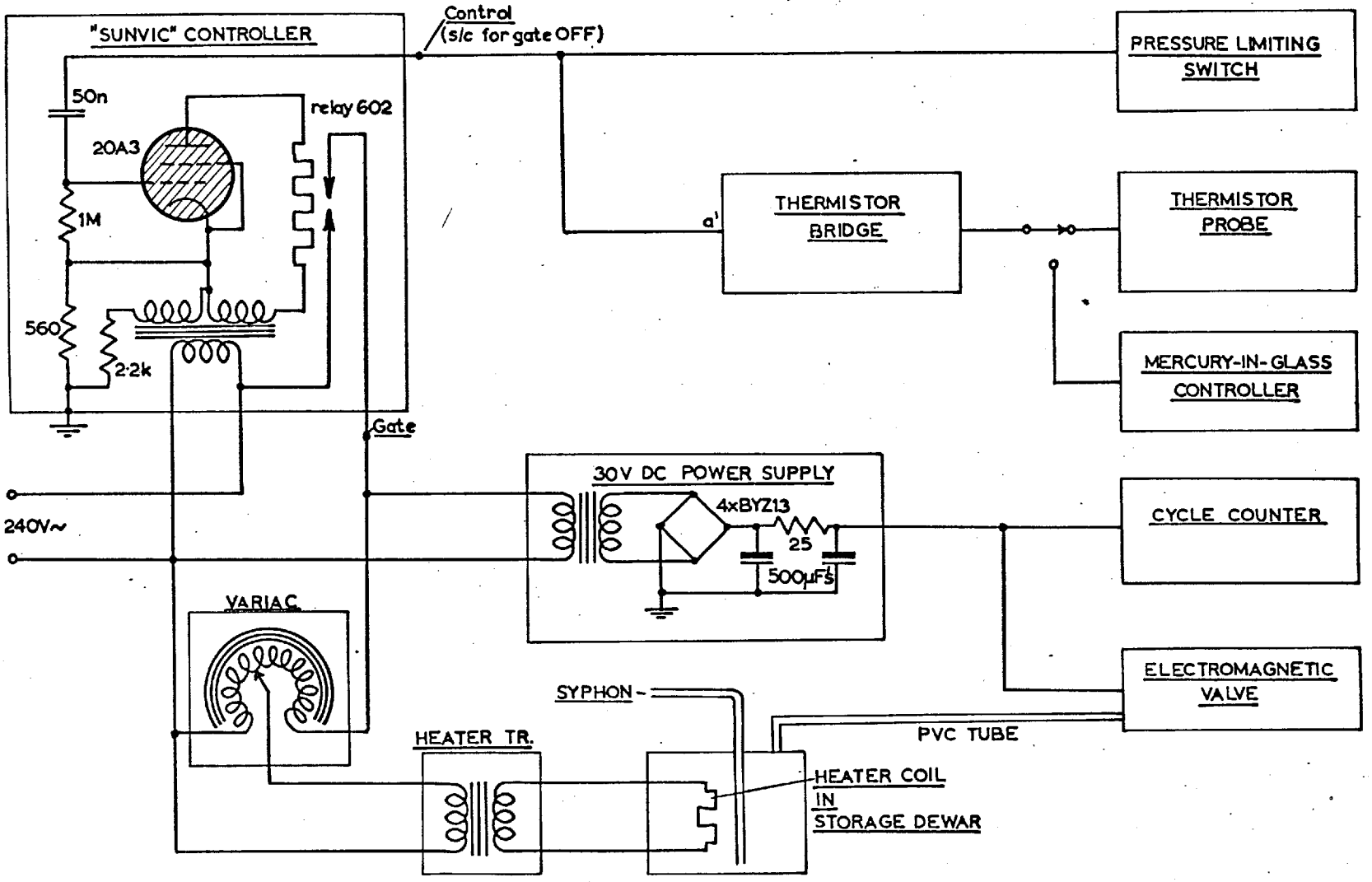


FIG. 9.3 LOW TEMPERATURE CONTROL

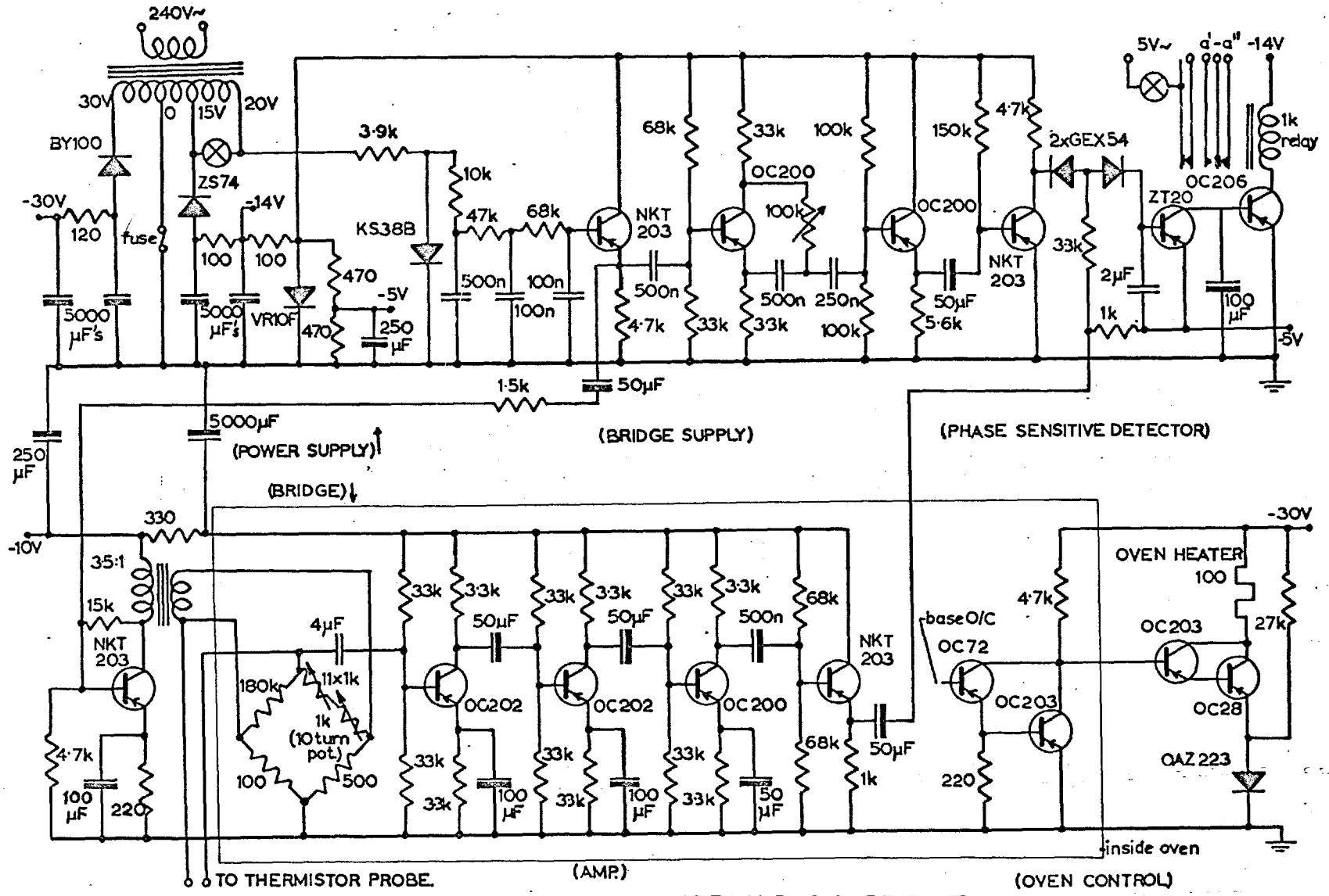


FIG. 9.4 THERMISTOR BRIDGE.

Down to a thermostatting temperature of -110°C the cyclic variation in the bath temperature as measured by a thermocouple encapsulated in a light brass cover was less than + or - 0.1°C. The temperature variation in the centre of the double-tuned cavity of large heat capacity is much less than this. (With the mercury-in-glass regulator the temperature cycling was slightly worse.) The actual temperature is measured by a thermocouple embedded in the metal wall of the cavity near the sample liquid.

Lowering the temperature of the bath containing the cavity was very quick, less than 1min./°C. During the long periods of continuous pumping of the initial coolings the pressure in the storage Dewar tended to build up to a value higher than could have been safely allowed. For this reason an overpressure switch was placed on top of the water manometer. If the water rose inside the space between the two concentric metal tubes of the switch it reduced the insulation between them sufficiently to operate the Sunvic controller and to release the pressure.

P A R T I V .

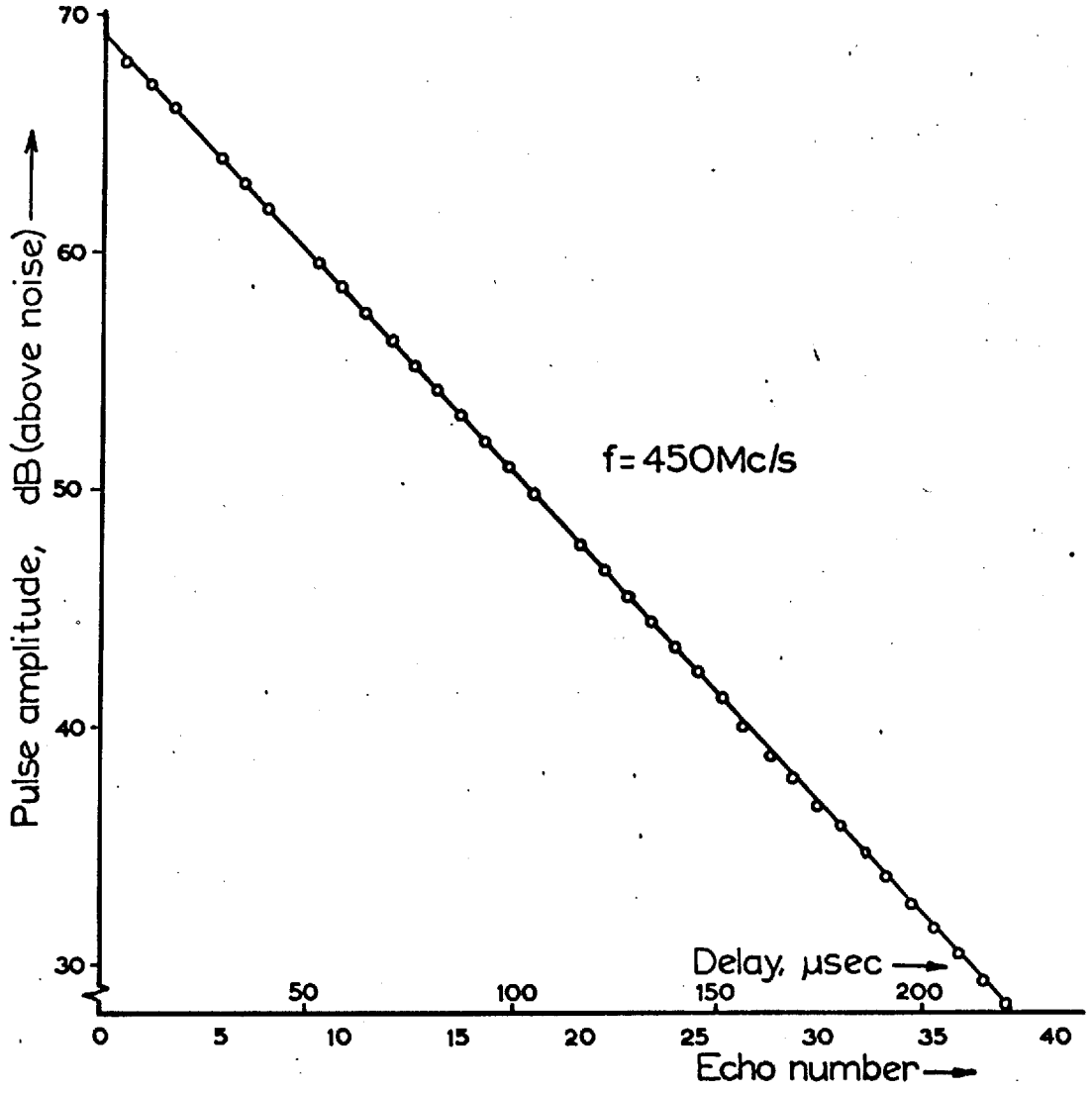
VISCOELASTIC MEASUREMENT TECHNIQUE AND RESULTS.

CHAPTER 10.
MEASUREMENT AND CALCULATION OF ANISOTROPIC ACOUSTIC ATTENUATION IN QUARTZ.

10.1 MEASUREMENTS OF ATTENUATION.

A study has been made of the attenuation of elastic waves for different directions of propagation in quartz, originally for the purpose of enabling directions with low attenuation to be selected in connection with the development of the experimental technique. The theoretical derivations prompted by these measurements are believed to have general application to the calculation of attenuation for acoustic waves in crystalline solids. The attenuation is assumed to be the result of viscoelastic behaviour. The measurements and calculations of this chapter will appear in a paper accepted for publication. (Lamb and Richter, 1966b).

The first attempts to measure the attenuation of acoustic waves were made using the Bömmel-Dransfeld type (Bömmel and Dransfeld, 1960) cavity resonator with axial symmetry, shown in Fig. 8.2. It was seldom found possible with this arrangement to obtain a decay pattern of some 30 or more echoes which was exponential within the required tolerance. Consequently, the novel method of excitation by the double-tuned cavity system of Chapter 8 was devised. This system enabled an excellent exponential decay pattern to be observed for reasons put forward in Section 8.6. A typical plot of echo height in dB versus reflected pulse number is shown in Fig. 10.1a using the FS mode in a BC-cut rod. 35 echo pulses are recorded in this diagram, all well above the noise level. The value of attenuation in dB/cm is calculated from the slope of the best fitting straight line through the points. The 4th, 8th and 19th pulses are omitted since these are approximately



a) TYPICAL ECHO PATTERN (FS MODE IN BC QUARTZ, 30°C)



b) DEVIATION OF RECORDED POINTS FROM STRAIGHT LINE.

FIG. 10.1

coincident with pulses of the very weakly excited SS mode. The deviation of the recorded amplitudes from the true exponential decay rate as a function of echo number is shown in Fig. 10.1b, where rms deviation is 0.050dB.

The acoustic attenuation was measured in most of the specimens listed in Table 7.1. The end surfaces of the quartz rods employed were polished flat to within one-tenth wavelength of visible light and parallel to better than 6 seconds of arc. The orientation of the axis of the rod to the specified crystallographic direction was guaranteed better than 0.5°. For measurement purposes, a particular crystal cut is selected and, in general, it is possible to excite in this some, or all, of the three acoustic modes L, FS or SS. Each mode, however, will have a preferred spatial direction of the electric field vector with respect to the plane of the end surface inside the dielectric for maximum excitation. In Chapter 4 it has been shown that the excitation will be proportional to the component of the electric field in the preferred direction.

In the double-tuned cavity the directions of the exciting electric field vector can be chosen either a) mainly tangential or b) mainly normal to the end surface of the quartz rod. One of these modes is, therefore, selected and the appropriate cavity tuning arrangements are taken for the frequency in question. The preferred angle θ of the E vector for maximum excitation can be read off from the contour maps of Figs. 5.9 - 5.11, and is summarised in Table 10.1 for six well known types of crystal cut. The velocity of propagation (v) of each mode is also listed, these values being calculated from values for the elastic constants of quartz given by Koga et al. (1958) with which later values of McSkimin (1962) are sensibly in agreement. The angle ϕ between the axis of the rod and the direction of energy propagation is also tabulated in Table 10.1

TABLE 10.1

Summary of the acoustic and piezoelectric properties of the various quartz specimens investigated

Crystal Cut	Mode	v (mm/μsec)	ϕ°	θ°	Selected Cavity Mode	α dB/cm
BC	L	6.31	6	0	a	-
	FS	5.11	0	31.5	a	0.340
	SS	3.76	12	0	a	0.780
AC	L	6.93	7	0	a	0.522
	FS	3.75	4	0	a	0.670
	SS	3.30	0	58.5	a	1.27
X	L	5.75	0	90	b	0.940
	FS	5.11	0	0	a	0.345
	SS	3.30	0	0	a	1.29
Z	L	6.33	0	Zero coupling		-
	S (degenerate)	4.68	17.5	0	a	-
Y	L	6.01	24.5	0	a	-
	FS	4.32	27	0	a	-
	SS	3.92	24.5	90	b	0.658
AT	L	7.02	4	0	a	0.502
	FS	3.79	9	0	a	0.618
	SS	3.32	4	54.5	a	1.23

The attenuation was measured over the frequency range 300-3000Mc/s. The 3000Mc/s measurements were made with the cavity resonant in the three-quarter wavelength mode and using waveguide equipment constructed by H. Seguin (Lamb and Seguin, 1966). For all the modes it was found that the measured attenuation is accurately proportional to the square of the frequency at the temperature of 30°C.

Attenuation results for the L, FS and SS modes in X-cut quartz are shown in Fig. 10.2, and similar results are given in Figs. 10.3 and 10.4 for AC quartz and BC quartz, respectively. (The figures in parentheses at the top of the diagram represent the grid point of the maps of Chapter 5, corresponding to the crystallographic orientation.) Usually three separate crystals were measured and the results found to be in agreement. The measured attenuation of the L-mode in the X-cut crystal is some 40% lower at 300Mc/s than previously published values (Lamb et al. 1959). At higher frequencies the difference becomes smaller, while at 3000Mc/s the present measurements extrapolate to the absorption measured with resonance method by Stewart and Stewart (1963b). There is a similar situation with the SS mode of the AC orientation: the triangles of Fig. 10.3 representing best measurements before the construction of the double-tuned cavity show a higher loss than the present data owing to extraneous effects masking the low intrinsic attenuation. For the BC cut the L-mode was very weakly excited and accurate attenuation measurement was not possible. Measured attenuation values (α) at a frequency of 450Mc/s for these and other directions are given in Table 10.1; these are estimated to be accurate within ± 5%.

All the attenuation values are given as measured and uncorrected, and represent intrinsic attenuation. Possible errors due to diffraction effects are considered to be negligible owing

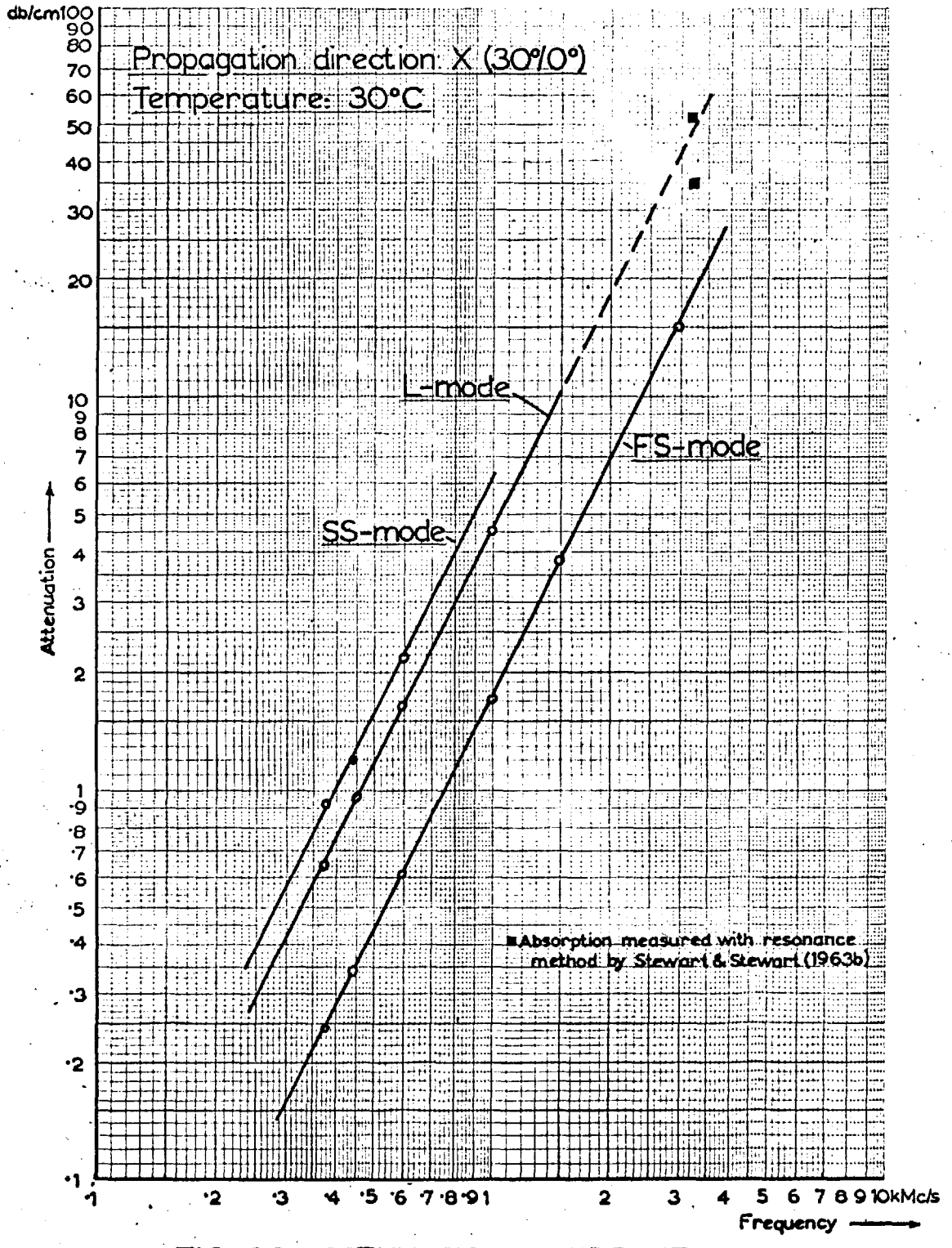


FIG. 10.2 ATTENUATION vs. FREQUENCY.

X-QUARTZ.

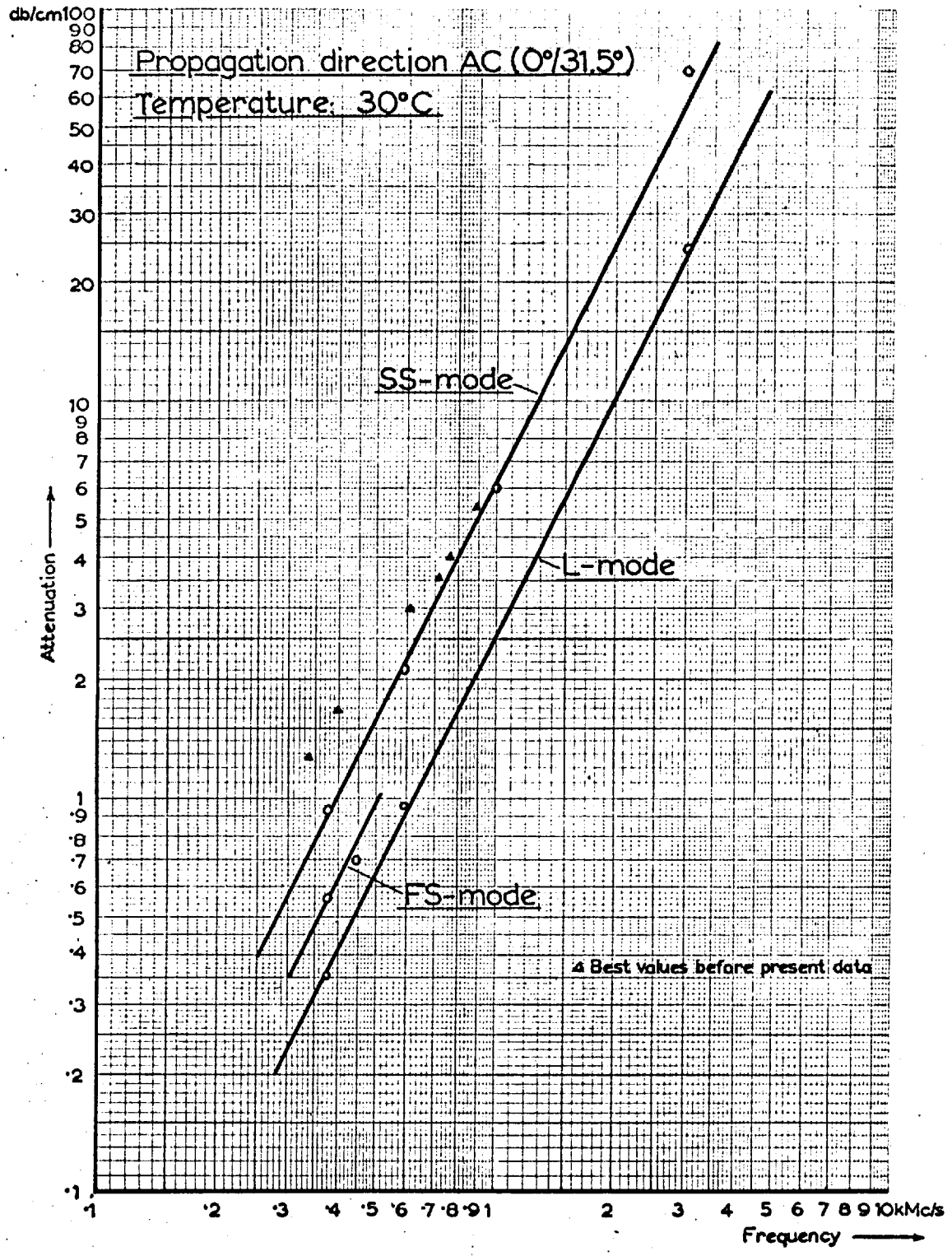


FIG. 10.3 ATTENUATION vs. FREQUENCY.

AC-QUARTZ.

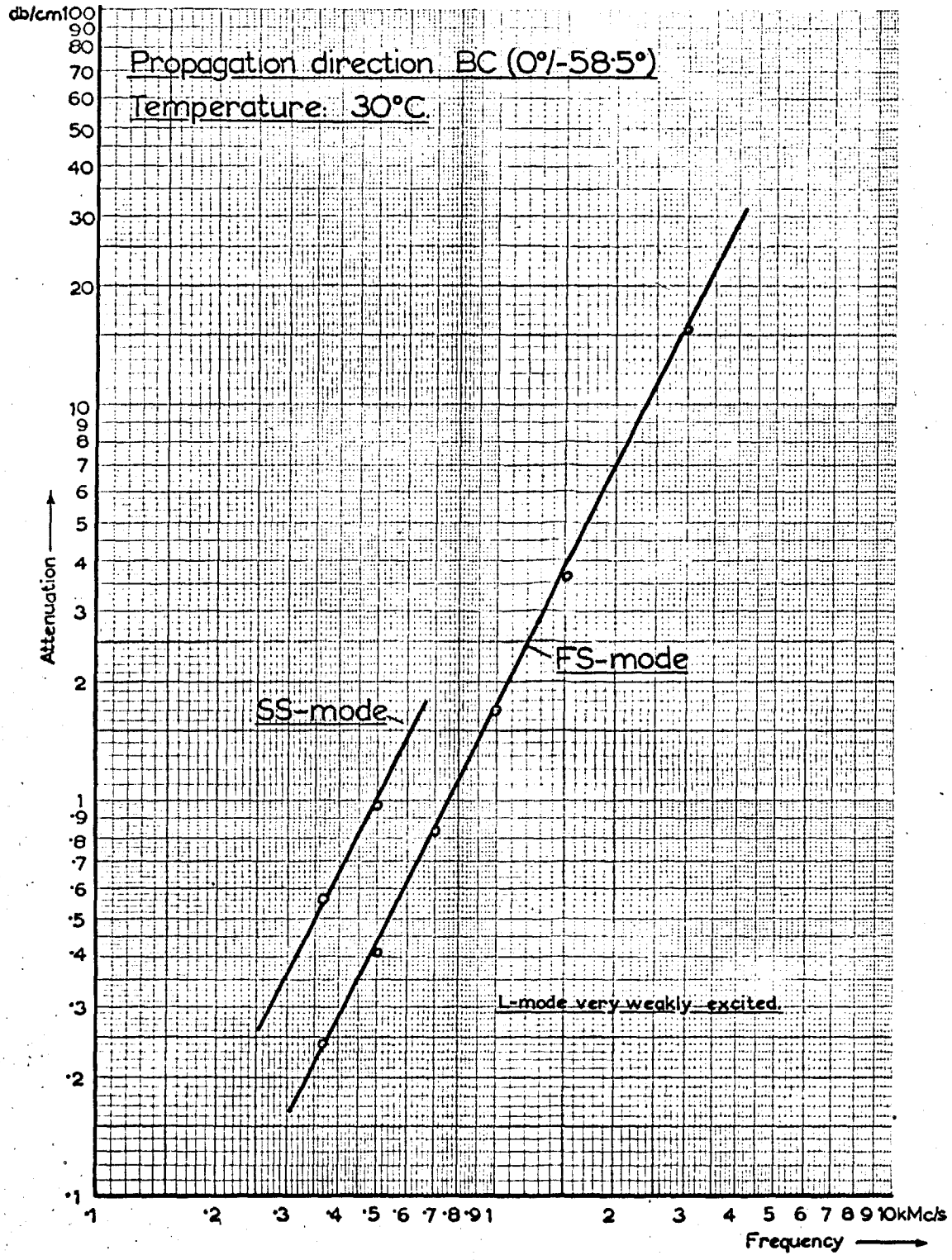


FIG. 10.4 ATTENUATION vs. FREQUENCY.
BC-QUARTZ.

to the highly directional beam generated at these frequencies, combined with the approximately cosine squared variation of the excitation across a diameter of the generating surface. There is no interaction with the side walls, since the amplitude of excitation is falling to zero at the cylindrical surface.

The advantage of using surface excitation for attenuation measurements in low-loss piezoelectric crystals is that this removes the uncertainty in loss caused by the attachment of a resonant transducer through a coupling film in the more conventional methods used hitherto (eg. Redwood and Lamb, 1956). Also, the relatively low electromechanical conversion efficiency of quartz ensures that only a small fraction of the acoustic energy is lost to the cavity at each reflection, (less than 1/1000) making corrections due to this transducer loss unnecessary.

10.2 ATTENUATION BY VISCOELASTICITY.

Comparison of the results given in Figs. 10.2, 10.3 and 10.4 shows that the attenuation of the FS mode in X-cut quartz is the same as that of the FS mode in the BC-cut crystal. The velocities of propagation, v, are also the same. Moreover, the attenuation of the SS mode in AC quartz is the same as that of the SS mode in X quartz and, again, the velocities of propagation of these modes are the same. A cursory inspection of attenuation measurements for the above mentioned best known shear modes would suggest that the attenuation is governed solely by the factor $1/v^3$ (eg. Bömmel and Dransfeld, 1960). This, however, is a coincidence and is not generally true for other modes and directions as is revealed by the more extensive results now available.

But calculations of attenuation assuming various microscopic

interactions always involve the factor $1/v^3$ (eg. Mason, 1960; Mason and Bateman, 1964; Nava et al. 1964). The purely phenomenological approach of Chapter 3 which disregards the actual loss process assumes a matrix of anisotropic complex elastic stiffness coefficients c^*_{ijkl}, giving a formula for the attenuation under the condition of small attenuation as (Equation 3.17):

$$\alpha = \frac{\omega^2}{2\rho v^3}\eta \qquad 10.1$$

where η is the effective viscosity, calculated by Equation 3.19 from a matrix of anisotropic viscosity coefficients η_{ijkl}. The symmetry of the η_{ijkl} matrix is determined in form by the class of the crystal and is the same as that of the c_{ijkl} matrix. For crystal quartz the expressions of effective viscosity values for selected directions of propagation are given in Table 10.2. The numerical coefficients of the various viscosity components depend upon the direction cosines of the selected direction of propagation in the crystallographic set of axes and the values of elastic constant. The experimentally determined values of effective viscosity, obtained by using Equation 10.1 at the frequency of 450Mc/s are also given in Table 10.2.

It is apparent from Table 10.2 that the formulae derived for the effective viscosity are the same for the FS mode in both BC and X quartz. A similar equality holds for the SS modes in the AC and X quartz. Agreement is also found between the corresponding values of effective viscosity obtained from the measurements of attenuation. The expressions of the effective viscosity values as given in Table 10.2 together with the measured values enables one to calculate the components of the matrix of the viscosity coefficients. In principle, only six independent measurements of attenuation for selected modes and propagation directions are

TABLE 10.2

MEASURED VALUES AND CALCULATED EXPRESSIONS FOR THE EFFECTIVE VISCOSITY IN CRYSTAL QUARTZ

Temperature = 30°C

Propagation direction	Mode	η(cP) measured	$\eta = \frac{1}{\omega} \mathrm{Im}(E^*)$
BC	L	Low coupling	$0.701\eta_{44} + 0.593\eta_{33} + 0.050\eta_{11} - 0.375\eta_{24} + 0.345\eta_{23}$
	FS	0.347	$0.727\eta_{44} + 0.273\eta_{66} - 0.891\eta_{56}$
	SS	0.318	$0.399\eta_{44} + 0.134\eta_{33} + 0.222\eta_{11} - 0.506\eta_{24} - 0.345\eta_{23}$
AC	L	1.33	$0.870\eta_{44} + 0.101\eta_{33} + 0.458\eta_{11} + 1.262\eta_{24} + 0.429\eta_{23}$
	FS	0.265	$0.129\eta_{44} + 0.172\eta_{33} + 0.269\eta_{11} - 0.372\eta_{24} - 0.429\eta_{23}$
	SS	0.352	$0.273\eta_{44} + 0.727\eta_{66} + 0.891\eta_{56}$
X	L	1.39	η_{11}
	FS	0.349	$0.727\eta_{44} + 0.273\eta_{66} - 0.891\eta_{56}$
	SS	0.352	$0.273\eta_{44} + 0.727\eta_{66} + 0.891\eta_{56}$

(Table continued overleaf)

TABLE 10.2 (continued)

Propagation direction	Mode	η(cP) measured	$\eta = \frac{1}{\omega}\mathrm{Im}(E^*)$
AT	L	1.32	$0.951\eta_{44} + 0.132\eta_{33} + 0.403\eta_{11} + 1.220\eta_{24} + 0.461\eta_{23}$
	FS	0.253	$0.049\eta_{44} + 0.205\eta_{33} + 0.260\eta_{11} - 0.276\eta_{24} - 0.461\eta_{23}$
	SS	0.342	$0.337\eta_{44} + 0.663\eta_{66} + 0.944\eta_{56}$
Z	L	0.975 (a)	η_{33}
	S	- (b)	η_{44}
Y	L	- (b)	$0.189\eta_{44} + 0.810\eta_{11} + 0.785\eta_{24}$
	FS	- (b)	$0.810\eta_{44} + 0.189\eta_{11} - 0.785\eta_{24}$
	SS	0.302	η_{66}

(a) Mason, McSkimin and Bateman (1962)

(b) No reliable measurement available.

required to determine the viscosity matrix of quartz. In actual fact some thirteen independent measurements have been made and the Glasgow University KDF9 digital computer was used to calculate the viscosity coefficients giving a least mean square fit to all the data obtained. Unfortunately, owing to the beam deviation angle for the shear mode in Z-cut quartz, the available specimens were too long to permit a direct measurement of η_{44} with reasonable accuracy. When the viscosity matrix of Table 10.3 is used to calculate effective viscosities it gives values which are within $\pm$ 3% of the measured values.

Effective viscosity values, and hence attenuation values for any direction of propagation in a selected mode can be calculated from the viscosity matrix once this has been determined. In this sense the procedure employed is analogous to the calculation of velocities of propagation from the matrix of elastic constants.

Calculated curves of the effective viscosity as function of angle for rotated Y-cuts obtained from the values of viscosity components of Table 10.3 are given in Fig. 10.5. Values of attenuation at the representative frequency of 450Mc/s for rotated Y-cuts, obtained from the effective viscosities of Fig. 10.5 are given in Figs. 10.6 and 10.7 in units of dB/cm and dB/μsec, respectively.

The fact that the attenuation is strictly proportional to the square of frequency indicates that the effective viscosity, and the viscosity matrix components are frequency independent constants at room temperature in the frequency range of the measurements. Hence it is concluded that the viscoelastic relaxation spectrum of quartz at room temperature does not contain components corresponding to this frequency range. The spectrum then must be similar to that given in Fig. 2.1 where the main relaxation is

TABLE 10.3

Viscosity Matrix (in cP) for Crystal Quartz at 30°C

Double figures (1 to 3) represent η_{ijkl} components

Single figures (1 to 6) represent conventional shorthand notation.

ij / kl	11 (1)	22 (2)	33 (3)	23 (4)	13 (5)	12 (6)
11 (1)	1.370	0.730	0.715	0.012	0	0
22 (2)	0.730	1.370	0.715	-0.012	0	0
33 (3)	0.715	0.715	0.969	0	0	0
23 (4)	0.012	-0.012	0	0.364	0	0
13 (5)	0	0	0	0	0.364	0.012
12 (6)	0	0	0	0	0.012	0.320

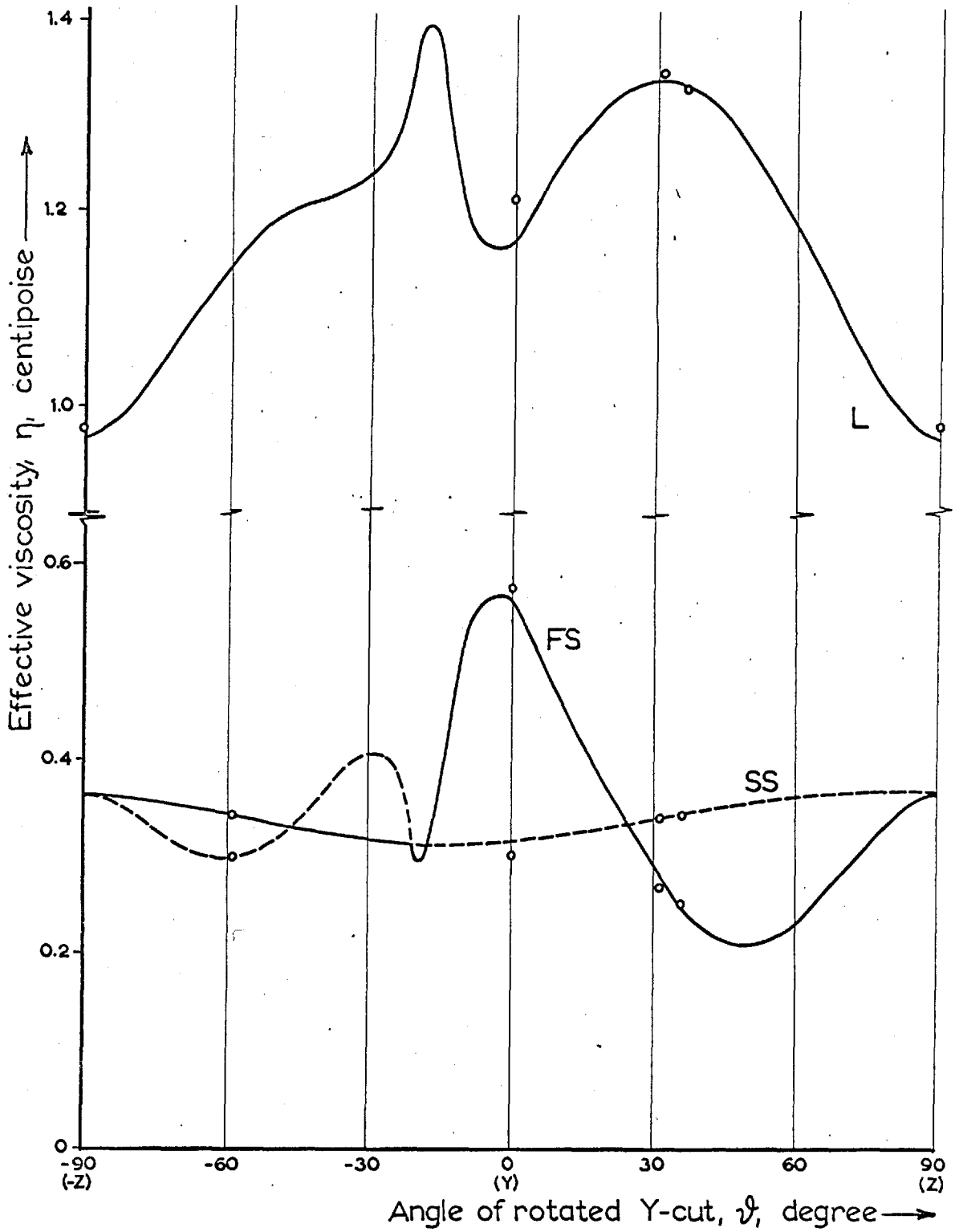


FIG. 10.5 CALCULATED VALUES OF EFFECTIVE VISCOSITY FOR ROTATED Y ORIENTATIONS IN QUARTZ AT 30°C.

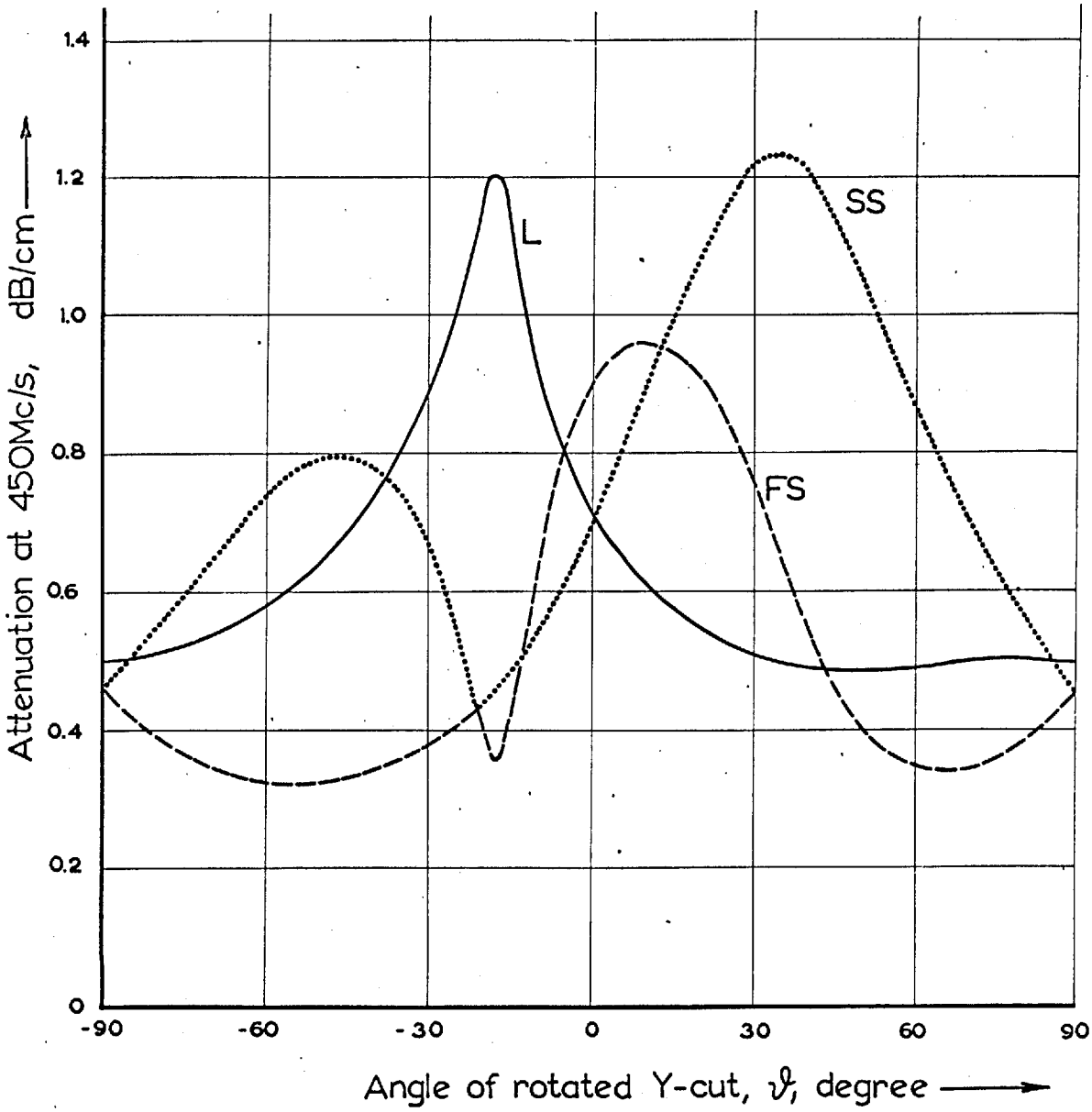


FIG. 10.6 CALCULATED ATTENUATION IN dB/cm AT 450Mc/s FOR ROTATED Y DIRECTIONS IN QUARTZ. (TEMP.=30°C)

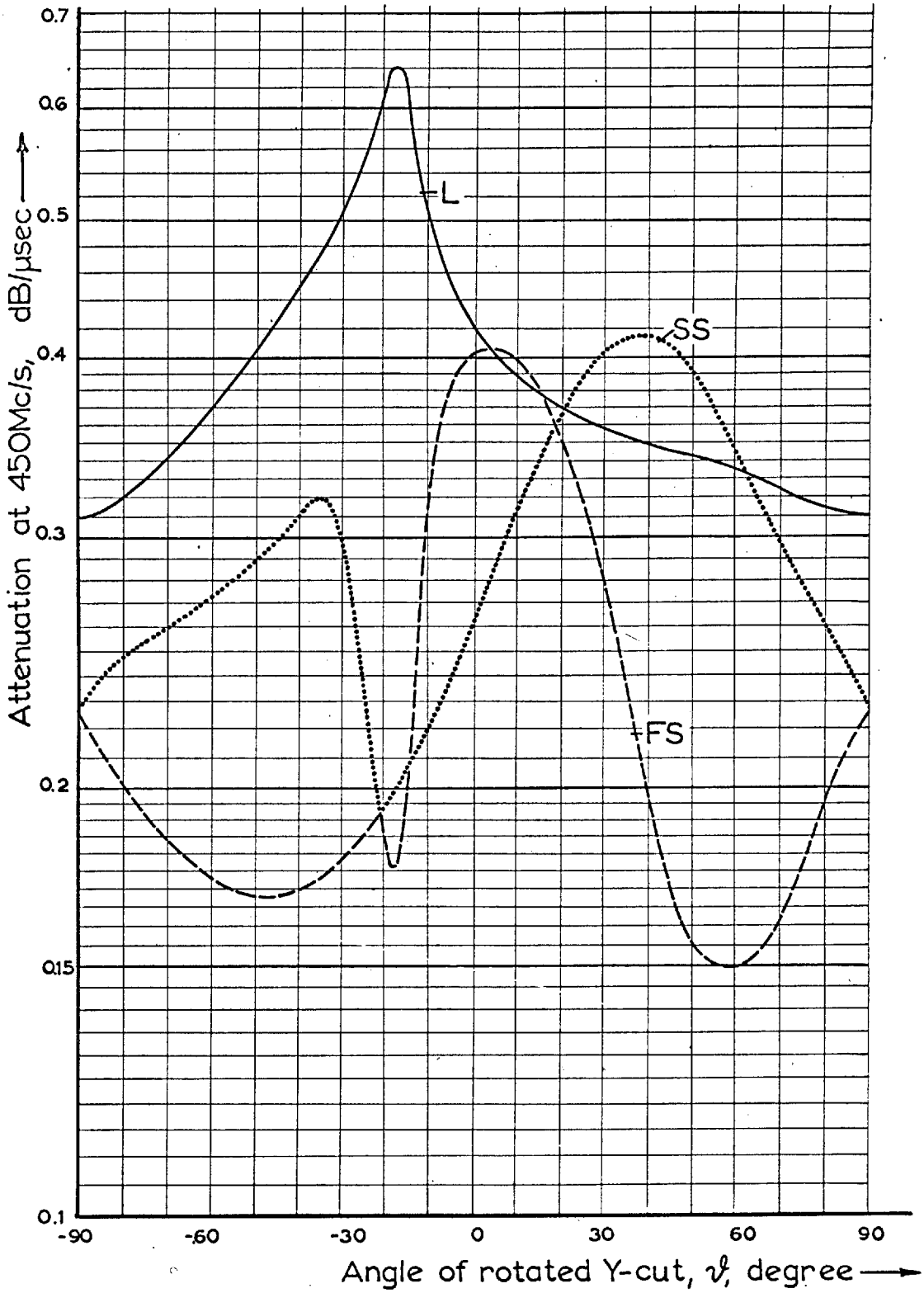


FIG. 10.7 CALCULATED ATTENUATION (dB/μsec) AT 450Mc/s FOR ROTATED Y DIRECTIONS IN QUARTZ. (TEMPERATURE 30°C)

occuring at much lower frequencies than the frequency of ordinary measurements resulting in the elastic stiffness (Equation 2.63) but with a small part of the spectrum at frequencies higher than the frequency of the present measurements causing the acoustic attenuation.

Although the attenuation and viscosity are functions of temperature, there is only a very small change in their values for quartz from room temperature down to 50°K at lower microwave frequencies. Below 50°K the attenuation quickly diminishes with reducing temperature.

The attenuation of the L mode in an X-cut quartz as a function of frequency at 30°K is plotted in Fig. 10.8a taking data from the paper of Nava et al. (1964). The square law dependence of attenuation is not obeyed at this temperature in the shown frequency range. The attenuation due to a relaxation mechanism with a single relaxation time is also plotted as curve b in Fig. 10.8 showing that the high frequency relaxation in quartz, responsible for the acoustic attenuation can be approximately described by a single relaxation process. The attenuation over a wavelength, $\alpha\lambda$, (specific attenuation) is plotted as curve c.

It is well known in relaxation theory (eg. Herzfeld and Litovitz, 1959, chapter II) that for a single relaxation the maximum of the specific attenuation occurs when $\omega\tau = 1$, and the value of the maximum is $\pi\Delta$, where Δ is the relative change in phase velocity due to the relaxation. The curve 10.7c gives a relaxation time of 2.10^{-10} sec at 30°K. The relative velocity change is 2.10^{-5} which is too small to be detected. A rather excessive extrapolation of the low temperature relaxation time data to room temperature gives an estimate of the order of 100kMc/s for the relaxation frequency with a limiting attenuation of the

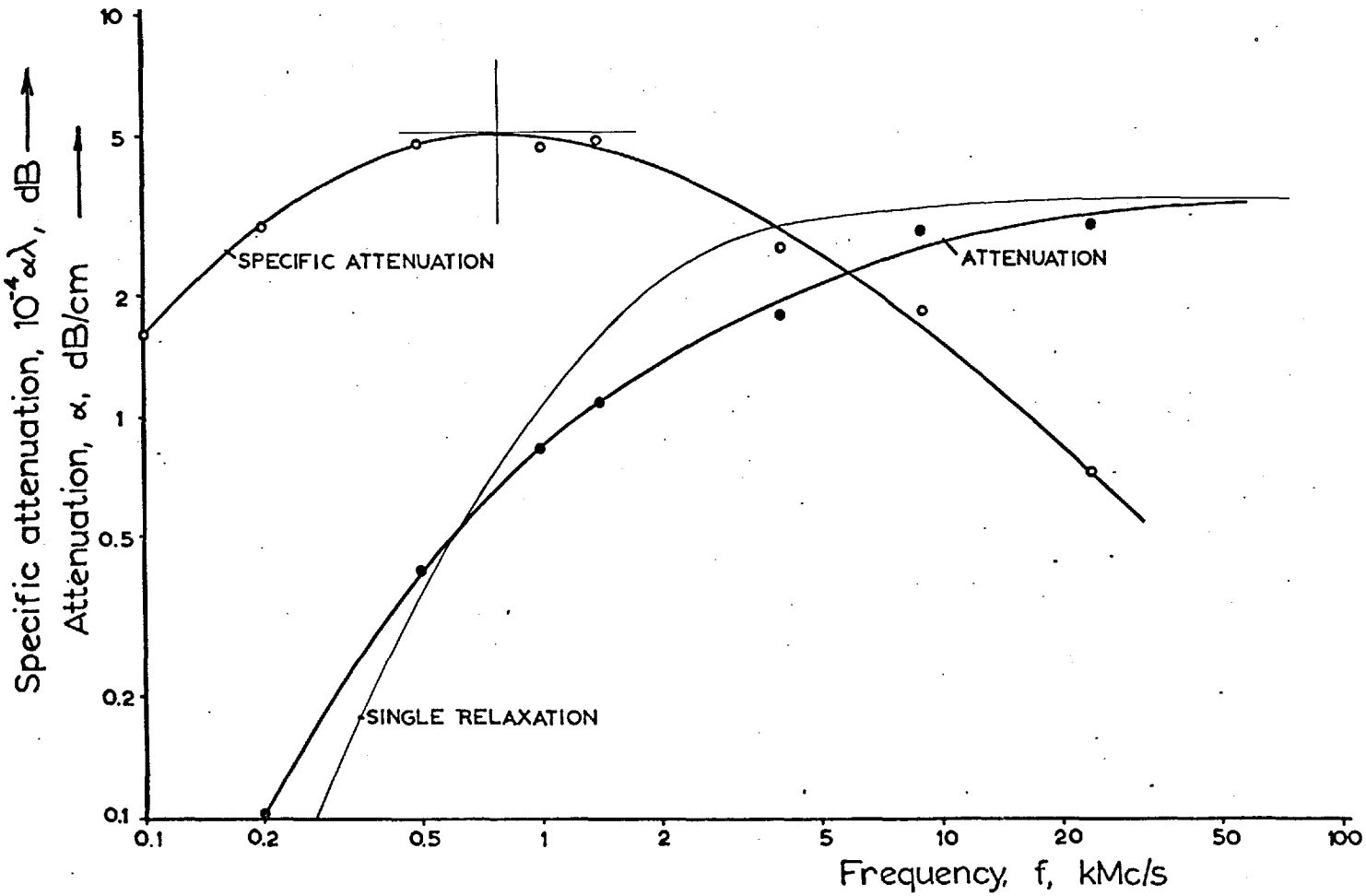


FIG. 10.8 ATTENUATION OF THE L-MODE IN X QUARTZ AT 30°K.
(USING DATA OF NAVA et al., 1964)

TABLE 10.4

Experimental Data and Calculated Expressions for the Effective Viscosity in Silicon.

Direction and mode	f Mc/s	α dB/cm	Ref.	η (cP)	Expression for η
100, L	480	2.16	(a)	1.45	η_{11}
100, S	495	0.70	(a)	0.49	η_{44}
111, L	500	1.90	(b)	0.83	$\frac{1}{3}(\eta_{11} + 2\eta_{12} + 4\eta_{44})$
110, L	300	0.985	(c)	1.13	$\frac{1}{2}(\eta_{11} + \eta_{12}) + \eta_{44}$
111, S	500	1.24	(d)	0.93	$\frac{1}{3}(\eta_{11} + \eta_{44} - \eta_{12})$

(a) Mason and Bateman (1964)

(b) Lamb, Redwood and Shteinshleifer (1959)

(c) Lücke (1956)

(d) Own measurements

TABLE 10.5

Components of the Viscosity Tensor.

$$\eta_{11} = 1.505 \text{ cP}$$
$$\eta_{12} = -0.532 \text{ cP}$$
$$\eta_{44} = 0.553 \text{ cP}$$

order of 1000dB/cm. Therefore the square law dependence of attenuation upon frequency is expected to hold up to 10kMc/s above which it will increase probably at a lesser rate.

As a further check on the applicability of the ideas of anisotropic viscosity to the calculation of acoustic attenuation in solids, the effective viscosities of cubic silicon at room temperature were calculated from available experimental data. A summary of the data and the appropriate expressions used in the calculations are given in Table 10.4. The components of the viscosity tensor giving calculated attenuations within $\pm$ 10% of measured values are shown in Table 10.5. In view of the limited experimental accuracy, this agreement between experimental and calculated values is considered adequate.

In the case of fused quartz the viscosity tensor is isotropic with a relatively high longitudinal viscosity of 5.9cP. The shear viscosity is approximately one order of magnitude less than this value.

10.3 CONCLUSIONS.

The new measurements of attenuation in quartz have been obtained by surface excitation in the specially designed double-tuned cavity. These measurements cover a much larger number of modes and orientations and are believed to be more accurate than previously known data. The attenuation is found to be proportional to the square of the frequency over the range 300 to 3000Mc/s at room temperatures. The square law dependence at room temperatures is expected to hold only up to a certain frequency, which is definitely higher than 10kMc/s.

Extending the ideas associated with the viscoelasticity of

liquids to crystalline solids, a general anisotropic viscosity tensor is defined whose symmetry is determined by the crystal class and is the same as the elastic constant matrix. Numerical values for the viscosity coefficients are specific to the material and from a knowledge of these the attenuation of a given mode in a selected direction of propagation can be calculated. The validity of this analysis is confirmed by the attenuation measurements in quartz and is further supported by data for silicon. It could with confidence be applied to other materials.

Calculated attenuation values for rotated Y-cut quartz show that the BC orientation has the lowest attenuation for shear waves over both a given length or given time delay when propagation takes place along these directions. The attenuation for the FS modes of the BC and X orientations is the same. Checking over directions not contained in the YZ crystallographic plane did not reveal other propagation directions with lower attenuation.

CHAPTER 11.
THE MEASUREMENT OF THE MECHANICAL IMPEDANCE OF LIQUIDS. THEORY AND TECHNIQUE.

11.1 MATHEMATICS OF MEASUREMENTS.

The complex acoustical impedance of an isotropic mechanical medium is defined for an acoustic mode by

$$Z = R + jX = -\frac{f}{j\omega u} \qquad 11.1$$

and it will be expressed in units of dynesecm^{-1} (mechanical cgs. Ohm) unless explicitly stated otherwise. f and u are the magnitudes of the vectors of force per unit area and displacement in the given mode over a surface normal to the direction of propagation. If propagation takes place along the x_2 direction in a general anisotropic medium, then the force f can be expressed as (c.f. Equation 3.10)

$$f_i = T_{i2} = -c_{i2k2}\, jku_k = -jkEu_i \qquad 11.2$$

where k and E are the wavevector and effective stiffness (bulk modulus K or shear rigidity G) respectively, of the mode under consideration. Equation 11.2 shows that the force and displacement are colinear just as in the isotropic case. Hence substitution of Equation 11.2 into Equation 11.1 yields (with $\frac{\omega}{k} = \sqrt{\frac{E}{\rho}}$)

$$Z^2 = \rho E \qquad 11.3$$

When only shear waves are considered:

$$Z^2 = \rho G = \rho(G' + jG'') \qquad 11.4$$

Equating real and imaginary parts of the above equation gives

$$G' = \frac{R^2 - X^2}{\rho} \quad \text{and} \quad G'' = \omega\eta' = \frac{2RX}{\rho} \qquad 11.5$$

showing how the real and imaginary parts of the complex rigidity modulus can be calculated from known values of R and X.

The quantity which is directly obtained from measurements in the present technique is only the real part of the mechanical impedance R_L of the test liquid. The measurement is based on the reflection coefficient method, used previously by Barlow and Lamb (1959), stemming from the original work of Mason et al. (1949) and McSkimin (1952). Now, for the first time, an anisotropic and piezoelectric crystal is used for the measurements.

When a plane acoustic wave is incident normally on the interface of two media it gives rise to reflected and transmitted acoustic waves (Chapter 4.1). Since now one of the media is piezoelectric, the incident acoustic wave also gives rise to electromagnetic fields. The equivalent circuit of the interface of BC quartz and an isotropic fluid is shown in Fig. 4.4 where the FS mode is propagated in the quartz. The impedance seen by the acoustic wave inoident at port 1) is the sum of the acoustic impedance at port 3) and the equivalent eleotromagnetic impedance of ports 2) and 4)

$$Z^{1)} = Z_A^{3)} + e^2 Z_{e-m} \qquad 11.6$$

The loaded interface is outside the cavity so the electromagnetic impedance is of the order of free-space impedance (337 Ohms). Since e^2 is no more than 10^{-2} MKS units for quartz, $e^2 Z_{e-m}$ is a few ohms only, which is negligible compared to the lowest measured acoustic impedance of 30 kOhm MKS (= 3 kOhm ogs). Therefore the impedance seen by the acoustic wave at reflection is the same for all practical purposes as the mechanical impedance of the liquid loading the quartz rod.

The reflection coefficient, ρ expressing the ratio of incident

to reflected displacement amplitude is given for normal incidence of a pure shear mode by

$$\varsigma = |\varsigma| e^{j\theta} = \frac{Z_S - Z_L}{Z_S + Z_L} \qquad 11.7$$

where Z_L and Z_S are the shear mechanical impedances of the liquid and quartz, respectively. For the FS mode of a BC crystal at room temperature the real part of Z_S is 1.356MΩ (cgs), and the imaginary part, calculated from the slight propagation loss is of the order of one ohm at the highest frequency of measurement. $|Z_L|$ is generally less than 2.10^5 Ω, and hence the value of $|\varsigma|$ is relatively close to unity. The real and imaginary parts of the liquid impedance can be expressed from Equation 11.7 as (e.g. Barlow, 1959)

$$R_L = R_S \frac{1 - |\varsigma|^2}{1 - |\varsigma|^2 - 2|\varsigma|\cos\theta} \qquad X_L = R_S \frac{-2|\varsigma|\sin\theta}{1 - |\varsigma|^2 - 2|\varsigma|\cos\theta} \qquad 11.8$$

The impedance of quartz is so much higher than the imaginary part of the liquid impedance, that the angle, θ of the reflection coefficient is never expected to exceed 3 degrees, and is usually much less. Therefore very small error is introduced ($< 0.25\%$) if $\cos\theta$ is taken as 1 in the equations of 11.8, when

$$R_L = R_S \frac{1 - |\varsigma|}{1 + |\varsigma|} \qquad 11.9$$

The real part of the liquid impedance is defined by the modulus alone of the reflection coefficient, according to Equation 11.9. The imaginary part could not be obtained in the present technique, so liquid investigations had to be confined to cases where X_L was either obtained by other means, or, as in connection with the measurements of Chapter 12, X_L was of no interest.

When r is defined as the modulus of the reflection coefficient

expressed in dB's relative to 1, Equation 11.9 takes the following form:

$$R_L = R_S \frac{1 - e^{\frac{\ell n 10}{20} r}}{1 + e^{\frac{\ell n 10}{20} r}} = -R_S \tanh \frac{\ell n 10}{40} r$$

$$= -R_S(0.05756r - 6.4\times10^{-5}r^3 + \ldots) \qquad 11.10$$

If $|\zeta|$ is not differing from 1 by more than 1.5dB, the following approximation of Equation 11.10 is valid within an error of 0.25%:

$$R_L = -R_S\ 0.05756r \qquad 11.11$$

When R_S is the impedance of BC quartz, the real part of the liquid impedance in kohms is given simply by

$$R_L = -78.0\ r \qquad 11.12$$

11.2 MEASUREMENT PROCEDURE.

The real part of the liquid impedance is calculated with the help of Equation 11.12, using measured values of the modulus of the reflection coefficient r. To obtain r, the amplitudes of pulses in a train of multiple echoes are recorded first with the outside surface of the quartz rod in air, and secondly, with the outside surface covered by a layer of the sample liquid. The amplitude of a given echo pulse is measured by adjusting the setting of the piston attenuator through which the comparison signal is fed, and noting the reading on the dial when the height of the echo and comparison pulses appear to be the same on the oscilloscope screen (c.f. Section 6.1). The liquid absorbs some of the energy of the acoustic wave at each reflection, therefore the reduction in amplitude due to the liquid loading is proportional to the echo number. When the reduction im amplitude, expressed in dB's as the difference of readings for a given echo pulse is plotted against the echo number, the slope of the best fitting straight line through these difference points gives the

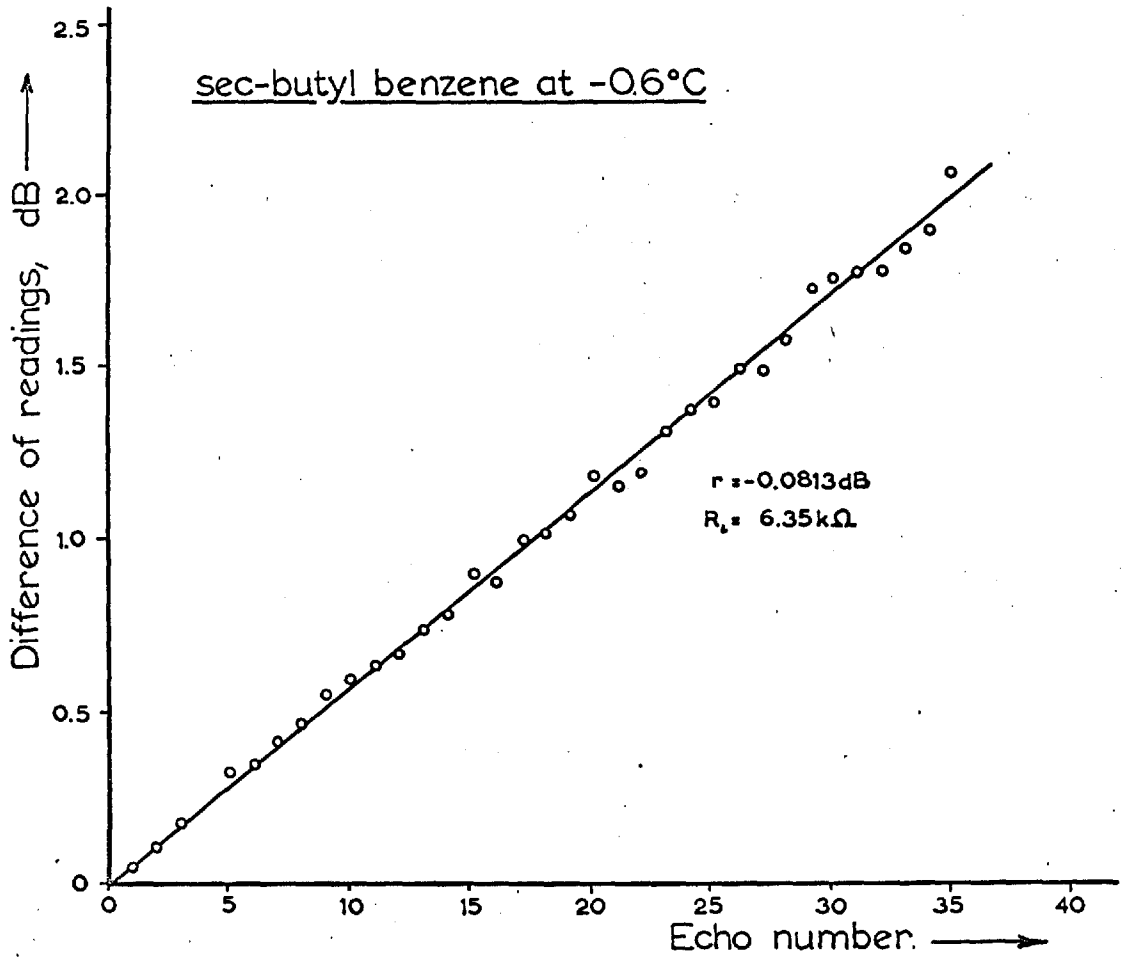
required value of r.

A typical measurement is shown in Fig. 11.1a, where the value of -0.0813 dB/reflection was obtained for r graphically. The deviation of the measured difference points from the straight line is also shown as Fig. 11.1b. A measurement was regarded unreliable if for the first 20 pulses the scatter in the difference points exceeded 0.1 dB or if it was of marked non-statistical nature.

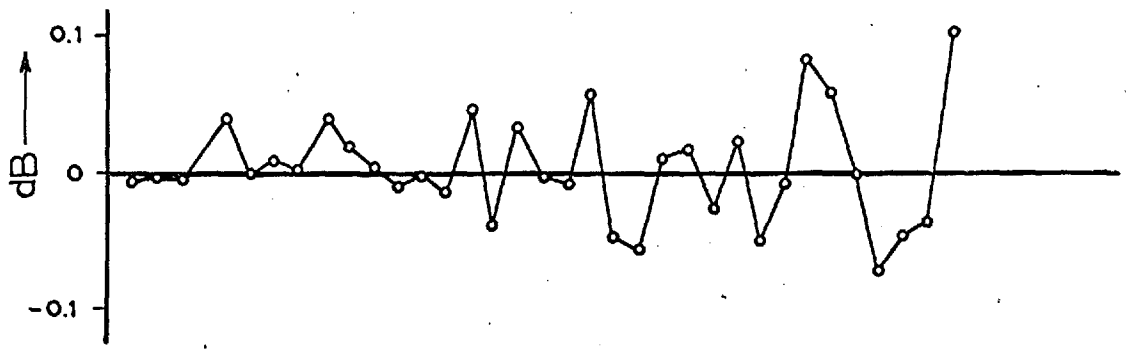
There is no restriction on the value of R_L of the liquid that can be measured. Liquids of low viscosity allow the reflection coefficient measurements to be made over 50 echoes, while with very viscous liquids only 15 echo pulses are available with sufficiently high signal-to-noise ratio.

The transducer cavity is immersed in a thermostat (c.f. Section 9.1) and held at the required constant temperature for two hours before taking a measurement. Prior to cooling to subzero temperatures the cavity system is flushed with dried and carbon dioxide free air.

The cleanliness of the quartz surfaces is checked through the central silica window before the application of the sample liquid. 2cc of fluid is injected on the top quartz surface by an all-glass syringe through a length of insulated polythene tubing. 50cc of cold dry air is pushed in from a second syringe behind the sample to ensure quick flow through the tubing. The liquid was usually injected at room temperature and about an hour was allowed for it to reach thermal equilibrium at the temperature of measurement. The liquid layer was inspected through the window before warming up and the measurement was discarded if it was found that the sample did not cover the whole surface, or if it crystallised or contained air bubbles.



a) REDUCTION IN PULSE HEIGHT DUE TO LIQUID LOADING.



b) DEVIATION OF POINTS IN a) FROM THE STRAIGHT LINE.

FIG. 11.1

11.3 ACCURACY CONSIDERATIONS.

In order to obtain a small scatter of the measured difference points (in plots similar to Fig. 11.1a) the echo pulses from which the difference is calculated must belong to as good exponential decay patterns as possible. The unloaded echo pattern used in the calculation of the difference points of Fig. 11.1a is shown in Fig. 10.1, where the r.m.s. deviation of the recorded amplitudes from a true exponential decay rate is 0.05dB. As explained in Section 8.6, only the double-tuned cavity was capable of generating in BC quartz an acoustic pulse that decayed so nearly exponentially. To demonstrate the effect of rather bad, non-exponential decays, the decay patterns shown in Fig. 11.2a) and b) were obtained by a BC-cut quartz in the axial cavity of Fig. 8.2 with flat centre post. When these echo trains are used to calculate the effect of the liquid loading, the resulting difference plot c) is found to deviate greatly from a straight line, making the precise determination of the reflection coefficient impossible.

The thickness of the layer of sample liquid over the quartz surface was about 1cm. Although the depth of penetration of a shear wave is of the order of microns for a not very viscous liquid at microwave frequencies (c.f. Equation 3.21), it can be considerably longer when the liquid is in the glassy state. But no reflection is expected from a 1cm thick layer even if the sample liquid solidifies.

The optical quality of polish of the end surfaces of the quartz rod ensures that there is no error introduced into the reflection coefficient by end surface scattering.

The maximum acoustic power flow is of the order of $1W/cm^2$.

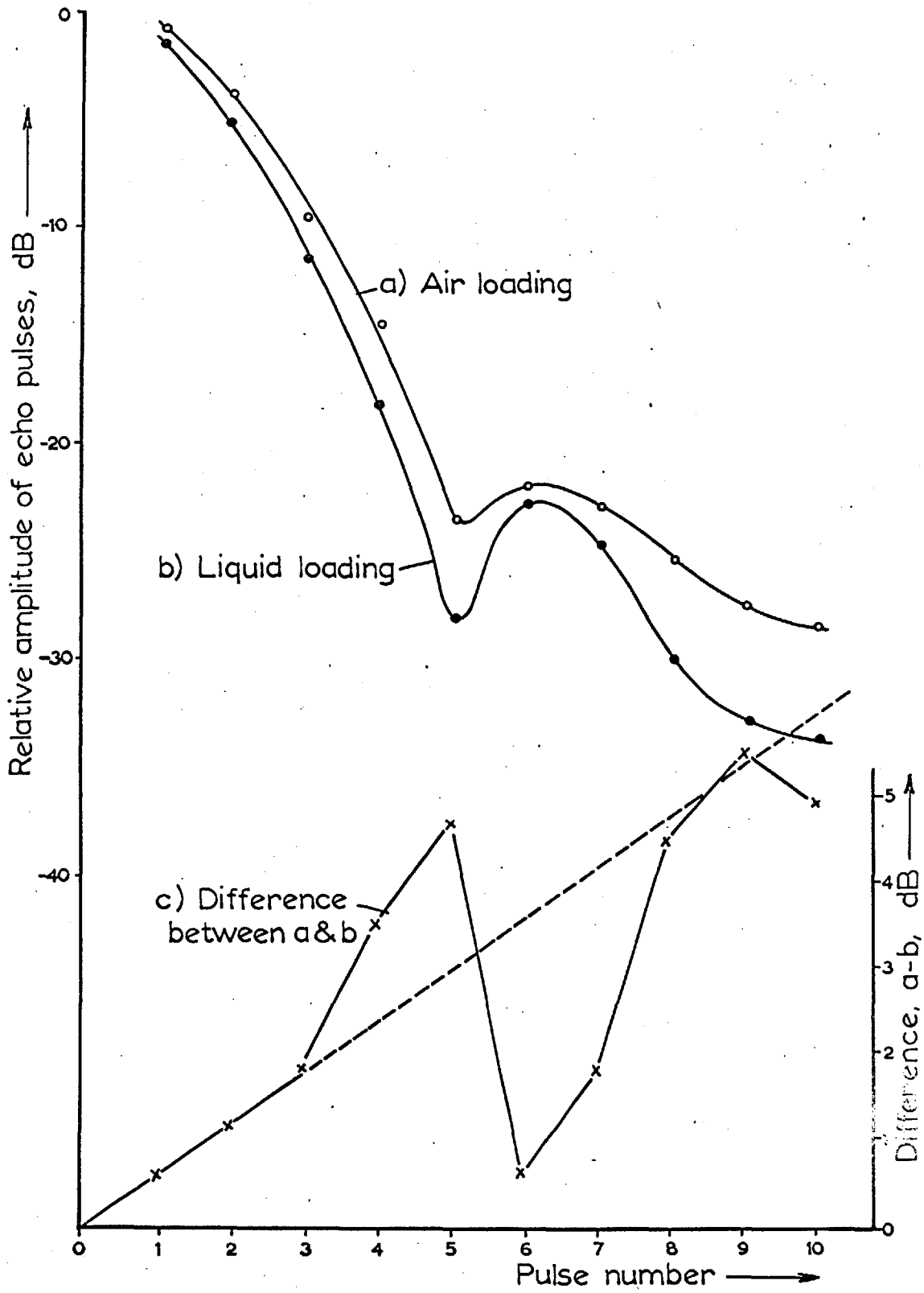


FIG. 11.2 TYPICAL NON-EXPONENTIAL DECAYS.

No non-linearity of the elastic response was observed at this power level either in the quartz or in the sample liquid. (At $1 W/cm^2$ and 500Mc/s in quartz the maximum particle displacement is 0.1Å, the maximum particle velocity is 3cm/sec and the maximum particle acceleration is $10^7 g$. Maximum strain is 10^{-5} and maximum stress is $2 kg/cm^2$.)

The fact that quartz is piezoelectric does not cause an error of more than 5Ω in the liquid impedance measurements. (c.f. Equation 11.6). Due to its anisotropy, however, there is the possibility of the shear wave having a longitudinal component if the axis of the rod deviates from the pure shear mode direction. The reflection coefficient giving the ratio of amplitudes in the reflected and incident quasi-shear modes of a propagation direction lying within the YZ crystallographic plane of quartz is obtained in Appendix G as

$$\frac{Z_S^s - Z_L^l - \sin^2\alpha (Z_S^l + Z_S^s)\dfrac{Z_L^l - Z_L^s}{Z_S^l + Z_L^l}}{Z_S^s + Z_L^s + \sin^2\alpha (Z_S^l - Z_S^s)\dfrac{Z_L^l - Z_L^s}{Z_S^l + Z_L^l}} \qquad 11.13$$

where Z^s and Z^l are shear and longitudinal impedances, respectively, with the subscript indicating whether of the solid or of the liquid. α is the angle of deviation of the acoustic displacement from the pure shear displacement direction (quasi-mode angle). Substituting practical values, it is found that as long as the quasi-mode angle does not exceed 2.5°, using the above quasi-shear mode for liquid impedance measurements causes an error of less than 250Ω. It is expected that similar values would be obtained for a quasi-mode resulting from misorientation away from the YZ plane, so that such a misorientation of $\pm 3^\circ$ from the true BC direction

would cause a maximum error of 250 Ohms in the liquid impedance value owing to the presence of a longitudinal component of the FS mode in that direction. Since the actual misorientation angle is less than 0.5°, the accuracy of the measurements cannot be impaired on this account.

The temperature of the liquid sample was measured by calibrated thermocouples. It was found useful to measure the temperature of the thermostatting bath against an ice reference temperature and to use a second thermocouple to detect any difference between the temperature of the bath and the quartz holder. A temperature difference of less than $0.1^{\circ}C$ was accepted to indicate that the cavity system reached the equilibrium temperature.

There was some ($\approx 3dB$) increase in the excitation efficiency when a BC-cut quartz was cooled from room temperatures to around $-120^{\circ}C$. The attenuation also increased by about 0.05dB/cm for causes not understood. This extra attenuation, however, tended to disappear if the quartz was held at the low temperature for a long enough time. Fig. 11.3 shows the measured attenuation at 450Mc/s when the quartz was held for several days at the temperature of $-100^{\circ}C$ with only slight warming-ups allowed overnight. Similar decrease in attenuation was noticed during routine measurements. Because of this unpredictability of the attenuation value at low temperatures the amplitudes of the pulses in both the air and liquid loaded echo trains had to be noted for every single (direct) liquid impedance measurement at a given temperature; a second (indirect) measurement was sometimes obtained before warming up and cleaning the quartz crystal. Due to the long thermostatting times necessary, only one direct measurement could be obtained per day.

The mechanical impedance of the quartz over the temperature

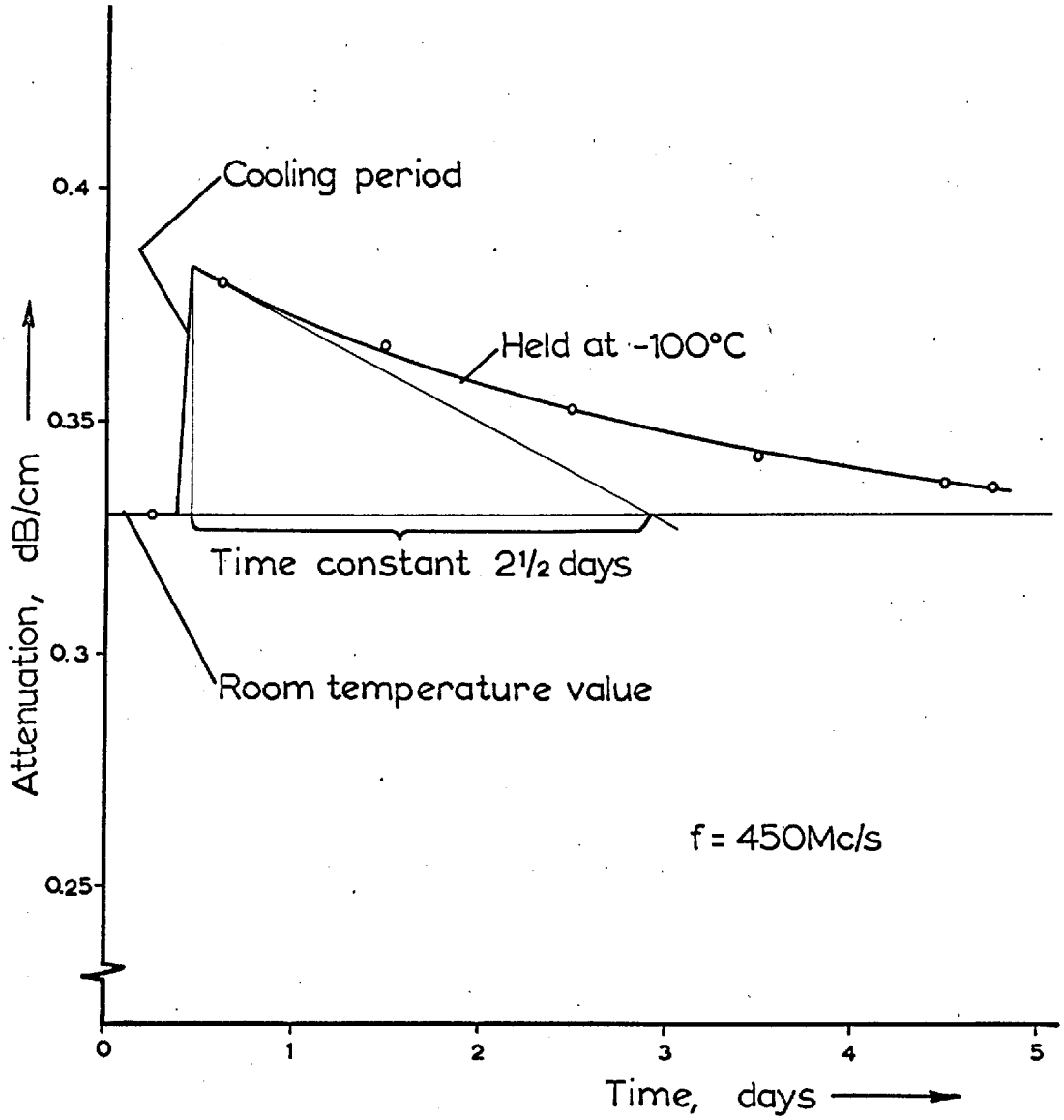


FIG. 11.3 CHANGE IN ATTENUATION FOR A BC-CUT QUARTZ AT -100°C.

range of the measurements (30°C to -150°C) could be considered constant. Small changes in the electrical properties of the transducer cavity system as a result of cooling, were easily compensated for by altering the transmitter frequency.

The c.w. r.f. heating power is of the order of 1W causing only a conservatively estimated 20 millidegree C rise in the temperature of the cavity body. The dielectric heating of the quartz crystal is negligibly small (0.1mW).

The amplitude stability of the electronic system was such that there was no noticeable change in the measured amplitudes over a time span of several hours, as was indicated by the fact that the straight lines fitted over the difference points always passed through the origin of the coordinate system (e.g. Fig. 11.1a). There was, however, some slow frequency drifting of the transmitter pulse. To overcome the detrimental effects of frequency drifting on the accuracy of the measurements, the amplitude of the received signal was often maximised during the measurements for example, at 450Mc/s by adjusting the feedback micrometer and thereby slightly altering the transmitter frequency. Since the thermostatted transducer cavity had a narrower operating bandwith than any other item in the r.f. electronic or transmission system, and its centre frequency was not subject to drifting, maximising the received signal restored the transmitter frequency to its original value.

Some saturation of the receiver system for a few microseconds after the transmitter firing did not affect the liquid measurements.

The accuracy of the calibration of the piston attenuators is better than 0.1dB per 10dB range. Amplitude changes could be measured to within 0.05dB. It is estimated that after the averaging effect of the many echoes measured the overall accuracy of the measured R_L values is $\pm$ 400 Ohms or $\pm$3%, whichever is the worst.

CHAPTER 12.

THE LIMITING HIGH FREQUENCY RIGIDITY MODULUS OF SOME LIQUIDS OF AROMATIC HYDROCARBONS.

12.1 MEASUREMENTS OF THE TEMPERATURE DEPENDENCE OF THE RIGIDITY MODULUS.

The real part of the mechanical impedance of a number of organic liquids have been measured as part of a general programme of investigations into the basic viscous and elastic properties of liquids with relatively simple molecular structures (Barlow, Lamb, Matheson and Richter, 1965; Barlow, Lamb, Matheson, Padmini and Richter, 1966; Barlow, Erginsav and Lamb, 1966). The following liquids have been investigated:

sec-butyl benzene
n-butyl benzene
n-propyl benzene
di-iso-butyl phthalate
di-(2-ethyl hexyl) phthalate.

The chemical symbols are given in conjunction with the diagrams of Figs. 12.2 - 12.6. Samples of sec-butyl benzene and n-butyl benzene were obtained from British Drug Houses Ltd., and of n-propyl benzene from the Aldrich Chemical Co. Ltd. Samples of di-iso-butyl phthalate were supplied by Messrs. A. Boake Roberts and Co. Ltd., and a sample of di-(2-ethyl hexyl) phthalate was obtained from Messrs. Hopkins and Williams Ltd.

All the above liquids can be supercooled to form rigid glasses with no crystallisation taking place for at least 3 hours, thus enabling measurements to be taken over a wide range of temperatures, from ambient down to $-150^{\circ}C$. All the various thermostats

mentioned in Section 9.1 were used to cover the temperature range. It was found necessary to keep the test liquids over P_2O_5 in an evacuated desiccator right until the time of injection into the transducer cavity.

The BC crystal listed as No. 1 in Table 7.1 was used for most of the measurements, though occasionally the BC No. 2, X No. 11 and X No. 12 crystals and a non-piezoelectric silicon metal single crystal with attached transducer were also used to check the consistency of the results obtained with different types of crystals and ~~liquid~~ Solid impedances.

Since the rigidity modulus is simply related to R_L^2/ρ (Equation 11.5a), it is this latter quantity that is given as the result of the measurements. R_L is calculated from Equation 11.11 and the density from the equation:

$$\rho = \rho_r \left[1 - a(T - 273.2) \right] \qquad 12.1$$

The values of the parameters in the density equation are given in Appendix J, as determined by A. J. Matheson (Barlow, Lamb and Matheson, 1965) for the benzene derivatives and by A. J. Barlow for phthalates to an accuracy of 0.1%.

For sec-butyl benzene a large number of measurements have been made from 30°C down to the glass transition temperature. The resulting R_L^2/ρ values are plotted in Fig. 12.1 as a function of temperature between -60°C to -145°C, at the frequencies of 450Mc/s and 1000Mc/s. In the same diagram are also shown R_L^2/ρ values measured by A. J. Matheson at 30Mc/s. For values of R_L^2/ρ greater than about 0.5×10^{10} dyn/cm^2 X_L is much less than R_L and the measured values then represent sensibly the temperature

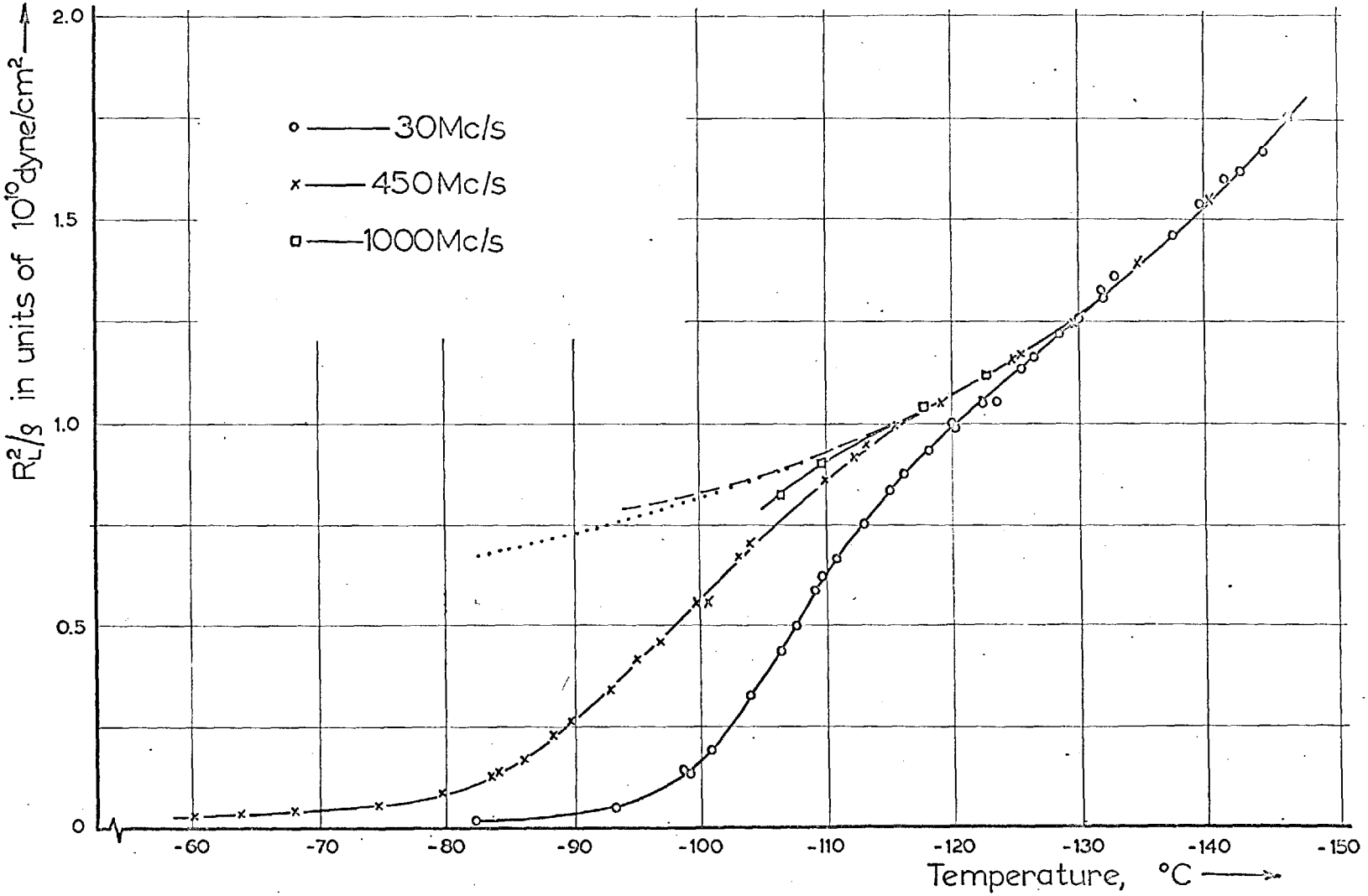


FIG. 12.1 TEMPERATURE DEPENDENCE OF R_L^2/g FOR sec-BUTYL BENZENE.

dependence of G'. At low temperatures the three curves for different frequencies coincide, showing that relaxation is no longer occuring. Therefore it is concluded, that the increase in G' with decreasing temperature in this region is due to the temperature dependence of the limiting high frequency modulus, G_∞, and not to relaxation.

The temperature dependence of G between $-145^\circ C$ and $-115^\circ C$ is given directly by the measured values of R_L^2/ς at 1000Mc/s. An estimate of G_∞ between $-115^\circ C$ and $-90^\circ C$ may be obtained by comparing the relaxation data at 450Mc/s and 30Mc/s in the following way: according to the principle of time-temperature superposition (Section 2.7) the ratio of R_L^2/ς at two different temperatures corresponding to the same reduced frequency ($\propto f$) is equal to the ratio of values of G_∞ at the two temperatures in question. Values of G_∞ obtained in this way are shown as a dashed line in Fig. 12.1.

The viscosity data, necessary for the calculation of the reduced frequencies is obtained from the paper by Barlow, Lamb and Matheson (1966). The viscosity values are calculated from the formula

$$\ln\eta = A' + \frac{B'}{T-T_o} \qquad 12.2$$

The parameters A', B' and T_o in given temperature ranges are listed in Appendix J. The viscosity data suggested to the above authors that four of the five liquids used in the present investigations existed either in a high temperature form or a low temperature form. Each form is described by a different set of parameters in Equation 12.2. The change from one form to the other occurs at the "intersection temperature", listed in the table of Appendix J. Equation 12.2 is predicted by Barlow et al, generalising

the free volume theory of Doolittle (1951, 1957).

The measured G_∞ values for sec-butyl benzene do not support the various available theories devised for the description of the temperature dependence of the limiting high frequency rigidity of liquids (Meister et al. 1960; Hirai et al. 1958). It is believed that, similarly to the value of viscosity, the value of G_∞ is intimately related to the free volume in the liquid. The simple form of

$$S = S_o(1 + D\, v_f) \qquad 12.3$$

is assumed for the dependence of the limiting high frequency compliance ($= 1/G_\infty$) on the free volume. In the equation D is a constant, v_f is the free volume, and S_o is the value of S at the temperature T_o. T_o is somewhat lower than the glass transition temperature T_g and is the fundamental reference temperature for all molecular transport processes (Barlow, Lamb and Matheson, 1966). At T_o the glass would possess no free volume other than the packing free volume, and it would have an infinite viscosity. For liquids (which can be supercooled to approach the temperature of T_o) the slowness of the molecular motion below the glass transition temperature makes it impossible to attain this equilibrium state, and the free volume does not decrease appreciably below its value at T_g. (At T_g the viscosity is 10^{13} Poise by definition and the molecular relaxation time is about 15 minutes.)

If ρ and ρ_o are the densities of the liquid at temperatures T and T_o, respectively, the free volume can be expressed as

$$v_f = \frac{1}{\rho} - \frac{1}{\rho_o} \qquad 12.4$$

For the supercooled liquids considered here the density is a linear function of temperature (Equation 12.1) so the free volume can also be approximately regarded within an error of 1 in 10^3

as linearly dependent on temperature. Then

$$S = \frac{1}{G_o}\left[\, 1 + P(T-T_o) \,\right] \qquad 12.5$$

or

$$G = \frac{G_o}{1 + P(T-T_o)} \qquad 12.6$$

The dotted curve in Fig. 12.1 has been fitted to this equation. At temperatures below $-115^{\circ}C$ this agrees with the measured values of G_∞. In the range $-115^{\circ}C$ to $-95^{\circ}C$ the agreement with the dashed curve is within the experimental error of $\pm 3\%$.

In Figs. 12.2 - 12.6 values of $1{:}R_L^2/\varrho$ measured at 450Mc/s are plotted versus temperature for the five liquids investigated. The appropriate values of T_o and T_g are also marked on the temperature scales. The measured values of $1{:}G_\infty$ given in these diagrams indicate that Equation 12.5 can be used with confidence in describing the temperature dependence of the limiting high frequency compliance of simple liquids. The measured values, as expected, do not follow the straight line below the glass transition temperature. Extending the straight line to the temperature of T_o gives a value for $1/G_o$ in all cases about 1 to 3×10^{-11} cm^2/dyne, comparable to the compliance of a crystalline solid. The graphically obtained parameters G_o and P of Equations 12.5 and 12.6 are given in Table 12.1 overleaf:

Table 12.1

Parameters of Equations 12.5 and 12.6

Test liquid:	T_o(°K)	G_o(dyne/cm^2)	P(°K^{-1})
sec-butyl benzene*	98.6	5.55×10^{10}	0.077
sec-butyl benzene**	128.9	5.55 "	0.190
n-butyl benzene	101.4	5.50 "	0.105
n-propyl benzene	109.7	3.0 "	0.059
di-iso-butyl phthalate	144.9	6.65 "	0.084
di-(2-ethyl hexyl) phthalate	150.6	4.0 "	0.068

* aggregated or low temperature form

**unaggregated or high temperature form

With sec-butyl benzene about 30% (randomly) of the measured points in the temperature range -100°C to -125°C did not fall on the main curve, but tended to form a second branch. Probably it is not fortuitous that a straight line through the points of this second branch defines the right $1/G_o$ value at the T_o temperature for the high temperature form of this liquid. The explanation suggested by Barlow, Lamb and Matheson (1966) for the existence of the two forms was the association of the molecules into small aggregates of two or three molecules which are the units of flow in the supercooled state. Now, it is thought, that on certain occasions when the cooling of the sample liquid on injection into the transducer cavity was so rapid that not only crystallisation, but the formation of aggregates was also prohibited, then the measurements gave the G_∞ value of the unaggregated liquid. The other aggregate forming liquids always appeared to be in the low temperature form below the "intersection temperature".

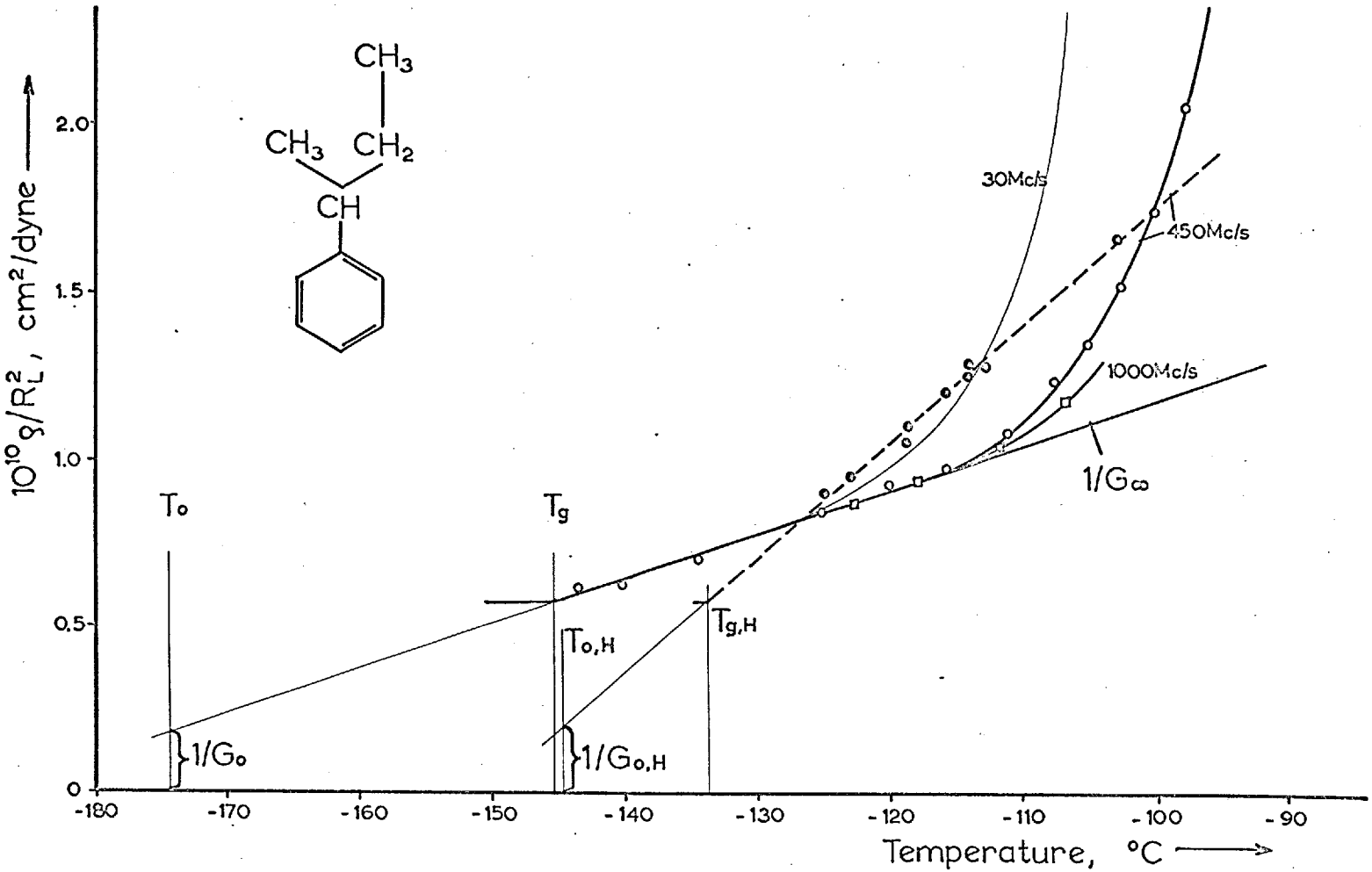


FIG. 12.2 TEMPERATURE DEPENDENCE OF THE LIMITING HIGH FREQUENCY COMPLIANCE FOR sec-BUTYL BENZENE.

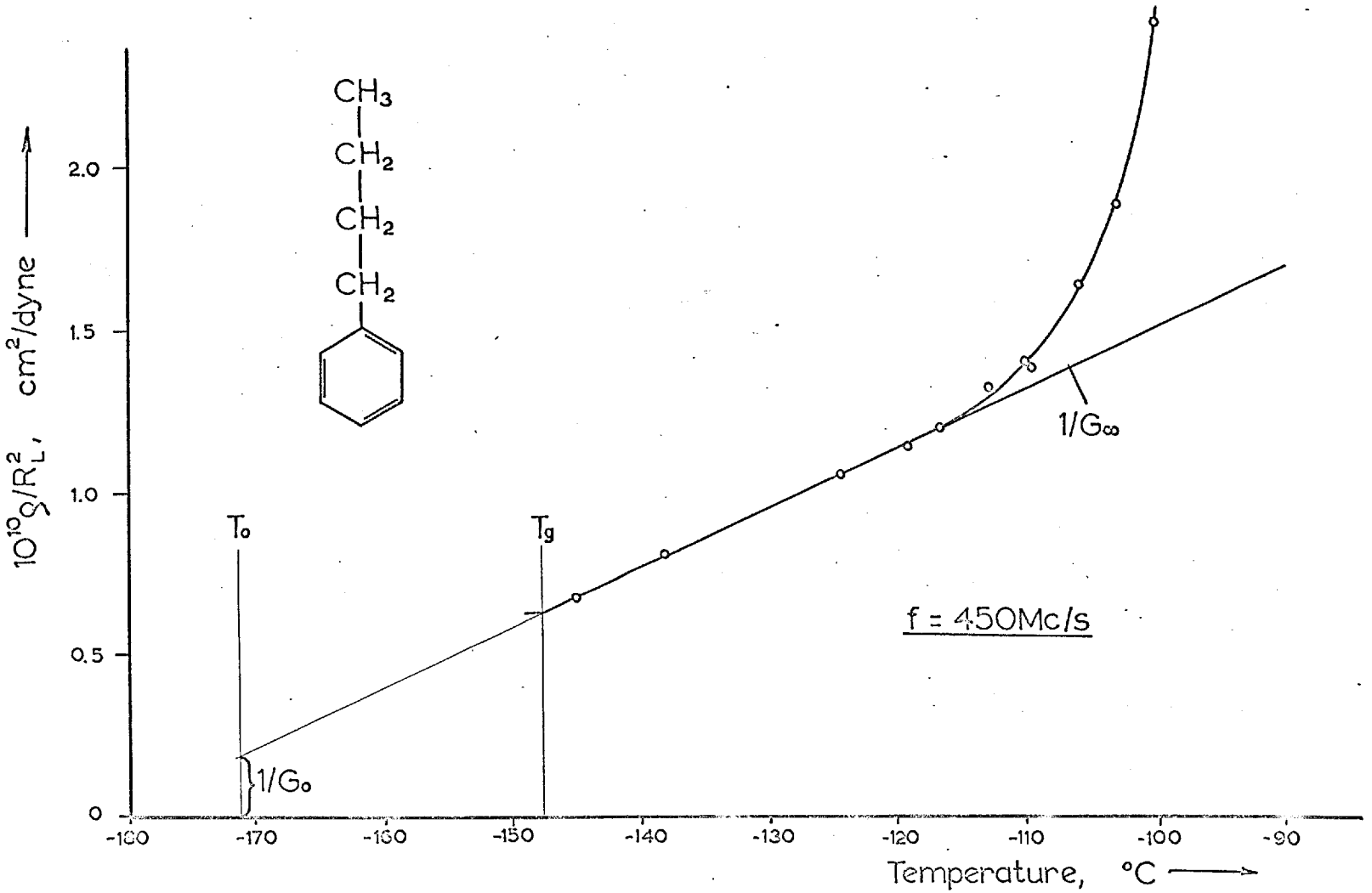


FIG. 12.3 TEMPERATURE DEPENDENCE OF THE LIMITING HIGH FREQUENCY COMPLIANCE FOR n-BUTYL BENZENE.

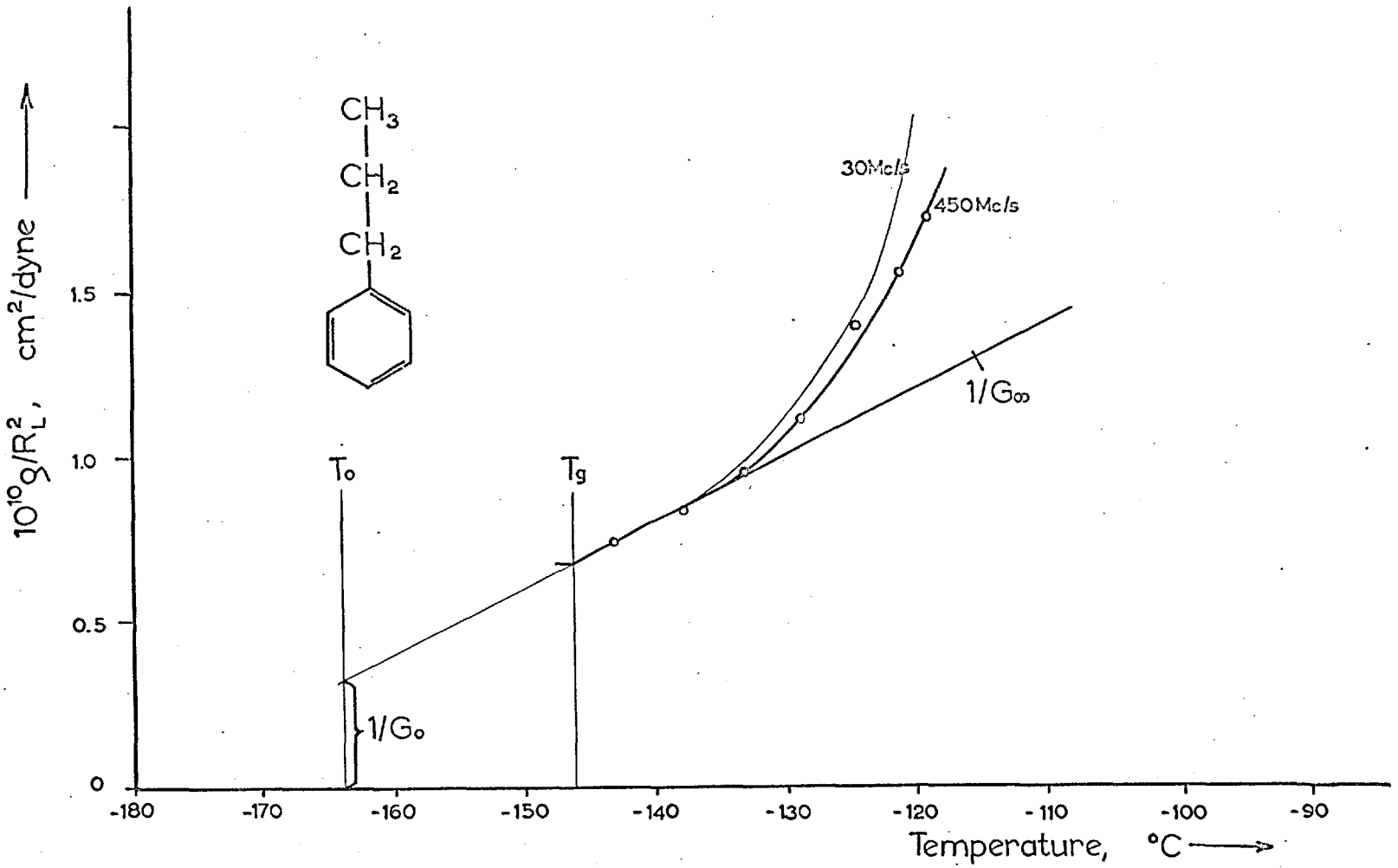


FIG. 12.4 TEMPERATURE DEPENDENCE OF THE LIMITING HIGH FREQUENCY COMPLIANCE FOR n-PROPYL BENZENE.

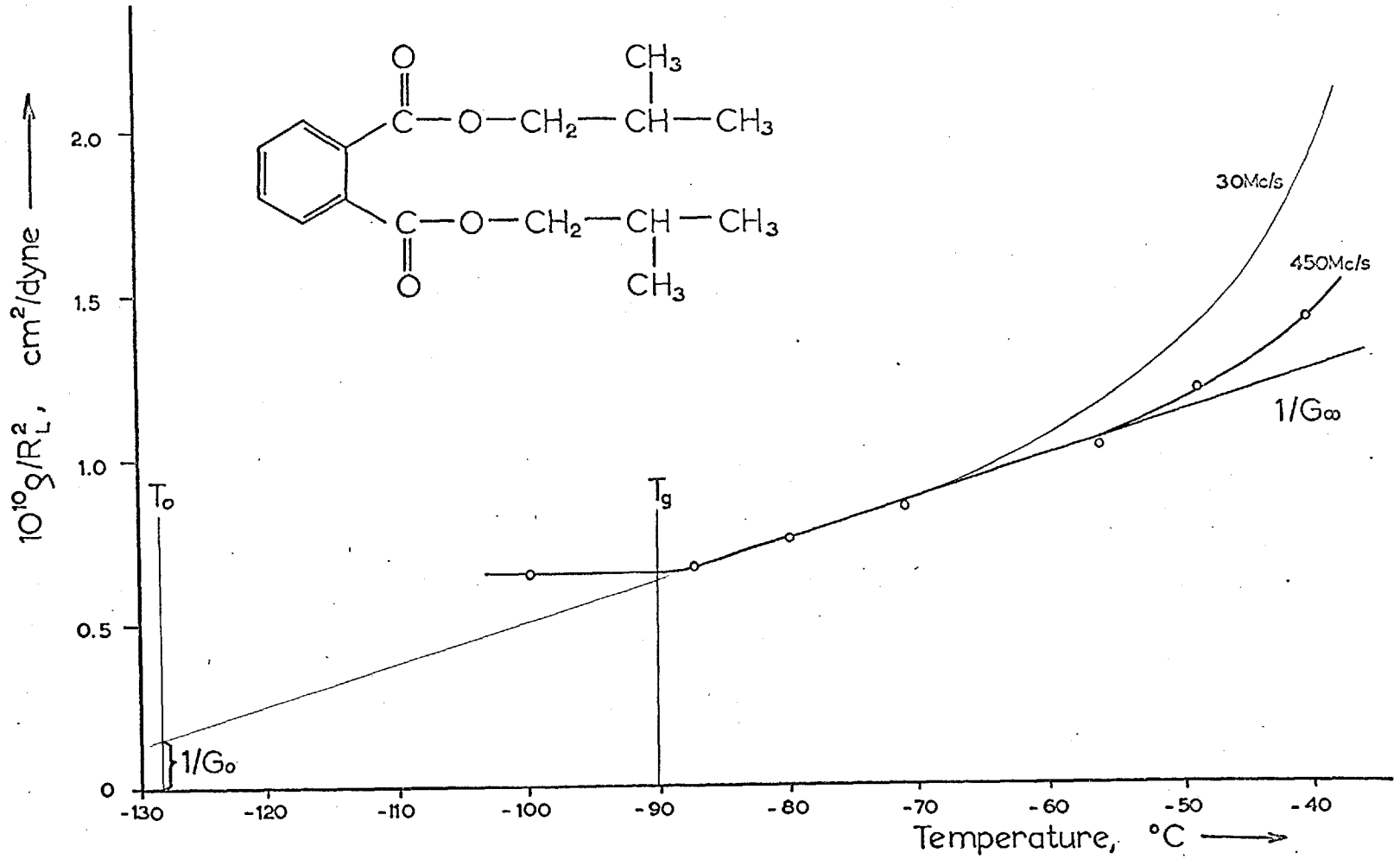


FIG. 12.5 TEMPERATURE DEPENDENCE OF THE LIMITING HIGH FREQUENCY COMPLIANCE FOR di-iso-BUTYL PHTHALATE.

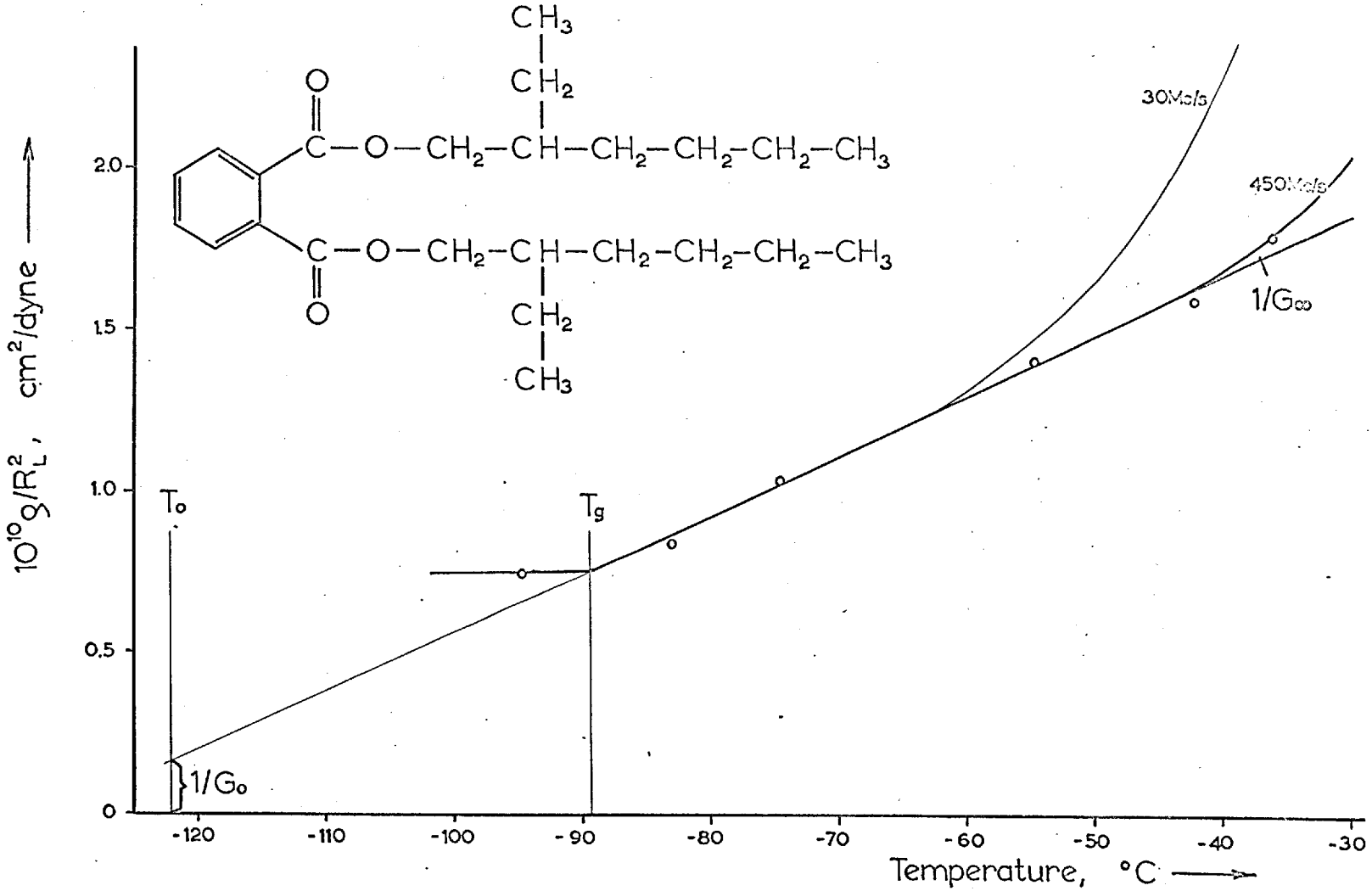


FIG. 12.6 TEMPERATURE DEPENDENCE OF THE LIMITING HIGH FREQUENCY COMPLIANCE FOR di-(2-ETHYL HEXYL) PHTHALATE.

12.2 DETERMINATION OF THE RELAXATION BEHAVIOUR OF sec-BUTYL BENZENE

The G_∞ value, and hence the normalising factor β can now be determined from Equation 12.6 at temperatures where viscoelastic relaxation occurs. In the knowledge of the value of β as a function of temperature the normalised plot of $R_L/\varsigma\beta G_\infty$ versus reduced frequency αf can be obtained and is shown in Fig. 12.7 for the aggregated form of sec-butyl benzene. G_{oo} is the limiting rigidity at an arbitrarily selected reference temperature T_{oo}. For comparison, the curve corresponding to a single relaxation time is also shown indicating that the relaxation region is about twice as broad as that of a single relaxation.

In Fig. 12.8 the plot of the logarithm of R_L^2/ς for sec-butyl benzene is shown against reduced frequency $\alpha\beta f$, at frequencies below the relaxation region, obtained at 450Mc/s and 1000Mc/s. The temperature range over which these measurements were made (30°C to -80°C) is too far removed from the range where G_∞ of the unaggregated liquid was measured to allow the use of Equation 12.6 for the calculation of the factor β. G_∞, however, is not expected to vary much at these relatively high temperatures.

The 45° line in Fig. 12.8 corresponds to Newtonian behaviour, when

$$R_L^2/\varsigma = \pi \eta_{30} f \alpha \beta \qquad 12.6$$

At low reduced frequencies the measured values should asymptotically approach the Newtonian line. (For single relaxation R_L^2/ς is 10% higher than Newtonian for $\omega\tau = 0.1$, and 1% higher for $\omega\tau = 0.01$.) According to the evidence of Fig. 12.8 at 450Mc/s the beginning of the relaxation has a noticeable effect on the liquid impedance even at 30°C, where the static viscosity of the liquid is less than 1cP.

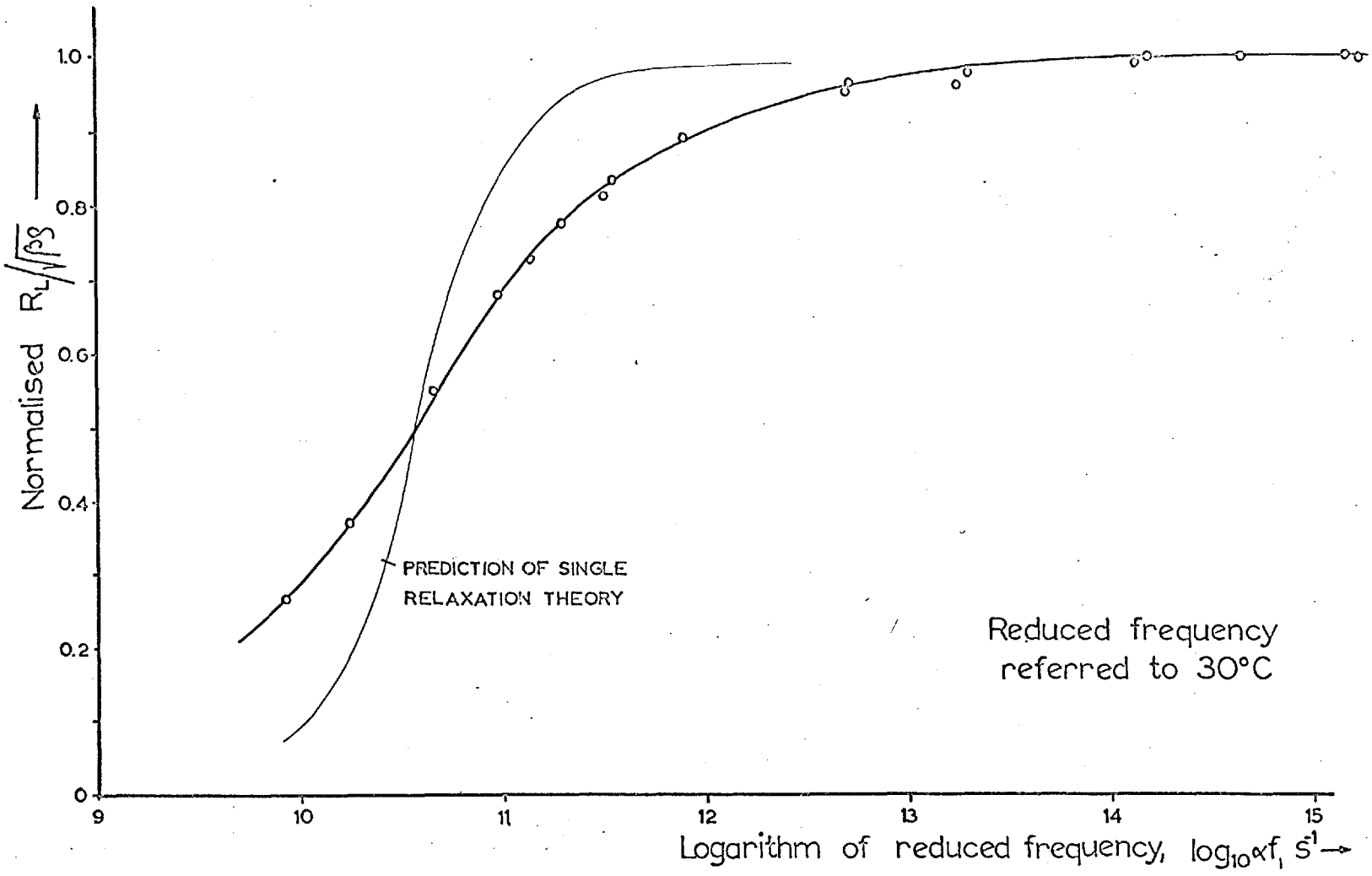


FIG. 12.7 VISCOELASTIC RELAXATION OF sec-BUTYL BENZENE.

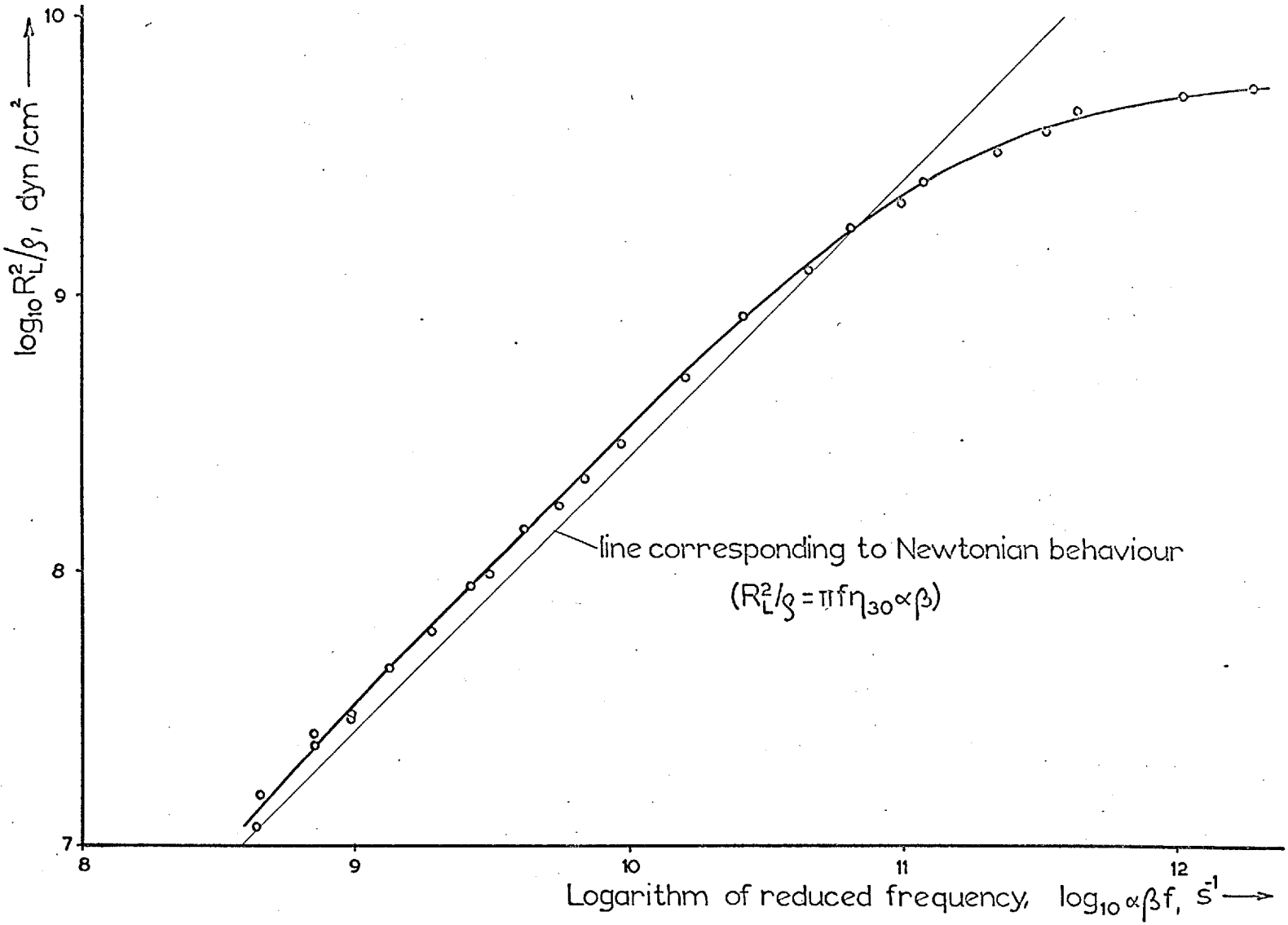


FIG. 12.8 THE BEGINNING OF THE RELAXATION REGION FOR sec-BUTYL BENZENE.

12.3 CONCLUSIONS.

As an example of the application of the newly developed experimental technique to the study of the viscoelastic properties of liquids, the temperature dependence of the limiting high frequency rigidity modulus has been determined for a number of supercooled hydrocarbons. Owing to the high frequency of the acoustic system, G_∞ could be measured over a much larger temperature range than was possible to early workers (Hirai et al. 1958; Meister et al. 1960). If the limiting high frequency compliance is linearly related to free volume in the liquid, the resulting temperature dependence of G_∞ is in good agreement with the measurements over the whole temperature range investigated. The results of these measurements together with further investigations into the relation of G_∞ and relaxation behaviour upon molecular structure is the subject of a forthcoming paper (Part I: Barlow, Lamb, Matheson, Padmini and Richter, 1966; Part II: Barlow, Erginsav and Lamb, 1966).

The operating frequency of the experimental system can be set anywhere between 300Mc/s and 2000Mc/s. 450Mc/s has been chosen for most of the liquid impedance measurements, because at this frequency the accuracy of $\pm 3\%$ could be achieved. At higher frequencies the increased acoustic attenuation in quartz reduces the number ofdetectable echoes considerably thereby reducing the available accuracy. At 2000Mc/s less accurate G_∞ measurements could be obtained over a temperature range which is increased by about 4°C compared with that at 450Mc/s. To extend the temperature range of the direct G_∞ measurements towards higher temperatures by more than 10°C, it would be necessary to raise the operating frequency considerably. Expected values of R_L^2/ρ as function

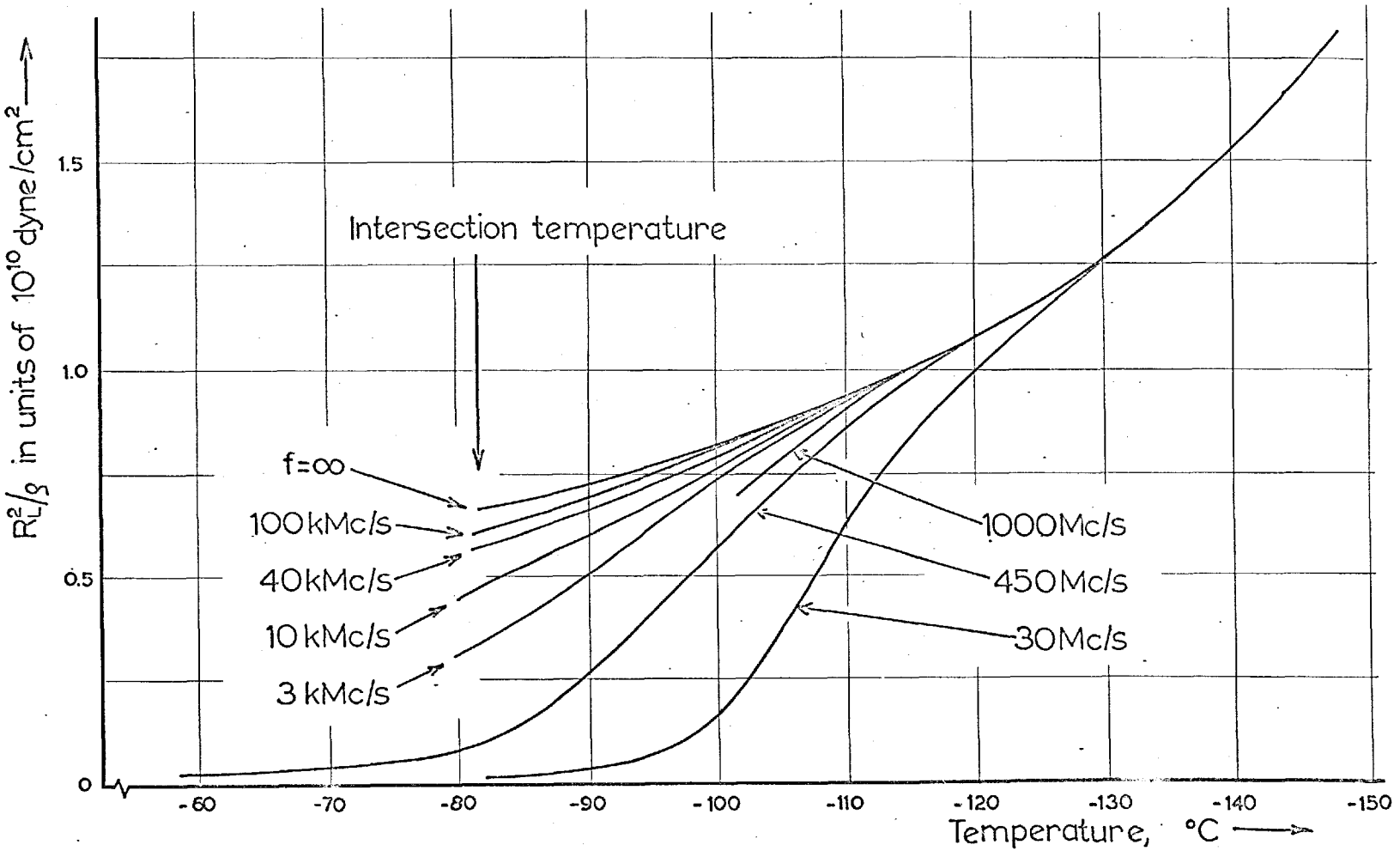


FIG. 12.9 EFFECT OF INCREASED FREQUENCY ON R_L^2/ρ MEASUREMENTS.
(EXPECTED VALUES FOR sec-BUTYL BENZENE.)

of temperature at different frequencies are shown in Fig. 12.9, according to which the development of a measuring system at 10,000Mc/s would be the next worth-while aim. Such a system would probably use one of the recently discovered low-loss piezoelectric crystals, for example lithium metaniobate.

It is concluded, that the experimental system is capable of making successful viscoelastic measurements on substances of all viscosities, including low viscosity liquids with less than 1cP viscosity, and also very viscous glasses. The measurements of liquid impedances at 450Mc/s and 1000Mc/s gave values that were in close agreement with values obtained at much lower frequencies using established measurement techniques. The various theoretical and practical investigations that have been made in connection with the present work and which are described in Parts II and III of this thesis also have application in research work into the solid state by microwave acoustics.

P A R T V .

APPENDICES.

APPENDIX A.
SYMMETRY AND DECOMPOSITION OF CARTESIAN TENSORS.

A polar tensor in Cartesian coordinate systems is defined by the following transformation rule:

$$A'_{ij....} = \frac{\partial x'_i}{\partial x_m} \cdot \frac{\partial x'_j}{\partial x_n} ..... A_{mn} \qquad A.1$$

Since there is no distinction between covariant and contravariant components in Cartesian rectangular coordinates, all indices are written as lower types, and repeated indices automatically mean summation.

An axial tensor is defined by the following transformation rule:

$$\hat{A}_{ij....} = (\Delta)^N \frac{\partial x'_i}{\partial x_m} \frac{\partial x'_j}{\partial x_n} ....\hat{A}_{mn} \qquad A.2$$

where Δ is the determinant formed by the differential coefficients:

$$\det \frac{\partial x'_i}{\partial x_m} \qquad (= \pm 1) \qquad A.3$$

and N is the rank of the tensor.

The alternating tensor ϵ_{ijk} is defined as (Prager 1961)

$$\epsilon_{ijk} = \begin{bmatrix} +1 \\ -1 \\ 0 \end{bmatrix} \text{according to whether i,j,k} \begin{bmatrix} \text{form an even} \\ \text{form an odd} \\ \text{do not form a} \end{bmatrix} \text{permutation of 1,2,3} \qquad A.4$$

With the use of the alternating tensor, the definition of the vector product of two vectors takes the form of:

$$p_i = \epsilon_{ijk} u_j \cdot v_k = (\underline{u} \times \underline{v}) \qquad A.5$$

and the vector operator curl can be written in the form of

$$(\text{curl } A_k)_i = \epsilon_{ijk} \frac{\partial A_k}{\partial x_j} \qquad \text{A.6}$$

A tensor A_{ij} of rank 2 can be decomposed (Weyl, 1946) into a symmetric part A^S_{ij} and an antisymmetric part A^A_{ij}:

$$A_{ij} = A^S_{ij} + A^A_{ij} \qquad \text{A.7}$$

with

$$A^S_{ij} = \tfrac{1}{2}(A_{ij} + A_{ji}) \qquad \text{A.8}$$

$$A^A_{ij} = \tfrac{1}{2}(A_{ij} - A_{ji}) \qquad \text{A.9}$$

The above decomposition is invariant under the group of all tensor transformations (i.e. a symmetric tensor will remain symmetric after a transformation of the type of Equation A.1 or A.2) and irreducible (i.e. there is no finer decomposition into invariant groups.)

The symmetric tensor is further decomposed (invariantly under transformations corresponding to a rotation of the coordinate axes) into a deviatoric (or traceless) and a spherical tensor:

$$A^S_{ij} = A^D_{ij} + \frac{1}{3} \text{tr } A^S_{kl} . I_{ij} \qquad \text{A.10}$$

where $$\text{tr } A^S_{kl} = A_{kk} = A_{11} + A_{22} + A_{33} \qquad \text{A.11}$$

and $$I_{ij} = \delta_{ij} \qquad \text{A.12}$$

The Kronecker delta δ_{ij} has the value of 1 when $i = j$, and 0 when $i \neq j$.

The scalar product of two symmetrical tensors of rank two can be given as (deGroot and Mazur, 1962)

$$A^{S}_{ij} \cdot B^{S}_{ij} = A^{D}_{ij} \cdot B^{D}_{ij} + \frac{1}{3} \text{tr } A_{ij} \cdot \text{tr } B_{kl} \qquad \text{A.13}$$

A tensor of rank 3 can be decomposed (under the group of all tensor transformations) into 4 irreducible parts: symmetric, antisymmetric, principal and antiprincipal. When the decomposition is applied to the couple stress of rank 3, where $G_{ijk} = -G_{jik}$, these four parts are obtained as (Toupin, 1962)

$$\begin{aligned} G^{S}_{ijk} &= 0 \\ G^{A}_{ijk} &= \frac{1}{3}(G_{ijk} + G_{jki} + G_{kij}) \\ G^{P}_{ijk} &= \frac{1}{3}(2G_{ijk} + G_{kji} - G_{kij}) \\ G^{\overline{P}}_{ijk} &= 0 \end{aligned} \qquad \text{A.14}$$

In Equation A.14 above G^{A}_{ijk} has one independent component, and G^{P}_{ijk} has 8 independent components.

An antisymmetric tensor of rank 2 has 3 independent components, therefore it is possible to associate it with a dual vector, that has the same 3 components. The following rule is adopted for the association:

$$\hat{t}_i = \epsilon_{ijk} T^{A}_{jk} \quad (= \epsilon_{ijk} T_{jk}) \qquad \text{A.15}$$

Multiplying the two sides of Equation A.15 by ϵ_{ilm} gives

$$T^{A}_{lm} = \tfrac{1}{2} \epsilon_{ilm} \hat{t}_i \qquad \text{A.16}$$

The 9 independent components of the couple stress of rank 3 define the dual axial tensor of rank 2 by

$$G_{il} = \tfrac{1}{2} \epsilon_{ijk} G_{jkl} \qquad \text{A.17}$$

By comparing Equations A.14 and A.17 one finds that

$$\tfrac{1}{2}\epsilon_{ijk} G^{A}_{jkl} = \frac{1}{3} \mathrm{tr}\,(\hat{G}_{il})$$

and

$$\tfrac{1}{2}\epsilon_{ijk} G^{P}_{jkl} = \hat{G}^{D}_{il} . \qquad \text{A.18}$$

APPENDIX B.

CRYSTALLOGRAPHIC SYMMETRY OPERATION OF QUARTZ.

The differential coefficients $\partial x'_i/\partial x_m$ in the tensor transformations of Equations A.1 or A.2 can be given as the components of a matrix, with i as the row number and m as the column number. Owing to the crystallographic symmetry of the class 32 to which quartz belongs, any of the following 6 matrix operators is an identity operator (Smith et al. 1963)

$$I_1 = \begin{pmatrix} 1 & 0 & 0 \\ 0 & 1 & 0 \\ 0 & 0 & 0 \end{pmatrix}$$

$$I_2 = \begin{pmatrix} -\frac{1}{2} & +\sqrt{\frac{3}{2}} & 0 \\ -\sqrt{\frac{3}{2}} & -\frac{1}{2} & 0 \\ 0 & 0 & 1 \end{pmatrix} \qquad \text{B.1}$$

$$I_3 = \begin{pmatrix} -\frac{1}{2} & -\sqrt{\frac{3}{2}} & 0 \\ \sqrt{\frac{3}{2}} & -\frac{1}{2} & 0 \\ 0 & 0 & 1 \end{pmatrix}$$

$$I_4 = \begin{pmatrix} 1 & 0 & 1 \\ 0 & -1 & 0 \\ 0 & 0 & -1 \end{pmatrix}$$

$$I_5 = \begin{pmatrix} -\frac{1}{2} & \sqrt{\frac{3}{2}} & 0 \\ \sqrt{\frac{3}{2}} & \frac{1}{2} & 0 \\ 0 & 0 & -1 \end{pmatrix} \qquad \text{B.1 (cont.)}$$

$$I_6 = \begin{pmatrix} -\frac{1}{2} & -\sqrt{\frac{3}{2}} & 0 \\ -\sqrt{\frac{3}{2}} & \frac{1}{2} & 0 \\ 0 & 0 & 1 \end{pmatrix}$$

APPENDIX C.

EXPLICIT FORMS FOR THE TENSORS OF STRAIN, ROTATION AND DISTORTION.

The strain is defined as the symmetrical part of the displacement gradient tensor:

$$S_{kl} = \begin{pmatrix} \frac{\partial u_1}{\partial x_1}, & \frac{1}{2}\left(\frac{\partial u_1}{\partial x_2} + \frac{\partial u_2}{\partial x_1}\right), & \frac{1}{2}\left(\frac{\partial u_1}{\partial x_3} + \frac{\partial u_3}{\partial x_1}\right), \\ \frac{1}{2}\left(\frac{\partial u_2}{\partial x_1} + \frac{\partial u_1}{\partial x_2}\right), & \frac{\partial u_2}{\partial x_2}, & \frac{1}{2}\left(\frac{\partial u_2}{\partial x_3} + \frac{\partial u_3}{\partial x_2}\right), \\ \frac{1}{2}\left(\frac{\partial u_3}{\partial x_1} + \frac{\partial u_1}{\partial x_3}\right), & \frac{1}{2}\left(\frac{\partial u_3}{\partial x_2} + \frac{\partial u_2}{\partial x_3}\right), & \frac{\partial u_3}{\partial x_3}, \end{pmatrix} \qquad \text{C.1}$$

The local rotation is defined in the case of infinitesimally small rotations as

$$R_{kl} = \begin{pmatrix} 0, & \frac{1}{2}\left(\frac{\partial u_1}{\partial x_2} - \frac{\partial u_2}{\partial x_1}\right), & -\frac{1}{2}\left(\frac{\partial u_3}{\partial x_1} - \frac{\partial u_1}{\partial x_3}\right), \\ -\frac{1}{2}\left(\frac{\partial u_1}{\partial x_2} - \frac{\partial u_2}{\partial x_1}\right), & 0, & \frac{1}{2}\left(\frac{\partial u_2}{\partial x_3} - \frac{\partial u_3}{\partial x_2}\right), \\ \frac{1}{2}\left(\frac{\partial u_3}{\partial x_1} - \frac{\partial u_1}{\partial x_3}\right), & -\frac{1}{2}\left(\frac{\partial u_2}{\partial x_3} - \frac{\partial u_3}{\partial x_2}\right), & 0, \end{pmatrix} \qquad \text{C.2}$$

The local distortion is defined as

$$\hat{x}_{kl} = \frac{\partial \hat{R}_k}{\partial x_1} \qquad \text{C.3}$$

hence

$$\hat{x}_{kl} = \begin{pmatrix} \frac{\partial^2 u_3}{\partial x_1 \partial x_2} - \frac{\partial^2 u_2}{\partial x_1 \partial x_3}, & \frac{\partial^2 u_3}{\partial x_2 \partial x_2} - \frac{\partial^2 u_2}{\partial x_2 \partial x_3}, & \frac{\partial^2 u_3}{\partial x_2 \partial x_3} - \frac{\partial^2 u_2}{\partial x_3 \partial x_3}, \\ \frac{\partial^2 u_1}{\partial x_1 \partial x_3} - \frac{\partial^2 u_3}{\partial x_1 \partial x_1}, & \frac{\partial^2 u_1}{\partial x_2 \partial x_3} - \frac{\partial^2 u_3}{\partial x_1 \partial x_2}, & \frac{\partial^2 u_1}{\partial x_3 \partial x_3} - \frac{\partial^2 u_3}{\partial x_1 \partial x_3}, \\ \frac{\partial^2 u_2}{\partial x_1 \partial x_1} - \frac{\partial^2 u_1}{\partial x_1 \partial x_2}, & \frac{\partial^2 u_2}{\partial x_1 \partial x_2} - \frac{\partial^2 u_1}{\partial x_2 \partial x_2}, & \frac{\partial^2 u_2}{\partial x_1 \partial x_3} - \frac{\partial^2 u_1}{\partial x_2 \partial x_3}, \end{pmatrix} \qquad \text{C.4}$$

It is evident that $\operatorname{tr} \hat{x} = 0$.

TABLES OF ADMISSIBLE MATERIAL COEFFICIENTS FOR QUARTZ WHEN THE ANTISYMMETRIC STRESS IS NOT NEGLECTED.

TABLE D.1

TABLE OF ADMISSIBLE PIEZOELECTRIC STRAIN COEFFICIENTS d_{m-ij} FOR QUARTZ.

	11(1)	22(2)	33(3)	23(4)	13(5)	12(6)	32(7)	31(8)	21(9)
1	d_{11}	$-d_{11}$	0	d_{14}	0	0	d_{14}	0	0
2	0	0	0	0	$-d_{14}$	d_{11}	0	$-d_{14}$	d_{11}
3	0	0	0	0	0	0	0	0	0

TABLE D.2

TABLE OF ADMISSIBLE PIEZOELECTRIC x-COEFFICIENTS f_{m-ij} FOR QUARTZ.

	11	22	33	23	13	12	32	31	21
1	f_{11}	$-f_{11}$	0	f_{14}	0	0	f_{17}	0	0
2	0	0	0	0	$-f_{14}$	f_{11}	0	$-f_{17}$	f_{11}
3	0	0	0	0	0	f_{36}	0	0	$-f_{36}$

TABLE D.3

TABLE OF ADMISSIBLE ACOUSTICAL ACTIVITY COEFFICIENTS b_{ijkl} FOR QUARTZ.

	11	22	33	23	13	12	32	31	21
11	b_{11}	$b_{11}-2b_{66}$	$2(b_{11}-b_{66})$	b_{14}	0	0	b_{17}	0	0
22	$b_{11}-2b_{66}$	b_{11}	$2(b_{11}-b_{66})$	$-b_{14}$	0	0	$-b_{17}$	0	0
33	$-\frac{1}{2}b_{33}$	$-\frac{1}{2}b_{33}$	b_{33}	0	0	0	0	0	0
23	b_{41}	$-b_{41}$	0	b_{44}	0	0	b_{77}	0	0
13	0	0	0	0	b_{44}	b_{41}	0	b_{77}	b_{41}
12	0	0	0	0	b_{14}	b_{66}	0	b_{17}	b_{66}
32	b_{41}	$-b_{41}$	0	b_{44}	0	0	b_{77}	0	0
31	0	0	0	0	b_{44}	b_{41}	0	b_{77}	b_{41}
21	0	0	0	0	b_{14}	b_{66}	0	b_{17}	b_{66}

TABLE D.4

TABLE OF ADMISSIBLE ELASTIC STIFFNESS COEFFICIENTS FOR QUARTZ. c_{ijkl}

	11	22	33	23	13	12	32	31	21
11	c_{11}	$\frac{1}{2}c_{11}-c_{66}$	c_{13}	c_{14}	0	0	c_{14}	0	0
22	$\frac{1}{2}c_{11}-c_{66}$	c_{11}	c_{13}	$-c_{14}$	0	0	$-c_{14}$	0	0
33	c_{13}	c_{13}	c_{33}	0	0	0	0	0	0
23	c_{14}	$-c_{14}$	0	c_{44}	0	0	c_{44}	0	0
13	0	0	0	0	c_{44}	c_{14}	0	c_{44}	c_{14}
12	0	0	0	0	c_{14}	c_{66}	0	c_{14}	c_{66}
32	c_{14}	$-c_{14}$	0	c_{44}	0	0	c_{44}	0	0
31	0	0	0	0	c_{44}	c_{14}	0	c_{44}	c_{14}
21	0	0	0	0	c_{14}	c_{66}	0	c_{14}	c_{66}

TABLE D.5

TABLE OF ADMISSIBLE x-STIFFNESS COEFFICIENTS a_{ijkl} FOR QUARTZ.

	11	22	33	23	13	12	32	31	21
11	a_{11}	$-a_{11}-\frac{1}{2}a_{33}$	$-\frac{1}{2}a_{33}$	a_{14}	0	0	a_{17}	0	0
22	$-a_{11}-\frac{1}{2}a_{33}$	a_{11}	$-\frac{1}{2}a_{33}$	$-a_{14}$	0	0	$-a_{17}$	0	0
33	$-\frac{1}{2}a_{33}$	$-\frac{1}{2}a_{33}$	a_{33}	0	0	0	0	0	0
23	a_{14}	$-a_{14}$	0	a_{44}	0	0	a_{47}	0	0
13	0	0	0	0	a_{44}	a_{14}	0	a_{47}	a_{14}
12	0	0	0	0	a_{14}	a_{66}	0	a_{17}	$2a_{11}-a_{66}-\frac{1}{2}a_{33}$
32	a_{17}	$-a_{17}$	0	a_{47}	0	0	a_{77}	0	0
31	0	0	0	0	a_{47}	a_{17}	0	a_{77}	a_{17}
21	0	0	0	0	a_{14}	$2a_{11}-a_{66}-\frac{1}{2}a_{33}$	0	a_{17}	a_{66}

APPENDIX E.

EXPLICIT FORMULAE FOR TENSOR TRANSFORMATIONS IN A MEDIUM POSSESSING THE CRYSTALLINE SYMMETRY OF QUARTZ.

The transformation can be described as consisting of two steps. First the original XYZ crystallographic coordinate system is rotated by an angle ϕ around the Z axis, into the X'Y'Z' system. The matrix of this coordinate transformation is

$$\left(\frac{\partial x_i'}{\partial x_j}\right) = \begin{pmatrix} \cos\phi & \sin\phi & 0 \\ -\sin\phi & \cos\phi & 0 \\ 0 & 0 & 1 \end{pmatrix} \qquad \text{E.1}$$

In the second step the X'Y'Z' coordinate system is rotated around the X' axis by an angle θ into the X"Y"Z" system. The matrix of this second transformation is

$$\left(\frac{\partial x_i''}{\partial x_j'}\right) = \begin{pmatrix} 1 & 0 & 0 \\ 0 & \cos\theta & \sin\theta \\ 0 & -\sin\theta & \cos\theta \end{pmatrix} \qquad \text{E.2}$$

Transformation of XYZ into X"Y"Z" is given by the product of the matrices of Equations E.1 and E.2:

$$\left(\frac{\partial x_i''}{\partial x_j}\right) = \begin{pmatrix} \cos\phi & \sin\phi & 0 \\ -\cos\theta\sin\phi & \cos\theta\cos\phi & \sin\theta \\ \sin\theta\sin\phi & -\sin\theta\cos\phi & \cos\theta \end{pmatrix} \qquad \text{E.3}$$

Transformation of some elastic stiffness coefficients (the following abbreviation is used $c = c_{11} - c_{12} - 2c_{44}$):

$$
\begin{aligned}
c''_{44} = &- \cos^4\theta\left[(c_{11} + c_{33} - 2c_{13} - 4c_{44}) - (\tfrac{1}{2}c \sin^2 2\phi)\right] \\
&+ 4\cos^3\theta \sin\theta\,(c_{14} \cos 3\phi) \\
&+ \cos^2\theta\left[(c_{11} + c_{33} - 2c_{13} - 4c_{44}) - (\tfrac{1}{2}c \sin^2 2\phi)\right] \\
&- \cos\theta \sin\theta\,(2c_{14} \cos 3\phi) \\
&+ c_{44}
\end{aligned}
\qquad \text{E.4}
$$

$$
\begin{aligned}
c''_{22} = &\ \cos^4\theta\left[c_{11} + c_{33} - 2c_{13} - 4c_{44} - \tfrac{1}{2}c \sin^2 2\phi\right] \\
&- \cos^3\theta \sin\theta\,(4c_{14} \cos 3\phi) \\
&+ \cos^2\theta\ 2(c_{13} - c_{33} - 2c_{44}) \\
&+ c_{33}
\end{aligned}
\qquad \text{E.5}
$$

$$
\begin{aligned}
c''_{66} = &\ \cos^2\theta\left[c_{66} - c_{44} + \tfrac{1}{2}c \sin^2 2\phi\right] \\
&+ \cos\theta \sin\theta\,(2c_{14} \cos 3\phi) \\
&+ c_{44}
\end{aligned}
\qquad \text{E.6}
$$

$$c''_{26} = \cos^3\theta\,(\tfrac{1}{2}c \sin 2\phi\cos2\phi) - \cos^2\theta\sin\theta\,(3c_{14}\sin 3\phi) \qquad \text{E.7}$$

$$c''_{46} = -\cos^3\theta\,(3c_{14}\sin3\phi) - \cos^2\theta\sin\theta\,(\tfrac{1}{2}c\sin2\phi\cos2\phi) + \cos\theta\,(2c_{14}\sin 3\phi) \qquad \text{E.8}$$

$$c''_{24} = \cos^4\theta\,(-4c_{14}\cos 3\phi) - \cos^3\theta\sin\theta\,(c_{11} + c_{33} - 2c_{13} - 4c_{44} - \tfrac{1}{2}c\sin^2 2\phi) + \cos^2\theta\,(3c_{14}\cos 3\phi) - \cos\theta\sin\theta\,(c_{13} - c_{33} + 2c_{44}) \qquad \text{E.9}$$

Transformation of the dielectric constant:

$$\epsilon''_{22} = \epsilon_{33} - \cos^2\theta\,(\epsilon_{33} - \epsilon_{11}) \qquad \text{E.10}$$

Transformation of piezoelectric constants:

$$e''_{112} = -\cos\theta\, e_{11}\sin3\phi \qquad \text{E.11}$$

$$e''_{122} = - \cos^2\theta\,(e_{11}\cos 3\phi) + \cos\theta\sin\theta\,(2e_{14}) \qquad \text{E.12}$$

$$e''_{132} = \cos^2\theta\,(2e_{14}) + \cos\theta\sin\theta\,e_{11}\cos 3\phi - e_{14} \qquad \text{E.13}$$

$$e''_{212} = - \cos^2\theta\,e_{11}\cos 3\phi - \cos\theta\sin\theta\,e_{14} \qquad \text{E.14}$$

$$e''_{222} = \cos^3\theta\,e_{11}\sin 3\phi \qquad \text{E.15}$$

$$e''_{232} = - \cos^2\theta\sin\theta\,e_{11}\sin 3\phi \qquad \text{E.16}$$

$$e''_{312} = - \cos^2\theta\,e_{14} + \cos\theta\sin\theta\,e_{11}\cos 3\phi + e_{14} \qquad \text{E.17}$$

$$e''_{322} = -\cos^2\theta \sin\theta \; e_{11} \sin 3\phi \qquad \text{E.18}$$

$$e''_{332} = -\cos^3\theta \; e_{11} \sin 3\phi + \cos \; e_{11} \sin 3\phi \qquad \text{E.19}$$

Transformation formulae of the elastic constants for the rotated Y direction ($\phi = 0$), when the transformation consists of a rotation about the X crystallographic axis (from any rotated Y system) by an angle θ counterclockwise, looking at the origin along the +X axis.

$$c'_{11} = c_{11}$$

$$c'_{22} = c_{22}\cos^4\theta + c_{33}\sin^4\theta + 2(2c_{44}+c_{23})\sin^2\theta \cos^2\theta + 4c_{24}\sin\theta\cos^3\theta + 4c_{34}\sin^3\theta \cos\theta$$

$$c'_{33} = c_{22}\sin^4\theta + c_{33}\cos^4\theta + 2(2c_{44}+c_{23})\sin^2\theta \cos^2\theta - 4c_{24}\sin^3\theta \cos\theta - 4c_{34}\sin\theta \cos^3\theta$$

$$c'_{44} = c_{44} + (c_{22}+c_{33}-4c_{44}-2c_{23})\sin^2\theta \cos^2\theta + 2(c_{24}-c_{34})(\sin^3\theta \cos\theta - \sin\theta \cos^3\theta) \qquad \text{E.20}$$

$$c'_{55} = c_{55}\cos^2\theta + c_{66}\sin^2\theta - 2c_{56} \sin\theta \cos\theta$$

$$c'_{66} = c_{55}\sin^2\theta + c_{66}\cos^2\theta + 2c_{56}\sin\theta \cos\theta$$

$$c'_{12} = c_{12}\cos^2\theta + c_{13}\sin^2\theta + 2c_{14}\sin\theta\cos\theta$$

$$c'_{13} = c_{12}\sin^2\theta + c_{13}\cos^2\theta - 2c_{14}\sin\theta\cos\theta$$

$$c'_{14} = c_{14}(\cos^2\theta - \sin^2\theta) + (c_{13}-c_{12})\sin\theta\cos\theta$$

$$c'_{23} = c_{23}(\cos^4\theta + \sin^4\theta) + (c_{22}+c_{33}-4c_{44})\cos^2\theta\sin^2\theta + 2(c_{24}-c_{34})(\sin^2\theta - \cos^2\theta)\sin\theta\cos\theta$$

$$c'_{24} = c_{24}\cos^4\theta - c_{34}\sin^4\theta - 3\sin^2\theta\cos^2\theta(c_{24}-c_{34}) + \left[c_{33}\sin^2\theta - c_{22}\cos^2\theta - (c_{23}+2c_{44})(\cos^2\theta - \sin^2\theta)\right]\sin\theta\cos\theta$$

$$c'_{34} = -c_{24}\sin^4\theta + c_{34}\cos^4\theta + 3\sin^2\theta\cos^2\theta(c_{24} - c_{34}) + \left[c_{33}\cos^2\theta - c_{22}\sin^2\theta - (c_{23}+2c_{44})(\cos^2\theta - \sin^2\theta)\right]\sin\theta\cos\theta$$

$$c'_{56} = c_{56}(\cos^2\theta - \sin^2\theta) - (c_{55}-c_{66})\sin\theta\cos\theta \qquad \text{E.20 (cont.)}$$

$$c'_{15} = 0$$

$$c'_{16} = 0$$

$$c'_{25} = 0$$

$$c'_{26} = 0$$

$$c'_{35} = 0$$

$$c'_{36} = 0$$

$$c'_{45} = 0$$

$$c'_{46} = 0$$

APPENDIX F.

TABLES OF THE MATERIAL CONSTANTS OF QUARTZ.

Data taken from a paper by Koga et al (1958)

TABLE F.1

Elastic stiffness coefficients c_{ijkl} or c_{ij} at constant electric field in units of 10^{10} N/cm^2 (or 10^{11} dyne/cm^2)

ij \ kl	11 (1)	22 (2)	33 (3)	23 (4)	13 (5)	12 (6)
11 (1)	8.683	0.709	1.193	-1.8064	0	0
22 (2)	0.709	8.683	1.193	1.8064	0	0
33 (3)	1.193	1.193	10.59	0	0	0
23 (4)	-1.8064	1.8064	0	5.826	0	0
13 (5)	0	0	0	0	5.826	-1.8064
12 (6)	0	0	0	0	-1.8064	3.987

TABLE F.2

Piezoelectric stress coefficient e_{ijk} or e_{ij} at constant strain, in units of $10^{-2}As/m^2$

i \ jk (j)	11 (1)	22 (2)	33 (3)	23 (4)	13 (5)	12 (6)
1	17.5	-17.5	0	-4.07	0	0
2	0	0	0	0	4.07	-17.5
3	0	0	0	0	0	0

TABLE F.3

Relative dielectric constant (at constant strain) ϵ_{ij}

$$\epsilon_{ij} = \begin{pmatrix} 4.50 & 0 & 0 \\ 0 & 4.50 & 0 \\ 0 & 0 & 4.70 \end{pmatrix}$$

TABLE F.4

The value of the coefficients for BC-quartz (coordinate system rotated by angle $\theta = -58^{\circ}29'10''$ around +X axis) are given below. Elastic stiffness coefficients are in units of $10^{10} N/m^2$.

$c'_{11} = 8.6830$	(0, 0)
$c'_{22} = 10.4588$	(-0.056, 0)
$c'_{33} = 12.8112$	(0.066, 0)
$c'_{44} = 3.8228$	(-0.005, 0)
$c'_{55} = 2.8792$	(0, 0)
$c'_{66} = 6.9319$	(0, 0)
$c'_{12} = 2.6698$	(0.020, 0)
$c'_{13} = -0.7681$	(-0.020, 0)
$c'_{14} = 0.6041$	(-0.061, 0)
$c'_{15} = 0$	(0, 0.010)
$c'_{16} = 0$	(0, 0.138)
$c'_{23} = -0.8139$	(-0.005, 0)
$c'_{24} = -0.7167$	(-0.063, 0)
$c'_{25} = 0$	(0, -0.014)
$c'_{26} = 0$	(0, -0.105)
$c'_{34} = -0.9520$	(0.104, 0)
$c'_{35} = 0$	(0, -0.017)
$c'_{36} = 0$	(0, 0.001)
$c'_{45} = 0$	(0, 0.017)
$c'_{46} = 0$	(0, -0.024)
$c'_{56} = 0$	(-0.071, 0)

The first number in the brackets indicates the change in the elastic constant due to $+1^{\circ}$ misorientation in the Y'Z' plane, the second number indicates the change due to $+1^{\circ}$ misorientation in the Y'X' plane.

TABLE F.5

Piezoelectric stress coefficients in units of $10^{-2}As/m^2$

$e'_{1,11}$	= 16.67	$e'_{2,13}$	= - 6.625
$e'_{1,22}$	= - 1.77	$e'_{2,12}$	= - 6.105
$e'_{1,33}$	= -15.02	$e'_{3,13}$	= -10.685
$e'_{1,23}$	= - 6.08	$e'_{3,12}$	= - 9.855

rest: $e'_{1,13} = e'_{1,12} = e'_{2,11} = e'_{2,22} = e'_{2,33} =$
$= e'_{2,23} = e'_{3,11} = e'_{3,22} = e'_{3,33} = e'_{3,23} = 0$

APPENDIX G.

PROPAGATION AND REFLECTION OF PLANE ACOUSTIC WAVES.

The direction of propagation of a given mode of acoustic plane wave is defined as the direction normal to the planes of equal phase, therefore the wave vector k_i and also the phase velocity vector v_i are parallel to the propagation direction. The direction of energy flow generally does not coincide with the direction of propagation in an anisotropic medium. (Synge, 1956; Merkulov and Yakovlev, 1962) The energy flow vector is given in Equation 2.27 as

$$J_j^E = - T_{ij} \frac{\partial u_i}{\partial t} \qquad \text{G.1}$$

hence, for the mode M a vector parallel to the energy velocity (or beam velocity) vector can be calculated as

$$J_j^{E(M)} = - c_{ijk\ell} \cos(x_\ell, n) \alpha_k^M \alpha_i^M k^M \omega U^2 \qquad \text{G.2}$$

(The definition of the various symbols used in Appendix G is found in Section 3.2) The component of the beam velocity along the direction of propagation equals the phase velocity.

The phase velocity vectors of the L, FS and SS modes when drawn from the same origin for all possible directions define the three sheets of the velocity surface. The inverse phase velocities $\left(\frac{1}{v}\right)_i = \frac{v_i}{v^2}$ similarly define the three sheets of the inverse surface. The beam velocities give the three sheets of the wave surface (Musgrave, 1954).

The mathematical relationship between the 3 types of surfaces result in the following simple geometrical relationship:

a) If a tangent plane is fitted to the wave surface at the point defined by the beam velocity direction, then the vector

emanating from the origin perpendicularly to the tangent plane, with its tip in the plane, is the velocity vector.

b) If a tangent plane is fitted to the inverse surface at the point defined by the propagation direction, then the vector emanating from the origin perpendicularly to the tangent plane, with its tip in the plane, is the inverse beam velocity vector.

From the above it is obvious, that the beam velocity is parallel to the propagation direction only when the velocity surface is normal to the phase velocity vector.

In Fig. G.1 a portion of one of the flat surfaces of a piezoelectric crystal is excited in uniform phase. This surface is the wavefront at time t. According to Huygens' principle, well known in optics, every point on the wavefront gives rise to elementary wavelets, and the envelope to these wavelets is the wavefront at time t+dt. For an anisotropic medium, the elementary wavelets have a shape similar to the previously defined wave surface. The wavefronts at various instances are indicated in Fig. G.1. For the sake of simplicity only one acoustic mode is shown. The beam to which the vibrational energy is confined deviates from the propagation direction by an angle ε. There is also a spreading of the beam owing to the finite lateral dimensions of the source. The plane surface of the wavefront is tangent to an elementary Huygens wavelet at a point defined by the beam velocity direction, according to the geometrical relationship a). No exact mathematical solutions of diffraction problems in anisotropic solids are available because of the complicated shape of the beam and velocity surfaces.

The deviation of the acoustic beam from the propagation direction causes the beam to strike the side walls if the crystal

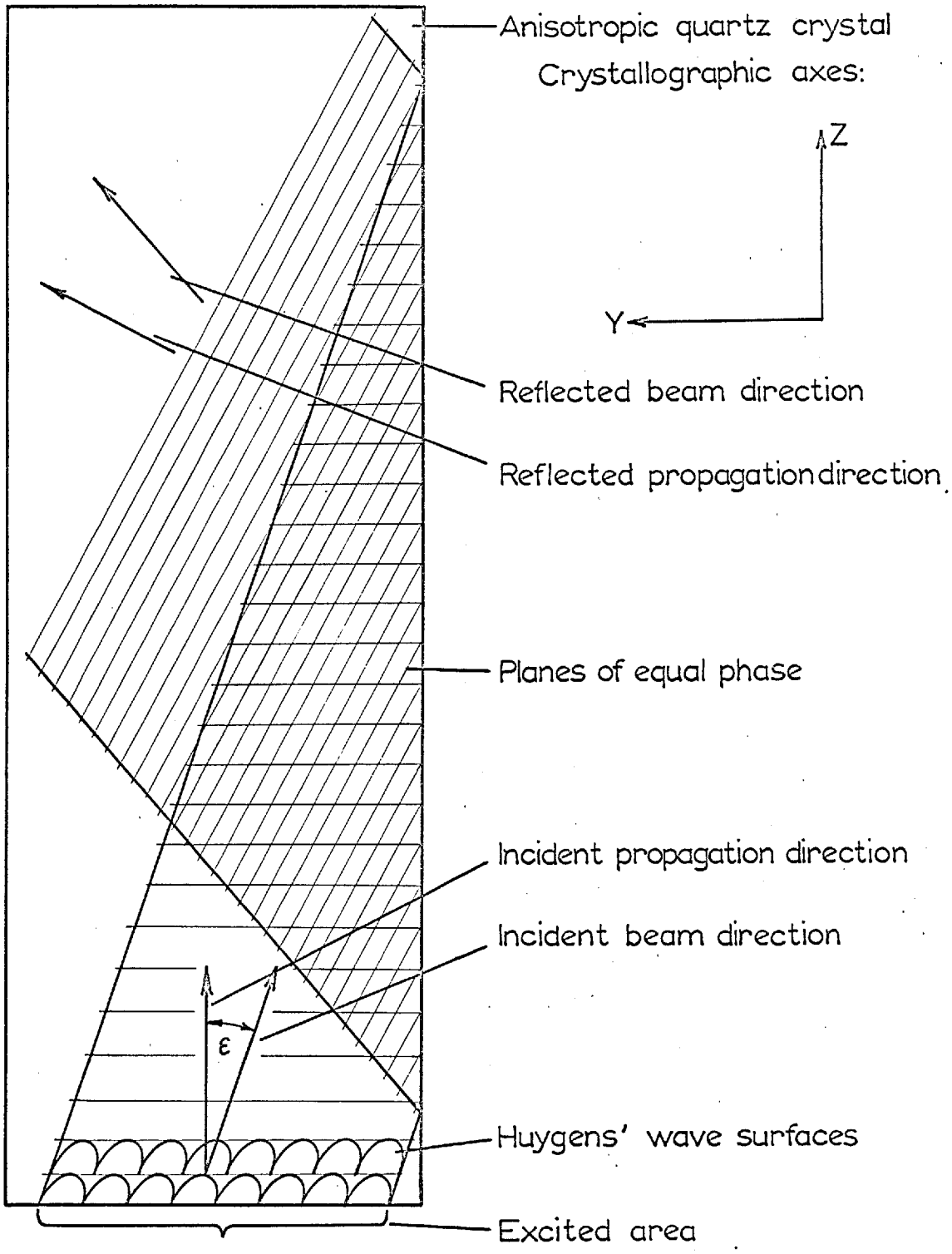


FIG. G.1 ACOUSTIC BEAM IN AN ANISOTROPIC MEDIUM.

rod is too long. The sketch of Fig. G.1 demonstrates this practical problem in a Z-cut rod for a shear wave mode with displacement u along the X axis. The wave incident on the sidewall is parallel to the surface, the single reflected wave is not. (In a case more general than the one illustrated, the incident wave gives rise to three reflected waves.) The directions of the reflected wave and beam are obtained in Fig. G.2 by a construction that makes use of Huygens' principle: the incident rays 1 and 2 reach the sidewall at times t_o and t_o+1 sec, respectively, giving rise to new waves starting from points A_1 and A_2. At time t_o+1 sec the Huygens wave generated at point A_1 grows into the wave surface, while that at point A_2 is a single point. A common tangent to these two wave surfaces is the reflected wave front, a normal to which gives the propagation direction of the reflected wave. The reflected beam lies in the direction defined by $\overline{AB}$.

The relative amplitudes of the various reflected (and transmitted, if any) waves can be found from the condition of continuity for the stress and displacement at the interface.

It can be seen from Fig. G.2 that the inverse velocities of the incident and reflected waves have the same value for their components along the surface. Also, the plane defined by the incident phase velocity and the surface normal contains all the reflected (and transmitted) phase velocity vectors. These geometrical relationships are generally true as they express the mathematical requirement that the conditions of continuity at the boundary be satisfied at all instances of time (Musgrave, 1960).

When the acoustic wave is incident normally on a solid-liquid interface, all the transmitted and reflected waves will be normal to the interface. The reflection coefficient ς_{SS}, expressing the ratio of the displacement amplitude in the reflected shear

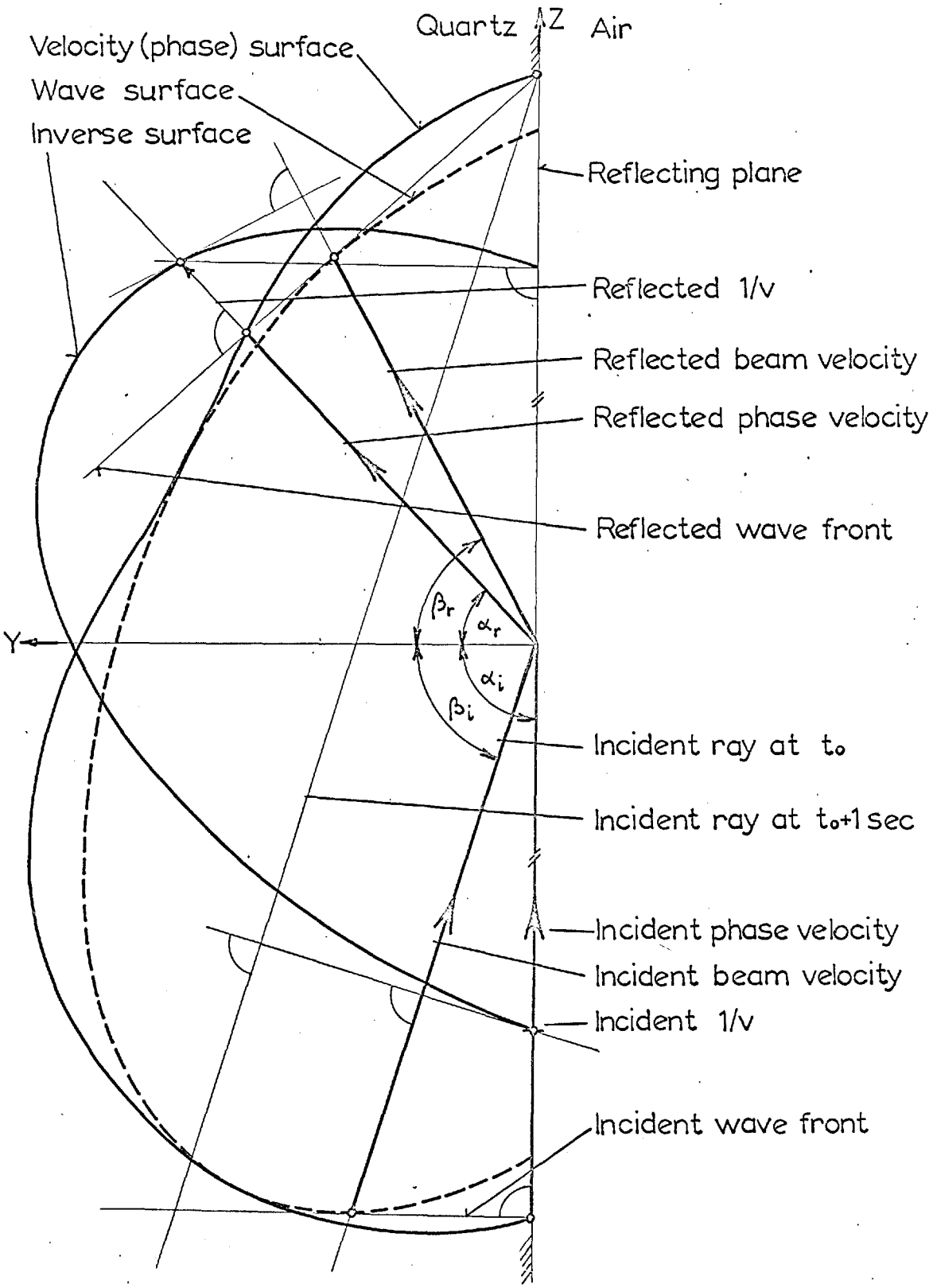


FIG. G.2 GEOMETRICAL RELATIONSHIPS AT PARALLEL INCIDENCE.

wave to that in the incident shear wave, with displacement directions parallel to the surface is given by the well known formula

$$\rho_{ss} = \frac{Z_S^s - Z_L^s}{Z_S^s + Z_L^s} \qquad G.3$$

If the normally incident wave is not a pure shear mode, it gives rise to reflected longitudinal waves, too. This situation is examined for the specific case when the incident wave is the quasi-shear mode along a rotated Y direction of quartz. The vectors of the displacements in the various waves are given below:

incident quasishear mode: $u_i^s = (\alpha_2 \bar{j} + \alpha_3 \bar{k})\, U_i^s$

reflected quasishear mode: $u_r^s = (\alpha_2 \bar{j} + \alpha_3 \bar{k})\, U_r^s$ G.4

reflected quasilongitudinal mode: $u_r^l = (\alpha_2 \bar{j} - \alpha_3 \bar{k})\, U_r^l$

where $\bar{j}$ and $\bar{k}$ are unit vectors in the x_2 and x_3 directions, respectively (the rest of the symbols are defined in Section 3.2). The other shear mode is parallel to the surface and is not generated by the incident quasimodes.

The continuity of displacement and stress can be expressed by the four equations below:

$$\begin{aligned}
\alpha_2(1 + \rho_{ss}) + \alpha_3 \rho_{ls} &= \tau_{ls} \\
-\alpha_2 \rho_{ls} + \alpha_3(1 + \rho_{ss}) &= \tau_{ss} \\
\alpha_2 Z_S^l{}_{ls} + \alpha_3 Z_S^s(1 - \rho_{ss}) &= Z_L^s \tau_{ss} \\
\alpha_2 Z_S^s(1 - \rho_{ss}) - \alpha_3 Z_S^l \rho_{ls} &= Z_L^l \tau_{ls}
\end{aligned} \qquad G.5$$

where ϱ_{ss} and ϱ_{ls} are the reflection coefficients for reflected shear wave and reflected longitudinal wave, resulting from an incident shear wave, respectively. Similarly τ_{ss} and τ_{ls} are transmission coefficients for transmitted shear wave and transmitted longitudinal wave, resulting from an incident shear wave. Furthermore, Z^l $(= \varrho v_l)$ and Z^s $(= \varrho v_s)$ are shear and longitudinal impedances respectively, and the subscript indicating whether of the solid or the liquid. The property expressed by Equation 11.2 has been used.

Solving Equation G.5 for ϱ_{ss}, one finds that (taking into account that $\alpha_2 = \sin\alpha$ and $\alpha_3 = \cos\alpha$):

$$\varrho_{ss} = \frac{Z_S^s - Z_L^s - \sin^2\alpha \, (Z_S^l + Z_S^s) \dfrac{Z_L^l - Z_L^s}{Z_S^l + Z_L^l}}{Z_S^s + Z_L^s + \sin^2\alpha \, (Z_S^l - Z_S^s) \dfrac{Z_L^l - Z_L^s}{Z_S^l + Z_L^l}} \qquad \text{G.6}$$

APPENDIX H.

DETAILS OF COMPUTER CALCULATIONS.

The elastic and piezoelectric properties of quartz were calculated for a large number of propagation directions using the University of Glasgow DEUCE computer. The same calculation was performed at each grid point given in Section 5.1. First the elastic, dielectric and piezoelectric constants were transformed according to the expressions of Appendix E (Equations E.4 - E.19), so that the x_2 direction lay along the direction of propagation, as defined by the selected grid point. The calculation of the rotated tensor coefficient could not be programmed according to the basic transformation formulae (Equations A.1 - A.2) because, due to the relative slowness of the DEUCE computer, such a programme would have needed excessively long computer times. The programming according to Appendix E could be organised to make use of the identical blocks appearing in the transformation expressions.

The rotated tensor coefficients were used to calculate the six rotated stiffened coefficients $c_1 - c_6$, with

$$c_1 = \bar{c}_{1212},\ c_2 = \bar{c}_{1222},\ c_3 = \bar{c}_{1223},\quad c_4 = \bar{c}_{2222},\ c_5 = \bar{c}_{2223},\ c_6 = \bar{c}_{2323}$$

The stiffened coefficients were substituted into the determinantal equation (Equation 3.54) giving the following cubic:

$$e^3 - 3ae^2 - be + c = 0 \qquad \text{H.1}$$

where $a = \frac{1}{3}(c_1 + c_4 + c_5)$

$$b = c_2^2 + c_3^2 + c_5^2 - c_1c_4 - c_4c_6 - c_6c_1 \qquad \text{H.2}$$

$$c = c_1c_5^2 + c_4c_3^2 + c_6c_2^2 - c_1c_4c_6 - 2c_2c_3c_5$$

The three solutions of the cubic are the three effective elastic constants

$$\text{L mode:} \quad e^1 = \frac{2}{\sqrt{3}}\sqrt{p}\,\cos\vartheta + a$$

$$\text{FS mode} \quad e^2 = \frac{2}{\sqrt{3}}\sqrt{p}\,\cos\left(\vartheta + \frac{2\pi}{3}\right) + a \qquad \text{H.3}$$

$$\text{SS mode} \quad e^3 = \frac{2}{\sqrt{3}}\sqrt{p}\,\cos\left(\vartheta + \frac{4\pi}{3}\right) + a$$

where

$$p = 3a^2 + b$$

$$q = 2a^3 + ab - c \qquad \text{H.4}$$

$$\vartheta = \frac{1}{3}\cos^{-1}\left(\frac{3\sqrt{3}\,q}{2p\sqrt{p}}\right)$$

The following calculation was repeated for each of the three modes.

The phase velocity of mode M was calculated by

$$v^M = \sqrt{\frac{e^M}{\rho}} \qquad \text{H.5}$$

Substituting the eigenvalue e^M back into the determinant, the 9 cofactors of the determinant were calculated. The ratio of the cofactors gives the ratio of the direction cosines of the eigenvectors, but it is possible that all cofactors belonging to one line are zero. To prevent failing of the programme, the sums of the squares of the three cofactors belonging to each row were calculated and the row with the largest sum selected. Then dividing the 3 cofactors of the selected row with the root of the sum of their squares gave directly the direction cosines α_1^M, α_2^M and α_3^M. The angle δ made by the displacement vector with the direction of propagation was obtained by

$$\delta = \cos^{-1}\alpha_2^M. \qquad \text{H.6}$$

The components of the internal excitation vector $\left(e_i^M\right)_I$ (Equation 4.38a) were calculated with the help of the direction cosines and the rotated piezoelectric coefficients. The sum of the squares

$$\left(e^M\right)_I^2 = \left(e_1^M\right)_I^2 + \left(e_2^M\right)_I^2 + \left(e_3^M\right)_I^2 \qquad \text{H.7}$$

gave the relative efficiency of excitation and the angle θ gave the inclination of the preferred direction of excitation when

$$\theta^M = \cos^{-1} \frac{\left(e_2^M\right)_I}{\sqrt{\left(e^M\right)_I^2}} \qquad \text{H.8}$$

The very large number of output data was obtained on punched cards, and so arranged that the following 10 data belonging to mode M at a given grid point, was punched on a single card:

Reference number of grid point,

$$\nu^M,\ \alpha_1^M,\ \delta^M,\ \alpha_3^M,\ \left(e_1^M\right)_I,\ \left(e_2^M\right)_I,\ \left(e_3^M\right)_I,\ \theta^M,\ \frac{1}{10\ \ell n 10} \cdot \ell n \left(e^M\right)_I^2$$

The cards were punched out automatically in the form of tables. The contour graphs of Figs. 5.3 - 5.14 were plotted manually from the printed data.

APPENDIX I.

ANALYSIS OF OPERATION OF PLANAR TRIODE OSCILLATORS.

Planar triodes extend the operational frequency range of ordinary triodes from about 200Mc/s up to 6kMc/s. The conventional low-frequency electronic tube is unsuitable for operation at microwave frequencies due mainly to transit time and lead impedance effects.

The transit time τ of the electrons travelling from cathode to grid should ideally be much smaller than a cycle of the frequency used, and is given approximately by (Diemer and Knol, 1952)

$$\tau = 0{,}67 \left(\frac{d}{J}\right)^{\frac{1}{3}} \qquad \text{(nanosec.)} \qquad \text{I.1}$$

where d is the distance in cm from cathode to grid and J is the peak current density in A/cm^2. For a short transit time the interelectrode spacing must be small and the cathode current density high. The favourable effect of a large cathode current density can be explained by the fact that the higher potential needed in the grid plane in order to obtain a denser current gives rise to higher electron velocities and thus to shorter transit times.

To combat lead impedance effects, planar triodes are constructed in such a manner that the connections to their electrodes are made by large discs or cylinders which can be made part of a distributed circuit (transmission line or cavity resonator). The large connecting surfaces have much lower inductance and also introduce a smaller series resistance (proportional to the square root of ω owing to skin effects) than the usual thin wire leads. With silver plating the effective series resistance of the disc seals is reduced to 0.1Ω at 3000Mc/s.

The valves used in the oscillators of Section 6.4 are type 2C39A, manufactured by Standard Telephones and Cables Ltd. With the highest current densities available from modern oxide-coated cathodes, these valves have a grid to cathode spacing of 0.005" for the transit angle ($\omega\tau$) to be 0.25 radian at 500Mc/s. All the electrodes are in parallel planes. The mesh grid is made of 0.002" diameter gold plated wires at a pitch of 0.0072" both ways. Mechanical and electrical data relating to the 2C39A valve are given in Table I.1.

TABLE I.1

SUMMARY OF PROPERTIES FOR THE VALVE 2C39A

	Cathode-Grid Gap	Grid-Anode Gap
Electrode spacing	0.005"	0.0225"
Capacitance (hot)	7.6 pF	2.0 pF
Admittance (typically) at 1000Mc/s		
Conductance	g_m = 25mMho	$1/r_a$ = 0.25mMho
Susceptance	b_c = 47mMho	b_a = 12mMho
Amplification factor		100
Max. DC anode voltage		
guaranteed		12kV
used regularly		3.5kV
Max. mean anode dissipation without cooling		15W
Max. mean grid dissipation		2W

The microwave triode oscillator or amplifier can be regarded not only as the high frequency extension of the common triode amplifier with values for the transconductance and input reactance modified by transit time effects but also as a kind of 2-cavity klystron. (Chodorow and Susskind, 1964) In the microwave triode an electron stream is formed in the space between the cathode and the grid, the velocity of the electrons in the stream depending upon the electric fields in the region, i.e. they are velocity modulated by the cathode-grid potential. The faster electrons get

through the grid, the slower ones do not: the conversion to density modulation (bunching) thus takes place by a sorting process. A beam of varying density accelerated by the positive collector (anode) potential then passes through the grid-anode region inducing an alternating voltage in these electrodes, or in other words, giving up some of its energy to the electromagnetic field of the grid-anode cavity. After delivering the energy the beam has to be collected. This is done by the anode in the triode, although a mesh anode and a separate collector would be possible in principle. To maintain oscillations a fraction of the output signal appearing in the anode-grid cavity has to be fed back to the cathode-grid cavity.

The small signal equivalent circuit of the oscillator is shown in Fig. I.1, where the small loading of the feedback circuit on the anode-grid cavity is represented by R_{fb} and the feedback path is not shown.

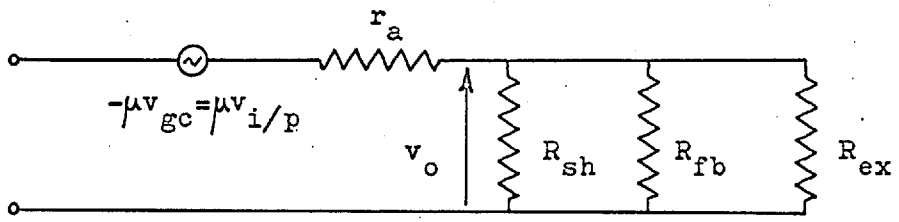


FIG. I.1. EQUIVALENT CIRCUIT OF OSCILLATOR.

The analysis by Llewellyn and Paterson (1944) showed that the effect of transit time upon the input admittance of a triode is a reduction in the value of transconductance by 16% for a transit angle of $\pi/2$. At 1500Mc/s the transit angle is estimated to be $\pi/4$ for the 2C39A valve therefore transit time effects are neglected in the following analysis of the oscillator.

Measurements on the anode-grid cavity of the 1000Mc/s oscillator gave the following results:

a) Unloaded Q with zero heater voltage and cathode short-circuit plunger right at the feedback loop:

$$Q_u = 292$$

Therefore shunt impedance (e.g. Moreno, 1958, Chapter 13) of cavity only:

$$R_{sh} = 5.9k\Omega$$

b) Unloaded Q with heater on and cathode plunger in optimum position:

$$Q_u = 152$$

Shunt impedance in this condition:

$$R = 3.04k\Omega$$

c) Input VSWR with coupling loop rotated to optimum working position:

$$S = 1.2, \text{ maximum at loop.}$$

Effective transformer ratio of loop:

$$n = \sqrt{3040/1.2x50} = 7.1$$

50Ω external load transformed into equivalent circuit of cavity:

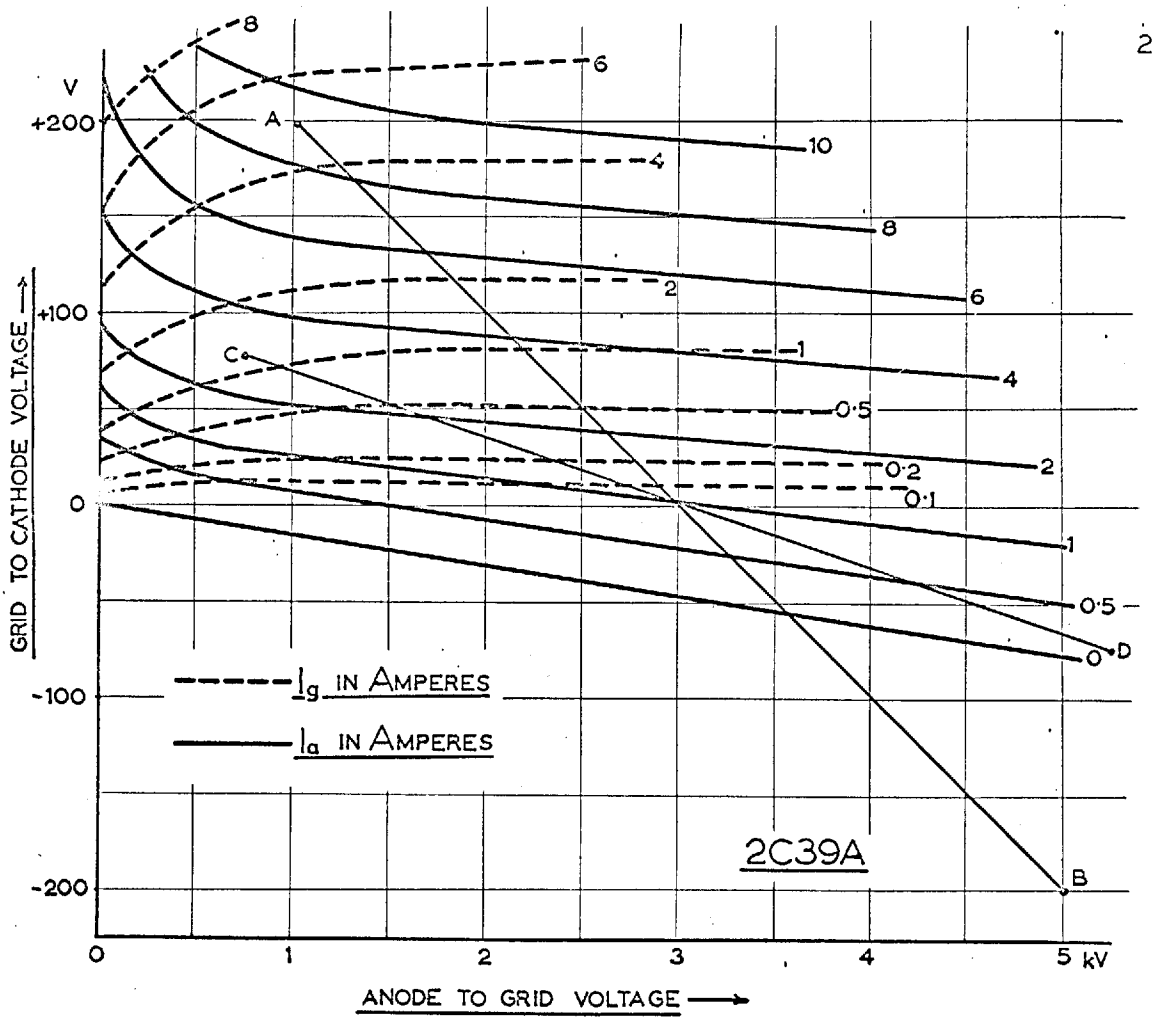
$$R_{ex} = 50x7.1^2 = 2.5k\Omega$$

Voltage to dissipate 1kW in external load:

$$V = \pm 2250V \text{ peak.}$$

With the values of circuit elements obtained for the 1000Mc/s equivalent circuit the stage input impedance is 56Ω and the voltage gain is 30 (power gain = 13dB). To maintain oscillations the minimum input voltage is ±75V peak, when R_{fb} is approximately 50kΩ and the effective driving impedance is 2Ω.

The resonant anode circuit owing to its high Q can support oscillations only of an odd number of times the fundamental frequency. It is assumed that both input and output waveforms are



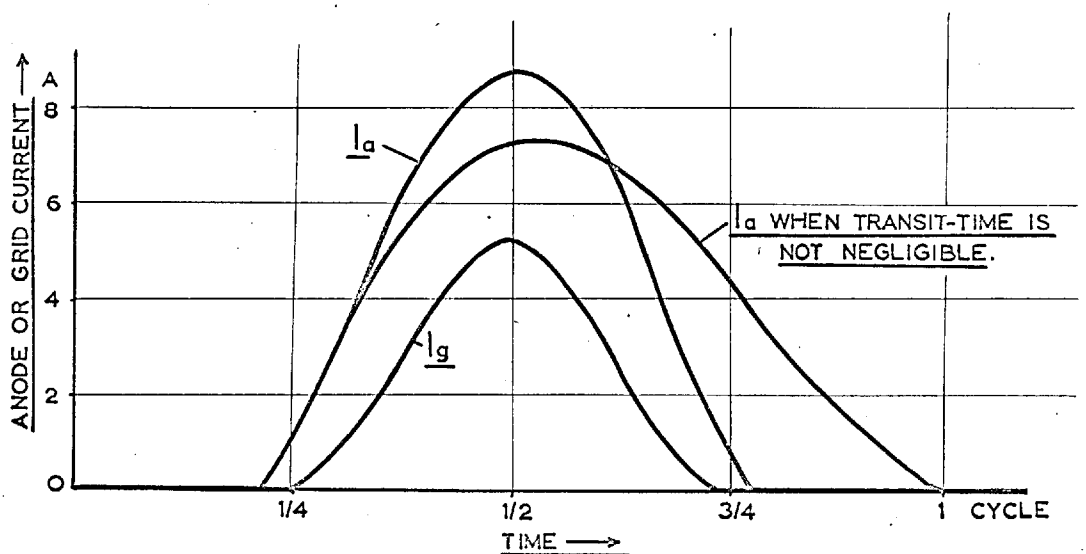


FIG. I. 2 CONSTANT CURRENT CHARACTERISTICS OF 2C39A AND SOME CURRENT PULSES OF OSCILLATOR.

pure sinewaves and are in phase if the oscillator is not overdriven. Therefore in the constant current characteristics of Fig. I.2 (slightly modified from published form to show anode-grid, rather than the usual anode-cathode voltages on the abscissa) a straight line represents all corresponding instantaneous values of anode and grid voltages. (Line CD). Instantaneous values of anode and grid currents can be read off from the characteristics indicating a class C type operation, since the currents flow during only a portion of the full cycle.

In the lower part of Fig. I.2 curves of the anode and grid waveforms are shown for operating line AB representing nearly the hardest possible drive. Harmonic analysis of the anode current waveform gave the amplitude of the 3rd harmonic as 10% of the fundamental in this grossly over-driven condition. (2nd and other even harmonics are not supported by the cavity.) Therefore for a more moderate feedback the current waveform is almost purely sinusoidal so the previous assumption of this condition is justified. The limit of maximum available pulse power is imposed by cathode saturation or grid dissipation if the pulse repetition frequency is high usually before the maximum rated anode dissipation is reached.

The effect of not negligible transit time in the cathode-grid gap is a reduced transconductance, and in the grid-anode gap a more extended current pulse, (Fig. I.2), thus a larger anode dissipation and lower efficiency. These effects reduce the power output of the oscillators at higher frequencies.

APPENDIX J.

DENSITY AND VISCOSITY DATA FOR THE LIQUIDS INVESTIGATED IN CHAPTER 12.

	sec-butyl benzene	n-butyl benzene	n-propyl benzene	di-iso-butyl phthalate	di-2-ethyl-hexyl phthalate
Melting point (°K)...	197.7	185.2	173.7	-	-
ρ_r (gm.ml^{-1}).....	0.878	0.876	0.879	1.052	0.996
a (°K^{-1}) 0.000903		0.000922	0.000951	0.000760	0.000753
Range of density measurements (°K)..160-320		160-320	150-320	250-300	250-300
High temperature form:					
A'	-7.149	-7.357	-7.180	-6.948	-9421
B' (°K)	414.8	499.9	422.0	593.0	1305.0
T_o (°K)	128.9	114.1	118.5	193.3	150.6
Range (°K)	303-196	330-187	320-182	370-283	328-253
T_g (°K)	140.1	127.5	129.9	209.4	183.7
v_f at T_g (ml.gm^{-1}).	0.010	0.011	0.010	0.011	0.023
Intersection temperature (°K)...	191	181	176	ca.278	-
Low temperature form:					
A'	-14.543	-12.235	-0.949	-12.018	-
B' (°K)	1306.4	1003.7	684.9	1598.2	-
T_o (°K)	98.6	101.4	109.7	144.9	-
Range (°K)	186	175	170	273	-
T_g (°K)	128.0	125.2	126.9	183.0	-
v_f at T_g (ml.gm^{-1}).	0.024	0.019	0.016	0.025	-

REFERENCES.

Baranskii, K. N. (1957)
Dokl. Akad. Nauk. SSSR 114 517

Barlow, A. J. (1959)
Ph.D. Thesis, University of London.

Barlow, A.J., Erginsav, A. & Lamb, J. (1966)
Viscoelastic Relaxation of Supercooled Liquids. Part II.
(to be published)

Barlow, A. J., Harrison, G., Richter, J., Seguin, H. & Lamb, J. (1961)
Lab. Practice 10 786

Barlow, A. J. & Lamb, J. (1959)
Proc. Roy. Soc. A253 52

Barlow, A. J., Lamb, J. & Matheson, A. J. (1966)
Proc. Roy. Soc. A292 322

Barlow, A. J., Lamb, J., Matheson, A. J., Padmini, P. R. K. L. &
Richter, J. (1966)
Viscoelastic Relaxation of Supercooled Liquids. Part I.
(to be published)

Barlow, A. J., Lamb, J., Matheson, A. J. & Richter, J. (1965)
Chem. Soc. Symposium, Aberystwith
(Chem. Soc. Special Publication No. 20,
Academic Press, London, 1966)

Bechmann, R. (1960)
Proc. I.R.E. 48 367

Bömmel, H. E. & Dransfeld, K. (1960)
Phys. Rev. 117 1245

Carr, P. H. & Strandberg, M. W. P. (1962)
J. Phys. Chem. Solids 23 923

Chadwick, P. & Sneddon, I. N. (1958)
J. Mech. Phys. Solids 6 223

Chadwick, P. (1960)
Progress in Solid Mechanis (ed. Sneddon & Hill) 1 265
North Holland Publ. Co. Amsterdam.

Chang, W. S. C., Cromack, J. & Siegman, A. E. (1959)
J. Electronics & Control 6 508

Chodorow, M. & Susskind, C. (1964)
Fundamentals of Microwave Electronics. McGraw-Hill, N.Y.

Christoffel, E. B. (1877)
Ann. Mat. (2) 8 193

Cosserat, E. & Cosserat, F. (1909)
pp 953-1173 of O. D. Chwolson: Traité de Physique, Paris.

Curie, P. (1908)
Oeuvres, p. 129 Paris.

deGroot, S. R. & Mazur, P. (1962)
Non-equilibrium Thermodynamics.
North Holland Publ. Co. Amsterdam.

Diemer, G. & Knol, K. S. (1952)
Philips Tech. Rev. 14 153

Doolittle, A. K. (1951)
J. App. Phys. 22 1471

Doolittle, A. K. & Doolittle, D. B. (1957)
J. App. Phys. 28 901

Eringen, A. C. (1962)
Non-linear Theory of Continuous Media.
McGraw-Hill, New York.

Farnell, G. W. (1961)
Canad. J. Phys. 39 65

Fein, A. E. & Smith, C. S. (1952)
J. App. Phys. 23 1212

Fano, R. M., Chu, L. J. & Adler, R. B. (1960)
Electromagnetic Energy, Field and Forces.
J. Wiley, New York.

Ferry, J. D. (1961)
Viscoelastic Properties of Polymers.
J. Wiley, New York.

Fujisawa, K. (1958)
I.R.E. Trans. MWTT. 6 344

Gold, L. (1950)
J. App. Phys. 21 541

Herzfeld, K. F. & Rice, F. O. (1928)
Phys. Rev. 31 691

Herzfeld, K. F. & Litovitz, T. A. (1959)
Absorption and Dispersion of Ultrasonic Waves.
Academic Press, New York.

Hirai, N. & Eyring, H. (1958)
J. App. Phys. 29 810

Hutson, A. R. & White, D. L. (1962)
J. App. Phys. 33 40

Jacobsen, E. H. (1959)
Phys. Rev. Lett. 2 249

Jacobsen, E. H. (1960)
J. Acoustic. Soc. Am. 32 949

Jaffe, H. & Smith, C. S. (1961)
Phys. Rev. 121 1604

Joel, N. & Wooster, W. A. (1958)
Nature 182 1078

Joel, N. & Wooster, W. A. (1960)
Acta Cryst. 13 516

Jones, C. K., Klemens, P. G., & Rayne, J. A. (1964)
Phys. Letters 8 31

Koga, I., Aruga, M. & Yoshinaka, Y. (1958)
Phys. Rev. 109 1467

Kyame, J. J. (1949)
J. Acoust. Soc. Am. 21 159

Lamb, J., Redwood, M. & Shteinshleifer, Z. (1959)
Phys. Rev. Lett. 3 28

Lamb, J. & Richter, J. (1966a)
Electronics Lett. 2 73

Lamb, J. & Richter, J. (1966b)
Proc. Roy. Soc. A293 (to be published)

Lamb, J. & Richter, J. (1966c)
Cavity Resonators for Piezoelectric Surface Excitation.
(to be published in J. Acoust. Soc. Am.)

Lamb, J. & Seguin, H. (1966)
J. Acoust. Soc. Am. 39 159

Laval, J. (1957)
J. Phys. Rad. 18 247, 289, 369

Lawson, J. L. & Uhlenbeck, G. E. (1950)
Threshold Signals. MIT. Rad. Lab. Series No. 24
McGraw-Hill, New York.

Lindon, P. (1965)
Ph.D. Thesis, University of Glasgow.

Llewellyn, F. B. & Paterson, L. C. (1944)
Proc. I.R.E. 32 144

Lücke, K. (1956)
J. App. Phys. 27 1433

Mason, W. P. (1958)
Physical Acoustics and the Properties of Solids.
D. Van Nostrand, New York.

Mason, W. P. (1960)
J. Acoust. Soc. Am. 32 458

Mason, W. P., Baker, W. O., McSkimin, H. J. & Heiss, J. H. (1949)
Phys. Rev. 75 936

Mason, W. P. & Bateman, T. B. (1964)
J. Acoustic. Soc. Am. 36 644

Mason, W. P., McSkimin, H. J. & Bateman, T. B. (1962)
4th Int. Congr. on Acoustics, Copenhagen.

Maxwell, J. C. (1867)
Phil. Trans. Roy. Soc. London A157 49

McSkimin, H. J. (1952)
J. Acoust. Soc. Am. 24 355

McSkimin, H. J. (1962)
J. Acoust. Soc. Am. 34 1271

McSkimin, H. J. (1964)
Phys. Acoustics (ed. Mason) Vol IA
Academic Press, New York.

Meister, R., Marhoeffer, C. J., Sciamanda, R., Cotter, L. &
Litovitz, T. (1960)
J. App. Phys. 31 854

Merkulov, L. G. & Yakovlev, L. A. (1962)
Sov. Phys. Acoustics 8 72

Mindlin, R. D. & Tiersten, H. F. (1962)
Arch. Rat. Mech. & Anal. 11 415

Moreno, T. (1958)
Microwave Transmission Design Data.
Dover Publ. Inc. New York.

Musgrave, M. J. P. (1954)
Proc. Roy. Soc. A226 339, 356.

Musgrave, M. J. P. (1956)
Proc. Roy. Soc. A236 352

Musgrave, M. J. P. (1959)
Rep. Prog. Phys. 22 74

Musgrave, M. J. P. (1960)
Geophys. J. Roy. Astron. Soc. 3 406

Musgrave, M. J. P. (1961)
Prog. Solid Mech. Vol. II 62
North Holland Publ. Co. Amsterdam

Nava, R., Azrt, R., Ciccarello, I. & Dransfeld, K. (1964)
Phys. Rev. 134 A581

Prager, W. (1961)
Introduction to Mechanics of Continua.
Ginn & Co. Boston

Raleigh, (Lord) (1945)
The Theory of Sound
Dover Publications, New York.

Redwood, M. (1957)
Ph.D. Thesis, University of London.

Redwood, M. & Lamb, J. (1956)
Proc. I.E.E. 103 773

Richter, J. (1962)
Modern Physical Acoustics
Notes for Postgraduate Lecture Series.

Richter, J. (1966)
Velocity, Polarisation and Optimum Surface Excitation of Acoustic Waves in Quartz. (to be published)

Schelkunoff, S. A. (1944)
Proc. I.R.E. 32 83

Smith, G. F., Smith, M. M. & Rivlin, R. S. (1963)
Arch. Rat. Mech. & Anal. 12 93

Smullin, L. D. & Montgomery, C. G. (1948)
Microwave Duplexers. MIT Rad. Lab. Series No. 14
McGraw-Hill, New York.

Stewart, J. L. & Stewart, E. S. (1963a)
J. Acoust. Soc. Am. 35 913

Stewart, E. S. & Stewart, J. L. (1963b)
J. Acoust. Soc. Am. 35 975

Schwartz, M. (1959)
Information, Transmission, Modulation and Noise.
McGraw-Hill, New York.

Synge, J. L. (1956)
Proc. Roy. Irish. Acad. 58A 13

Tempest, W. (1963)
Electronic Eng. 35 814

Toupin, R. A. (1962)
Arch. Rat. Mech. & Anal. 11 385

Toupin, R. A. (1964)
Arch. Rat. Mech. & Anal. 17 85

Truesdell, C. (1960)
The Classical Field Theories. Physics Handbook III/1
Springer Verlag, Berlin.

Turnbull, H. W. (1939)
Theory of Equations
Oliver & Boyd, Edinburgh.

Voigt, W. (1892)
Ann. d. Phys. 47 671

Weyl, H. (1946)
The Classical Groups, their Invariants and Representation.
Princeton University Press

Zubov, V. G. & Firsova, M. N. (1956)
Kristallografia, 1 546